Blood Flow Dynamics in Surviving Patients with Repaired Tetralogy of Fallot

Maria Boumpouli

Department of Biomedical Engineering

University of Strathclyde

This thesis is submitted for the degree of

Doctor of Philosophy

2021

This thesis is the result of the author's original research. It has been composed by the author and has not been previously submitted for examination which has led to the award of a degree.

The copyright of this thesis belongs to the author under the terms of the United Kingdom Copyright Acts as qualified by University of Strathclyde Regulation 3.50. Due acknowledgement must always be made of the use of any material contained in, or derived from, this thesis.

Signed:

Date:

Abstract

Tetralogy of Fallot (TOF) is a congenital heart disease that causes structural abnormalities in the pulmonary arteries, which in turn disrupt the blood flow. Surgical repair is necessary early in childhood, but chronic complications are common in the adult surviving patients. Pulmonary valve replacement is an operation performed in the repaired TOF (rTOF) patients to overcome the right ventricular overload, but the optimal timing remains a challenge. The main research question is whether the haemodynamic environment of the pulmonary junction can clarify the interplay between the upstream and downstream pulmonary vasculature. Therefore, an extensive analysis of the effect of morphological and flow characteristics in healthy and rTOF models was performed, under various boundary conditions (BCs). The effects of branch angle and origin, branch stenosis, flow splits and pulmonary resistance were investigated in idealised two-dimensional geometries, representative of healthy and rTOF cases, explaining the elevated pressure in the LPA, and clearly showing that downstream pressure and peripheral resistance alter the flow development and the flow split between the two daughter branches. Various modelling parameters were also tested, demonstrating the importance of the valve, and how it disturbs the flow patterns along the MPA. The elasticity of arterial wall had a minimal effect on the flow development while the WSS deviated based on the rheological model assumed. Finally, anatomically-realistic three-dimensional models of rTOF patients and healthy volunteers were reconstructed and morphological and flow features were analysed. Higher curvature and tortuosity were correlated with more complex secondary flow patterns, and higher Reynolds and Dean numbers, with

increased regions of time-averaged wall shear stress. More importantly, the importance of patient-specificity in the rTOF models, and the variability of the geometric and flow characteristics within the population was highlighted, contrary to the observations in the healthy models. The results of this work could help clinicians evaluate the haemodynamic environment in the rTOF population and potentially predict patients at higher risk, prior to the appearance of severe complications.

List of Publications

Journal articles:

- Boumpouli M., Danton M.H.D., Gourlay T., Kazakidi A., 2020. Blood flow simulations in the pulmonary bifurcation in relation to adult patients with repaired tetralogy of Fallot. Medical Engineering and Physics. 85, 123-138. DOI: 10.1016/j.medengphy.2020.09.014 [published]. The research paper has received two citations.
- Boumpouli M., Sauvage E., Capelli C., Schievano S., Kazakidi A., 2021. Characterization of flow dynamics in the pulmonary bifurcation of patients with repaired Tetralogy of Fallot: a computational approach. Frontiers in Cardiovascular Medicine. DOI: 10.3389/fcvm.2021.703717 [published].
- Johnston L., Boumpouli M., Kazakidi A., 2021. Hemodynamics in the Aorta and Pulmonary Arteries of Congenital Heart Disease Patients: A Mini Review. Journal of Cardiology and Cardiovascular Sciences. 5, 1-5. DOI : 10.29245/2578-3025/2021/2.1213 [published].

Journal/Conference proceedings contributions:

- Boumpouli M, Danton M, Gourlay T, Kazakidi A., 2020. Understanding the blood flow in realistic and idealised models of the pulmonary bifurcation. Heart Journal. 106, A3–4. DOI: 10.1136/heartjnl-2020-SCF.7.
- Boumpouli M., Danton M., Gourlay T., Kazakidi A., 2018. Hemodynamics in the Pulmonary Bifurcation in Relation to Adults with Congenital Heart Disease: Effect of Branching Angle and Origin. In: Proceedings of the 6th

European Conference on Computational Mechanics. International Centre for Numerical Methods in Engineering, CIMNE, GBR. 1833-1844. The conference paper has received one citation.

Conference Presentations:

- Boumpouli M., Sauvage E., Capelli C., Schievano S., Kazakidi A. Patient-specific blood flow simulations in the pulmonary bifurcation of patients with tetralogy of Fallot. Virtual 14th WCCM-8th ECCOMAS, Paris, 01/2021 [oral]
- Boumpouli M., Sauvage E., Capelli C., Schievano S., Gourlay T., Kazakidi A. A methodology to investigate the blood flow in patient-specific models of tetralogy of Fallot. 33rd Scottish Fluid Mechanics Meeting, online, 05/2020 [oral]
- Boumpouli M., Danton M., Gourlay T., Kazakidi A. Understanding the blood flow in realistic and idealised models of the pulmonary bifurcation. 23rd Annual Meeting- Scottish Cardiovascular Forum, Glasgow, UK, 02/2020 [oral]
- Boumpouli M., Danton M., Gourlay T., Kazakidi A. Hemodynamics in the pulmonary bifurcation: Effect of geometry and boundary conditions. BioMedEng19, London, UK, 09/2019 [poster]
- Boumpouli M., Danton M., Gourlay T., Kazakidi A. Blood flow in the pulmonary bifurcation under healthy and diseased conditions. 32nd Scottish Fluid Mechanics Meeting, Dundee, UK, 05/2019 [poster]
- Boumpouli M., Danton M., Gourlay T., Kazakidi A. Computation of blood flow in the pulmonary bifurcation: towards a more effective treatment for adults with congenital heart disease. BioMedEng18, London, UK, 09/2018 [poster].

- Boumpouli M., Danton M., Gourlay T., Kazakidi A. Haemodynamic Analysis in Arterial Models in relation to Pulmonary Valve Treatment in Adults with Congenital Heart Disease. 13th World Congress on Computational Mechanics-2nd Pan American Congress on Computational Mechanics, New York City, USA, 07/2018 [oral].
- Boumpouli M., Danton M., Gourlay T., Kazakidi A. Blood flow simulations in the pulmonary bifurcation for the assessment of valve replacement in adult patients with congenital heart disease. 8th World Congress of Biomechanics, Dublin, Ireland, 07/2018 [poster].
- Boumpouli M., Danton M., Gourlay T., Kazakidi A. Haemodynamic Analysis in Arterial Models in relation to Pulmonary Valve Treatment in Adults with Congenital Heart Disease. ECCOMAS ECCM-ECFD 2018, Glasgow UK, 06/2018 [oral].
- Boumpouli M., Danton M., Gourlay T., Kazakidi A. Blood flow simulations in models of the pulmonary bifurcation to facilitate treatment of adults with congenital heart disease. 31st Scottish Fluid Mechanics Meeting, Aberdeen, UK, 05/2018 [oral].

Contents

List of Figures

3.8 Non-dimensionalised wall shear stress (WSS) distribution along the inner wall of the models of Fig. 3.5, for steady Newtonian flow, Re=650: (a) models with different branching angles; (b) asymmetric models with different branch origins; (c) symmetric Y-Junction without and with local stenosis; (d) asymmetric and symmetric Y-Junctions without and with hypoplastic LPA. The zero position in the abscissae signifies the stagnation point (S, SR, or SL, see Fig. 3.5).

3.9 Effect of pressure boundary condition at branch outlet. (a) Non-dimensionalised velocity contours overlaid by streamlines. (b) velocity profiles along the RPA and LPA. (c) Non-dimensionalised WSS distribution along the inner wall for the geometry of Fig. 3.5 (vi) (solid line) and model with (i) an extended right pulmonary branch with $\frac{|\Delta P|}{0.5\rho U^2}$=0, (ii) $\frac{|\Delta P|}{0.5\rho U^2}$=0.026 with PLPA > PRPA and (iii) $\frac{|\Delta P|}{0.5\rho U^2}$=0.015 with PLPA > PRPA. Steady Newtonian flow, Re=650.

3.10 Effect of outlet boundary conditions. (a) Non-dimensionalised velocity contours. (b) Non-dimensionalised WSS distribution along the inner wall for the geometry of Fig. 3.5 (ix) (solid line) with (i)-(ii) flow split dictated by (i) Murray's Law (Q_{LPA}:Q_{RPA} is 11:89%) and (ii) "outflow splitting" method (Q_{LPA}:Q_{RPA} is 20:80%), and (iii)-(iv) coupled lumped parameter models with , (iii) a peripheral resistance (Q_{LPA}:Q_{RPA} is 22:78%) and (iv) a three-element Windkessel (WK) model (Q_{LPA}:Q_{RPA} is 14:86%). Steady Newtonian flow, Re=650.

3.11 Effect of pulsatility in the symmetric Y-Junction with hypoplastic LPA and the peripheral resistance boundary condition. (a) Instantaneous non-

dimensionalised velocity contours and WSS distribution along the inner wall, at maximum acceleration, middle of deceleration, maximum deceleration, and middle of acceleration of a sinusoidal waveform (Eq. (3.2)). (b) Steady and time-averaged non-dimensional wall shear stress distribution for steady and unsteady flow. Newtonian flow, mean Re=650.

3.12 (a) Points where the pressure values were measured, overlaying contours of pressure in the symmetric Y-Junction. Pressure is depicted relative to the reference pressure at the outlets, and normalised by $0.5\rho U^2$.(b) Pressure ratios for the models examined: (i) T-Junction (Fig. 3.5 (i)); (ii)-(v) asymmetric Y-Junction models, with (ii) common origin (Fig. 3.5 (ii)), (iii) one (Fig. 3.5 (iii)) or (iv) both branch origins displaced (Fig. 3.5 (iv)), or (v) hypoplastic LPA (Fig. 3.5 (v)); (vi) symmetric Y-Junction (Fig. 3.5 (vi)), with (vii) local asymmetric stenosis (Fig. 3.5 (vii)), (viii) local symmetric stenosis (Fig. 3.5 (viii)), or (ix) hypoplastic LPA (Fig. 3.5 (ix)); (x) symmetric Y model with extended RPA (Fig. 3.9a (i)); (xi)-(xii) symmetric Y model with PLPA > PRPA and with $\frac{|\Delta P|}{0.5\rho U^2}$=0.026 (Fig. 3.9a (ii)), and with $\frac{|\Delta P|}{0.5\rho U^2}$=0.015 (Fig. 3.9a (iii)), respectively; (xiii)-(xvi) symmetric Y model with hypoplastic LPA and (xiii)-(xiv) prescribed flow splits (Fig. 3.10a (i),(ii)), and (xv)-(xvi) lumped parameter models coupled at the branch outlets (Fig. 3.10a (iii),(iv)). Steady Newtonian flow, Re=650.

4.1 Schematic representation of 3D geometry.

4.2 Apparent viscosity against shear rate for the different rheological models used. The high shear rate region in which the models of this study are

5.7 Secondary flow visualised by in plane velocity vectors and contours of normalised velocity normal to the slice during (i) peak flow; (ii) mid deceleration at systole; and (iii) mid diastole, for (a) model 2; (b) model 3; and (c) the average model. Non-dimensionalisation was performed by division with the maximum velocity of each patient during the cardiac cycle. Points where slices α and γ are taken are visible in Fig. 5.1b. Cross-sections are oriented with the top and the bottom edges corresponding to the cranial and caudal positions, respectively and left and right to the anterior and posterior of the pulmonary artery, for the RPA, and to the posterior and anterior of the pulmonary artery, for the LPA, respectively. Cross-sections are in scale.

5.8 Non-dimensionalised time-averaged wall shear stress ($TAWSS_n$) distribution, normalised with the corresponding value at the inlet of each model, for (a) model 1; (b) model 2; (c) model 3; (d) model 4; (e) model 5; (f) model 6; (g) model 7; (h) the average model. Averaged boundary conditions are used at the inlet and the outlets of all models.

5.9 Left to Right: Patient-specific flow waveforms and velocity streamlines at (i) peak flow; (ii) mid deceleration at systole; and (iii) mid diastole, for (a) model 1; (b) model 2; (c) model 3; (d) model 4; (e) model 5; (f) model 6; (g) model 7. Streamlines are coloured by non-dimensionalised velocity magnitude based on the maximum velocity during the cardiac cycle of each patient. The RPA and the LPA branches are indicated in model 1.

5.10 Secondary flow visualised by in plane velocity vectors and contours of normalised velocity normal to the slice during peak flow, for (a) model 1; (b)

curvature value closer to the bifurcating branches. Shaded areas represent the standard deviation of the patient-specific values from the average calculated.

6.4 Left to Right: Subject-specific flow waveforms with (i) peak flow; (ii) mid-deceleration at systole; and (iii) mid-diastole, for (a) model 1; (b) model 2; (c) model 3; (d) model 4; (e) model 5; (f) the average model. Velocity streamlines coloured by non-dimensionalised velocity based on the maximum velocity during the cardiac cycle of each healthy subject at the three time points (a), (b), and (c). The RPA and the LPA are indicated in model 1.

6.5 Non-dimensionalised time-averaged wall shear stress distribution normalised with the wall shear stress developed at the inlet of each model, respectively, for (a) model 1; (b) model 2; (c) model 3; (d) model 4; (e) model 5; (f) the average model. Insets show the back view of the models. The LPA and the RPA and indicated in model 1.

6.6 Time-averaged wall shear stress (TAWSS) plot, derived from the TAWSS values of eight points located along the perimeter of cross-sections (α) and (γ), and presented in dynes/cm^2, for (a) model 1; (b) model 2; (c) model 3; (d) model 4; (e) model 5; (f) the average model.

6.7 Oscillatory Shear Index distribution, for (a) model 1; (b) model 2; (c) model 3; (d) model 4; (e) model 5; (f) the average model. The RPA and LPA branches are indicated in model 1.

List of Tables

Acknowledgements

I cannot thank enough my first supervisor, Dr Asimina Kazakidi for all of her support throughout this study. She has been a great mentor for me, guiding me and advising me in every step of the process, proof-reading many documents, including this thesis and pass on her values and morals as a person and as a researcher. She was always very patient and encouraging which gave me strength to continue the hard work all the years. I would also like to thank my second supervisor Prof Terence Gourlay for all his support in presenting my work in many conferences. His inputs were also valuable for defining the topic of the thesis and establishing collaboration with Dr Mark Danton. I would like to thank Dr Mark Danton, for providing us his insights as a clinician and proof-reading several abstracts submitted in conferences and the manuscript of the paper we published. Furthermore, I am grateful and would like to thank the people from the Biomedical Engineering Department, where I completed my MSc course. They provided me with fundamental knowledge and skills to proceed in my studies.

I would also like to thank our collaborators from University College London, Dr Emilie Sauvage, Dr Claudio Capelli, Prof Silvia Schievano and the rest of the group, whom I visit for a month. They shared with us clinical data, fundamental for the outcome of the thesis. In addition, they guided and advised me, and proof-read several documents, all invaluable for conducting part of this study. I would also like to thank the UK Fluids Network that made my visit possible with their Sort Research Visit fund.

In addition, I would like to thank Dr Jazmin-Aguado Sierra, Dr Kostantyn Butakov, Dr Mariano Vazquez and the rest of the group, including Dr Alfonso Santiago and Dr

Eva Casoni at the Barcelona Supercomputing Centre, in Spain. During this time, I tried using their in-house code to overcome some common assumptions in the computational studies of blood vessels, including the rigid walls and the omittance of the pulmonary valve. I would also like to thank the MacRobertson Travel Scholarship for awarding me the funds for this visit.

This PhD work was financially supported in part from the University of Strathclyde Research Studentship Scheme (SRSS) Research Excellence Awards (REA), Project No. 1208. Also, parts of the results were obtained using the ARCHIE-WeSt High Performance Computer (www.archie-west.ac.uk) based at the University of Strathclyde. I am thankful to all.

I am also grateful to the people involved in the STEM Equals project, including Dr Pauline Hall-Barientos who provided the 4D flow of the healthy subjects, Prof Victorita Dolean Maini, who helped in the development of the 0D three element Windkessel model and Prof Mandy MacLean who provided her expertise in arterial pulmonary hypertension. I would also like to thank Scott Black for processing the 4D flow data and providing me with the high quality DICOM images used for the reconstruction of the models.

It would be impossible to forget the rest of the Biofluids group Marianna Syntouka, Lauren Johnston, George Linaker. They were not only great co-workers and collaborators but also friends that made this journey unforgettable. Also, to my friend and roommate Yuly, with whom I shared all the good and bad times and all the rest of my friends Silvia, Valia, Despoina, Dimitra, Alexandros, Anna, Giorgos, Dimitris for all the fun and the great memories.

Finally, a special thank you to my family Aris, Angeliki, Alkis, Ellie, Maria, and my beloved Keith for their encouragement, their support and for truly believing in me.

Chapter 1

Introduction

Tetralogy of Fallot (TOF) is a congenital heart disease (CHD) that affects the right ventricle and the pulmonary arteries of new-borns. It has a prevalence of 1 in 3000 births and accounts for approximately 10% of all congenital heart diseases (Apitz et al., 2009, Marelli et al, 2018). Improvements in the diagnosis, surgical operations and healthcare has enabled the survival of children with CHD into adulthood (approximately 95%). Therefore, the number of adults with CHD has increased dramatically, with an estimated increase of 85% from 1985 to 2000; by 2010, the adults with moderate or severe symptoms outnumbered the children with CHD, with adults accounting for two-thirds of the most severe cases. Several complications are apparent in this new group of patient population, who require frequent monitoring and further surgical interventions, making the treatment and care of these patients rather difficult (Marelli et al., 2018, Nicolarsen and Kay, 2019).

Pulmonary valve replacement is an operation performed in repaired TOF (rTOF) patients to preserve right ventricle (RV) function. However, the timing for the surgical intervention is still ambiguous between the clinicians, and there is no consensus on the reliability of current indices, which are based on the RV end-systolic and end-diastolic volumes (Geva, 2001, Kordybach-Prokopiuk et al., 2015). Understanding the haemodynamic environment in the pulmonary arteries is therefore essential, in order to improve therapy and care of these patients, and optimise surgical interventions.

There are a few recent studies published on describing morphological parameters and flow patterns in the pulmonary bifurcation of healthy volunteers and in patients with rTOF, highlighting the importance and research interest in this topic. In the review paper of Conijn and Krings (2021), they identify 34 original research papers that investigate the blood flow in the pulmonary arteries, with 17 being published after 2016. The work presented in Boumpouli et al. (2020) (parts of Chapter 3 and 4) is included and cited as one of the most recent studies on the topic. The focus of this thesis is on the blood flow in the pulmonary arteries in relation to rTOF patients, and the novelty of this project lies in the comparison of both morphological and flow patterns, observed in the diseased models with those noticed in the healthy cases. The main research hypothesis is that the haemodynamics of the pulmonary bifurcation can provide a good indication of the flow characteristics and contribute to the understanding of the interplay between the upstream and downstream pulmonary vasculature.

This chapter starts by providing a brief overview of the heart's anatomy and function, before it describes congenital heart diseases, and more specifically Tetralogy of Fallot. An overview of the current treatment methods and the most common complications that the patients experience are then given. It further discusses the basic concepts of fluid mechanics in blood vessels and ends with the motivation for this thesis, the publications that arose from this work and a synopsis of the remaining chapters.

1.1. Cardiovascular System

The heart, the blood and the vessels are the three main components that contribute to the normal function of the cardiovascular system. The human heart is a hollow

muscular organ that is positioned between the lungs and is composed by four chambers: the right and left atrium at the upper part, and the right and left ventricle at the lower part of the heart. The right side of the heart is associated with the pulmonary circulation and the left side of the heart with the systemic circulation (Martini et al., 2014, Martinsen and Lohr, 2015).

The development of the human heart starts on day 15 on the embryo, where the first mesodermal cells migrate anterior and laterally and are the cells to become myocytes or heart cells (Martinsen and Lohr, 2015). A linear heart tube formed on day 22 (Fig. 1.1a) gives the first heartbeat. Lengthening and looping of the primary heart tube (Fig. 1.1b) are important prior to septation (Fig. 1.1c) and by day 28 the champers of the heart are in position (Fig. 1.1b). This process is crucial for the alignment of the inflow and outflow tracts and if it does not occur normally, it can lead to ventricular septal defects and malpositioning of the aorta (Martinsen and Lohr, 2015).

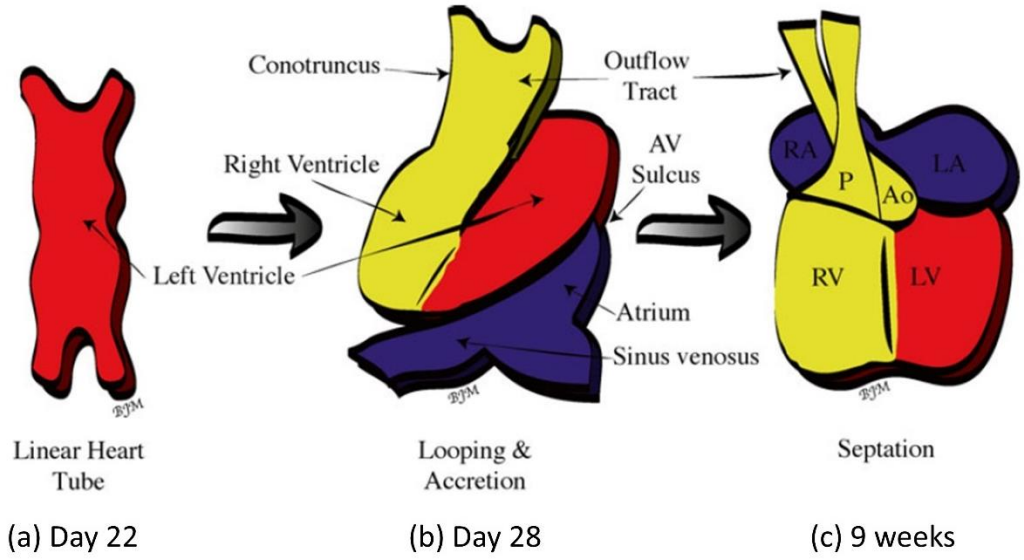

Figure 1.1: Development of human heart embryology (After Martinsen and Lohr, 2015).

Extensive remodelling takes place between weeks 4 and 7 of the human embryonic development, during the septation process (Fig. 1.2a). At that time, cardiac neural crest (CNC), migrate from the neural tube and through the aortic arch and are responsible for the septation of the outflow tract and ventricles, and the formation of the parasympathetic plexus which regulates heart rate. If CNC fails to migrate a rare congenital heart disease called persistent truncus arteriosus (TA) occurs. TA is characterised by a ventricular septal defect, a common ventricular outflow tract and a single truncal valve. It is the result of the absence of the truncoconal septal wall and the single truncal root which does not separate the aortic and pulmonary outflow tracts (Bhansali and Phoon, 2021). Failure during the outflow tract septation can also lead to congenital heart diseases, including ventricular septal defects, transposition of the great vessels and tetralogy of Fallot (Martinsen and Lohr, 2015).

Pulmonary system is not used during intrauterine life; high-volume oxygenated blood from the placenta, flows through the foramen ovale and ostium secundum from the right atrium to the left ventricle (right-to-left shunting). The lungs create a high resistance environment which results in low-volume flow from the pulmonary veins to the left atrium. During birth, when the oxygenation from the placenta is interrupted, the pulmonary vessels open, the resistance in the lungs drops and a reverse pressure difference environment is created leading to the closure of the foramen ovale and the ostium secundum (Martinsen and Lohr, 2015).

After birth, the right atrium receives deoxygenated blood from the systemic circulation and through the tricuspid valve passes it to the right ventricle (Fig. 1.2b). From the right ventricle, the blood is delivered to the lungs through the pulmonary valve, for exchange of O_2 and CO_2. The left atrium collects the oxygenated blood from the

pulmonary circulation and through the mitral valve transfers it to the left ventricle and to the tissues through the aortic valve (Fig. 1.2b).

The total blood that flows out of the left ventricle is known as cardiac output and the period of the heartbeat as the cardiac cycle. The flow of the blood from one chamber to the next is pressure driven, which means that blood travels from a high to a low-pressure environment, and therefore only if the pressure in one chamber exceeds that of the following chamber, the blood will flow (Martini et al., 2014).

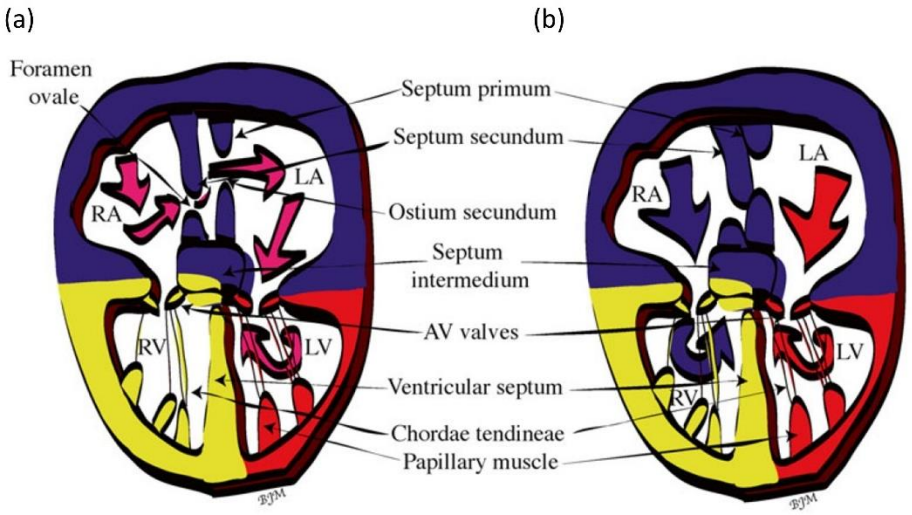

Figure 1.2: (a) Circulation in foetal heart. Arrows indicate the right-to-left shunting where the placentally oxygenated blood flows through the foramen ovale and ostium secundum (b) Circulation after birth. The foramen ovale and ostium secundum close and septation of the heart chambers occurs. The pulmonary (blue arrow) and systemic (red arrows) circulation are separated. RA: right atrium; RV: right ventricle; LA: left atrium; LV: left ventricle (After Martinsen and Lohr, 2015).

1.2. Congenital Heart Diseases

Congenital Heart Disease lesions occur during embryonic development and are defined according to Mitchell et al. (1971) as "gross structural abnormalities of the heart or intrathoracic great vessels that are actually or potentially of functional significance". The birth prevalence is estimated to be 8 per 1,000 live births, although it varies among studies worldwide (van der Linde et al., 2011, Marelli et al., 2018).

CHD can be classified into two types, the cyanotic that lower the amount of oxygen delivered in the tissues of the body, and the acyanotic if the oxygen in the body is not affected. In the cyanotic heart defects, the oxygen-rich blood is mixed with the oxygen-poor blood, and therefore less oxygenated blood is distributed to the body causing a bluish tint colour or cyanosis in the new-born. Children born with a cyanotic heart defect require a surgical intervention in order to survive to adulthood (Brickner et al., 2000a,b).

During the 50s, only 10-15% of new-borns with such lesions survived until puberty (MacMahon et al., 1953). However, due to advancements in medical diagnostic modalities and the success of surgical procedures, over the last decades, most children survive to adulthood and as a result, the disease is no longer limited to paediatric clinical practice (Cetta et al., 1992 and Skorton et al., 1993). Adult congenital heart disease emerged as a new cardiovascular speciality in 1991; this increasing population of patients experience complex cardiovascular abnormalities which require frequent monitoring, reoperations and new surgical treatments (Perloff, 1991), with an estimated rate of increase of the population of 5% per year (Brickner et al., 2000a).

1.2.1. Tetralogy of Fallot

Tetralogy of Fallot (TOF) is the most common cyanotic congenital heart disease and is characterised by four defects: a ventricular septal defect (Fig. 1.3a), an overriding aorta (Fig. 1.3b), a hypertrophy of the right ventricle (Fig. 1.3c) and an obstruction of the right ventricular outflow tract (RVOT) (Fig. 1.3d) (Bricker et al., 2000b). Niels Stensen in 1671 was the first who described TOF disease, and the anatomical description was later illustrated in 1784 by William Hunter: "…the passage from the

right ventricle into the pulmonary artery, which should have admitted a finger, was not so wide as a goose quill; and there was a hole in the partition of the two ventricles, large enough to pass the thumb from one to the other. The greatest part of the blood in the right ventricle was driven with that of the left ventricle into the aorta, or great artery, and so lost all the advantage which it ought to have had from breathing".

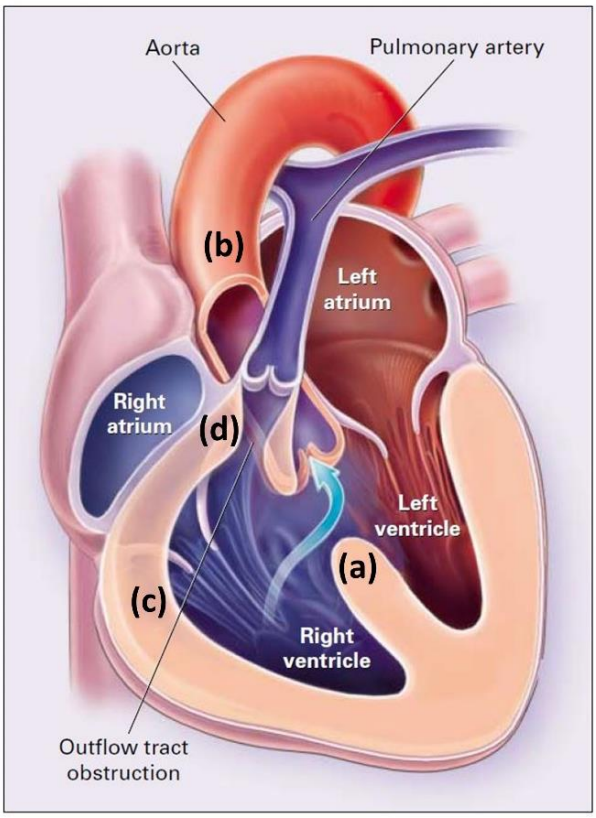

Figure 1.3: Anatomical representation of heart defects in Tetralogy of Fallot. (a) ventricular septal defect; (b) overriding aorta; (c)hypertrophy of the right ventricle; and (d) obstruction of the outflow tract (After Brickner et al., 2000).

The exact cause of TOF, similarly to most of congenital heart diseases, is unknown (Apitz et al., 2009, Babu-Narayan and Gatzoulis, 2018). Nevertheless, with the increase in the population of offspring from the surviving adult patients, there is a strong correlation of genetics in TOF (Digilio et al., 1997). A deletion of chromosome 22q11 has been identified in 15% of TOF patients (Babu-Narayan and Gatzoulis, 2018), and in approximately 20% of cases there is an association of TOF with genetic

syndromes, such as DiGeorge disease and velocardiofacial syndrome (both have 22q11 deletion), Alagille syndrome, trisomy 21, trisomy 22 (Marino et al., 1996, Digilio et al., 1997, Michielon et al., 2006, Rauch et al., 2010). These patients are termed as syndromic. For the non-syndromic patients, which account for the majority of cases, mutations in a number of genes, *gata4*, *jag1*, *nkx2.5*, *tbx1*, *tbx5*, that play a key role in fetal and cardiac development, have been implicated in TOF (Lyons et al., 1995, Benson et al., 1999, Griffin et al., 2010, Rauch et al., 2010, Yang et al., 2013, Grochowski et al., 2016, Steimle and Moskowitz, 2017, Morgenthau and Frishman, 2018).

1.2.1.1. Pathophysiology and Treatment

Most patients with TOF present cyanosis due to the right-to-left shunting from the ventricular septal defect, which allows deoxygenated blood to return to the body. It is the result of the narrowing of the RVOT which increases the resistance to flow, and the timing and severity of cyanosis is determined by the degree of the RVOT obstruction (Apitz et al., 2009, Babu-Narayan and Gatzoulis, 2018). The right and left ventricular pressures are equal due to the ventricular septal defect and at systemic levels (Apitz et al., 2009, Babu-Narayan and Gatzoulis, 2018, Brickner et al., 2000). Since the resistance to flow, due to the obstruction in the right ventricular outflow track, is relatively fixed, any changes in the systemic vascular resistance are translated into a change in the magnitude of right-to-left shunting (Brickner et al., 2000).

The degree of the overriding aorta can vary from 5% up to 95%. Normally, during the heart development, the aorticopulmonary septum will form within the truncus arteriosus and separate the aortic and pulmonary artery, but regression of the muscle

results in the incorrect alignment of the aorta over the ventricles. When the percentage of override exceeds 50% then it is considered a double outlet right ventricle, and a larger patch is required to connect the aorta with the left ventricle (Kloessel et al., 2016, Babu-Narayan and Gatzoulis, 2018, Gu et al., 2018). Finally, hypertrophy of the right ventricle is the results of pressure and volume overload which cause the wall thickening and chamber enlargement. Although it is rarely extreme in TOF patients, it is considered essential to decide the suitability of patients for biventricular repair (Babu-Narayan and Gatzoulis, 2018, Goldberger et al., 2018).

Unoperated patients have a death rate of 25% in the first year, which increases to 40% and 70% before 3 and 10 years of age (Babu-Narayan and Gatzoulis, 2018). Surgical repair is therefore recommended in order to increase survival rate and relieve symptoms. The surgical repair can be either palliative, or reparative. Palliative procedures include the Blalock-Taussig operation, which involves anastomosis of the subclavian artery to the pulmonary artery, the Waterston operation, which requires the anastomosis of the ascending aorta to the right pulmonary artery and the Potts operation that includes the anastomosis of the descending aorta to the left pulmonary artery (Kiran et al., 2017). Although palliative procedures are associated with long-term complications, including pulmonary hypertension and left ventricular volume overload, they are still performed in severe cases where complete repair is unsuitable (Brickner et al., 2000). Reparative procedures are the currently preferred surgical corrections that include the closing of the ventricular septal defect and relief of the RVOT obstruction, and can involve a pulmonary valvotomy, an RVOT or transannular patch (Babu-Narayan and Gatzoulis, 2018).

1.2.1.2. Chronic Complications in Repaired Patients

Patients with rTOF are usually asymptomatic and they have long survival rates (estimated to be 86% 32 years following the surgical repair), however chronic complications and reintervention are not uncommon. Among the most common complications are pulmonary regurgitation (PR), and residual or recurrent pulmonary valve or branch stenosis (Brickner et al., 2000).

Pulmonary regurgitation involves the diastolic reversal of blood flow into the right ventricle (RV) and, for TOF patients, is a consequence of loss of pulmonary valve competence, due to the long-term postoperative outcome of repaired right ventricular outflow tract obstruction during infancy, and the necessary surgical opening of the dysplastic valve (Harris et al., 2011, Geva, 2011). It is the result of the pressure difference between the right ventricle and the pulmonary artery, during diastole (Chaturvedi et al., 2007) and small changes in intrathoracic or airway pressure can have a notably effect in PR (Chaturvedi et al., 1997). Other factors that also contribute to pulmonary regurgitation in the rTOF patients are associated with the geometry of the branch pulmonary arteries, such as the orientation, and with factors that affect the blood flow, unequal and abnormal pulmonary vascularity and perfusion, pulmonary vascular resistance and pressure (Kang et al., 2003, Ammash et al., 2007). Although chronic PR can be tolerated for an extended period of time, if mild or moderate, and remain asymptomatic, it typically results in right ventricular dilatation and dysfunction, exercise intolerance, and ventricular and atrial arrhythmias, when prolonged and severe (Ammash et al., 2007, Babu-Narayan et al., 2013). It may also have an adverse effect on the left ventricular function, correlated with the RV

dysfunction (Davlouros et al., 2002, Menting et al., 2015). In chronic cases of PR, the assessment of the RV stiffness and afterload are the most important factors to consider. Increase stiffness will increase the RV pressure and therefore decrease the PR gradient, while increase in the RV afterload, usually driven by branch or peripheral pulmonary artery stenosis, will increase pulmonary regurgitation (Chaturvedi et al., 1997, 2007). However, recent studies have observed that PR is associated with differential retrograde flow of various flow splits in the left and right branch pulmonary arteries in patients with rTOF, irrespective of the presence of stenosis (Harris et al., 2011, Kang et al., 2003).

Branch pulmonary obstruction is most commonly observed in the left pulmonary artery (LPA) (Harris et al., 2011) in the form of a local stenosis. Proximal LPA obstruction can also occur with general artery hypoplasia in pulmonary atresia and following complex repair of nonconfluent arteries, that is, when the right and the left branches are not interconnected and originate separately (Puga et al., 1982), or artery kinking, when pulmonary regurgitation is present in patients with dilated RVOT. The dilatation of the right ventricle and the pulmonary trunk, due to PR, restrict the RVOT, which turns cranially and left-laterally, causing the angle between the pulmonary trunk and LPA to become acute and eventually form LPA kinking (Fig. 1.4). As a consequence of such morphological differentiations, RV afterload increases, which may intensify PR, resulting in turn in further enlargement of the right ventricle and kinking. It is, hence, likely that a two-way link between pulmonary regurgitation and LPA kinking may be present (Chaturvedi et al., 1997, McElhinney et al., 1998).

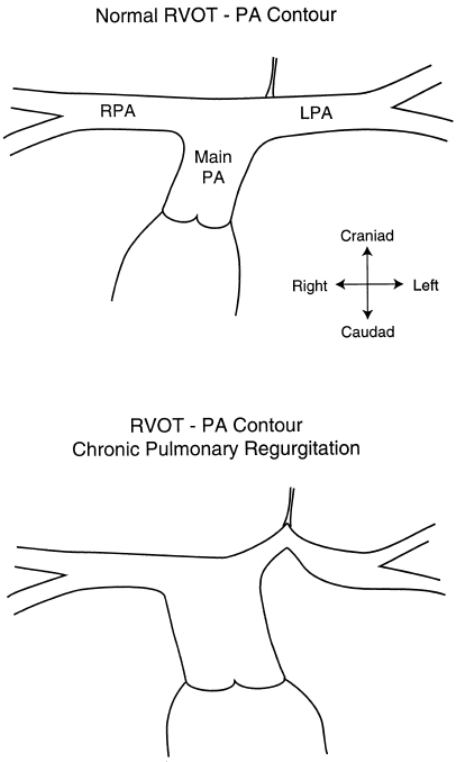

Figure 1.4: Left pulmonary artery kinking in repaired tetralogy of Fallot patients (After McElhinney et al., 1998).

1.2.1.3. Pulmonary Valve Replacement

Pulmonary valve replacement (PVR) is an operation performed to prevent ongoing volume overloading in the right ventricle and dilatation and is deemed necessary when PR and LPA kinking are present to preserve the right ventricular function. PVR is recommended prior to the onset of significant clinical symptoms and right ventricular dysfunction, to increase the likelihood of successful RV remodelling, restore the function of the pulmonary valve, decrease arrythmias and improve exercise tolerances (Babu-Narayan and Gatzoulis 2018, Geva 2011, Chaturvedi et al., 2007).

The assessment of the optimal timing for PVR is, therefore, crucial and remains a key challenge to clinicians, relying their decision upon balancing the risk between RV

dysfunction and the finite lifespan of the available bioprosthetic valves used in PVR (Babu-Narayan and Gatzoulis 2018, Geva 2011). Several studies have tried to identify threshold values of the RV end-diastolic and end-systolic volumes that postoperative will result in successful RV remodelling. Therrien et al. (2005) reported a RV end-diastolic volume ≤ 170 ml/m^2, Oosterhof et al. (2007) identified a RV end-diastolic volume <160 ml/m^2 and an RV end-systolic volume < 82 ml/m^2, while Buechel et al. (2005) and Frigiola et al. (2008) proposed a RV end-diastolic volume of <150 ml/m^2. However, there is yet no consensus on the reliability and effectiveness of these current indices in the clinical practice (Geva, 2001, Kordybach-Prokopiuk et al., 2015).

1.3. Pulmonary arteries

The origin of the word artery is the Greek word *ἀρτηρία* which means to contain air and was believed to be the role of the arteries before the knowledge of blood. Nowadays, an artery is defined as a vessel that transports blood away from the heart, including the pulmonary artery that carries deoxygenated blood (Rubenstein et al., 2016).

The pulmonary arteries consist of three distinct layers, the tunica intima, the tunica media and the tunica externa. The tunica intima is the inner layer of the blood vessels and consists of endothelial cells and elastic fibers that are organised in a layer of connective tissue that surrounds the endothelial lining. The tunica media is the middle layer and consists of smooth muscle cells and a connective tissue consisting of collagen fibers, and the function of these cells regulates the diameter of the blood vessel. Tunica externa is the outer layer of the blood vessel and is a connective tissue of collagen and elastic fibers (Martini et al., 2014, Rubenstein et al., 2016).

Endothelial cells play a crucial role in regulating vascular homeostasis (Gimbrone 1995, Sabri et al., 2013), and remodel in response to the wall shear stress (WSS), the stress applied tangentially to the vessel's wall, and to the oscillatory shear index (OSI), the variations in the WSS during the cardiac cycle. The levels of WSS affect the production of endothelin-1 (ET-1) and nitric oxide (NO), a potent vasoconstrictor and a potent vasodilator, respectively, which in turn regulate the proliferation of smooth muscle cells and collagen synthesis. Increased WSS results in an increase of NO, while decreased WSS in the production of ET-1 (Taylor et al., 2009). Although pulmonary arteries have higher shear stress (approximately 20 dynes/cm^2 in the proximal healthy pulmonary arteries) (Tang et al., 2012) and lower OSI (approximately 0.1 in the proximal healthy pulmonary arteries) (Tang et al., 2011) compared to other arteries of the systemic circulation, which is linked with fewer incidents of atherosclerosis (Tang et al., 2011), changes that are observed in the pulmonary vasculature of patients could still affect endothelial function and remodelling (Tang et al., 2012).

1.3.1. Physiological environment

Blood flow in the arteries is determined by two parameters, pressure (P) and resistance to flow (R) (Eq. (1.1)).

$$Q = \frac{\Delta P}{R} \tag{1.1}$$

where Q is the flow rate and ΔP is the pressure difference (Iaizoo, 2015).

Q and R depend on many factors, including the radius (r) and the length (L) of the vessel, and blood viscosity (η). Flow rate in a cylindrical tube can be calculated using Poiseuille equation (Iaizoo, 2015):

$$Q = \frac{\Delta P \pi r^4}{8 L \eta} \tag{1.2}$$

And combining Eq. (1.1) and (1.2), the resistance to flow can be approximated (Iaizoo, 2015):

$$R = \frac{8 L \eta}{\pi r^4} \tag{1.3}$$

The pressure difference between two vessels is what drives the blood flow, rather than the absolute pressure, as seen from Eq. (1.1) and (1.2). In addition, a small change in the radius will have a relatively large influence in the resistance to flow (Eq. (1.3)) (Iaizoo, 2015). Pulmonary arteries are generally low-pressure, with values about 20 mmHg, and a high flow rate environment (Martini et al., 2014, Ghio et al., 2015).

One way to calculate the pulmonary vascular resistance is by dividing the difference of the mean pulmonary arterial pressure (*mPAP*) and the pulmonary artery occlusion pressure (*PAOP*) with the cardiac output (*CO*), and multiplying the result with 80, to convert the output to dynes sec/cm^{-5} (Breitenbach, 2007):

$$R = \frac{80 \times (mPAP - PAOP)}{CO} \tag{1.4}$$

In a normal subject, pulmonary vascular resistance is found 100-200 dynes sec/cm^{-5} (Breitenbach, 2007).

Another important parameter in the arterial blood flow is the compliance of the blood vessels. Compliance measures arterial distensibility, or arterial stiffness, and describes the ability of the vessels to regulate the accumulation or release of blood, during the cardiac cycle. The pulmonary pressure, *P*, and the stroke volume (*SV*) are used to calculate pulmonary arterial compliance (*C*) through the equation (Ghio et al., 2015):

$$P = \frac{SV}{C} \tag{1.5}$$

Pulmonary vascular resistance is responsible for the regulation of the flow (when elevated flow slows down in the peripheral circulation), and compliance regulates the volume of blood which is accumulated and released during systole and diastole, respectively. Therefore, both parameters are important for the decrease of pulmonary arterial pressure during diastole. The pulmonary arterial time constant, τ, (illustrated in Fig. 1.5), connects *R* and *C* with the following equation (Ghio et al., 2015):

$$\tau = RC \tag{1.6}$$

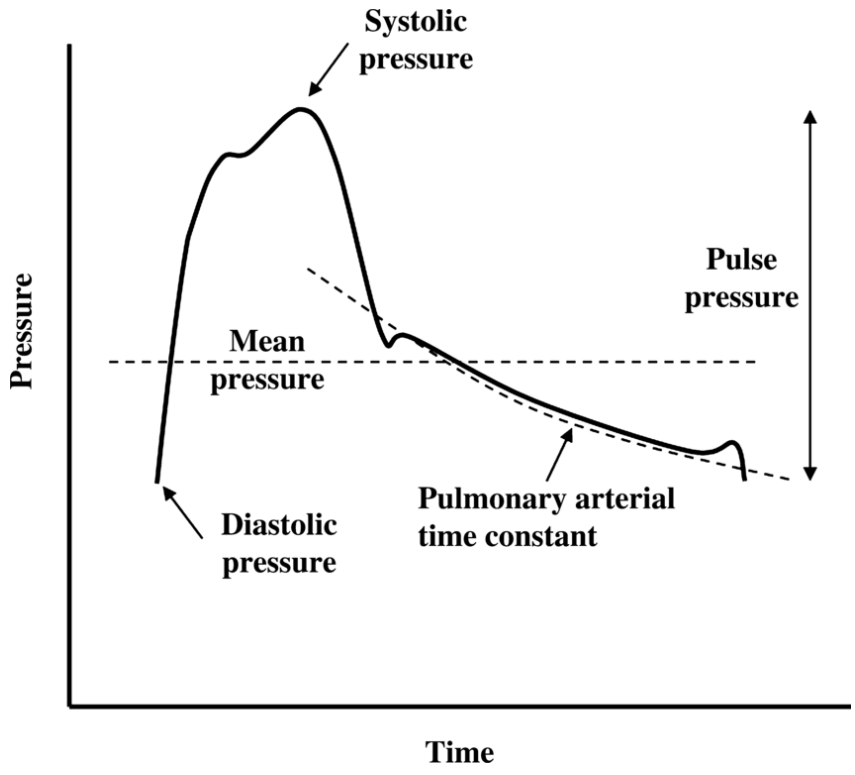

Figure 1.5: Pulmonary arterial pressure waveform showing the pulmonary arterial time constant (τ) during diastole (After MacKenzie Ross et al., 2013).

1.4. Blood flow in arteries

Fluid dynamics is a branch of fluid mechanics, that studies the effect of forces on fluid motion and has a wide range of applications including the biomedical engineering. The

fundamental principles of fluid mechanics go back to ancient Greek when Archimedes published on 250 BC his work on Archimedes' Principle or the law of buoyancy. Major advancements have been made ever since, with Isaac Newton investigating viscosity and defining it in his 1687 work "Philosophie Principia Mathematica", Blaise Pascal formulating Pascal's law and demonstrating the equilibrium of liquids in 1653, Daniel Bernoulli introducing the mathematical fluid dynamics with the principle published in 1738 in his book Hydrodynamica, Leonhard Euler publishing Euler equations around 1748 for inviscid flow to name a few.

Studying the blood flow in arteries can be quite challenging and several assumptions are usually made, which are considered acceptable in large arteries. Some of the most common simplifications are the description of blood as a Newtonian fluid (Samyn and LaDisa, 2016), the consideration of arteries as circular tubes with rigid walls (Caro et al., 1978) and the no-slip boundary, where the velocity adjacent to the vessel walls is assumed to be zero (Samyn and LaDisa, 2016).

In the following subsections some of these concepts are discussed, starting with blood rheology and differences between Newtonian and non-Newtonian fluids. Subsequently, the basic principles in fluid mechanics are presented and finally the development of flow is analysed in a straight pipe under steady laminar and turbulent flow, and under unsteady flow, and flow in a bifurcating vessel.

1.4.1. Blood rheology

Rheology, a term derived by the Greek word *ῥέω* meaning flow, is the study of flowing materials and their mechanical properties. To characterise the flow behaviour, the relationship between the stress (τ) and strain rate $(\dot{\gamma})$ is studied. Apparent viscosity (η)

measures the resistance of a fluid to deform and is defined as $\eta = \tau/\dot{\gamma}$, or $\eta = \tau/\frac{dU}{dy}$, where $\frac{dU}{dy}$ is the gradient of velocity. Different types of flow behaviour are recognised, with the simplest being the Newtonian, characterised by a linear relationship between the stress and strain. When the viscosity decreases as the strain rate increases then the fluid exhibits a pseudoplastic, or shear thinning behaviour, while when the viscosity increases as the strain rate increases the fluid behaviour is characterised as dilatant, or shear thickening (Fig. 1.6) The shear viscosity in this case, and by making use of the power law model for shear stress ($\tau = k\dot{\gamma}^n$), can be defined as (Struble and Ji, 2001, Tao et al., 2020):

$$\tau = k\dot{\gamma}^{n-1} \tag{1.7}$$

where *n* is the behaviour flow index and *k* the consistency index (numerically equal to viscosity at 1 s^{-1}). For n<1 it describes pseudoplastic fluids, for n=1 Newtonian fluids and for n>1 dilatant fluids. Some highly shear-thinning fluids are said to exhibit a plastic behaviour, when a specific level of stress needs to be reached, known as the yield stress, in order to start flowing (Fig. 1.6). These fluids are considered to possess both solid and fluid properties, and Herschel-Bulkley model is a representative of these fluids:

$$\tau = \tau_\gamma + k\dot{\gamma}^n \tag{1.8}$$

where τ_γ the yield stress. It is therefore a power law model but includes the yield stress. For $k=\eta$, it describes a Bingham fluid, where similar to Herschel-Bulkley, has a yield stress, but once it starts flowing it exhibits a Newtonian behaviour. For $\tau_\gamma=0$ and n=1

it reduces to a Newtonian fluid (George and Qureshi, 2013, Tao et al., 2020). In fluid dynamics, another term of viscosity is adopted to describe the fluids, known as kinematic viscosity (v), and is defined as the dynamic viscosity (μ), coefficient of viscosity as defined by Newton's law, divided by the density of the fluid (ρ) (George and Qureshi, 2013).

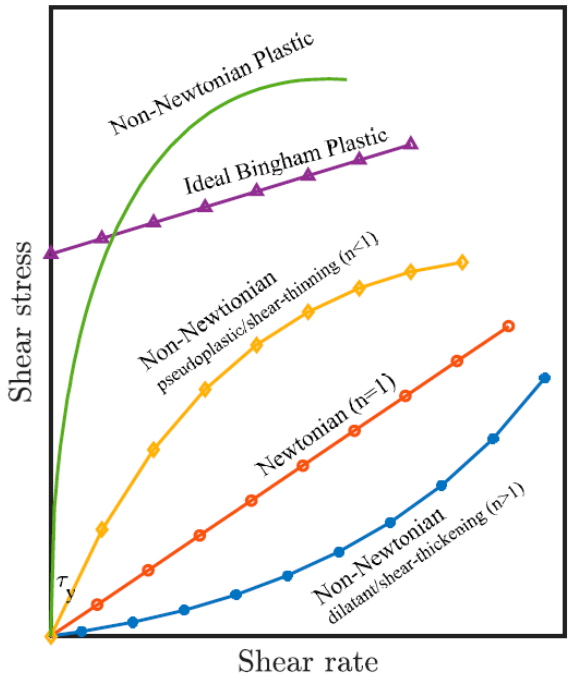

Figure 1.6: Classification of fluids based on rheological behaviour (After Tao et al., 2020).

Blood is composed of plasma and several types of cells. Plasma under physiological conditions has a Newtonian fluid behaviour, but when it is considered as a whole, it exhibits a shear-thinning behaviour. Parameters such as temperature, haematocrit, disease conditions and the shear rate, can affect the viscosity of blood (Struble and Ji, 2001, Samyn and LaDisa, 2016). Many different non-Newtonian models have been developed, by parameter-fitting experimental data, in an attempt to more accurately capture the change of blood viscosity in blood flow studies (Ballyk et al., 1994, Cho and Kensey, 1991, Walburn and Schneck. 1976). However, blood viscosity varies

widely between individuals and it is unlikely that one rheological model can precisely capture the rheological properties of blood (Vijayaratnam et al., 2015).

1.4.2. Basic principles of fluid mechanics

In many fluid dynamic problems, including in this work, the fluid can be considered as a continuum and studied in the macro scale, while the molecular interactions of the micro scale are not considered (Fig. 1.7). The macroscopic properties of the fluid, including density, viscosity, pressure and velocity, do not exhibit in this case any statistical microscopic fluctuations (Colin, 2014, Drikakis et al., 2019).

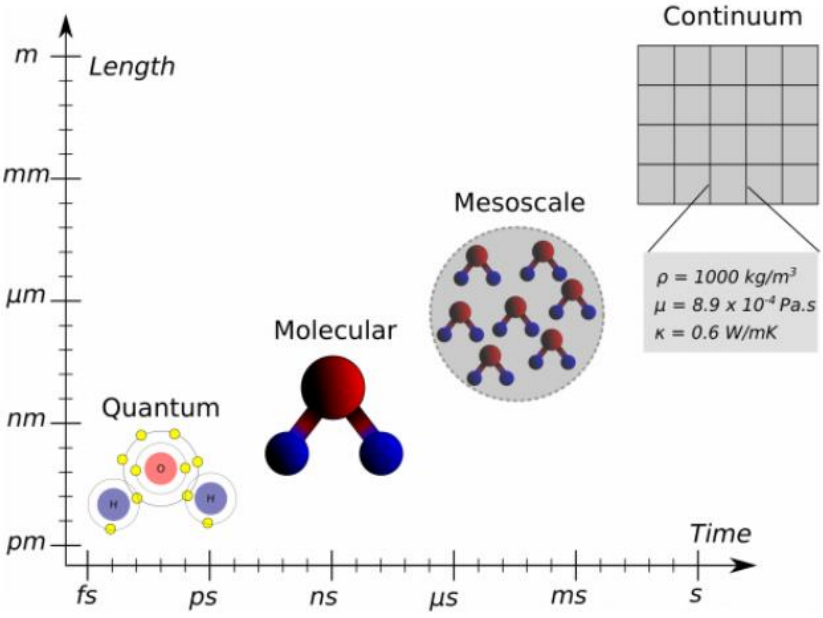

Figure 1.7: Different scales at which a fluid can be modelled (After Drikakis et al., 2019).

Three conservations laws form the fundamental principles in fluid dynamics and can be applied in a region of the flow, to solve fluid dynamic problems. For any conserved intensive property φ, which are independent of the amount of matter, the extensive property Φ can be defined as (Ferziger and Perić, 2002):

$$\Phi = \int_{\Omega_{CM}} \rho\varphi d\Omega \tag{1.9}$$

where CM is the control mass, representing a certain spatial region of the fluid, and Ω_{CM} the volume occupied by the control mass. For $\varphi=1$ it describes the mass conservation, while for $\varphi=\boldsymbol{u}$ the momentum. This definition can be used for any conservation law and the equation derived is known as the Reynolds' transport theorem:

$$\frac{d}{dt}\int_{\Omega_{CM}} \rho\varphi d\Omega = \frac{d}{dt}\int_{\Omega_{CV}} \rho\varphi d\Omega + \int_{S_{CV}} \rho\varphi(\boldsymbol{u}-\boldsymbol{u}_b)\cdot\boldsymbol{n}dS \tag{1.10}$$

where Ω_{CV} the control volume, S the surface of the control volume, **u** the fluid velocity, $\mathbf{u}_b$ the velocity of the moving CV, and $\boldsymbol{n}$ the unit vector orthogonal to S_{CV}.

1. Conservation of mass states that the mass that flows into a system must flow out of it. Alternatively, should be accounted either with a change in the density (density is defined as mass over volume) of the fluid or a change in the mass of the system, therefore $\frac{dm}{dt} = 0$. Using Eq. (1.10) and with $\varphi=1$, the integral form of the equation is (Ferziger and Perić, 2002, Rubenstein et al., 2016):

$$\frac{\partial}{\partial t}\int_{\Omega} \rho d\Omega + \int_{S} \rho\boldsymbol{u}\cdot\boldsymbol{n}dS = 0 \tag{1.11}$$

2. Conservation of momentum states that when a net force is acting upon a body then the body will move in the same direction and with a velocity proportional to that force, $\sum f = \frac{\mathrm{d}(\mathrm{m}\mathbf{u})}{dt}$. The integral form of the equation, using Eq. (1.10) and

with $\varphi=\boldsymbol{u}$, for a fixed fluid-containing volume is (Ferziger and Perić, 2002, Rubenstein et al., 2016):

$$\frac{\partial}{\partial t}\int_{\Omega}\rho\boldsymbol{u}d\Omega+\int_{S}\rho\boldsymbol{u}\boldsymbol{u}\cdot\boldsymbol{n}dS=\sum f \tag{1.12}$$

3. Conservation of energy states that the change of the energy of a system (δU) is equal to the energy added ($through\ heat, \delta Q$) minus the energy lost by the system ($through\ work, \delta w$). Therefore, in a closed system the total energy remains constant $\delta U = \delta Q - \delta w$. The integral form of the energy equation applicable in most flows is (Ferziger and Perić, 2002, Rubenstein et al., 2016):

$$\frac{\partial}{\partial t}\int_{\Omega}\rho\boldsymbol{h}d\Omega+\int_{S}\rho\boldsymbol{h}\boldsymbol{u}\cdot\boldsymbol{n}dS = \int_{S}kgradT\cdot\boldsymbol{n}dS+\int_{\Omega}(\boldsymbol{u}\cdot gradp+S{:}\,grad\boldsymbol{u})d\Omega+\frac{\partial}{\partial t}\int_{\Omega}\rho d\Omega \tag{1.13}$$

where h is the enthalpy, k is the thermal conductivity, T is the temperature and S the viscous part of stress tensor, or deviatoric stress.

Flow can be characterised as compressible or incompressible depending on whether the density of the fluid changes or not. Blood is assumed an incompressible flow with parameters such as pressure and temperature not affecting its density.

Flows are further characterised as laminar or turbulent to distinguish a smooth and highly ordered flow from flow with time-dependent fluctuations. Reynolds number (*Re*) is a dimensionless parameter that is used to differentiate the two, measuring the ratio of inertial (ρU^2) to viscous forces ($\mu U/D$):

$$Re = \frac{\rho U D}{\mu} \tag{1.14}$$

where *D* is the characteristic length (for a circular tube that would be the diameter) and *U* is the characteristic velocity. At high Reynolds numbers the inertial forces are dominant, and the viscous forces cannot prevent fluctuations, thus the flow is turbulent (Formaggia et al., 2009, White 2011). On small or moderate Reynolds numbers, viscous forces become significant, and the flow is laminar. For flow in circular tubes, the flow is considered to transition to turbulent at a Reynolds number of Re ≈ 2300, known as the critical Reynolds number (Zhang, 2017).

Fluid flow can mathematically be described by the Navier-Stokes (momentum conservation) equations. It is a group of partial differential equations that are based on the laws of conservation of mass, conservation of momentum and conservation of energy (White, 2011). Starting with the general partial differential equation of continuity, where all properties of fluid are assumed to uniformly vary in time and position, is given by:

$$\frac{\partial \rho}{\partial t} + \frac{\partial}{\partial x}(\rho u) + \frac{\partial}{\partial y}(\rho v) + \frac{\partial}{\partial z}(\rho w) = 0 \tag{1.15}$$

or using the vector gradient operator it simplifies to:

$$\frac{\partial \rho}{\partial t} + \nabla \cdot (\rho \boldsymbol{u}) = 0 \tag{1.16}$$

where **u**=[u, v, w] the velocity vector, and $\nabla = i\frac{\partial}{\partial x} + j\frac{\partial}{\partial y} + k\frac{\partial}{\partial z}$.

For incompressible flows, the density of the fluid is considered constant, and Eq. (1.16) is further reduced to:

$$\nabla \cdot \boldsymbol{u} = 0 \tag{1.17}$$

The force acting on the surface of an element are due to stresses, which are the sum of the divergence of viscous stress tensor and hydrostatic pressure gradient. For an infinitesimal element, the differential momentum equation is derived:

$$\rho g - \nabla \mathrm{p} + \nabla \cdot \tau_{ij} = \rho \frac{\partial \boldsymbol{u}}{\partial t} \tag{1.18}$$

where τ_{ij} is the viscous tensor acting on the element:

$$\tau_{ij} = \begin{bmatrix} \tau_{xx} & \tau_{yx} & \tau_{zx} \\ \tau_{xy} & \tau_{yy} & \tau_{zy} \\ \tau_{xy} & \tau_{yz} & \tau_{zz} \end{bmatrix} \tag{1.19}$$

Assuming a frictionless flow $\tau_{ij} = 0$ Eq. (1.18) is reduced to Euler's equation for inviscid flow:

$$\rho g - \nabla \mathrm{p} = \rho \frac{\partial \boldsymbol{u}}{\partial t} \tag{1.20}$$

For a Newtonian fluid (where stress is proportional to strain and can be calculated with Eq. (1.8)) and assuming an incompressible flow (Eq. (1.17)), Eq. (1.18) becomes:

$$\rho g - \nabla \mathrm{p} + \mu \nabla^2 \boldsymbol{u} = \rho \frac{\partial \boldsymbol{u}}{\partial t} \tag{1.21}$$

which are the second-order nonlinear partial differential Navier-Stokes equations (White, 2011).

1.4.2.1. Development of a steady laminar flow

Let us assume a steady laminar flow in a straight tube, with a uniform velocity profile at the entrance. Due to the no-slip condition, the fluid particles at the walls have a zero velocity. A velocity gradient is generated along the tube, where fluid particles at the middle of the tube acquire increased values of velocities while particles at layers

adjacent to the wall gradually slow down (Fig. 1.8). The boundary layer that is formed is the effect of the viscous forces triggered by the fluid viscosity which results in a high shear stress. The velocity profile eventually develops into a parabolic or fully developed velocity profile (*Poiseuille flow*). The region from the entrance of the tube until the flow is fully developed is known as the 'entrance region' and the length of that region is called 'entrance length'. Shear stress is also gradually reduced until it is stabilised when the flow is fully developed. An estimate of the entry length can be approximated as $L = 0.05ReD$ (Cengel and Cimbala, 2014).

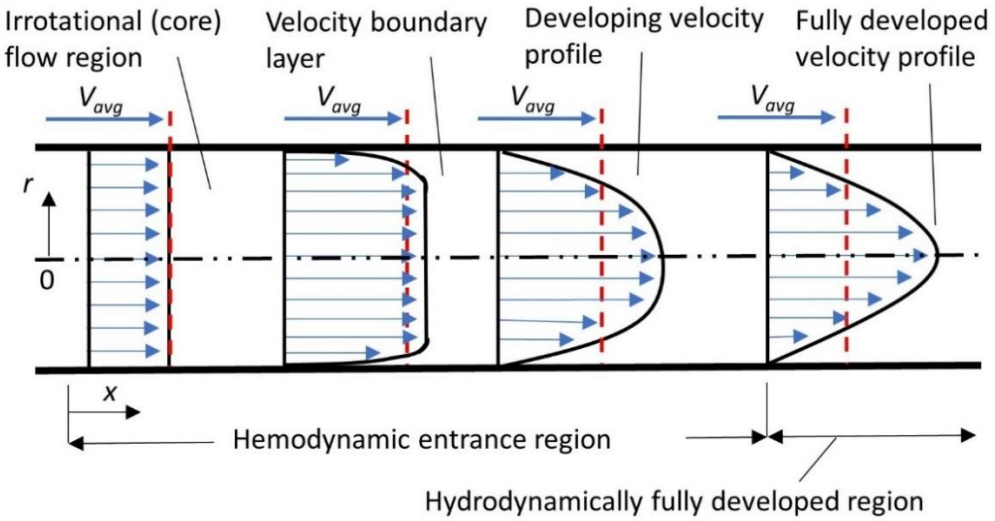

Figure 1.8: Development of a laminar flow (Reproduced by Cengel and Cimbala, 2014).

1.4.2.2. Turbulent flow

Contrary to the fully developed velocity profile that is observed in laminar flow, a much fuller velocity profile (flatter at the centre of the pipe) is evident in turbulent flow and is the effect of fluctuation in the velocity or eddy motion. Due to the no-slip boundary, velocity is zero and eddy motion diminishes at the wall. The velocity gradient which develops is large, and the turbulent boundary layer is thick and steep

adjacent to the wall. The wall shear stress is also higher compared to laminar flow as a result of the large velocity gradient. The turbulent boundary layer is characterised by four layers: the viscous or laminar sublayer, the buffer layer, the overlap or transition layer (also called inertial sublayer), and the turbulent or outer layer (Fig. 1.9). The flow characteristics are quite different in each region; the velocity at the viscous sublayer is almost laminar and is dominated by viscous effects, while flow is dominated by turbulent effects at the outer layer (Cengel and Cimbala, 2014).

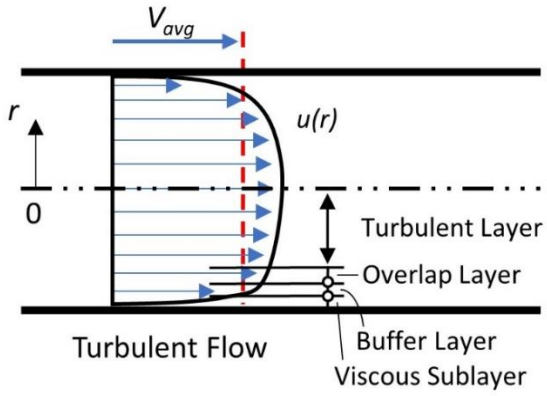

Figure 1.9: Velocity profile of a turbulent flow (Reproduced by Cengel and Cimbala, 2014)

1.4.2.3. Development of unsteady flow

Blood flow in arteries is highly pulsatile due to the contractions of the heart during the cardiac cycle. It is therefore crucial to understand the development of unsteady flows in order to be able to investigate the blood flow in arteries.

The simplest example of an unsteady flow to be consider is a sinusoidally oscillating pressure gradient. A dimensionless parameter that is used to characterise unsteady flows is the Womersley number *Wo* (or α), which is considered an equivalent of Reynolds number for steady flows. For flows in a straight pipe, *Wo* is given by:

$$Wo = \frac{D}{2}\sqrt{\frac{\omega}{\nu}} \tag{1.22}$$

where ω is the angular frequency ($2\pi/T$). The Womersley number provides an indication of how much the velocity differs from the characteristic Poiseuille profile. At low Womersley numbers ($Wo < 1$), the viscous forces dominate the inertial forces, and the flow is considered 'quasi-steady' (Fig. 1.10). In this case, velocity preserves its parabolic profile, and it is synchronous with the pressure gradient. Flow still oscillates but the instantaneous flow is determined by the instantaneous pressure gradient. At high Womersley numbers ($Wo > 1$), the inertial forces dominate, the velocity profile is no longer parabolic, and the flow is asynchronous with the pressure gradient (Caro et al., 1978).

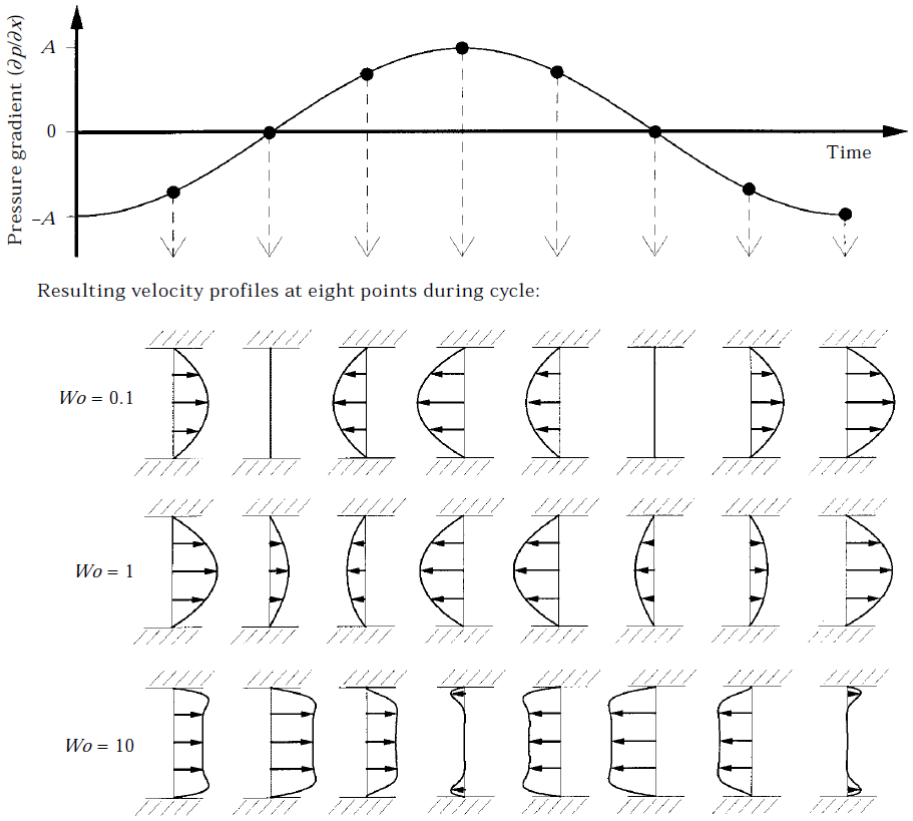

Figure 1.10: Velocity profiles (non-dimensionalised) at different Womersley numbers for a sinusoidally oscillating pressure gradient (Loudon and Tordesillas, 1998).

The effect of Womersley number on the flow can be better comprehended through the visualisation of the velocity profiles, presented by Loudon and Tordesillas (1998), for a flow between two parallel plates. In Figure (1.10), non-dimensionalised velocity profiles at different points in time along a sinusoidally oscillating pressure gradient and for different *Wo* numbers are presented. For $Wo < 1$, the flow is quasi-steady; the velocity profiles are parabolic, and velocity is in phase with pressure. For $Wo = 1$, the velocity profiles are still parabolic, but the velocity exhibits a phase lag with pressure. For $Wo > 1$, velocity is no longer parabolic, highest velocities are observed closer to the walls and not at the center, and the flow is unable to follow the rapidly changing pressure gradient (Loudon and Tordesillas, 1998).

1.4.2.4. Flow through a bifurcating artery

The pulmonary arteries consist of a network of branching arteries, which starts with the main pulmonary artery, bifurcating into the left and the right pulmonary arteries, and continuing for many branching generations. The flow through an idealised bifurcation can be viewed in Fig. (1.11). When the flow from the main branch reaches the bifurcation, it is divided and follows the two daughter branches. The point that the flow division occurs is known as the ‘stagnation point’, and the velocity at this point is zero. Flow that enters the daughter branches is skewed and diverted towards the inner walls of the bifurcation, as the acting pressure gradient is unable to displace the high inertia of the flow. The adverse (positive) pressure gradient causes the fluid particles to slow down in the boundary layer close to the outer wall, and flow separation occurs. The flow is trapped within that recirculation zone due to its inability to overcome the flowing fluid pressure (Caro et al., 1978, Rubenstein et al., 2016). The

displacement of the velocity from the centreline of the branch towards the inner wall, generates secondary motion and results in a transverse recirculation of counter-rotating vortices. A dimensionless parameter that is used to characterise the flows in curved pipes is the Dean number (*De*):

$$\mathrm{De} = Re\sqrt{\frac{D}{2R}} \tag{1.23}$$

where R is the radius of curvature (1/curvature). *De* determines the formation of vortices resulting from the centrifugal instability based on the curvature of the wall. Dean (1928), found that when the Dean number is higher than 36.6 then secondary flow would be present.

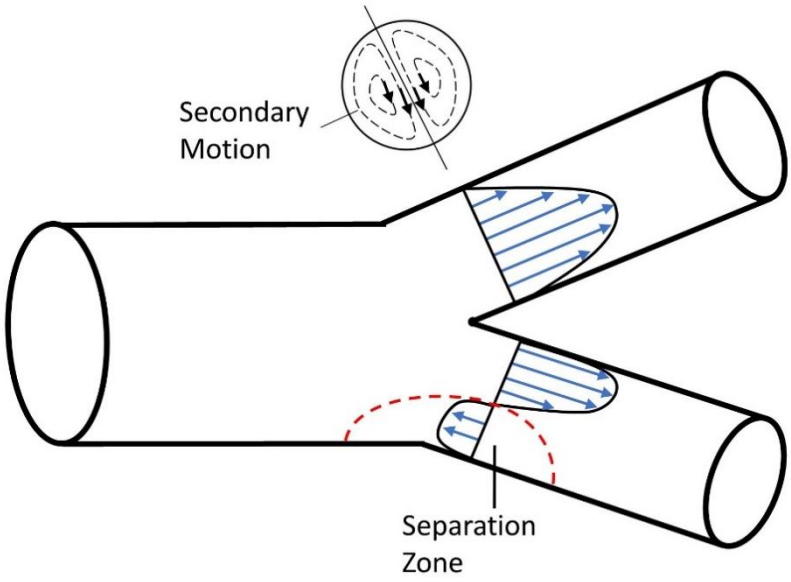

Figure 1.11: Flow through a bifurcating artery. Secondary motion with two counter rotating vortices is presented in one daughter branch, and a separation zone on the other (Reproduced after Kazakidi, 2008).

1.5. Motivation and Objectives

Driven by these considerations, in this thesis the flow environment in the pulmonary arteries of idealised (Chapter 3 and 4) and patient-specific models (Chapter 5 and 6) was investigated. The aim was to clarify the effect of morphology, flow features and boundary conditions (BCs), in the haemodynamic environment of the pulmonary bifurcation, and, contribute towards understanding the interplay between geometry and upstream and downstream pulmonary vasculature. Flow patterns including velocity streamlines and wall shear stresses were analysed.

In Chapter 3, idealised geometries representative of the pulmonary bifurcation of rTOF patients were used to investigate the effects of the branch angle, branching origin, and different forms of stenosis on the flow development. The objective of this part of the thesis was to understand how the wall shear stress and the pressure are affected by these changes, and whether the percentage of flow diverted to each daughter branch could correlate with the abovementioned parameters. This work aims to answer the following questions:

- Can morphological features affect the flow development in the pulmonary arteries?
- Which characteristics can explain the variations in the haemodynamic environment found in TOF patients?
- Can WSS patterns and pressure ratios explain the flow splits in the daughter branches?

The main contributions of this work are: 1) an extended analysis of the effect of various geometrical characteristics, and how these alter the WSS patterns and pressure ratios,

2) the consideration of branch origin, the effect of which has not been previously attempted, 3) an understanding of flow splits in the pulmonary arteries.

In Chapter 4, the work of Chapter 3 was extended by conducting a parametric analysis to test different boundary conditions. This work helped to evaluate the effect of some of the assumptions considered in the simulations of Chapter 3, including steady laminar flow and the two-dimensional geometries. Finally, an attempt was made to evaluate the effect of some common limitations on blood flow simulations, such as the assumption of rigid walls and omitting the peripheral vascular resistance. The research questions this project attempts to answer are:

- Which modelling parameters have the most significant effect in the computational results?
- What is the effect of the pulmonary valve in the flow development?
- Does wall motion alters the flow in the pulmonary bifurcation?

The main contribution of this work lies on the better understanding of the effect of the boundary conditions in computational simulations, and more specifically: 1) an analysis of the effects of steady and unsteady flow, turbulent flow, blood rheology, pulmonary resistance and elasticity of the arterial wall, on recirculation zones and wall shear stress patterns, 2) an appreciation of how pulmonary valve can alter the flow development, 3) an understanding of the more physiological pressures with the coupling of the pulmonary resistance.

Chapter 5 progresses to patient-specific models from a population of repaired tetralogy of Fallot. The aim of this project is to correlate morphological patterns of curvature and tortuosity, and flow characteristics of Reynolds and Dean numbers, with wall shear

stress and secondary flow patterns. In addition, using the patient-specific models and boundary conditions, an average geometry and average boundary conditions were calculated, to comprehend the significance of patient-specificity in such computational studies. This work attempts to address the following questions:

- Which morphological features are altered in the rTOF population?
- What is the time-averaged wall shear stress distribution in the pulmonary bifurcation of these patients?
- Are there differences between the flow developed in the right and left pulmonary branches? Can these be correlated with the flow splits or the inlet flow?
- Are patient-specificity and spatially-varying flow important in the characterisation of flow?

The main contributions of this work are: 1) an analysis of the haemodynamic environment in the pulmonary bifurcation of rTOF patients, 2) an understanding of the effect of morphological and flow parameters in the flow development, 3) the importance of flow splits and spatially-varying flow in the flow development.

Finally, in Chapter 6, the morphology and the flow development in a healthy population were analysed. The objective of this part of the thesis is to enable a better understanding of the haemodynamic environment in the pulmonary arteries under healthy conditions and allow the comparison with the results acquired for the rTOF models on Chapter 5. This project attempts to address the following research questions:

- What are the differences between the RPA and the LPA in the normal pulmonary bifurcation?
- What is the time-averaged wall shear stress distribution in the healthy population, and is it comparable to the TAWSS patterns observed in the rTOF patients?
- How much does subject-specificity affect the flow development in this case?

The main contributions of this work are: 1) an analysis of the morphological and flow characteristics in normal pulmonary arteries, 2) an appreciation of the differences with the rTOF patients.

1.6. Publications

Most of the results presented in Chapter 3 are published in the Journal of Medical Engineering and Physics, while parts of Chapter 4 are included as Supplementary Material (Boumpouli et al., 2020). In addition, a preliminary version of the results of Chapter 3 has been published in the conference proceedings of the 6th European Conference on Computational Mechanics (ECCM 6), 7th European Conference on Computational Fluid Dynamics (ECFD 7), Glasgow, UK, 11-15 June 2018 (Boumpouli et al., 2018). A conference abstract has also been published in the Heart Journal concerning parts of the work of Chapters 3 and 4 (Boumpouli et al., 2020), while the results of Chapter 5 have been published at the Frontiers in Cardiovascular Medicine journal (Boumpouli et al. 2021). A mini review has also been published in the Journal of Cardiology and Cardiovascular Sciences (Johnston et al., 2021). In the course of this PhD, there were at least three new studies published on the flow in the

pulmonary arteries (Capuano et al., 2019, Conijn and Krings, 2021, Ling et al., 2021), which cited this research work, highlighting how this is a novel and timely study.

Posters with results from Chapters 3 and 4 have been presented in the 8th World Congress of Biomechanics, Dublin, Ireland, 8-12 July, 2018, BioMedEng18, London, UK, 6-7 September 2018 and 5-6 September 2019, 32nd Scottish Fluid Mechanics Meeting, Dundee, UK, 30 May 2019. Finally, oral presentations with results from Chapters 3, 4 and 5 were given at the 31st Scottish Fluid Mechanics Meeting, Aberdeen, UK, 29 May 2018, the 6th European Conference on Computational Mechanics (ECCM 6) - 7th European Conference on Computational Fluid Dynamics (ECFD 7). Glasgow, UK, 11-15 June 2018, 13th World Congress on Computational Mechanics-2nd Pan American Congress on Computational Mechanics, New York City, USA, 22-27 July 2018, 23rd Annual Meeting- Scottish Cardiovascular Forum, Glasgow, UK, 5 February 2020, 33nd Scottish Fluid Mechanics Meeting, online, 28 May 2020, the virtual 14th World Congress in Computational Mechanics (WCCM) and 8th European Congress on Computational Methods in Applied Sciences and Engineering (ECCOMAS) Congress, Paris, 11-15 January 2021.

1.7. Synopsis

The remainder of this thesis is organised as follows:

Chapter 2 describes the computational fluid dynamics methodologies and the modelling methods used. Chapter 3 presents the results of the simulations in two-dimensional idealised models of the pulmonary bifurcation and investigates the effect of geometry on the blood flow development. Chapter 4 is a parametric analysis which

is conducted in order to understand the effect of boundary conditions on the computational models of Chapter 3. Chapter 5 introduces patient-specific models and analyses the morphology and flow characteristics in the pulmonary arterial haemodynamic environment of rTOF patients. Chapter 6 investigates the blood flow in the pulmonary bifurcation of a healthy group and makes comparisons with the results discussed in Chapter 5. Finally, in Chapter 7 some general conclusions, limitations and suggestions for future work are provided.

Chapter 2

Methods

In this chapter, the methodologies used in this thesis are discussed, divided into two main subsections. The first one, provides an introduction to Computational Fluid Dynamics and discusses the concepts of the discretisation process and numerical algorithms used in this work. In the second subsection, cardiovascular modelling is discussed and an overview of the different types of models that can be utilised is provided, based on complexity and the availability of clinical data.

2.1. Computational Fluid Dynamics

Computational Fluid Dynamics (CFD) is a Computer-Aided Engineering (CAE) tool that is used widely in a broad range of fields, such as aerospace and chemical engineering, bioengineering, power generation etc. (Moukalled et al., 2016). CFD also provides a non-invasive simulation method to examine the flow development in blood vessels and is therefore increasingly used to support clinical diagnosis, treatment and surgical planning (Taylor and Figueroa, 2009, Marsden and Feinstein, 2015).

Different numerical techniques exist in CFD to approximate the solution of the partial differential equations (Chapter 1.4.2.). In this work, most of the simulations presented in Chapters 3 to 6 are performed using the open-source software OpenFoam®, a finite volume solver (FVM), while some of the simulations of Chapter 4, are performed using an in-house code Alya-Red which uses the finite element method (FEM) in combination with a variational multiscale method (described by Houzeaux and

Principe, 2008) for the space discretisation (Vazquez et al., 2015). Several numerical solution algorithms can be implemented within each solver which can produce varying convergence. The first step in the process of both FV and FE methods, is the discretisation of the domain into non-overlapping elements (Moukalled et al., 2016), a process also known as meshing. In this study, the commercial software ANSA (BETA CAE Systems, www.beta-cae.com/ansa.htm) was used to generate the computational mesh. In the next paragraphs a brief introduction on OpenFOAM® and Alya-Red is first given. Then, on Section 2.1.1, the principles of mesh generation are discussed, while the basics of each numerical method (FVM and FEM) are provided on Section 2.1.2.

OpenFOAM®

OpenFOAM® is an object-oriented library for numerical simulations written in the C++ programming language, that builds individual software components (classes) to group data and functions, together (Jasak et al., 2007). Its development began by Prof. D. Gosman and Dr. R. Issa, with H. Weller and Dr H. Jasak the principal developers. Over sixty customised numerical solvers are available that can perform simulations of basic CFD, turbulence modelling, heat transfer, combustion, multiphase flow (Chen et al., 2014). The design of OpenFOAM® is based on the easy implementation of complex physical problems, complex geometry handling and robust discretisation, and open-source development. There are five main objects in OpenFOAM®: 1) Space and time, where space is captured as computational mesh and time as a finite number of time steps; 2) Field variable, with tensors, scalars and vectors numerically approximated as list of values at pre-defined points of the mesh; 3) Matrix and linear system, that hold the results of discretisation; 4) Discretisation method, either implicit

or explicit implemented through interpolation, differentiation and discretisation ; 5) physical modelling libraries where the user can recognise object families that can be repeated in the physics modelling level. In general, its advantage lies on its modularity and flexibility (Jasak et al., 2007, Jasak 2009).

Alya-Red

Alya is a High-Performance Computing (HPC) multi-physics simulation code that operates in a modular way: 1) A *kernel* includes all the functionalities to solve physical problems; 2) Sets of *modules*, where each *module* represents a different PDE; 3) *Services*, which are supplementary, including parallelisation services (Vazquez et al., 2014, 2015). A system of algebraic equations is created, following the time and space discretisation of the governing equations, which are programmed in a module. Different iterative methods, either explicit or implicit can be utilised to solve the algebraic system of equations. Coupling modules are also available to simulate multi-physics problems, and staggered and monolithic schemes can be programmed, depending on the case (Vazquez et al., 2014, 2015). Finally, parallelisation is based on mesh partitioning using a Master-Worker strategy. The mesh is read by the Master, which performs partition of the element graph with METIS, while the Workers are charged with each subdomain, and are responsible for the resulting solution. (Houzeaux et al., 2009, 2011, Löhner et al., 2011). Most of the iterative solvers implemented in Alya, like the generalised minimal residual (GMRES), and preconditioners, such as the multigrid or deflated conjugate gradient, are independent of the number of CPUs. Domain decomposition methods and subdomain dependent preconditioners are also implemented for more complex cases.

2.1.1. Mesh Generation

The discretisation of the domain into subdomains that fit the entire geometric space results in a mesh in which the conservation equation will be solved. To obtain an accurate solution, a good quality mesh is essential. There are different element options available to consider when discretising the domain, including a structured grid, consisting of prismatic elements or structured quadrilateral, or an unstructured grid, consisting more often of triangular or tetrahedra elements, in 2D (Fig. 2.1a), and tetrahedra or hexahedra, in 3D (Fig. 2.1b). For complex vascular geometries, an unstructured grid is preferred which can be automatically generated by existing algorithms. For viscous flows, a layer of structured elements is usually adopted near the wall boundary to better capture the viscous effects of the flow, known as the boundary layer (Ferziger and Perić, 2002).

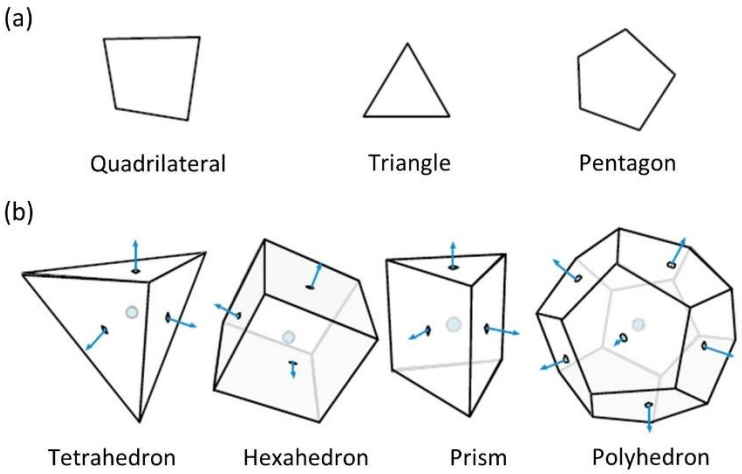

Figure 2.1: Different types of (a) 2D and (b) 3D elements (After Moukalled et al., 2016).

The process of the mesh generation starts with the geometrical representation, and follows a “bottom up” approach, where first the boundary edges are discretised, then

the surface of the computational domain, and finally volume mesh is generated (Lintermann, 2021).

Considering the domain to be discretised, it consists of an area, for the 2D case, or a volume, for the 3D case, and is defined by a set of vertices or points connected by curves or boundary edges that form the boundary faces (Fig. 2.2). The elements representing the geometrical domain are bounded by the faces, and the same faces are shared between neighbour elements, unless located at the boundaries of the model. The direction of the surface normal points towards the interior of the domain, important for the boundary layer generation which proceeds along the surface normal (Blazek, 2015).

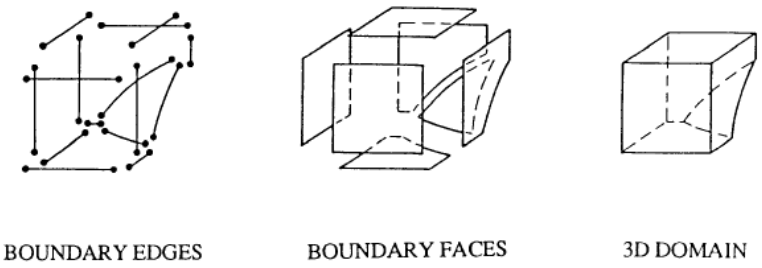

Figure 2.2: Decomposition of 3D domain (After Peiró et al., 1994).

Surface mesh

The advancing front method (Peraire et al., 1988, Löhner, 1996) was used for the triangulation of the surface boundaries. The technique proceeds by adding one element at a time, and the region which separates the gridded from the ungridded is known as the *front*.

The boundaries of the domain are discretised by points, or nodes, added at the boundary edges and lines connecting the nodes. A spatial variation of the element size is prescribed to control the number of nodes and the length of the lines. Using the

information about the element size, element shape and the line-definitions of the boundaries of the domain, an initial *front* of faces is defined, which is updated during the discretisation process. New elements, points and faces are added simultaneously on the surface of the domain and until the *front* is empty, noting that the surface is meshed (Peraire and Morgan, 1997). Mesh spacing can be specified at the boundaries of the domain to improve the surface mesh. This allows the local mesh refinement in regions of interest and gives the flexibility of elements of various sizes.

Boundary layer

Once the surface of the model is meshed, the viscous boundary layer is generated near the wall boundaries. The advancing-layers method (Pirzadeh, 1994, 1996) generates prismatic or structured tetrahedral elements, by connecting new nodes added towards the interior of the domain, for internal flow problems, and as an extrusion of the surface mesh. Multiple layers are usually generated starting with a minimum distance between the first element of the boundary layer and the wall, and progressively increasing by a specified growth factor rate to reach the desired layer thickness (Fig. 2.3).

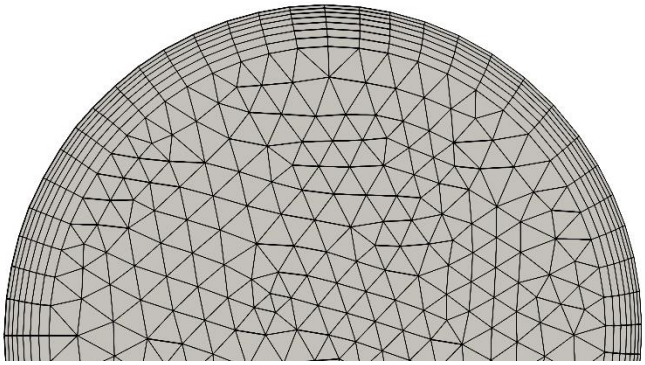

Figure 2.3: A boundary layer mesh consisting of 7 layers of prismatic elements. The first layer is at a distance of 0.005 cm away from the wall and progressively increases with a growth factor rate of 1.1.

To characterise the quality of the near-wall mesh, the non-dimensional distance of the first element node from the wall, known as the y+ value, can be used to determine the height of the first layer Δy_1 (Defraeye et al., 2010):

$$\Delta y_1 = \frac{\mu y +}{\rho U_T} \tag{2.1}$$

where y+ satisfying the value of 1 (Lewandowska and Mosiężny, 2019) and U_T the friction velocity:

$$U_T = \sqrt{\tau_w / \rho} \tag{2.2}$$

where τ_w is the wall shear stress calculated as:

$$\tau_w = \frac{1}{2} C_f \rho U_{mean}^2 \tag{2.3}$$

where U_{mean} the mean velocity and C_f the skin friction coefficient developed by Churchill (Churchill, 1977) that spans all fluid flow regimes (laminar, transitional and turbulent) and measures the resistance to flow by a pipe:

$$C_f = 2 * \left[\left(\frac{8}{Re} \right)^{12} + \left(\left(2.457 \ln \left(\left(\frac{Re}{7} \right)^{0.9} \right) \right)^{16} + \left(\frac{37530}{Re} \right)^{16} \right)^{-1.5} \right]^{1/12} \tag{2.4}$$

Volume mesh

The interior of the domain is discretised, generating the volume mesh, using a hybrid advancing front Delaunay algorithm (Skaperdas and Ashton, 2018). The elements of the boundary layer form the background grid from where triangulation starts. Points are inserted using a method similar to the advancing front, described for the surface mesh. The background grid is used to determine any intersections and nearby fronts.

The boundary grid is updated, and the generation of the isotropic elements proceeds according to the Delaunay triangulation (Holmes and Snyder, 1988).

2.1.2. Numerical Methods

Numerical methods are utilised in order to approximate the solution of partial differential equations, and involves the discretisation of the domain (as described in Section 2.1.1.) and the equations to be solved. Many different discretisation schemes exist today, such as the finite difference method (FDM), FVM, FEM, the spectral methods (SM) etc (Rapp, 2017). In general, FEM is one of the most widely applicable methods. It requires the conversion of the partial differential equations to an integral form and, if first order accurate, approximates the solution by a linear shape function, within each element of the domain (Peiró and Sherwin, 2005). FVM integrates the equations over a finite number of control volumes. The volume integral is then interpolated at the surface of the control volume. Volume and surface integrals can be approximated with suitable numerical approximations (Moukalled et al., 2016). FDM is less flexible for cardiovascular models as it uses structured elements, *e.g.*, rectangular and hexahedral elements, and is difficult to be adapted to more complex models. FDM approximates the derivatives of the differential form of the fluid equations, in contrast to the integral approximations in the aforementioned methods (Feriziger and Perić, 2002, Peiró and Sherwin, 2005). Taylor series expansion is used to approximate the first and second order derivatives of the variables, with the forward, backward and central difference schemes being some of the most commonly utilised numerical schemes. Spectral methods are robust and of high-accuracy but are limited to problems of periodic boundary conditions. In SM the solution is approximated using

an integral form of the differential equations and is represented globally in the solution domain. The books of Ferziger and Perić (2002) and Rapp (2017) are suggested for a more detailed description of the most commonly used schemes.

This subsection starts by introducing the most commonly used boundary conditions, namely Dirichlet and Neumann. Then, the finite volume and finite element methods are discussed. Finally, some of the properties of numerical methods and the difference between explicit and implicit schemes are provided. Further details about the FVM and the FEM can be found on the books of Moukalled et al. (2016) and Zienkiewicz et al. (2014), for each method, respectively.

2.1.2.1. Boundary Conditions

In both the FV and FE numerical methods, a lot of attention should be given in the boundary conditions assigned at the boundary faces of the domain. To evaluate the fluxes at the boundary faces, the Dirichlet and Neumann boundary conditions, are most commonly used. In the first case, a specific scalar value is assigned at the boundary face, while in the second case, the derivative of the scalar is the known quantity which is specified (Ferziger and Perić, 2002). The effect and the importance of different boundary conditions is further discussed within this thesis, briefly in Section 2.2, and Chapters 3-5, with respect to blood flow dynamics in the pulmonary arteries.

2.1.2.2. Finite Volume Method

The finite volume method solves the partial differential equations of the conservation laws (Chapter 1.4.2.) by discretising them into algebraic equations over finite volumes. The algebraic equations are solved at each of the elements of the geometric domain to

compute the value of the dependent variables of velocity and pressure, which are consequently stored at the centre of the finite volume for the majority of the finite volume methods (cell-centered FVM, Fig. 2.4), including in the OpenFOAM® software (Moukalled et al., 2016). In FVM, the flux entering a given volume is equal to the flux leaving the adjacent volume, which makes it a conservative approach (Fig. 2.5a).

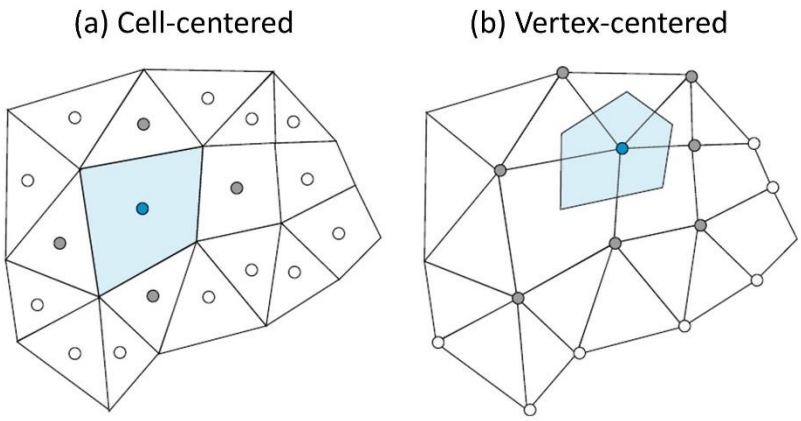

Figure 2.4: (a) Cell-centered and (b) vertex-centered arrangements (After Moukalled et al., 2016).

Equation Discretisation

The general form of the conservation equation (Eqs. (1.10)-(1.13)) for a scalar φ is given by:

$$\frac{\partial(\rho\varphi)}{\partial t} + \nabla \cdot (\rho \boldsymbol{u}\varphi) = \nabla \cdot (\Gamma^{\phi}\nabla\varphi) + Q^{\varphi} \tag{2.5}$$

where $\frac{\partial(\rho\varphi)}{\partial t}$ the transient term, $\nabla \cdot (\rho \boldsymbol{u}\varphi)$ the convective term, $\nabla \cdot (\Gamma^{\phi}\nabla\varphi)$ the diffusion term and Q^{φ} the source term (Moukalled et al., 2016).

Following the integration of the governing equations over the finite volumes and for a steady state form, in which case the transient term is removed (Eq. (2.6)), the volume

integrals are transformed using the Gauss theorem* into surface integrals for the convection and diffusion terms of the conservation equation (Eq. (2.7)) (Moukalled et al., 2016).

$$\int_{\Omega} \nabla \cdot (\rho \boldsymbol{u} \varphi) d\Omega = \int_{\Omega} \nabla \cdot (\Gamma^{\phi} \nabla \varphi) d\Omega + \int_{\Omega} Q^{\varphi} d\Omega \tag{2.6}$$

$$\int_{S} (\rho \boldsymbol{u} \varphi) \cdot dS = \int_{S} (\Gamma^{\phi} \nabla \varphi) \cdot dS + \int_{V} Q^{\varphi} dV \tag{2.7}$$

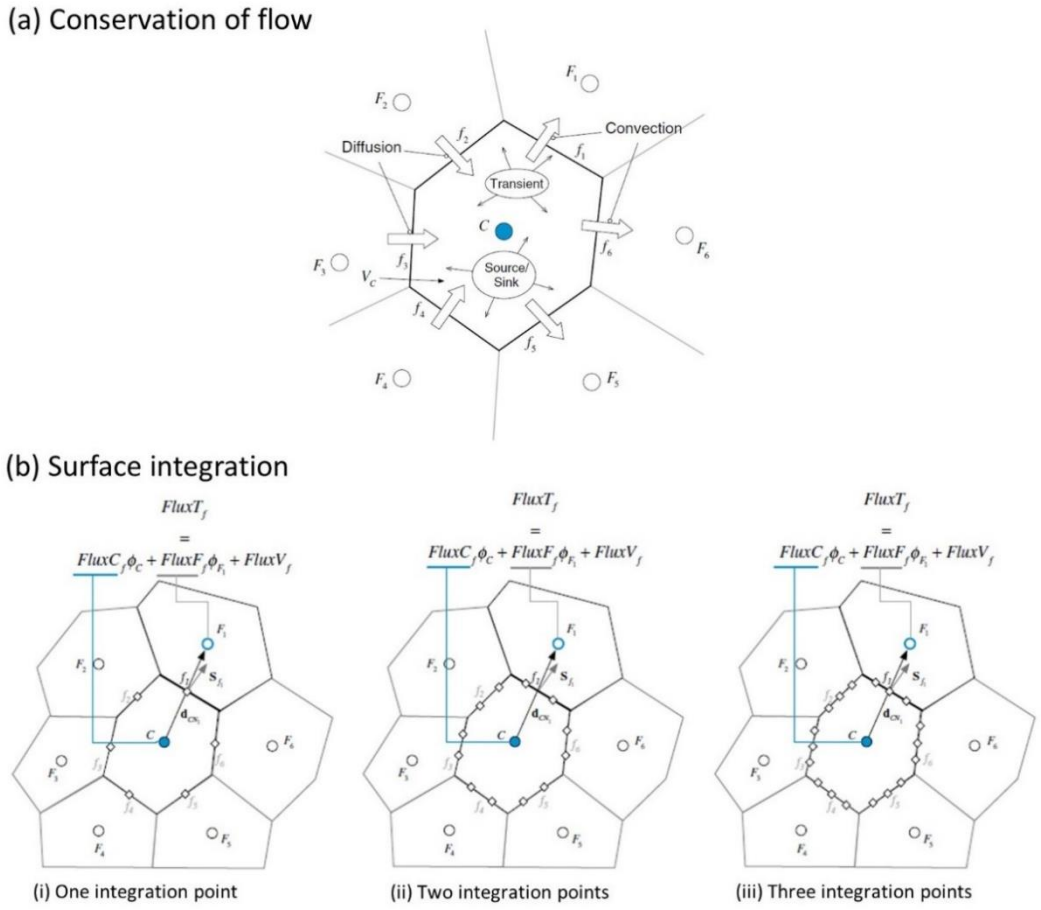

Figure 2.5: (a) Conservation of flow. Flux entering a discrete element equals flux leaving; (b) Surface integration using (i) one, (ii) two and (iii) three integration points, respectively (After Moukalled et al., 2016).

*Gauss' theorem: $\int_{\Omega} \nabla \cdot \boldsymbol{f} d\Omega = \int_{S} \boldsymbol{f} \cdot \boldsymbol{n} dS$, where the left part denotes the volume integral over the volume Ω and the right side the surface integral over the boundary of the volume Ω (Spiegel et al., 2009).

Integration points are used along the surface (for the convection and diffusion fluxes), or volume (for the source term), of the elements, in which the discrete form of the surface and volume integrals are numerically integrated, and the number of points affect the accuracy of the solution (Fig. 2.5b). Most FV methods use a single integration point for a simple mean value integration, allowing a second-order accurate approximation, which is found adequate in terms of accuracy and computational cost. Increasing the number of points along the surface or volume of the element, increases the accuracy of the solution, respectively (Moukalled et al., 2016). Once the convection and diffusion fluxes and the source term are discretised with a specified number of integration points, the next step in the discretisation process is to convert the finite volume equations of each element into an algebraic equation and relate the face and volume fluxes with the values of the variables of the neighbouring cells. Flux linearisaton is used in the second discretisation process and the evaluation of the fluxes dependents on the boundary conditions assumed (Section 2.1.2.1).

2.1.2.3. Finite Element Method

The Finite Element Method was originally developed for solid-state mechanics problem but is used in a wide range of applications since then, including CFD (Rapp, 2017). There are many similarities between the FE and FV method. Firstly, the domain is discretised into finite elements or volumes, where the algebraic equations will be solved. In the FE methods it is only a list of vertices that is needed; the solution is approximated at the vertices of the domain and linearly interpolated in between these points (Rapp, 2017). To allow the creation of a function to interpolate the solution linearly between the adjacent edges of the element, each element in the domain is defined based on the Lagrangian coordinate system which makes use of the area of the

element instead of the Cartesian coordinate system (Fig. 2.6) (Rapp, 2017). Before the solution is integrated over the entire domain, FEM uses a weight function, with which the algebraic equations are multiplied (Ferziger and Perić, 2002). The Galerkin method is the most commonly used weighted residual method to approximate the solution.

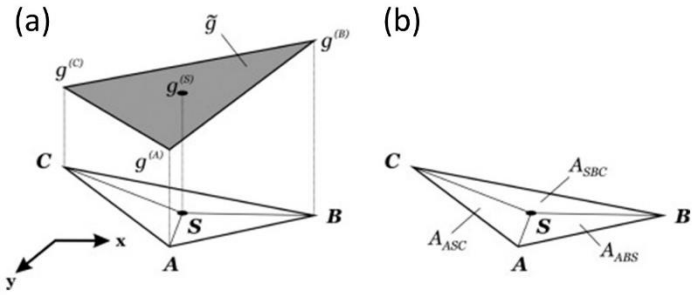

Figure 2.6: Lagrangian coordinate system in an FEM mesh. (a) Approximation of the dependent function g using $\tilde{g}$. (b) Definition of the Lagrangian coordinates using the area of the subtriangles created within a single triangle (After Rapp, 2016).

Restricting the analysis to a one-dimensional space, a scalar variable *u(x,t)* is considered in the domain $\Omega = \{x, t: 0 \leq x \leq 1, 0 \leq t \leq T\}$. The convection-diffusion-reaction equation is then given by (Peiŕo and Sherwin, 2005):

$$L(u) = \frac{\partial u}{\partial t} + \frac{\partial}{\partial x}(au - b\frac{\partial u}{\partial x}) - ru = s \tag{2.8}$$

where *L(u)* a linear differential operator, and *a*, *b* and *r* the convection, diffusion and reaction coefficients, and *s* the source term (Peiró and Sherwin, 2005).

The integral of Eq. (2.8) is:

$$\int_0^1 L(u)\omega(x)dx = \int_0^1 s\omega(x)dx \tag{2.9}$$

where $\omega(x)$ is the weight function.

Discretising the region of interest into N-1 subdomains $\Omega_i = \{x : x_{i-1} \leq x \leq x_{i-1}\}$, the approximate solution can be assumed as:

$$u(x,t) = \sum_{i=1}^{N} u_i(t) N_i(x) \tag{2.10}$$

where $N_i(x)$ the expansion basis (Peiŕo and Sherwin, 2005).

The Galerkin method sets the weight function same as the expansion basis. Substituting to Eq. (2.9), and by approximating the solution to the elliptic equation $L(u) = \frac{\partial^2 u}{\partial x^2} = s(x)$ with boundary conditions $u(0)=a$ (Dirichlet boundary condition) and $\frac{\partial u}{\partial x}(1)=g$ (Neumann boundary condition):

$$\int_0^1 \omega(x) \frac{\partial^2 u}{\partial x^2} dx = \int_0^1 \omega(x) s(x) dx \tag{2.11}$$

Finally, integrating the left-hand side of Eq. (2.11) the weak form is derived:

$$-\int_0^1 \omega(x) \frac{\partial u}{\partial x} dx + \omega(1) \frac{\partial u}{\partial x}(1) - \omega(0) \frac{\partial u}{\partial x}(0) = \int_0^1 \omega(x) s(x) dx \tag{2.12}$$

Although the Neumann BC can be easily imposed, the Dirichlet BC can be applied by imposing $u_{1=} a$ under the requirement that $\omega(x)=0$ (Peiŕo and Sherwin, 2005).

2.1.2.4. Properties of Numerical Methods

To ensure that the solution obtained during the discretisation process is meaningful, there are some key properties to be considered (Ferziger and Perić, 2002, Peiŕo and Sherwin, 2005):

- Conservation: the numerical scheme should respect the conservation laws.

- Accuracy: numerical solution are only approximated solutions of the fluid flow problems.
- Convergence of the solution: the computed and the exact solution of the PDE tends to zero with decreasing mesh size.
- Consistency: the discretised numerical equation approaches the exact differential equation as grid spacing tends to zero.
- Stability of the system: the difference between the computed and exact solution should not be magnified during the solution process, for a given grid spacing.

2.1.2.5. Implicit and Explicit Methods

To solve the equations in each of the discretised elements, implicit or explicit numerical methods can be used. In an explicit method, the unknown variable is directly computed by the known variables. On the other hand, in an implicit method, a set of equations are formed to compute the dependent variable, which is usually performed through an iterative process. The conservation equations in CFD are most usually solved using the implicit numerical method. Although they are more complicated and computationally expensive, they facilitate larger time steps and are unconditionally stable (Moukalled et al., 2016).

2.2. Cardiovascular Modelling

Modelling in cardiovascular research goes back decades when computers became available to the university research and the industry (Schievano and Taylor). In the late 1990s, imaged-based modelling techniques immerged, and with the advancements made ever since, especially the magnetic resonance imaging (MRI) and computed

tomography (CT), the quantification of cardiovascular mechanics, the non-invasive characterisation of physiological pressures and flows, and the computation of parameters that cannot be measured *in-vivo*, became possible (Taylor and Figueroa 2009). Nowadays, cardiovascular modelling is broadly used to answer clinical questions, from image segmentation and morphology charasterisation, to diagnosis and quantification of physiological responses under a range of conditions (Schievano and Taylor, 2020, Johnston 2020, Black et al., 2020, Hyde-Linaker et al., 2020).

In cardiovascular modelling, as with any CFD problem, the first step is the pre-processing stage where the fluid domain needs to be defined. Depending on the aims, numerical complexity, accuracy and patient-specificity, required to address the problem, the domain can be approached with a zero- (0D), one- (1D), two- (2D) or three- (3D) dimensional model, as shown in Fig. 2.7 (Shi, 2011).

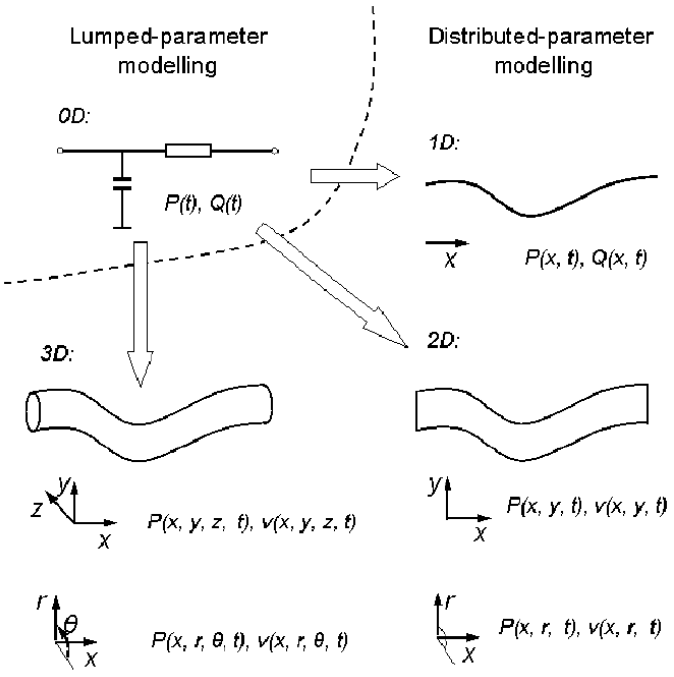

Figure 2.7: Different scales of modelling (After Shi, 2011).

Zero-dimensional (or lumped-parameter) models are governed by ordinary differential equations; they do not recognise the spatial variation of variables (pressure, flow and volume), and are used to model various components of the human body, the heart, heart valves, vasculature. They examine the interaction of such compartments as well as the global distribution of the abovementioned variables. To model the cardiovascular system using 0D-modelling, one needs to consider a hydraulic electric analogue where the volumetric blood flow rate is represented by an electric current. Blood pressure is analogous to voltage, the resistance to flow is equivalent to the electrical resistance of the electric circuit, inductance represents the inertia in blood flow and the compliance of the vessel is modelled by capacitors (Fig. 2.8).

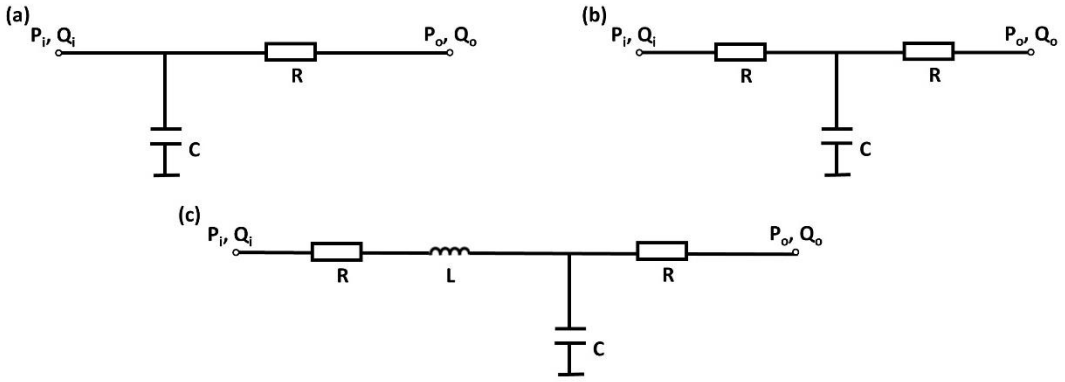

Figure 2.8: Two-element (a), three-element (b), and four-element (c) Windkessel models (Reproduced after Shi, 2011).

Equivalently, for the conservation of mass and momentum, which need to be satisfied to describe the blood flow, Kirchhoff's current law and Ohm's law are used in 0D-modelling (Shi, 2011). Kirchhoff's current law states that the current entering a node must be equal with the sum of currents exiting the node (Eq. (2.13)), while Ohm's law states that the current in an electric circuit is equal to the voltage divided by the resistance (Eq. (2.14)).

$$\sum_{k=1}^{n} I_k = 0 \tag{2.13}$$

$$I = \frac{V}{R} \tag{2.14}$$

Substituting with the equivalent parameters of cardiovascular system, Eq. 2.14 takes the form of Eq. (1.1).

The two-element Windkessel model, introduced mathematically by Otto Frank (1899), is the first and simplest 0D model that makes use of these principles and can be used either in isolation or as part of a multi-compartment electrical circuit. It is a RC model (Fig. 2.8a), with the resistance and capacitance connected in parallel. Different alterations have been made to this model ever since; the three-element Windkessel model (Fig. 2.8b) has an additional resistance connected in series with the RC model (Landes, 1943), or, using an alternative configuration, a resistance is connected in series with the capacitor of the RC model (Burattini and Natalucci, 1998). Other developments have included the inertia of blood flow in the RCR Windkessel model (Fig. 2.8c), or extra resistances, connected in different configurations, which are known as four-element Windkessel models (Landes 1943, Jager et al., 1965, Stergiopulos et al., 1999).

A three-element Windkessel model was developed in MATLAB®, R2017b, MathWorks to account for the pulmonary vascular resistance and capacitance (Appendix 1). The code was tested using clinical flow data, extracted from the MPA, LPA and RPA branches, of a healthy volunteer. The 0D model developed was then used in order to compile a new solver in OpenFOAM®, for the coupling of the lumped-parameter model in an idealised 2D model (the results of the coupled model are presented in Chapter 3).

One-dimensional models use the conservation of mass and momentum to describe the blood flow using the 1D form of the Navier-Stokes equations in combination with equations for the forces acting on the vessel wall. They are most often used to represent wave transmission and to improve the boundary conditions for 3D models in order to capture arterial wave reflections (Shi, 2011). The unstressed radius of the domain, the length and the wall thickness of the vessel and the Young's modulus are the initial parameters needed, while the radius of the vessel, pressure and flow are information that can be obtained from the 1D analysis (Arimon, 2006).

Two-dimensional and three-dimensional models are governed by the partial differentia Navier-Stokes (Eq. (1.19)). 2D models can provide information on the radial variation of local flow in an axisymmetric domain and further improve the boundary conditions for 3D models (Shi, 2011), while with 3D models the study of the flow in the full 3D domain is feasible. Such higher dimensional models can predict in more detail the haemodynamic parameters of the vessels, but due to the higher complexity, modelling is usually limited to smaller segments (Malatos et al., 2016). Currently, the preferred method in cardiovascular modelling is using patient-specific 3D models, which can be reconstructed using clinical image data (Analysed on Section 2.2.3.).

2.2.1. Coupled models

Coupling of the 0D models to 1D, 2D or 3D models was introduced in cardiovascular modelling in order to overcome one of the main limitations of zero pressure at the outlets of the models. 0D models can be coupled at the boundary outlets to represent, with reduced complexity, the downstream peripheral circulation which is neglected in the 3D modes (Malatos et al., 2016). Applications of this methodology can be found

in many studies, especially in cases of virtual surgeries, to test different surgical plans and optimise the anatomical configuration of the region. Several studies of univentricular circulation and cavopulmonary anastomosis, a congenital heart disease where one ventricular chamber is absent and an operation is performed to bypass the absent ventricle, named cavopulmonary anastomosis, have utilised such methods (Pennati et al., 1997, Migliavacca et al., 1999, Lagana et al., 2005, Migliavacca et al., 2006, Bove et al., 2008, Baretta et al., 2011, Pennati et al., 2011). Nevertheless, lower-order models can be coupled either upstream or downstream of the higher-order models, depending on the availability of data, and the information to be acquired through the model (Vosse, 2003).

2.2.1.1. Fluid Structure Interaction

Fluid structure interaction (FSI) refers to the co-simulation of a fluid and a solid structure. In cardiovascular modelling, it can be used to simulate the motion of the vascular walls or the heart valves (Taylor and Figueroa, 2009). Although it has been found that neglecting vessel compliance the regional shear stress is overestimated (Bazilevs et al., 2009), it is more computationally expensive, and the vessel's mechanical properties, need to be specified (Hunter et al., 2010).

FSI simulations require the coupling of the fluid and the solid domain, and two of the most well-known techniques adopted are the Arbitrary Lagrangian Eulerian (ALE) and the Immersed Boundary Method (IBM). A brief description of each method is provided here, but more details can be found on Donea et al., 2004, and Peskin, 1972, for the ALE and IMB methods, respectively. In the present study, the ALE method was implemented to simulate the elasticity of arterial walls (Chapter 4).

The ALE method is a body-fitted, also known as body-conforming method, where a structured/unstructured mesh is generated, with the grid being updated in each time step (Fig. 2.9a). The fluid domain is moving according to the motion of the vascular interface, and therefore the Navier-Stokes equations need to be solved on a moving reference system. For the solid domain, the elastodynamics equations (provided at the end of this Section) are solved, usually based on a Lagrangian reference system. Finally, the flow for the grid points of the fluid domain which are not at the interface with the moving solid domain need to be defined (Hughes 1981, Hu 1996).

There are two approaches for solving FSI problems, the monolithic or non-modular, and the modular or partitioned. In the partitioned approach, the equations governing the fluid and the solid domain are solved separately, allowing more specialised solvers to be used for each domain. However, a coupling algorithm is required to allow the interaction of the two and the acquisition of a solution for the coupled problem. These algorithms exhibit stability issues and poor convergence due to the "added mass effect", related to the mass density of the fluid versus the solid structure. In the monolithic approach, the fluid and the solid equations are solved simultaneously, which has the advantage of stability and faster solution of the problem (Hu 1996, Taylor and Figueroa, 2009, Bhakade et al., 2016).

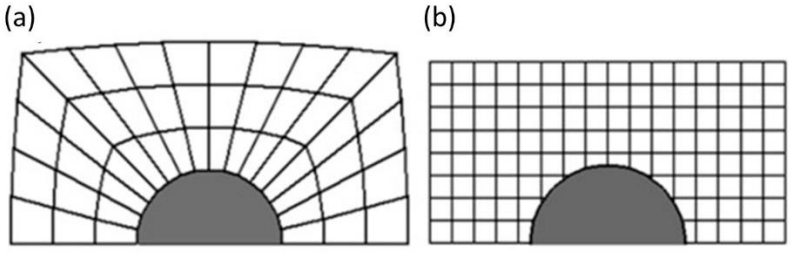

Figure 2.9: (a) Body-fitted meshes, in the Arbitrary Lagrangian-Eulerian method, and (b) non-fitted meshes, in the Immersed Boundary Method (After Hashemi, 2018).

The IBM was introduced by Peskin (1982) and is a non-body-fitted, also known as fixed-rigid method which does not require the computational grid of the fluid domain to be changed or deformed (Fig. 2.9b). IBM instead uses two sets of independent grids, a fixed Eulerian and a moving structured or unstructured grid, for the fluid and the solid domains, respectively (Hashemi, 2018). The advantage of this method is that it does not involve the update of the mesh and therefore, is more effecting in handling arbitrarily large deformations. Additional external forces are incorporated in the governing equations of motion to account for the moving body in the fixed computational domain (Peskin, 1982). Some of the challenges are related to the application of boundary conditions and the more accurate definition of the moving body. In addition, IBM requires increased spatial resolution due to the delta function which is introduced to avoid numerical instabilities (Kazakidi et al., 2015). The immersed interface method (LeVeque and Li, 1997) and the hybrid Cartesian/immersed boundary method are two approaches to overcome these limitations (Gilmanov and Sotiropoulos, 2005).

Hyperelastic models

Let *B* be a body in a bounded domain Ω (the reference configuration), with *P* a generic material point of *B*, and X(*P*) indicating the position vector of *P*. The kinematics of deformation can be described locally with the deformation gradient tensor **F**:

$$\boldsymbol{F} = \frac{\partial x}{\partial X} \tag{2.16}$$

The equation of motion in Ω is then given by:

$$\rho \frac{\partial^2 d}{\partial t^2} - div(\boldsymbol{P}) = \boldsymbol{f} \tag{2.17}$$

where $d = x\text{-}X$, the displacement of the material point, **P** the first Piola-Kirchhoff stress tensor and f an external force.

In equilibrium, Eq. (2.17) is reduced to:

$$-div(\boldsymbol{P}) = \boldsymbol{f} \tag{2.18}$$

Different constitute laws can complement Eqs. (2.17), (2.18) to quantify the displacement of the body, with the simplest being linear elasticity (Gurtin, 1982).

In this work, the incompressible Neo-Hookean model is considered, which splits the the deformation gradient and the strain energy function, ψ, into volumetric and isochoric isotropic terms (Nolan et al., 2014):

$$\boldsymbol{F} = (J^{1/3}\boldsymbol{I})\bar{\boldsymbol{F}} \tag{2.19}$$

where J the determinant of **F**, $J^{1/3}\boldsymbol{I}$ the volumetric portion of **F** and $\bar{\mathbf{F}}$ the isochoric portion, and:

$$\psi(\boldsymbol{F}) = \frac{1}{2}\kappa_o(J-1)^2 + \frac{1}{2}\mu_o(\bar{I}_1 - 3) \tag{2.20}$$

where κ_o the bulk modulus, μ_o the shear modulus and $\bar{I}=J^{-2/3}I_1$ the isochoric counterparts of I_1.

The Cauchy stress (σ) for a hyperelastic material with free energy ψ is given by:

$$\sigma = \frac{1}{J}\boldsymbol{F}\frac{\partial\psi}{\partial\boldsymbol{F}} \tag{2.21}$$

and is related to the Piola-Kirchhoff stress tensor with $\mathbf{P} = J\sigma\mathbf{F}^{-T}$ (Gurtin, 1982, Nolan et al., 2014).

2.2.2. Image-based computational modelling

Computerised tomography (CT) and magnetic resonance imaging (MRI) are diagnostic tools that enable the acquisition of medical images and can be used to reconstruct the computational domain based on the patient's anatomy. Briefly, the process, in order to conduct patient-specific computational simulations, would start with the image segmentation, followed by several steps of pre-processing, including the smoothing of the model and the addition of flow extensions. The next step is the discretisation, or meshing (as described in Section 2.1.1) of the computational domain. Appropriate boundary conditions should be assigned at the boundaries of the models, where for patient-specific cases they can be extracted from phase contrast-MRI images, or 4D flow MRI data. The last step involves the post-processing of the computational results. A schematic representation of the steps is presented on Fig 2.10. In the following paragraphs the segmentation and smoothing processes are discussed. Examples will also be described in Chapters 5 and 6 which involve subject-specific models.

The clinical images used for the model segmentation are a stack of two-dimensional slices, with each slice consisting of a matrix of pixels with different intensities of a grayscale value. There are many open-access and commercial software that allow the segmentation of the vasculature using automatic, semi-automatic or manual tools. The Insight Segmentation and Registration Tool Kit, ITK-Snap (www.itksnap.org), SimVascular (www.simvascular.github.io) and Mimics (Materialise, Belgium) are some of the most frequently used; the reconstruction of the models in this work was conducted using ITK-Snap. In the manual segmentation, the user progresses slice-by-

slice and draws the region of interest with suitable tools. In the semiautomatic segmentation, ITK-Snap implements the Geodesic Active Contours (Caselles et al., 1993, 1997) and the Region Competition (Zhu and Yuille, 1996) methods.

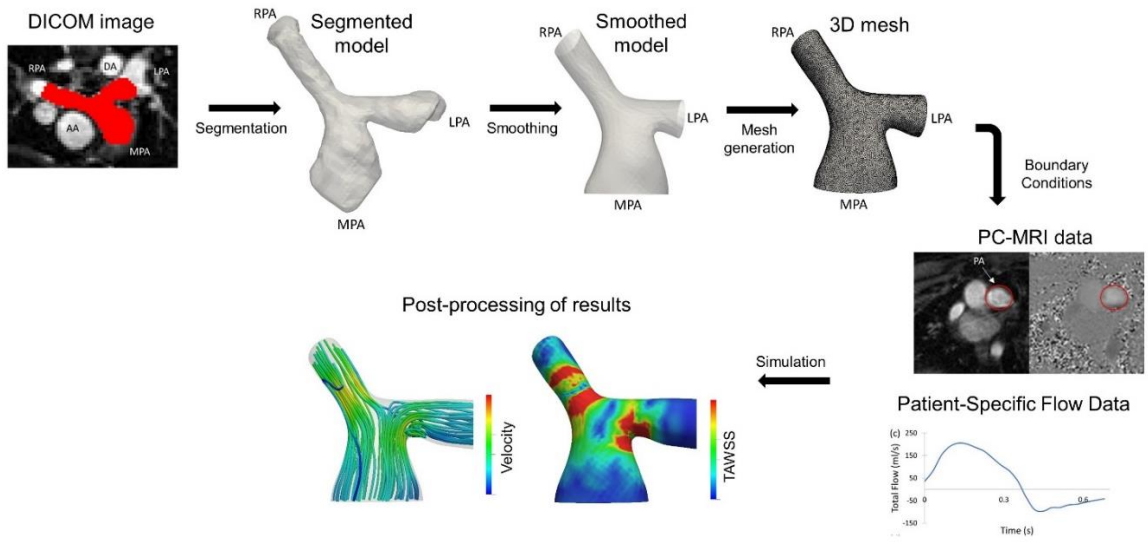

Figure 2.10: Steps followed in reconstructing and modelling a patient-specific geometry: segmentation of the computational domain from clinical images, smoothing and mesh generation, extraction of flow information to set patient-specific boundary conditions and finally post-processing of the computational results.

Let *C* be the contour represented as a level-set of a function φ, in space $\mathbb{R}^3$. Contour evolution evolves in time according to the equation:

$$C_t(t, \boldsymbol{q}) = F_{internal} + F_{external} \tag{2.22}$$

where $C(t,\boldsymbol{q})$ is the contour at time t parameterised by $\boldsymbol{q}^*$. Internal ($F_{internal}$) and external ($F_{external}$) forces, acting in the normal direction on the contour, are used to constraint the shape of the contour based on the contours geometry and include information from the image segmented, respectively (Yushkevich et al., 2006).

There are two implementations of this method, the Geodesic Active Contours (Caselles et al., 1993, 1997) and the Region Competition (Zhu and Yuille, 1996) and they differ

[*] $\boldsymbol{q}$ can be represented in terms of the arc length of the contour, or parametrically using B-splines or Fourier coefficients (Zhu and Yuille, 1996).

in the way the compute the external forces. Caselles et al. (1993, 1997), computes the external forces based on the intensity of the image's gradient magnitude:

$$C_t(t, \boldsymbol{q}) = (\alpha g_I + \beta \kappa g_I + \gamma \nabla g_I \cdot \boldsymbol{N})\, \boldsymbol{N} \tag{2.23}$$

where α, β and γ are modulating weights, defined by the user, κ is the mean curvature of C, **N** the contour normal and g_I of the image I given by:

$$g_I = f_{map}\left(\frac{\|\nabla(G_\sigma * I)\|}{max\|\nabla(G_\sigma * I)\|}\right), f_{map}(x) = \frac{1}{1 + (x/\nu)^\lambda} \tag{2.24}$$

where $G_\sigma * I$ indicating convolution with a Gaussian kernel (Sherstyuk, 1999), and ν, λ and σ, user defined parameters, g_I decreases monotonically with the gradient magnitude of image I. αg_I, $\beta \kappa g_I$ and $\gamma \nabla g_I \cdot \boldsymbol{N}$, represents the external, internal and external advection forces, respectively, with the latter acting inwards when C reaches the edges of I (Yushkevich et al., 2005, 2006).

The method by Zhu and Yuille (1996) is based on a voxel probability map, where, by setting a threshold, the probability of a voxel to belong to the region of interest is estimated. At the implementation of this method, the external force is proportional to the difference of probabilities P_{obj} and P_{bg}, with P_{obj} = P(voxel ∈ object) and P_{bg} = P(voxel ∈ background):

$$C_t(t, \boldsymbol{u}) = [\alpha(P_{obj} - P_{back}) + \beta \kappa]\, \boldsymbol{N} \tag{2.25}$$

Contour evolution is implemented with the level set active contour algorithm (Osher and Sethian, 1988, Sethian, 1999) and using the relationship $\boldsymbol{N} = \nabla\varphi\|\nabla\varphi\|$, Eqs. (2.23) and (2.25), are transformed to PDEs in φ and solved iteratively using the extreme narrow banding method (Whitaker, 1998). Spherical seed points are placed, from

which the contour evolution begins, and the result is updated after each iteration (Yushkevich et al., 2006).

In this work, the semi-automatic segmentation based on the Region Competition method was adopted, and the segmentation was afterwards manually corrected, were appropriate, going through each slice. The segmented models were exported as surface mesh, using the marching cube algorithm that processes 3D medical data and creates triangle vertices of constant density surfaces using linear interpolation (Lorensen and Cline, 1987).

The smoothing of the models was conducted with the opensource software Autodesk Meshmixer (www.meshmixer.com). The smooth type was the default Shape Preserving smoothing filter. The smoothing scale controls the features that must be smoothed based on their size. In the geometries presented in Chapters 5 and 6 of this thesis, the scale was around 4-8 depending on the model, and approximately 16 and 8 for the interfaces of the inlet and outlet boundaries, respectively, where the extensions were added. For the constraint rings, the default value was maintained to allow tangent continuity at the edges and preserve the shape at the boundaries. Finally, extensions were added using the Vascular Modeling Toolkit, vmtk (www.vmtk.org), normal to the surface of the inlet and the outlets of the models, to avoid any effects from the boundaries.

Information about the number and type of elements, and the boundary conditions, are provided separately in each Chapter, for the respective models. In addition, information about the MRI data used for the reconstruction of the patient-specific

models, and the extraction of the patient-specific boundary conditions of Chapter 5 and 6, are included in the methodology section of each Chapter.

Chapter 3

Blood flow simulations in two-dimensional idealised models of the pulmonary bifurcation

In this chapter, the flow in nine different geometries and under seven different boundary conditions, assigned at the model's outlets, is investigated under steady and unsteady flow conditions. Section 3.1. provides a brief introduction to this work, while Section 3.2. describes the numerical methodology, including model generation and boundary conditions. Section 3.3. presents the main results of this chapter, divided in the effects of geometry, outflow boundary conditions and a parametric investigation. Section 3.4. discusses the results in the context of previous studies, and Section 3.5. concludes this chapter with some final remarks.

3.1. Introduction

Tetralogy of Fallot patients require surgical correction in infancy. It is performed to provide a bi-ventricular circulation and normal arterial saturations. With advancements in medical paediatric healthcare, the expected survival and quality of life have improved immensely, similar to normal population. However, as these patients progress into adulthood, they are at risk of late complications and further re-interventions. Pulmonary regurgitation and branch pulmonary obstruction, usually in the form of LPA kinking, are the most common indications for reintervention, including pulmonary valve replacement and arterial stenting (Zhang et al., 2016, Babu-

Narayan and Gatzoulis 2018). The assessment of the optimal timing for PVR is crucial in order to allow the successful RV remodelling and is recommended before the development of significant clinical symptoms. Nevertheless, it remains a key challenge to clinicians, relying their decision upon balancing the risk between RV dysfunction and the finite lifespan of the available bioprosthetic valves used in PVR (Geva, 2011, Babu-Narayan and Gatzoulis, 2018). Recent studies have observed that PR is associated with differential retrograde flow of various flow splits in the left and right branch pulmonary arteries in patients with rTOF, irrespective of the presence of stenosis (Kang et al., 2003, Harris et al., 2011). To clarify this, a better understanding of the subtle haemodynamic alterations in the pulmonary arterial bifurcation is required, with the scope to contribute towards a more accurate evaluation of the right timing for PVR and the prognosis and treatment of the above conditions.

Optimisation of flow delivered to the daughter branches of an arterial junction is essential in order to ensure that blood vessels supply the peripheral tissue and organs with sufficient amount of blood, compared to the energy consumed by the tissue and organs (Rubenstein and Yin, 2015). Murray's law, an early mathematical model, makes use of the branches radii in order to optimise work, through minimisation of energy consumption at bifurcations (Murray, 1926). However, there are many fluid dynamic principles that can affect fluid flow and need to be taken into account. Several previous studies on physiological flows in branching arteries (Pedley et at., 1971, Rubenstein and Yin, 2015) have demonstrated flow separation near branch entrances and the formation of recirculating zones, with fluid particles trapped within, due to their inability to re-enter the mainstream flow (Rubenstein and Yin, 2015, Sochi, 2015). Nevertheless, the haemodynamics of arterial bifurcations may further be

affected by local morphology, such as the branching angle, and various other factors, including non-Newtonian rheology, turbulent flow, time-dependency, and loss of wall deformability (Sochi, 2015). The pulmonary bifurcation in rTOF patients is a particular junction with varied and often abnormal geometrical and boundary conditions, and their detailed effects on blood flow need further analysis.

Computational fluid dynamic (CFD) methods are valuable tools for non-invasively simulating blood flow through vessels and allow for the examination of various effects that may influence flow development. Computational models are increasingly used to support clinical diagnosis, treatment, and surgical planning, through the quantification of haemodynamic parameters, such as velocity, pressure, and wall shear stress, and the investigation of blood flow patterns. Previous studies on blood flow in the pulmonary arteries have shown that in healthy subjects the pulmonary bifurcation is haemodynamically efficient with small separation of flow along the inner wall (Capuano et al., 2019). However, in congenital heart patients, reversal of flow has been observed in the LPA which precedes and contributes to pulmonary valve regurgitation (Samyn and LaDisa, 2016), while flow becomes more disturbed for decreasing branching angle (Chern et al., 2008, Chern et al., 2012, Guibert et al., 2014, Zhang et al., 2016, Samyn and LaDisa, 2016). In most of these studies, blood was modelled as a Newtonian fluid, which is an accepted approximation in large arteries (Samyn and LaDisa, 2016).

In the present chapter, the blood flow in idealised two-dimensional models of the pulmonary bifurcation is investigated using computational fluid dynamics tools. Although simplified, the use of such geometries allows for a detailed parametric analysis of the influence of various conditions on blood flow, improving our

understanding of the underlying flow mechanisms of more complex systems, while being much less computationally demanding (Alegre-Martinez et al., 2019). Different geometries were considered here, representative of healthy and abnormal morphologies of the pulmonary trunk. The novelty of this work lies in the extended analysis of bifurcating flows in relation to TOF patients and a haemodynamic assessment in the pulmonary arteries, which may be useful to clinicians and adult congenital heart patients.

3.2. Computational approximations

3.2.1. Models of the pulmonary bifurcation

Nine different geometries of the pulmonary bifurcation were created in the two-dimensional space in order to investigate the effects of branching angle, branch origin, and LPA stenosis (Fig. 3.1). These simplified models make it possible to analyse healthy and abnormal flow conditions and identify critical parameters. The diameter of the main pulmonary artery (MPA), denoted as *D*, was assumed 2.6 cm, while both daughter branch diameters were taken, for the majority of the models, equal to 2 cm (denoted as *d*). These values are within the normal physiological ranges, without attempting to replicate exact patient cases (Tang et al., 2012). The MPA length was assumed ~7.7*D*, while the LPA and RPA lengths were chosen to be ~115*D*, the minimum branch length at which no effect on the maximum wall shear stress (WSS) from the boundaries was found. More specifically, to establish the branch length, WSS was plotted along the inner wall (shown on Fig. 3.1 (vi)) for models with different

branch lengths, and until the maximum WSS value reached a plateau. The nine geometries (Fig. 3.1 shows only a section of each model) are as follows (Table 3.1):

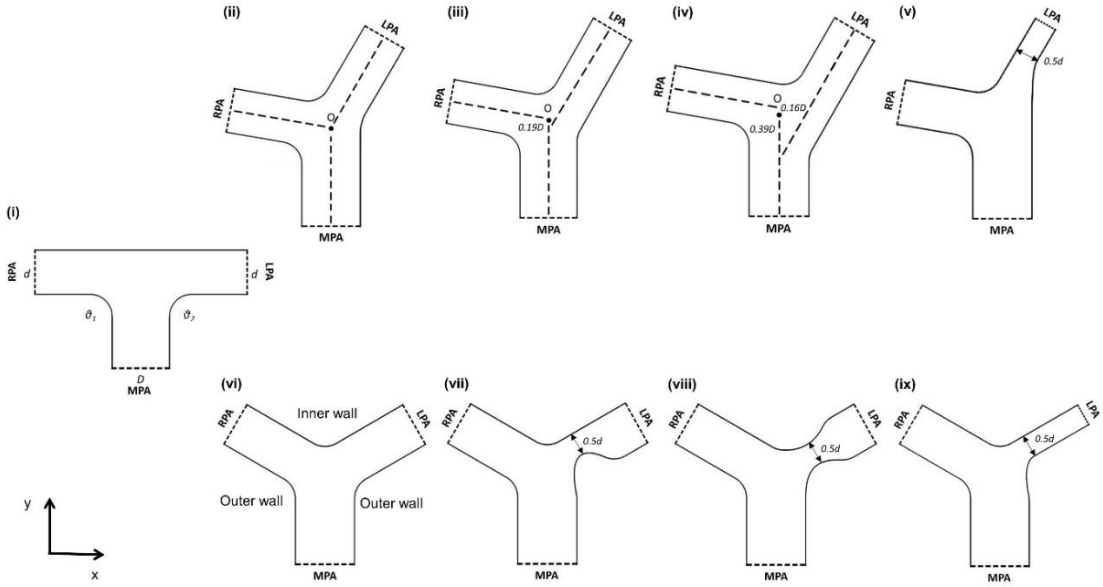

Figure 3.1: Schematic representation of nine different models of the pulmonary bifurcation. (i) T-Junction; (ii) asymmetric Y-Junction with common branch origin at point O; (iii)-(iv) asymmetric Y-Junctions with displaced branch origins; (v) asymmetric Y-Junction with displaced origin and hypoplastic LPA; (vi) symmetric Y-Junction; (vii)-(ix) symmetric Y-Junctions with local stenosis and hypoplastic LPA, respectively. The inner and outer walls are annotated on (vi).

a. A T-Junction where the angle between the MPA and daughter branches is 90º (denoted as θ_1 for RPA and θ_2 for LPA); this geometry represents the shape of the pulmonary bifurcation in patients repaired for both LPA and RPA stenosis (Nina, 2014), or in the context of pulmonary atresia with RV pulmonary artery conduit and/or confluence constriction (Fig. 3.1 (i)).

b. An asymmetric Y-Junction with θ_1 = 100º and θ_2 = 150º; this geometry can be seen as the normal shape for the pulmonary bifurcation, assuming a common origin of the two branches, at point O (Fig. 3.1 (ii)). An axial black-blood MRI image of the pulmonary bifurcation of a healthy volunteer (male, 27 years old) can be seen in Fig. 3.2a obtained with ethical approval from the Glasgow CRIF

approval group, and written informed consent, REC name WoS REC3, reference 16/WS/0220.

c. An asymmetric Y-Junction, with θ_1, θ_2 as in (b), which assumes a displaced origin for the LPA centreline, by 0.5 cm (~0.19*D*) upstream of point O (Fig. 3.1 (iii)), and can also be considered physiological.

d. An asymmetric Y-Junction, with θ_1, θ_2 as in (b) and displaced origins for both LPA and RPA, by 0.3 cm (~0.12*D*) downstream and 1 cm (~0.39*D*) upstream of point O, respectively (Fig. 3.1 (iv)).

e. An asymmetric Y-Junction, with θ_1, θ_2 as in (b), but with a displaced origin and a reduced diameter for LPA by 1 cm (0.5*d*), representing a uniform small calibre of the pulmonary branch or, in the context of this work, a hypoplastic branch (Fig. 3.1 (v)) (Jang et al., 2017).

f. A symmetric Y-Junction with $\theta_1 = \theta_2 = 120^{\circ}$, representing the pulmonary bifurcation of repaired patients with TOF, including cases where the MPA may be directly attached to the RV without conduit (Fig. 3.1 (vi)) (Nina, 2014).

g. A symmetric Y-Junction, with $\theta_1 = \theta_2$ as in (f), and a local 50% asymmetric stenosis within the LPA, positioned 1.7 cm (~0.65*D*) downstream of the pulmonary bifurcation. This geometry represents the case of LPA kinking (Fig. 3.1 (vii)) (Nina, 2014).

h. A symmetric Y-Junction, with $\theta_1 = \theta_2$ as in (f), and a local 50% symmetric stenosis within the LPA, positioned 1.7 cm (~0.65*D*) downstream of the pulmonary bifurcation (Fig. 3.1 (viii)).

i. A symmetric Y-Junction, with $\theta_1 = \theta_2$ as in (f), but with a displaced origin and a hypoplastic LPA (Jang et al., 2017), with a reduced diameter by 1 cm (0.5*d*) (Fig. 3.1 (ix)).

Table 3.1: Characteristics of the nine different models created to represent the pulmonary bifurcation.

Model	**Type**	**Angle θ_1**	**Angle θ_2**	**Branch Origin in relation to point O**	**LPA**	**Clinical Relevance**
(i)	T-Junction	90º	90º	Common	-	rTOF
(ii)	Asymmetric Y-Junction	100º	150º	Common	-	Physiological case
(iii)	Asymmetric Y-Junction	100º	150º	Displaced for LPA	-	Physiological case
(iv)	Asymmetric Y-Junction	100º	150º	Displaced for both branches	-	Physiological case
(v)	Asymmetric Y-Junction	100º	150º	Displaced for LPA	Hypoplastic	Hypoplastic LPA
(vi)	Symmetric Y-Junction	120º	120º	Common	-	rTOF
(vii)	Symmetric Y-Junction	120º	120º	Common	Local asymmetric stenosis	LPA kinking – asymmetric stenosis
(viii)	Symmetric Y-Junction	120º	120º	Common	Local symmetric stenosis	Branch LPA stenosis – symmetric stenosis
(ix)	Symmetric Y-Junction	120º	120º	Displaced for LPA	Hypoplastic	Hypoplastic LPA

3.2.2. Numerical approximations

The computational meshes for all geometries of Fig. 3.1 were generated using the commercial software ANSA v17.1 (BETA CAE Systems). Each mesh consisted primarily of quadrilateral elements, with a few triangular elements in the middle of the bifurcation (Fig. 3.2b).

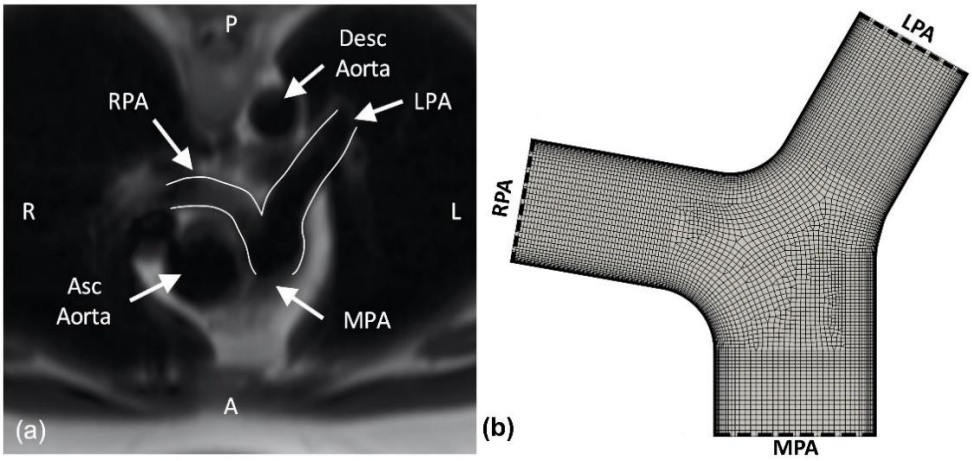

Figure 3.2: (a) An axial black-blood MRI image from a healthy male volunteer (27 years old), overlaid with an outline of the inner and outer walls of the pulmonary bifurcation. (b) Computational mesh for the geometry of Fig. 3.1 (ii), consisting mainly of quadrilateral elements, a few triangular elements in the middle of the bifurcation and a boundary layer near the wall.

A boundary layer mesh was also added near the arterial wall boundaries to capture the viscous effects, which included 17 layers with the first layer being at a distance of ~0.002*D* away from the wall. This was determined based on a low y+ wall treatment, calculated using Eqs. (2.1), (2.2), where ρ is the fluid density (1060 kg/m^3), and μ is the dynamic viscosity (4x10^{-3-} Pa s), and was equal to 0.18. This implies that the viscous boundary layer is sufficiently resolved within the fine layered mesh. The total number of elements for the nine geometries of Fig. 3.1 was between 90 000 - 125 000 and was based on a grid independence test performed previously in a similar model. More specifically, a symmetric Y-Junction (Fig. 3.3a), with the diameters of the models and the length of the MPA, as those of Fig. 3.1 (vi), was conducted. The length of the RPA and LPA branches of this geometry was 8*D*, and the number of elements deemed sufficient for the flow regimes was 5000, based on the integral of the velocity profile at a reference line located ~0.019*D* from point O (Fig. 3.1 (ii)) before the pulmonary junction. In addition, the use of triangular (Fig. 3.3b) or primarily quadrilateral elements (Fig. 3.3a) in the mesh was compared and showed no difference

in the integral of velocity at the entrance of the bifurcation. The number of elements was roughly the same for both meshes (Fig. 3.3): (a) 4798 and (b) 4888 (Boumpouli et al., 2018).

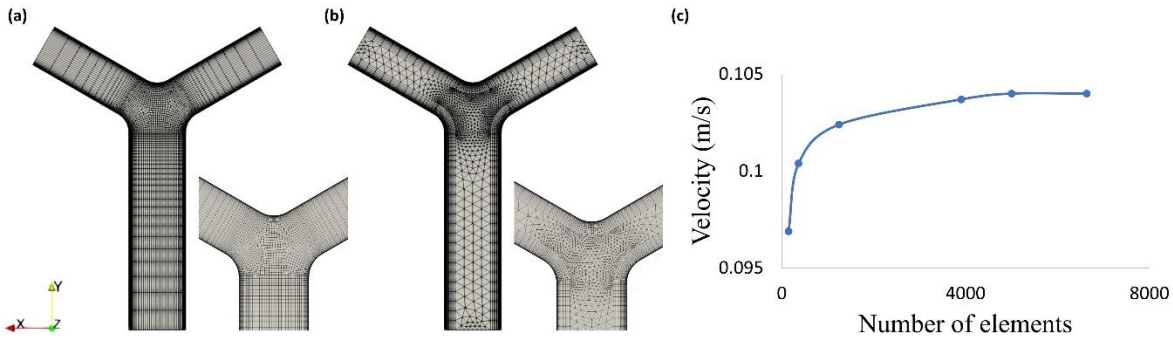

Figure 3.3: Computational grids of the pulmonary models with a surface mesh of (a) primarily quadrilateral elements and (b) primarily triangle elements. A boundary layer mesh is adopted near the walls of the models. (c) Grip independence analysis test, based on the integral of the velocity profile obtained at a reference point (~0.019D from point O) of the symmetric Y-Junction model.

The latter type of elements was chosen to avoid non-orthogonality issues. The angle between a line which connects two cell centres in a face normal vector and a mesh is defined as mesh non-orthogonality. Non-orthogonality of triangular meshes is higher compared to quadrilateral elements and although non-orthogonal correctors can be utilised in OpenFOAM®, their use is not necessary for low non-orthogonality meshes (Ishigaki et al., 2017). The decision regarding the elements used have been previously validated by Arbia et al. (2014), where better results were obtained when axisymmetric elements oriented along the direction of flow were used. The length of the daughter branches was afterwards increased as it was found to affect the wall shear stress calculated at the inner wall. Nevertheless, as the number of elements around the region of interest (pulmonary bifurcation) was not altered, a mesh independence test was not performed.

For the simulations presented here, blood flow was considered Newtonian, laminar and incompressible, governed by the Navier-Stokes equations (Eqs. (1.17), (1.21)). In the models of Fig. 3.1, a steady, parabolic inlet velocity profile was assigned at the MPA (Vignon-Clementel et al., 2006, Sochi, 2015), using the "codedFixedValue" boundary of the OpenFOAM® open-source library, according to the equation:

$$u_{par}(x) = \frac{3}{2} U \left(1 - \frac{4x^2}{D^2}\right) \tag{3.1}$$

with mean velocity $\mathrm{U} = 0.1\ \mathrm{m/s}$, an average physiological value noted in healthy subjects (Gabe et al., 1969, Bronzino, 2000), and rigid walls. This boundary condition enables you to implement your own boundary conditions by adding a piece of C++ code to calculate the boundary value (Appendix A.2.1). It is the simplest way to implement a new boundary without using high level programming or an external library.

The Reynolds number (Eq. (1.14)), calculated based on the MPA diameter, was 650 for all cases. The semi-implicit method for pressure linked equations (SIMPLE) algorithm by Caretto et al. (1973), adopted by many CFD studies (Neofytou et al., 2014), of the OpenFOAM® v.1806 (https://www.openfoam.com/) was utilised for the pressure–velocity coupling in all the numerical calculations. The SIMPLE algorithm solves the equations in a successive manner: an initial guess is made for the pressure distribution to calculate an intermediate velocity field that satisfy the momentum equation and then velocities and pressures are corrected based on the mass conversation (under-relaxation is applied on the calculation process) (Caretto et al., 1973). The Gauss linear gradient and the second order bounded Gauss linear upwind

divergence numerical schemes (Warming and Beam, 1976) were used. This means that the finite volume discretisation is performed using the Gauss theorem, where the interpolation from cell to face centres is necessary, while the interpolation scheme is specified as linear, or central differencing. Residual control was set to 10^{-6} for pressure and velocity.

To account for the unsteady nature of blood flow, a sinusoidal variation of the velocity profile at the MPA inlet was assumed for the geometry of Fig. 3.1 (ix), based on the following expression:

$$u(x,t) = u_{par}[1 + sin(2\pi ft)] \tag{3.2}$$

where f is the frequency, assumed as 2 Hz (Young, 2014). Time-averaged results over a single cycle were compared with the steady-state numerical results for the same mean velocity. A combination of the SIMPLE and the pressure implicit with splitting of operators (PISO) (Issa, 1986) algorithms for pressure–velocity coupling within OpenFOAM® (PIMPLE) was utilised for the unsteady numerical calculations. The main difference of the PISO from the SIMPLE algorithm is that the momentum corrector step is applied for as many times as specified, and no under-relaxation is applied. PIMPLE operates by using outer correction loops to ensure convergence of the explicit parts of the equations, when the simulation moves on in time. At each time step a steady-state solution is searched based on the number of outer correctors specified. Once this solution is reached then the outer correction loop is bypassed and the simulation continues in time (Holzmann, 2016).

3.2.3. Effect of outlet boundary conditions

For the geometries of Fig. 3.1, a condition of zero-pressure was initially applied at the LPA and RPA outlets (Zhang et al., 2016), which corresponds to a mean pressure at rest of 8-20 mmHg. The zero-pressure assumption is commonly used in simplified geometries without available patient-specific information of flow and pressure waveforms or peripheral resistances (McElroy and Keshmiri, 2018). However, in order to acquire more clinically relevant results and flow splits in the daughter branches, an investigation on the outflow boundary condition was conducted, in three different ways:

Prescribed pressure outlet conditions: Using the symmetric Y-Junction geometry (Fig. 3.1 (vi)), first, the RPA branch was elongated to double its original length, since physiologically the RPA is longer than the LPA (Qureshi and Hill, 2015), with zero pressure assigned at both outlets; second, a pressure difference of $|\Delta P| = |P_{RPA} - P_{LPA}|$, normalised by $0.5\rho U^2$, was prescribed at the branch outlets. A range of different $|\Delta P|$values were tested and the approximate values of 0.026 and 0.015 were chosen, since these pressure difference values provided more clinically relevant flow splits in the daughter branches, closer to 40:60% (Tang et al., 2011).

Prescribed flow splits: Murray's Law formula can be used to calculate the flow expected in each branch outlet, based on the branch diameter, and, for the LPA, it could be expressed as:

$$Q_{LPA}/(Q_{LPA} + Q_{RPA}) = [{D_{LPA}}^n/({D_{LPA}}^n + {D_{RPA}}^n)] \quad (3.3)$$

where Q_{LPA}, Q_{RPA} are, respectively, the flow rates at the LPA and RPA branches, D_{LPA}, D_{RPA} the branch diameters, while, customarily, n is considered equal to 3.

Eq. (3.3) can be rewritten based on the "outflow splitting" method (Chnafa et al., 2018), which calculates the flow division locally for each bifurcation generation, assuming n=2. For the pulmonary bifurcation, this is expressed as:

$$Q_{LPA}/Q_{RPA} = (D_{LPA}/D_{RPA})^n \tag{3.4}$$

The symmetric Y-Junction model with the hypoplastic LPA (Fig. 3.1 (ix)) was used as a reference geometry for this investigation, due to the difference in the diameter of the daughter branches. Based on the conservation of mass, the flow splits were calculated as $Q_{LPA}/Q_{RPA} = (1/2)^n$, resulting in 11:89% flow split with the Murray's Law and 20:80% with the "outflow splitting" method. The flow splits in the outlets of the models were prescribe utilising the "codedFixedValue" boundary (Appendix A.2.2).

Lumped parameter models: A lumped model made of a peripheral resistance was coupled and implemented on each of the outlets of the symmetric hypoplastic model (Fig. 3.1 (ix)) to capture effects of the downstream vasculature (Grinberg and Karniadakis, 2008). The pressure, *p*, was calculated based on the flow rate, *Q*, and the resistance, *R*, according to Eq. (1.1). R_{LPA} and R_{RPA} were assumed both equal to 300 dyn s cm^{-5} (Guibert et al., 2014), matching the distal resistance assumed in the three-element Windkessel model (Capuano et al., 2019), described in the next paragraph. The effect of a pulsatile inlet flow condition was also investigated for the peripheral resistance boundary condition.

Furthermore, a three-element Windkessel (WK) lumped parameter model was coupled at the outlets of the geometries to represent the peripheral resistance and wall compliance of the pulmonary vessels (Guibert et al., 2014), according to the following differential equation:

$$p(t) + R_d C \frac{\partial P(t)}{\partial t} = \left(R_p + R_d\right) Q(t) + R_p R_d C * \frac{\partial Q(t)}{\partial t} \tag{3.5}$$

where R_p and R_d are the proximal and distal resistances, and C is the capacitance, assumed as 40 dyn s cm^{-5}, 300 dyn s cm^{-5}, and 10^{-3} cm^5 dyn^{-1}, respectively (Guibert et al., 2014). The geometry of Fig. 3.1 (ix) was used for this investigation. A new solver was compiled for each lumped parameter model, utilising the PIMPLE algorithm for pressure–velocity coupling within OpenFOAM®, with the relaxation factors for pressure and velocity equal to 0.3 and 0.7, respectively.

3.2.4. Post-processing

To characterise the flow development in the arterial models, contours of velocity, velocity profiles and streamlines, WSS distribution along the inner wall of the bifurcation (connecting the LPA and RPA as shown in Fig. 3.1 (vi)), as well as pressure ratios and flow splits were analysed. Velocity values were non-dimensionalised by division with the mean MPA velocity U. WSS was non-dimensionalised with the value corresponding to the inlet WSS magnitude of a long straight segment that has the same diameter of MPA inlet and same inflow conditions as the pulmonary bifurcation model. For a two-dimensional channel, this can be calculated for a Newtonian model with a fully developed axial velocity profile as $\tau_{w_{2D}} = 6\mu U/D$ (Katritsis et al., 2007). The calculation of flow splits was based on the velocity profiles at a distance of 3cm

(1.15*D*) from the branch origin for each model. The choice of the distance was decided so that no flow recirculation of flow would be present at any of the branches of the models. The time-averaged wall shear stress (TAWSS) was further used and was determined according to the following equation:

$$\tau_{mean} = \frac{1}{T}\int_0^T |\tau_w| dt \tag{3.6}$$

where $|\tau_w|$ is the magnitude of the instantaneous WSS vector.

3.2.5. Verification and validation

Three different tests were employed to confirm the results of this study. First, a benchmark validation test was conducted based on a two-dimensional T-Junction model, as presented by Neofytou et al. (Neofytou et al., 2014), who compared their result with experimental measurements from the commonly used benchmark case of Liepsch and Moravec (Liepsch and Moravec, 1982), with a mean velocity of $U = 0.16\ m/s$, corresponding to a Reynolds number of 400. A good agreement was found between the computational results of this study and those obtained by Neofytou and colleagues (Neofytou et al., 2014), with a percentage difference in the velocity integrals below 0.2% for the parent channel (min/max, ±SD, -0.0015/1.3 in this study vs 0.0054/1.558 on Neofytou et al., 2014, ±0.0345/0.129) and less than 1.4% (min/max, ±SD, -0.144/0.82 in this study vs -0.106/0.79 on Neofytou et al., 2014, ±0.019/0.015) for the daughter channels. Second, computational results obtained in the symmetric Y-Junction with OpenFOAM® appeared in very good agreement with calculations performed in ANSYS Fluent®, for the same geometry and flow and boundary conditions (Fig. 3.4). More specifically, a percentage difference of 0.047%

was quantified for the integral of velocity profiles (min/max, ±SD, 0.0012/0.1286 in OpenFOAM® vs 0.0012/0.124 on ANSYS Fluent®, ±0/0.0023) positioned at the entrance of the bifurcation (at a distance 0.01 m from the origin O). A comparison between the simpleFoam and the pisoFoam solvers of the OpenFOAM® library was conducted for the symmetric Y-Junction model, assuming steady flow. For a laminar flow model and a mean velocity of $U = 0.1\, m/s$ at the MPA inlet, the length difference of the recirculation zone formed at the outer wall of the LPA was 1.3%. For a turbulent flow model (specification of turbulent model are provided in Chapter 4.2) with a mean MPA velocity of $U = 0.5\, m/s$, the LPA recirculation length difference was 2% between the two solvers, based on the results from simpleFoam, which is slightly greater, but still in good agreement, since the pisoFoam solver is more time-accurate for incompressible turbulent flows, using the PISO algorithm. Finally, a similar comparison was conducted between the simpleFoam and pimpleFoam solvers for the symmetric Y-Junction with a hypoplastic LPA, assuming steady flow. The length difference of a localised recirculation area at the entrance of the outer wall of the LPA was 10%, while for the recirculation zone in the RPA, the difference was 2.7%.

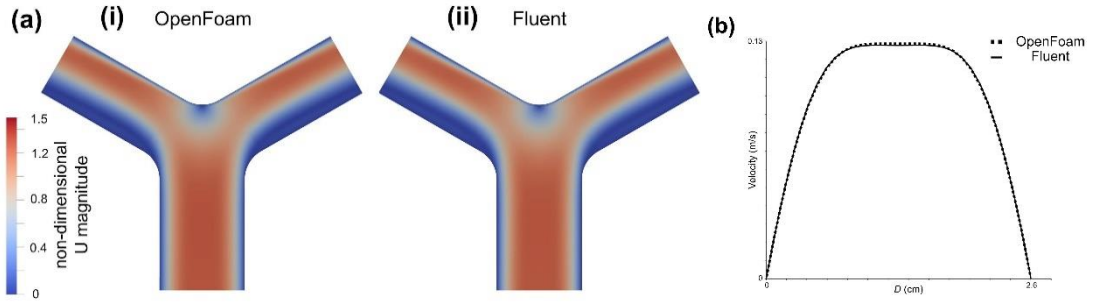

Figure 3.4: Comparison of OpenFOAM® and Ansys Fluent. (a) Non-dimensionalised velocity contours. (b) Velocity profiles at the entrance of the bifurcation and at a distance of 0.01 m from the branch origin. Steady Newtonian flow, Re=650.

3.3. Results

The results of this study are presented in a series of figures that explore the effects of different geometric features on the haemodynamics of the pulmonary bifurcation (Figs. 3.5-3.8), and, the effect of boundary conditions on velocity and WSS in the symmetric Y-Junction, with and without a hypoplastic LPA (Figs. 3.9-3.11). The geometries reflect normal and abnormal cases of congenital heart patients, as described in Section 3.2.1 (Table 3.1).

3.3.1. Effect of bifurcation geometry

3.3.1.1. Contours of velocity magnitude

Contours of non-dimensional velocity magnitude are presented in Fig. 3.5 for a segment of each of the nine bifurcation models described in Section 3.2.1 (Fig. 3.1). A zero-pressure boundary condition is used at the outlets of the models, with a parabolic velocity profile, of Re=650, assigned at the inlet. Due to the parabolic inlet profile, the highest values of velocity in the MPA were observed along the centreline and the lowest were found adjacent to the walls, for all models. For the geometries of Figs. 3.5 (i-iv), (vi-viii), flow entering the bifurcation experienced an abrupt deceleration, with the maximum axial velocity value dropping rapidly, until becoming instantaneously zero when impinged on the wall (stagnation point, indicated with the letter S in Fig. 3.5). As a result, flow in the daughter branches was shifted towards the inner walls, with the highest values of velocity occurring adjacent to it, while extended low-velocity regions developed along the outer walls of the bifurcation.

The most substantial differences among the various models were observed for those with an LPA local stenosis (Figs. 3.5 (vii-viii)) or hypoplastic LPA (Figs. 3.5 (v), (ix)). For the models with local constriction (Figs. 3.5 (vii-viii)), the highest velocities were found inside the stenosis where the diameter of the artery was halved. Downstream of the stenosis, an extended region of low velocity values developed near the outer wall of the LPA, with an additional small-scale low-velocity region occurring at the inner wall of the model with symmetric narrowing (Fig. 3.5 (viii)). No substantial changes were noticed in the RPA velocity distribution of these models when compared with the symmetric non-stenotic model (Fig. 3.5 (vi)). In contrast, for hypoplastic models (Figs. 3.5 (v), (ix)), where the LPA diameter was also halved, the highest velocities were observed in the RPA while very low velocities were exhibited in the hypoplastic LPA. The velocity distribution in these models deviated significantly from their respective non-stenotic symmetric and asymmetric models, and an altered flow split between the daughter branches was apparent.

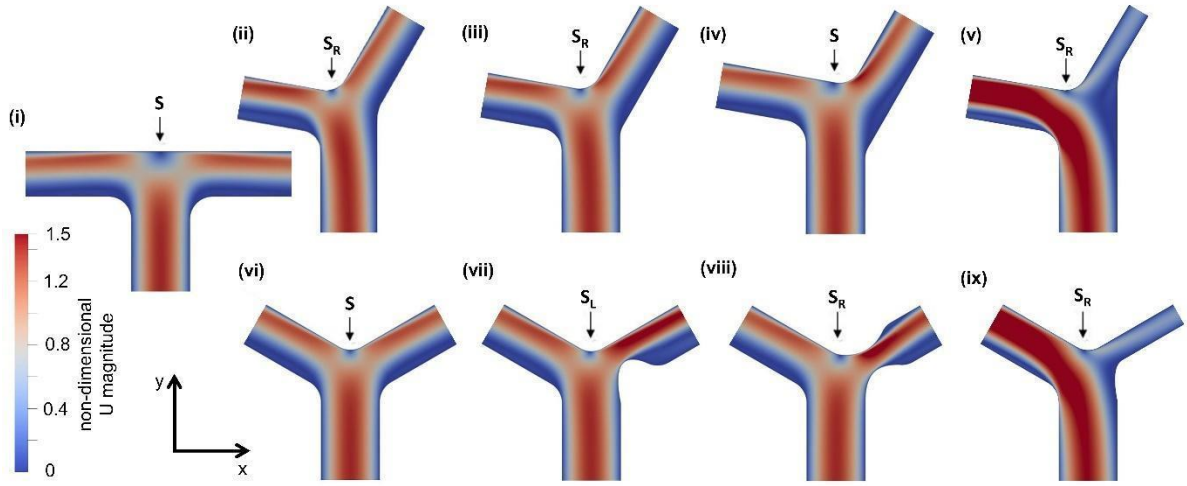

Figure 3.5: Contours of non-dimensionalised velocity magnitude in models of the pulmonary bifurcation: (i) T-Junction; (ii)-(v) asymmetric Y-Junction with (iii)-(iv) different branch origins and (v) hypoplastic LPA; (vi-ix) symmetric Y-Junction (vi) without and (vii)-(viii) with local stenosis or (ix) hypoplastic LPA. Steady Newtonian flow, Re=650. The stagnation point on the MPA centreline is indicated with the letter S; or S_R and S_L if deviated towards the RPA and LPA, respectively.

The stagnation point, S, was further identified for all models. It was located along the centreline of the MPA for the T-Junction (Fig. 3.5 (i)), the symmetric Y-Junction (Fig. 3.5 (vi)), and the asymmetric Y-Junction with non-common branch origins (Fig. 3.5 (iv)). For the remaining models, most stagnation points were found shifted away from the MPA centreline towards the RPA (denoted as S_R in Fig. 3.5), by 0.77 cm (~0.3*D*) and 0.47 cm (~0.18*D*), respectively, for the asymmetric Y-Junctions of Fig. 3.5 (ii-iii); 0.96 cm (~0.37*D*) for the asymmetric Y-Junction with hypoplastic LPA (Fig. 3.5 (v)); 0.20 cm (~0.077*D*) for the symmetric Y-Junction with local symmetric stenosis (Fig. 3.5 (viii)); and 0.22cm (~0.085*D*) for the hypoplastic LPA model (Fig. 3.5 (ix)). The only stagnation point found towards the LPA (denoted as S_L) was for the local asymmetric stenotic model (Fig. 3.5 (vii)), shifted by 0.075 cm (~0.029*D*) from the MPA centreline. The results indicate that the local geometric features of the pulmonary bifurcation can alter the stagnation point where fluid division takes place.

3.3.1.2. Velocity profiles and flow splits

In addition to the velocity contours, Fig. 3.6 presents non-dimensional velocity profiles at a distance of 3 cm (~1.15*D*) from the origin of the branches, for each of the models. As described, for most geometries (Figs. 3.6 (i-iv), (vi-viii)), flow velocities downstream of the bifurcation were skewed towards the inner walls of the daughter branches and away from the outer walls, where reverse (retrograde) flow was observed. However, the shape and extreme values of the velocity profiles exhibited differences in each of the LPA and RPA branches, as seen on Fig. 3.6b. With the exception of the axisymmetric models (Figs. 3.6 (i), (vi)), peak velocities in the RPA were in general closer to the inner wall, compared to peak velocities in the LPA. The

highest peak LPA velocity values were found for the symmetric models with local LPA stenosis (Figs. 3.6 (vii-viii)), which is consistent with the velocity increase due to the local decrease in the branch diameter. The highest peak RPA values were calculated for the models with hypoplastic LPA (Figs. 3.6 (v), (ix)).

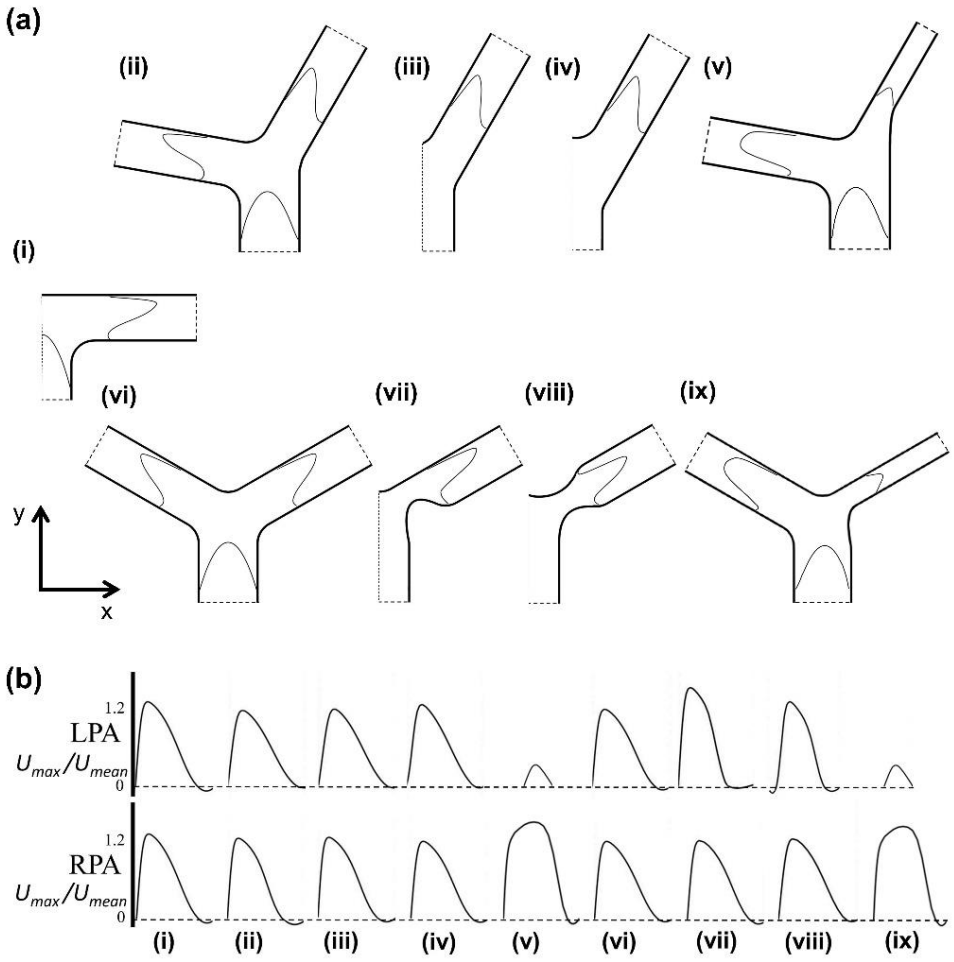

Figure 3.6: Velocity profiles at a distance of 3 cm (~1.15D) from each branch origin presented (a) on top of each geometry and (b) placed comparatively next to each other. Dashed lines indicate cropped branch ends and symmetry planes (a) or the position of zero non-dimensionalised velocity (b). (i) T-Junction; (ii)-(v) asymmetric Y-Junction, with the different branch origins or hypoplastic LPA; (vi)-(xi) symmetric Y-Junction, without or with local stenosis or hypoplastic LPA. Steady Newtonian flow, Re=650.

In the asymmetric model of Fig. 3.6 (ii), the velocity profile in the RPA exhibited the most extended reverse flow along the outer wall. A smaller extent in the reverse flow in the RPA was noticed for the models of Figs. 3.6 (i), (iii-iv), (vi-viii), with the shortest of all for models of Figs. 3.6 (v), (ix). The most extended reverse flow in the

LPA branch was observed in the model with asymmetric local stenosis (Fig. 3.6 (vii)). Similar LPA flow reversal was seen in all other models, with the exception of the hypoplastic LPA geometries (Figs. 3.6 (v-ix)) where there was no reversal of flow in LPA. In the model with symmetric stenosis (Fig. 3.6 (viii)), flow was also reversed near the inner wall of the LPA.

As seen, the geometries with hypoplastic LPA (Figs. 3.6 (v), (ix)) had the biggest deviation in the velocity profiles in both daughter branches, as compared to all other models. There was a considerable increase in the RPA velocity in these cases, with a concomitant decrease in the LPA velocity. These profiles indicate that the flow was diverted primarily towards the RPA. To examine this further, the integrals of the velocity profiles were calculated to evaluate the flow rate in the MPA, RPA, and LPA. With the exception of the two models with hypoplastic LPA (Figs. 3.6 (v), (ix)), all other models (Figs. 3.6 (i-iv), (vi-viii)) exhibited an equal flow rate in the right and left arterial branches (50:50% for Q_{LPA}:Q_{RPA}), as measured at a distance of 3cm (1.15*D*) from the branch origin. However, a flow split ratio of approximately 12:88% (Q_{LPA}:Q_{RPA}) was estimated for both hypoplastic models (Figs. 3.6 (v), (ix)), demonstrating that halving the diameter of one of the branches can significantly affect the distribution of flow in the pulmonary bifurcation.

3.3.1.3. Velocity streamlines

Fig. 3.7 presents velocity streamlines in the nine geometries of Fig. 3.1. Arrows along the streamlines indicate the direction of fluid flow from the main pulmonary artery to the daughter branches. It is evident that recirculation zones develop in all models, independent of the branching angle for RPA or LPA, that is, at 90º (Fig. 3.7 (i)), 100º

(Figs. 3.7 (ii-iv)), 120º (Figs. 3.7 (vi-ix)), and 150º (Figs. 3.7 (ii-iv)). In the asymmetric Y-Junction of Fig. 3.7 (ii), the 100º angle between the MPA and RPA (θ_1) had an extended recirculation area, while only a small region of recirculating fluid was observed for the 150º MPA-LPA angle (θ_2). For the same branching angles but with different origins (Figs. 3.7 (iii-iv)), the recirculation zones at the RPA ($\theta_1 = 100º$) were reduced, while at the entrance of the LPA ($\theta_2 = 150º$) they were extended considerably.

Elongated recirculation regions were also observed in the symmetric models with local stenosis (Figs. 3.7 (vii), (viii)). In Fig. 3.7 (vii), recirculation of flow occurred downstream of the asymmetric stenosis, along the outer wall of the bifurcation, while similar zones downstream of the symmetric stenosis in Fig. 3.7 (viii) were seen adjacent to both the outer and inner walls of the arterial branch. For the two hypoplastic models (Figs. 3.7 (v), (ix)), flow recirculation occurred at the entrance to the RPA and immediately before entering the left pulmonary artery. This zone was more extended in the asymmetric model (Fig. 3.7 (v)). For all models, there is a region of accelerating flow downstream of the stagnation point (S, Fig. 3.5), which becomes more pronounced within the stenosis for the models of Figs. 3.7 (vii), (viii).

Flow separation is a common phenomenon in bifurcations and occurs when the fluid velocity cannot expand with the geometry or when an adverse pressure gradient is present. Fluid particles in these cases are captured within the recirculation area and cannot re-enter the bulk flow due to their incapacity to overcome the flowing fluid pressure (Rubenstein et al., 2015). The results of Fig. 3.7 indicate that the upstream separation point, where recirculation zones start to develop, was at the same position for all non-stenotic models, that is, at the entrance of the bifurcation. However, the extent of these zones appears to be affected by the branch origin, resulting in different

locations of the downstream flow reattachment points. Increased regions of recirculation cannot be correlated with an increase in the branching angle, as previous studies have indicated (Chern et al., 2012, Zhang et al., 2016). The models with local stenosis (Figs. 3.7 (vii-viii)) and hypoplastic LPA (Figs. 3.7 (v), (ix)) have zones developed downstream of the stenosis or upstream of the entrance to the left pulmonary branch, respectively. Local stenosis appeared to cause extension of recirculation zones downstream of the stenosis (Figs. 3.7 (vii), (viii)), while the hypoplastic models cannot be correlated with increased regions of recirculation further downstream within the LPA (Figs. 3.7 (v), (ix)).

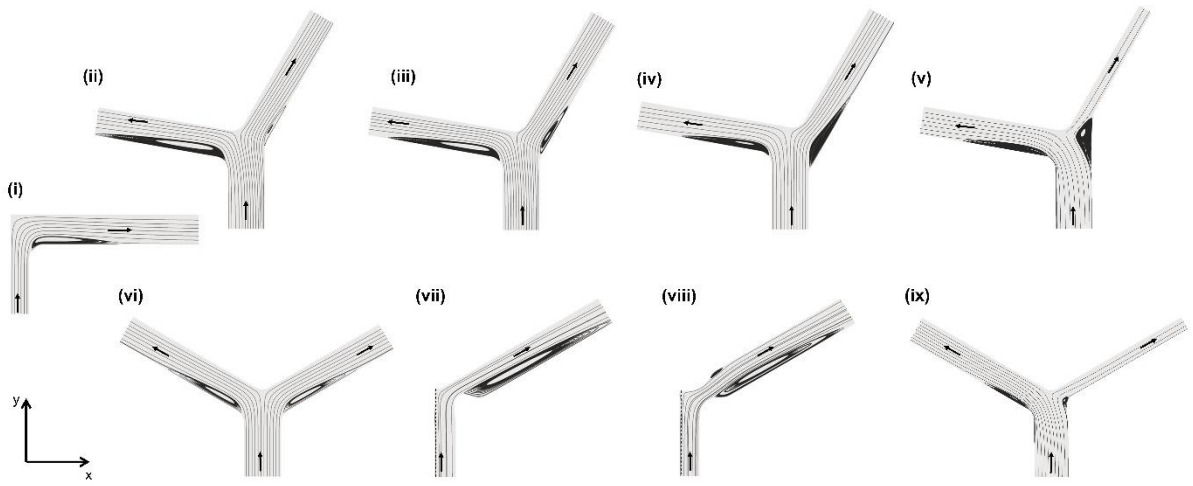

Figure 3.7: Velocity streamlines in the models of Fig. 3.1: (i) T-Junction; (ii)-(iv) asymmetric Y-Junction models with different branch origins and (v) with hypoplastic LPA; (vi) symmetric Y-Junction; (vii)-(viii) models with local stenosis; (ix) model with hypoplastic LPA. Steady Newtonian flow, Re=650.

3.3.1.4. Wall shear stress profiles

Wall shear stress distribution along the inner wall of the bifurcation is presented in Fig. 3.8, non-dimensionalised according to the WSS value at the MPA inlet, as described in Section 3.2.5. The zero position in the abscissae of these plots signifies

the stagnation point (S, S_R, or S_L, see Fig. 3.5), while normalisation of the distance (l) from point S along the inner wall is based on the MPA diameter, D.

Examining the effect of branching angle (Fig. 3.8a), it appears that while the symmetric Y-Junction (dotted line in Fig. 3.8a) and the T-Junction model (dash line in Fig. 3.8a) presented symmetric WSS profiles on both branches, the asymmetric Y-Junction (solid line in Fig. 3.8a) obtained significantly increased WSS values towards the LPA ($\theta_2 = 150^o$). The location of the maximum WSS values for each model was also different, with that for the T-Junction being the furthest away from the stagnation point.

Displacing the origins of one or both branches (of the same angle) caused a further increase of non-dimensionalised WSS values in the LPA of the asymmetric Y-Junctions and a simultaneous WSS reduction in the RPA (Fig. 3.8b). In addition, the location of the highest WSS values for each model moved further away from the stagnation point in both branch directions. The geometry of Fig. 3.5 (iv) resulted in a well-defined high WSS region at the short distance from the stagnation point towards the LPA, taking on very low values further downstream.

For the models with local stenosis (Fig. 3.8c), there was a clear increase at the WSS values along the inner wall of the LPA, without a strong influence to the WSS in the RPA. This was particularly evident for the symmetric stenotic model which exhibited a very different WSS distribution in the LPA.

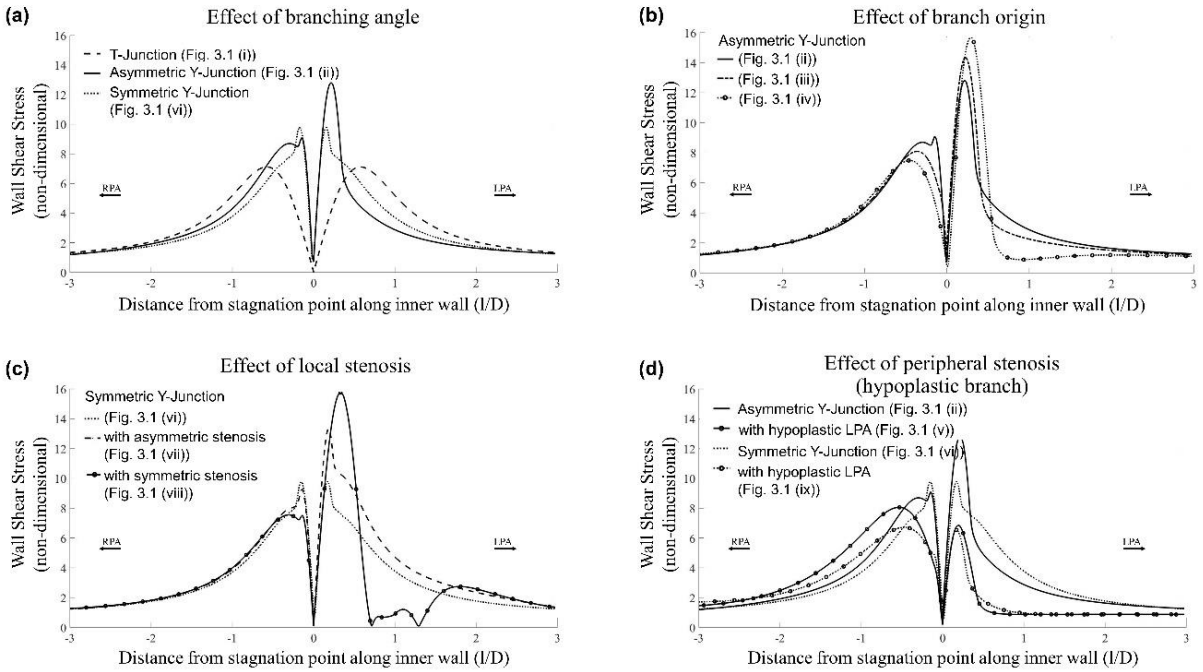

Figure 3.8: Non-dimensionalised wall shear stress (WSS) distribution along the inner wall of the models of Fig. 3.5, for steady Newtonian flow, Re=650: (a) models with different branching angles; (b) asymmetric models with different branch origins; (c) symmetric Y-Junction without and with local stenosis; (d) asymmetric and symmetric Y-Junctions without and with hypoplastic LPA. The zero position in the abscissae signifies the stagnation point (S, S_R, or S_L, see Fig. 3.5).

Finally, for the geometries with hypoplastic LPA (Fig. 3.8d), the WSS in the LPA dropped to approximately the same values irrespective of the branching angle of the LPA bifurcation (120º or 150º). WSS in the RPA also decreased but obtained different values for the asymmetric and symmetric models, and the peak WSS was shifted away from the stagnation point; these profiles resembled somewhat the WSS distribution at the RPA of the T-Junction (dash line in Fig. 3.8a).

3.3.2. Effect of outlet boundary conditions

3.3.2.1. Prescribed pressure outlet conditions

The effect of the pressure boundary condition at the branch outlets was tested in two ways (Fig. 3.9). Flow was diverted towards the LPA branch where higher velocities

were observed for the extended RPA model (Fig. 3.9a (i)); in this model, lower velocities were noticed in the RPA with strong recirculation zones. The opposite was observed in the models with a normalised branch pressure difference $\frac{|\Delta P|}{0.5\rho U^2}$ of 0.026 (for $P_{LPA} > P_{RPA}$, Fig. 3.9a (ii)) and 0.015 (also $P_{LPA} > P_{RPA}$, Fig. 3.9a (iii)), where flow diverted towards the right branch. The streamlines of the model in Fig. 3.9a (iii) present decreased recirculation zones when compared to Fig. 3.9a (ii) both at RPA and LPA.

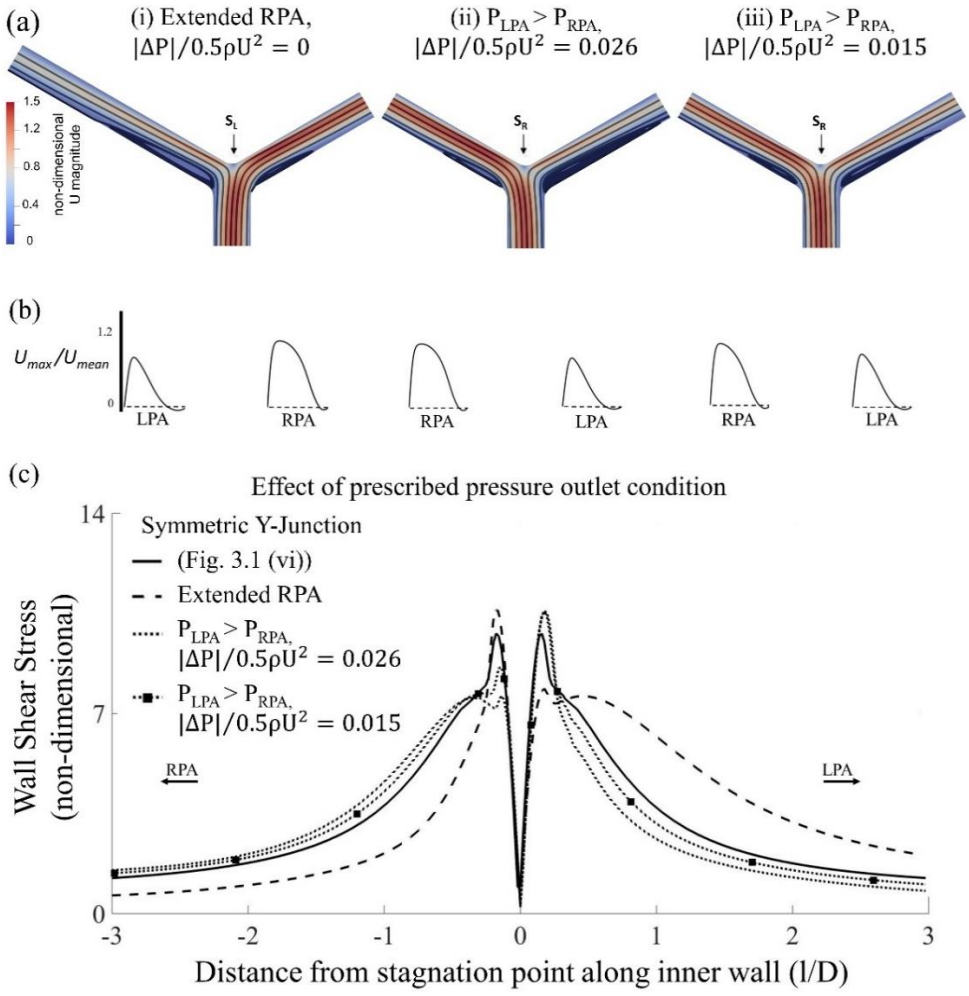

Figure 3.9: Effect of pressure boundary condition at branch outlet. (a) Non-dimensionalised velocity contours overlaid by streamlines. (b) velocity profiles along the RPA and LPA. (c) Non-dimensionalised WSS distribution along the inner wall for the geometry of Fig. 3.5 (vi) (solid line) and model with (i) an extended right pulmonary branch with $\frac{|\Delta P|}{0.5\rho U^2} = 0$, *(ii)* $\frac{|\Delta P|}{0.5\rho U^2} = 0.026$ *with* $P_{LPA} > P_{RPA}$ *and (iii)* $\frac{|\Delta P|}{0.5\rho U^2} = 0.015$ *with* $P_{LPA} > P_{RPA}$. *Steady Newtonian flow, Re=650.*

Velocity profiles at a distance of 3cm (1.15*D*) from the branch origin were also plotted for the RPA and LPA branches (Fig. 3.9b), confirming the above observations. A slight increase in the forward velocity in the LPA was seen in the case of Fig. 3.9a (iii), as compared to Fig. 3.9a (ii). The velocity profiles for these models indicate variations in the branch flow splits, with the flow diverted towards the LPA (Fig. 3.9a (i)) and towards the RPA (Figs. 3.9a (ii), (iii)). The flow rates in the LPA and RPA were calculated for all models and flow split ratios were found approximately 67:33% for Fig. 3.9a (i), 33:67% for Fig. 3.9a (ii) and 40:60% for Fig. 3.9a (iii) (Q_{LPA}:Q_{RPA}). As expected, the results indicate that the pressure boundary condition can alter the flow split in the pulmonary bifurcation from the 50:50% ratio in the daughter branches.

The stagnation point was further identified for these three models. For the geometries of Figs. 3.9a (i) and 3.9a (ii), the stagnation point was found 0.12 cm (0.046*D*) towards the LPA and the RPA, respectively, while for the model of Fig. 3.9a (iii), the stagnation point was located 0.0075 cm (0.0029*D*) towards the RPA.

Non-dimensionalised wall shear stress profiles are presented in Fig. 3.9c and are compared with the WSS obtained for the symmetric geometry of Fig. 3.5 (vi) with zero pressure at both branch outlets (dash line in Fig. 3.8a, repeated as solid line in Fig. 3.9c). A slight increase is observed in the WSS developed at the inner wall of the RPA, with a simultaneous WSS reduction at the LPA wall for the model of Fig. 3.9a (i). Accordingly, a decrease was observed in the WSS along the inner wall of the RPA of the models with the pressure difference at the branch outlets (Figs. 3.9a (ii), (iii)).

3.3.2.2. Prescribed flow splits

Contours of non-dimensional velocity magnitude are presented in Fig. 3.10a (i) (Q_{LPA}:Q_{RPA}= 11:89%) and Fig. 3.10a (ii) (Q_{LPA}:Q_{RPA}=20:80%) for Murray's Law and the "outflow splitting" method (Eqs. (3.3) and (3.4), Section 3.2.3), respectively. As expected, the results are comparable with those of Fig. 3.5 (ix), with the majority of the flow diverted to the RPA. The stagnation point, S, was found 0.22cm (~0.085*D*) and 0.17cm (~0.065*D*) towards the RPA, for the models of Figs. 3.10a (i) and 3.10a (ii), respectively. The non-dimensionalised WSS distributions along the inner wall of the bifurcation are shown in Fig. 3.10b. With Murray's Law (Fig. 3.10a (i)), the WSS is very similar to that with zero-pressure boundary condition (Fig 3.8d), with slightly lower peak WSS value in the LPA. WSS is increased in both branches for the model with the "outflow splitting" method (Fig. 3.10a (ii)), which is more prominent in the LPA (Fig. 3.10b).

3.3.2.3. Coupled Lumped Parameter Models

Fig. 3.10a also presents non-dimensionalised velocity contours for a peripheral resistance boundary condition (Fig. 3.10a (iii), Q_{LPA}:Q_{RPA}=22:78%), and a three-element Windkessel model (Fig. 3.10a (iv), Q_{LPA}:Q_{RPA}=14:86%), for steady-state inlet flow. Similar to cases Figs. 3.10a (i), (ii) and Fig. 3.5 (ix), most of the flow is directed towards the RPA. For both cases, the stagnation point is shifted towards the RPA by 0.12 cm (~0.046*D*) (Fig. 3.10a (iii)) and 0.17 cm (~0.065*D*) (Fig. 3.10a (iv)). The WSS for the simulation with the peripheral resistance (Fig. 3.10a (iii)) exhibits an increase in both daughter branches, similar to Fig. 3.10a (ii). With the Windkessel model

assumption (Fig. 3.10a (iv)), the WSS resembles that of Fig. 3.8d, but with a small increase in the WSS in the LPA (Fig. 3.10b).

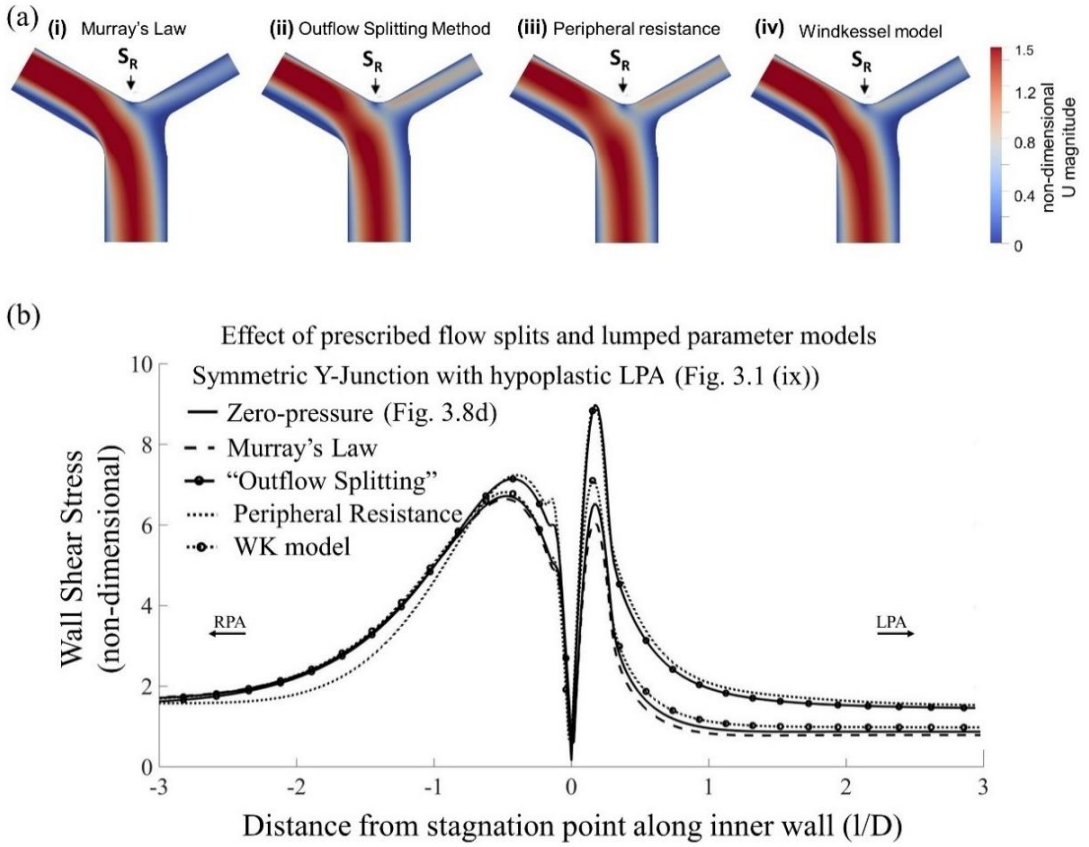

Figure 3.10: Effect of outlet boundary conditions. (a) Non-dimensionalised velocity contours. (b) Non-dimensionalised WSS distribution along the inner wall for the geometry of Fig. 3.5 (ix) (solid line) with (i)-(ii) flow split dictated by (i) Murray's Law (Q_{LPA}:Q_{RPA} is 11:89%) and (ii) "outflow splitting" method (Q_{LPA}:Q_{RPA} is 20:80%), and (iii)-(iv) coupled lumped parameter models with , (iii) a peripheral resistance (Q_{LPA}:Q_{RPA} is 22:78%) and (iv) a three-element Windkessel (WK) model (Q_{LPA}:Q_{RPA} is 14:86%). Steady Newtonian flow, Re=650.

Instantaneous non-dimensionalised velocity contours and wall shear stress distribution are presented in Fig 3.11a for the model of Fig. 3.5 (ix) with time-dependent sinusoidal inlet profile. At maximum velocity, the WSS and velocity magnitude take the highest values during the cycle (Fig. 3.11a (i)). During deceleration, both the velocity and WSS decrease until they reach the lowest values, at maximum deceleration (Figs. 3.11a (ii), a (iii)). The peak WSS is higher along the inner wall of the LPA, except at the middle of acceleration (Figs. 3.11a (iv)). The flow splits for each of the four time

points were Q_{LPA}:Q_{RPA}=28:72% (Figs. 3.11a (i)), 22:78% (Fig. 3.11a (ii)), 51:49% (Fig. 3.11a (iii)), and 22:78% (Fig. 3.11a (iv)). An average flow split of Q_{LPA}:Q_{RPA}=22:78% was calculated over one cycle. The stagnation point was also identified and was found shifted towards the RPA by 0.075 cm (~0.028*D*), 0.22 cm (~0.085*D*), 0.54 cm (~0.21*D*), and 0.12 cm (~0.046*D*) for the four time-points (Figs. 3.11a (i-iv)), respectively. The time- averaged WSS for the unsteady flow is compared with the steady flow in Fig. 3.11b. A similar pattern in the wall shear stress distribution is observed, but with slightly higher values for the TAWSS.

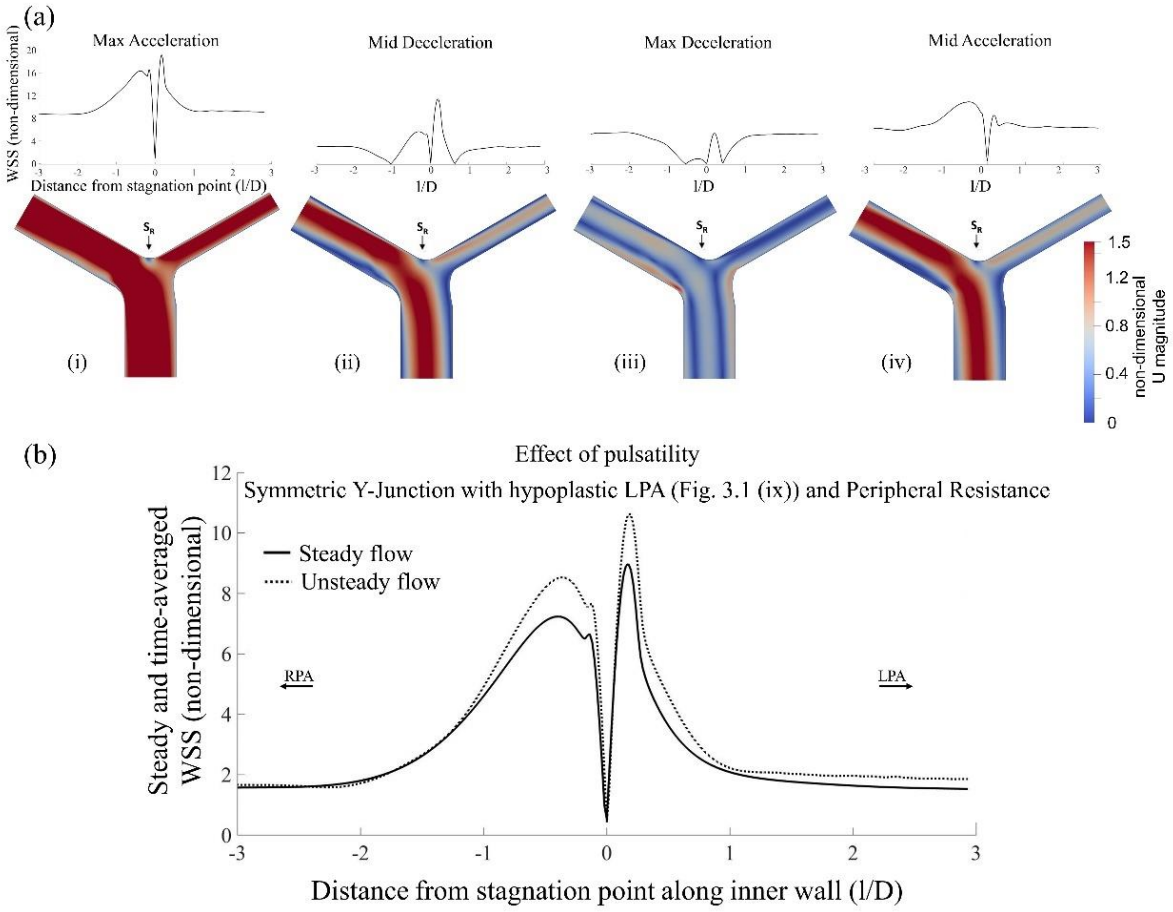

Figure 3.11: Effect of pulsatility in the symmetric Y-Junction with hypoplastic LPA and the peripheral resistance boundary condition. (a) Instantaneous non-dimensionalised velocity contours and WSS distribution along the inner wall, at maximum acceleration, middle of deceleration, maximum deceleration, and middle of acceleration of a sinusoidal waveform (Eq. (3.2)). (b) Steady and time-averaged non-dimensional wall shear stress distribution for steady and unsteady flow. Newtonian flow, mean Re=650.

3.4. Discussion

Adult patients with repaired tetralogy of Fallot constitute an increasing population that require regular monitoring and specialised care due to unpredictable and long-term complications. Pulmonary regurgitation and left pulmonary kinking are the most frequent causes for re-intervention, commonly treated through pulmonary valve replacement (Geva, 2011). Analysis of the blood flow development in the pulmonary arteries of these patients is important and may improve clinical evaluation and decision-making for PVR (Guibert et al., 2014, Chern et al., 2008, Tang et al., 2012). To that end, the focus of the present study was to elucidate computationally the effects of different geometric parameters and outlet BCs on the haemodynamics in simplified models of the pulmonary bifurcation.

3.4.1 Simplifying assumptions

Arguably, the most important simplification of this study was the assumption of 2D geometries for the pulmonary bifurcation. This choice was made to facilitate an extensive investigation of different geometric parameters and boundary conditions and was supported by a comparison with a three-dimensional geometry demonstrating qualitative similarities in the shape of the WSS distribution along the inner wall of the bifurcation, for both 2D and 3D models, despite the quantitative differences (Fig. 4.3a). The use of the simplified models is explained since the aim of this work was to capture the main characteristics of the flow and WSS distribution in the pulmonary bifurcations under a range of different conditions. This would be difficult to perform with three-dimensional patient-specific geometries since the parametric variation would be more complex to define.

Another important simplification was the assumption of steady flow. Some aspects of unsteadiness can be considered negligible for large vessels (Kazakidi et al., 2009, Kazakidi et al., 2011), particularly since physiological fluctuations in mean velocity during the cardiac cycle are adequately slow to assume quasi-steady flow. This was confirmed here by the similarity in WSS values between steady and unsteady sinusoidal flows, for both 2D and 3D geometries (Fig. 3.11b and Fig. 4.3a). Finally, the assumption of rigid walls is another assumption that may influence the computational results. Nevertheless, wall compliance has been found to have a minimal effect on the overall flow (Capuano et al., 2019). Indeed, the radial aortic wall deformation is also relatively small during the cardiac cycle compared with the axial unsteady flow into the pulmonary branches (Thenappan et al., 2016), and could be neglected. It is, therefore, reasonable to expect that the work presented here provides a good indication of the effects of the same or similar conditions in the respective 3D models and captures qualitatively the characteristics of 3D unsteady flow.

3.4.2. Comparison with other works

Previous studies have investigated the effect of angle in the pulmonary bifurcation and found that recirculation zones develop for branch angles close to or equal to 100º (Zhang et al., 2016), but not for an angle of 150º (Chern et al., 2008). This is in agreement with the results of this study for branch angles 90º, 100º and 150º (Figs. 3.7 (i), (vi), (ii), respectively); however, Figs. 3.7 (iii), (iv) demonstrate that new recirculation zones develop simply by the displacement of the branch origins (which can relate to altered pressure gradient and centripetal force), for the same branch angle of 150º. The results of this work, therefore, clarify that increased recirculation cannot

be correlated only with increased branching angle, and that further to the branch angle, the origin of the pulmonary branches is also important in analysing the local flow development. For the local stenotic models (Figs. 3.7 (vii-viii)), the flow separation, and the WSS profiles (Fig. 3.8c) obtained is in comparison to the study of Kanokjaruvijit et al. (Kanokjaruvijit et al., 2017), where different types of stenotic bifurcations were investigated, and with Katritsis et al. (Katritsis et al., 2010). Major flow separation was found to occur when the diameter inside the stenosis decreased to 50%, and wall shear stress was increased inside the stenotic branches, followed by a rapid decrease downstream (Kanokjaruvijit et al., 2017). The contours of the non-dimensionalised velocity magnitude, as presented in Fig. 3.5, are also in agreement with those reported in similar studies (Katritsis et al., 2010). In addition, this work is comparable to the work of Szymanski et al. (Szymanski et al., 2008), who observed a similar WSS pattern on the inner wall of a T-Junction, and analysed the importance of the stagnation point. Immediately downstream of the stagnation point, where the velocity is zero and the wall shear stress is very low, a region of high WSS was present, followed by low WSS values (Szymanski et al., 2008), similar to the results presented here. This study, further, demonstrates that the WSS distribution on the inner wall is a result of the location of flow division in bifurcating flows, as shown in Figs. 3.8, 3.9c, 3.10b, however no previous studies were found investigating this effect.

3.4.3. Physiological, pathological, and clinical relevance

It has been proposed that in the presence of pulmonary valve regurgitation, branch stenosis limits the flow to the corresponding lung and possibly aggravates the severity of PR (Chen and Kilner, 2013). In addition, differential reverse flow between the

pulmonary branches (branch regurgitation) may be positively correlated with pulmonary vascular resistance (Harris et al., 2011). Patients without pulmonary branch stenosis appear to have increased LPA regurgitation, while patients with stenosis or a hypoplastic branch are associated with increased retrograde flow in the larger artery and consequently increased pulmonary vascular resistance. Therefore, patients with stenosis or a hypoplastic branch and significantly differential branch regurgitation, are expected to have elevated pulmonary vascular resistance in the enlarged non-stenotic branch (Harris et al., 2011). The percentage of diameter reduction also dictates the flow split between the two branch arteries. With the majority of flow diverted to the enlarged RPA, the differential backflow is expected to increase accordingly, along with the pulmonary vascular resistance and pressure in the non-stenotic branch, increasing the risk of pulmonary vascular diseases and hypertension during childhood. In general, reduced flow in the LPA is a clinical observation in many TOF patients, due to anatomical variations, which complicates flow in their pulmonary arteries (Zhang et al., 2016). Flow imbalance between the LPA and the RPA may also have several clinical consequences, leading to ventilation or perfusion mismatch, or adversely influence pulmonary microvascular growth if preserved for extended periods during childhood. To reflect on these views, an analysis on the pressure ratios and flow splits in the models presented in this study is extended in the following paragraphs.

3.4.3.1. Pressure ratios

The importance of appropriate pressure conditions in arterial models has been broadly discussed in the literature (Pijls et al., 1993, Young et al., 2014). In this study, the

effect of different conditions at the branch outlets was investigated (Section 3.3.2.2), including the use of more realistic pressure values (Figs. 3.9, 3.10). These values fall within the range of pressures computationally calculated in the study of Arbia et al. (Arbia et al., 2014), expressed relative to a reference pressure at the outlets of the models.

A more clinically-relevant way of understanding the pressure changes along the pulmonary bifurcation is through comparison of the pressure ratios between the two branches (P_{LPA}:P_{RPA}) and between the daughter and parent vessels (P_{LPA}:P_{MPA} and P_{RPA}:P_{MPA}). For that, the static pressure within each vessel was measured at four locations along the centreline, at distances 4 to 7 cm (~1.5*D* to ~2.7*D*) from the branch origin, and at additional symmetrical locations on either side of the centreline, at 0.65 cm (0.25*D*) from the walls of the MPA and 0.5 cm (~0.2*D*) from the walls of both the RPA and LPA (total of 12 points, as shown in Fig. 3.12a, overlaying pressure contours in the symmetric Y-Junction, non-dimensionalised by $0.5\rho U^2$). The mean arterial pressure ratios, along with the standard deviation, were then calculated based on the 12 measurements for each vessel. Table 3.2 provides the measured pressure ratios and standard deviation, while Fig. 3.12b presents the P_{LPA}:P_{RPA} and P_{LPA}:P_{MPA} ratios, where 1 indicates equal pressure values.

For the symmetric T- and Y-Junctions, the left and right pulmonary branches have the same mean pressure, which is slightly higher than that in the MPA (cases (i) and (vi) in Table 3.2 and Fig. 3.12b). Introducing asymmetry in the bifurcation (asymmetric Y-Junction models (ii-v) in Table 3.2 and Fig. 3.12b), results in an increase in the mean pressure developed in the LPA with a concomitant decrease in the RPA, as compared to the pressure in the MPA; an exception to this is for the asymmetric model with both

branch origins displaced (Table 3.2 (iv)) which exhibits almost the same mean pressure in both RPA and MPA. The asymmetric Y-Junction with hypoplastic LPA (Table 3.2 (v), Fig. 3.12b) has the highest mean pressure difference between the left and right pulmonary branches among all models, with the pressure in the LPA being clearly higher than that in the RPA. The symmetric models with local stenosis (Table 3.2 (vii-viii), Fig. 3.12b) exhibit a distinctive decrease in the mean LPA pressure, while the mean RPA pressure is very similar to that of the MPA. For the symmetric model with hypoplastic LPA (Table 3.2 (ix), Fig. 3.12b), the mean LPA pressure is elevated, like in the asymmetric model (Table 3.2 (v)), and is higher than the RPA pressure, which in turn is lower than that in the MPA. The opposite is found for the model with an extended RPA branch (Table 3.2 (x), Fig. 3.12b), where the mean LPA pressure is lower than the mean RPA and MPA pressures. For the models with the pressure difference at the outlets (Table 3.2 (xi-xii), Fig. 3.12b), the mean LPA pressures are higher than those in the RPA. Finally, for the four different outflow conditions tested in the symmetric Y-Junction with the hypoplastic LPA (Table 3.2 (xiii-xvi), Fig. 3.12b), the mean LPA pressure is elevated while the mean pressure in the RPA is reduced, similar to case (ix), Table 3.2. All pressure ratios for the model with the flow splits as predicted by the Murray's Law (Table 3.2 (xiii)) are almost identical to those of case (ix) and slightly different to case (xvi) with the coupled Windkessel model. Among the last four cases (xiii-xvi), the model with the peripheral resistance at the branch outlets (Table 3.2 (xv)) has the largest deviation in the P_{LPA}:P_{RPA} ratio from case (ix) in Table 3.2.

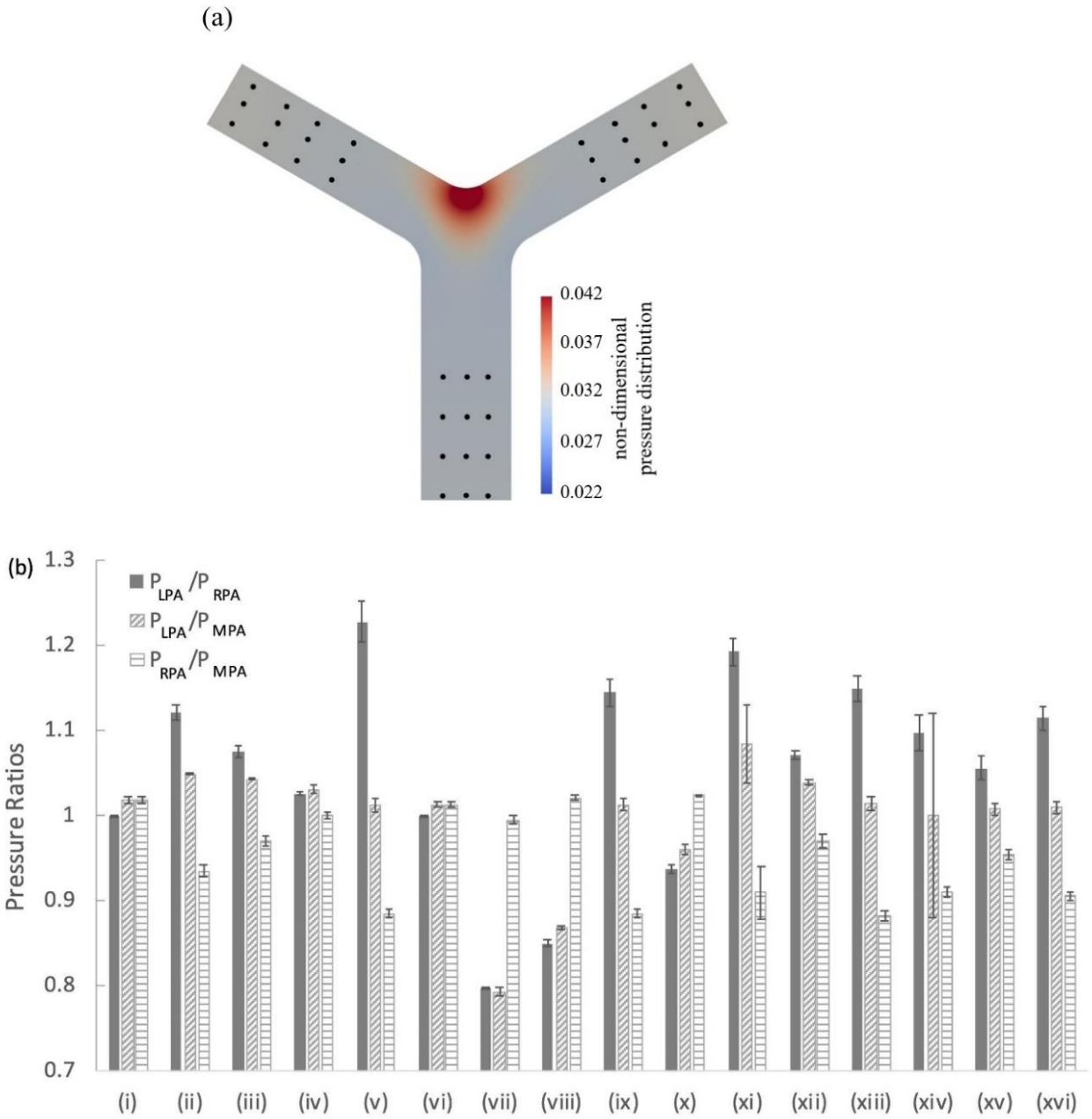

Figure 3.12: (a) Points where the pressure values were measured, overlaying contours of pressure in the symmetric Y-Junction. Pressure is depicted relative to the reference pressure at the outlets, and normalised by $0.5\rho U^2$. *(b) Pressure ratios for the models examined: (i) T-Junction (Fig. 3.5 (i)); (ii)-(v) asymmetric Y-Junction models, with (ii) common origin (Fig. 3.5 (ii)), (iii) one (Fig. 3.5 (iii)) or (iv) both branch origins displaced (Fig. 3.5 (iv)), or (v) hypoplastic LPA (Fig. 3.5 (v)); (vi) symmetric Y-Junction (Fig. 3.5 (vi)), with (vii) local asymmetric stenosis (Fig. 3.5 (vii)), (viii) local symmetric stenosis (Fig. 3.5 (viii)), or (ix) hypoplastic LPA (Fig. 3.5 (ix)); (x) symmetric Y model with extended RPA (Fig. 3.9a (i)); (xi)-(xii) symmetric Y model with* $P_{LPA} > P_{RPA}$ *and with* $\frac{|\Delta P|}{0.5\rho U^2} = 0.026$ *(Fig. 3.9a (ii)), and with* $\frac{|\Delta P|}{0.5\rho U^2} = 0.015$ *(Fig. 3.9a (iii)), respectively; (xiii)-(xvi) symmetric Y model with hypoplastic LPA and (xiii)-(xiv) prescribed flow splits (Fig. 3.10a (i),(ii)), and (xv)-(xvi) lumped parameter models coupled at the branch outlets (Fig. 3.10a (iii),(iv)). Steady Newtonian flow, Re=650.*

Table 3.2: Pressure ratios with standard deviation from the mean value, as calculated from measurements of relative pressure at different points in the pulmonary branches (locations of measurement are shown at inset of Fig. 3.12a), under steady flow.

		P_{LPA}:P_{RPA}	P_{LPA}:P_{MPA}	P_{RPA}:P_{MPA}
(i)	T-Junction (Fig. 3.5 (i))	1.000 ± 5.5e-6	1.018 ± 3.6e-3	1.018 ± 3.6e-3
(ii)	Asymmetric Y-Junction with branch origin at O (Fig. 3.5 (ii))	1.122 ± 9.2e-3	1.049 ± 6.8e-4	0.935 ± 7.1e-3
(iii)	Asymmetric Y-Junction with displaced LPA origin (Fig. 3.5 (iii))	1.075 ± 7.0e-3	1.043 ± 7.1e-4	0.970 ± 6.5e-3
(iv)	Asymmetric Y-Junction with both origins displaced (Fig. 3.5 (iv))	1.026 ± 2.6e-3	1.031 ± 4.6e-3	1.000 ± 3.9e-3
(v)	Asymmetric Y-Junction with hypoplastic LPA (Fig. 3.5 (v))	1.228 ± 2.4e-2	1.013 ± 8.2e-3	0.885 ± 5.5e-3
(vi)	Symmetric Y-Junction (Fig. 3.5 (vi))	1.000 ± 1.6e-5	1.013 ± 3.7e-3	1.013 ± 3.6e-3
(vii)	Symmetric Y-Junction with local asymmetric stenosis in LPA (Fig. 3.5 (vii))	0.797 ± 1.5e-3	0.793 ± 4.8e-3	0.995 ± 4.7e-3
(viii)	Symmetric Y-Junction with local symmetric stenosis in LPA (Fig. 3.5 (viii))	0.850 ± 3.3e-3	0.868 ± 2.1e-3	1.021 ± 2.6e-3
(ix)	Symmetric Y-Junction hypoplastic LPA (Fig. 3.5 (ix))	1.145 ± 1.6e-2	1.013 ± 7.5e-3	0.885 ± 5.5e-3
(x)	Symmetric Y-Junction with extended RPA (Fig. 3.9a (i))	0.937± 4.3e-3	0.960± 5.3e-3	1.024 ± 9.5e-4
(xi)	Symmetric Y-Junction with $\frac{\lvert\Delta P\rvert}{0.5\rho U^2} = 0.026$ (Fig. 3.9a (ii))	1.193 ± 1.6e-2	1.085 ± 4.6e-2	0.910 ± 3.1e-2
(xii)	Symmetric Y-Junction with $\frac{\lvert\Delta P\rvert}{0.5\rho U^2} = 0.015$ (Fig. 3.9a (iii))	1.071 ± 5.6e-3	1.039 ± 2.6e-3	0.970 ± 7.5e-3
(xiii)	Murray's Law (Fig. 3.10a (i))	1.150 ± 1.5e-2	1.014 ± 7.3e-3	0.882 ± 5.6e-3
(xiv)	Outflow Splitting Method (Fig. 3.10a (ii))	1.097 ± 2.1e-2	1.000 ± 1.2e-1	0.910 ± 6.3e-3
(xv)	Peripheral Resistance (Fig. 3.10a (iii))	1.056 ± 1.4e-2	1.008 ±7.1e-3	0.954 ± 5.7e-3
(xvi)	Windkessel model (Fig. 3.10a (iv))	1.115 ±1.4e-2	1.010 ± 7.1e-3	0.906 ± 4.9e-3

Following the analysis in the pressure ratios and the identification of the stagnation point (Figs. 3.5, 3.9a, 3.10a), it can be observed that a P_{LPA}:P_{RPA} ratio in the range of 1±0.026 exists in the models where the stagnation point was found along the MPA centerline; that is, the T- and symmetric Y- Junctions, and the asymmetric Y-Junction with both branch origins displaced. Therefore, these models have approximately equal

mean pressures in the pulmonary branches. For the remaining models, where the stagnation point was shifted, the P_{LPA}:P_{RPA} ratio deviated further from the value of 1, indicating the existence of differential pressures between the two branches.

In short, this study demonstrates a relation between the stagnation point and pressure ratios in the pulmonary bifurcation. These ratios also clarify that the pressure in the left pulmonary artery is generally higher than the pressure in the right and main pulmonary arteries, unless there is a local obstruction in the LPA branch and with the exception of the symmetric T- and Y- Junctions. These findings correlate well with clinical observations in TOF patients (Muster et al., 1982) indicating that measurement of the mean pressure ratios could be a useful haemodynamic index in the clinical practice for the assessment of LPA stenosis and PVR.

3.4.3.2. Flow Splits

Further to identifying pressure differences between the left and right pulmonary branches, it is also clinically relevant to estimate the branch flow splits. The flow split difference between the arterial branches becomes particularly important when taking into account the pulmonary vascular resistance. Chronic thromboembolic pulmonary hypertension (CTEPH), a type of pulmonary hypertension, develops in cases of stenosed pulmonary arterial vessels. Rarefaction, the process where the density of small capillaries and arterioles are reduced, results in elevated pulmonary vascular resistance, and flow in this case is diverted towards the non-stenosed branch (Olufsen et al., 2012, Spazzapan et al., 2018). Furthermore, long-term pulmonary stenosis in patients with TOF is thought to lead to differential lung growth (Ilbawi et al., 1987). Many studies have focused their investigations towards the effect of pulmonary

stenosis and hypertension on the distribution of flow between the left and right pulmonary arteries. Spazzapan et al. (Spazzapan et al., 2018) investigated the flow split in stenosed arteries of patients with CTEPH and found that the percentage of flow directed towards the stenosed branch was between 22% to 46%, depending on the degree of stenosis. An increase of 10%-60% in the flow directed towards the previously stenosed branch is reported upon removal of stenosis (Spazzapan et al., 2018). Pekkan et al. (Pekkan et al., 2005) investigated the effect of left pulmonary stenosis in patients with total cavopulmonary connection, showing that decreased stenosis resulted in a more balanced flow split in the pulmonary arteries which improved lung perfusion. Pressure values in their models, with reference to the LPA pressure, were also found to increase in hypoplastic branches, more than the local stenosis. They concluded that a uniform calibre (also called diffuse stenosis) results in reduced left lung perfusion. In another study of Schiavazzi et al. (Schiavazzi et al., 2015), the effect of pulmonary stenosis was also considered in single-ventricle patients. Their results indicated that the flow split between the LPA and RPA becomes clinically important when local stenosis is greater than 65%, where the percentage of flow to the LPA is less than 30% and the pressure drop in the LPA is higher than 3.0 mmHg.

Nevertheless, it is still ambiguous whether surgical repair of the pulmonary stenosis will benefit the patient. In the study of Cheng et al. (Cheng et al., 2005), computed flow splits in the RPA and LPA branches of healthy children were compared with those from the study of Pederson et al. (Pederson et al., 2002) from children with cavopulmonary connection, and the ratios were similar. In addition, Spilker et al. (Spilker et al., 2007) found no apparent benefit to a patient with surgically repaired

stenosis. Furthermore, Kheyfets et al. (Kheyfets et al., 2015), investigated the flow in the pulmonary arterial network of a healthy patient using various outflow BCs (zero-traction, a constant peripheral resistance, and an arterial tree of several generations) and found minimal impact on the proximal arteries but considerable effect on the flow distribution in distal tree vessels.

The above studies demonstrate that peripheral pulmonary vascular resistance and downstream pressure may influence the flow rates within the pulmonary arteries. Clinical measurement of the flow splits between the LPA and RPA branches may therefore indicate altered peripheral and proximal conditions, and serve as another haemodynamic marker for PVR evaluation.

In the results presented here (Figs. 3.9, 3.10), peripheral resistance and downstream pressure altered the flow splits in the daughter branches. Table 3.3 summarises different flow split percentages for nine of the cases presented, with flow splits other than 50:50%, as calculated based on velocity profiles at a distance of 3cm (1.15*D*) from the branch origin for each model. The symmetric and asymmetric hypoplastic models significantly reduce the flow rate in the left branch; a flow split of approximately 12:88% (Q_{LPA}:Q_{RPA}) was observed, which is considered an extreme case (Schiavazzi et al., 2015). Nevertheless, similar flow ratios were predicted with Murray's law (11:89% Q_{LPA}:Q_{RPA}), and with a three-element Windkessel model (14:86% Q_{LPA}:Q_{RPA}). Somewhat different flow splits were observed with the "outflow splitting" method (Chnafa et al., 2018) (20:80% Q_{LPA}:Q_{RPA}), and the coupling of a peripheral resistance (22:78% Q_{LPA}:Q_{RPA}), accounting to a maximum of 10% difference compared to a zero pressure boundary (Figs. 3.10a, 3.11a). In the study of Vignon-Clementel et al. (Vignon-Clementel et al., 2006), a 20% difference in the flow

splits (50:50% vs. 30:70%) was found when using, respectively, an impedance boundary condition and a constant pressure (90 mmHg), in a 3D symmetric stenotic model with a 75% reduction in the area within the stenosis and pulsatile inflow.

Table 3.3: Flow Split percentages at the left and the right pulmonary branches, as calculated using velocity profiles data, extracted at a distance of 3cm (1.15D) from the branch origin of each model.

Type of Y-Junction		Branch diameter (D_{LPA} : D_{RPA})	Branch length (L_{LPA}: L_{RPA})	$\frac{\lvert\Delta P\rvert}{0.5\rho U^2}$	Flow Split (%) (~Q_{LPA} : ~Q_{RPA})
Asymmetric	with hypoplastic LPA	1:2	1:1	0	12:88
Symmetric	with hypoplastic LPA	1:2	1:1	0	12:88
Symmetric	With extended RPA	1:1	1:2	0	67:33
Symmetric	with $\frac{\lvert\Delta P\rvert}{0.5\rho U^2} = 0.026$	1:1	1:1	0.026	33:67
Symmetric	with $\frac{\lvert\Delta P\rvert}{0.5\rho U^2} = 0.015$	1:1	1:1	0.015	40:60
Symmetric	with hypoplastic LPA - Murray's Law	1:2	1:1	0	11:89
Symmetric	with hypoplastic LPA - "outflow splitting method"	1:2	1:1	0	20:80
Symmetric	with hypoplastic LPA - peripheral resistance	1:2	1:1	0	22:78
Symmetric	with hypoplastic LPA - Windkessel model	1:2	1:1	0	14:86

This deviation might be explained due to the dissimilarity between the two geometries. More physiologically realistic flow splits of 33:67% and 40:60% (Q_{LPA}:Q_{RPA}), were achieved by modifying the length or the outlet pressure of the branch (Table 3.3), representing different peripheral pressure conditions. Similar values, in the range of 40:60% to 51:49% (Q_{LPA}:Q_{RPA}) have been observed in healthy subjects (Tang et al., 2011). Patients with repaired tetralogy of Fallot may exhibit flow ratios within the

normal range of 39:61% to 57:43% (Q_{LPA}:Q_{RPA}) (Kang et al., 2003). Abnormally low flow rates have been also reported in the literature for congenital heart patients, with flow percentages less than 39% to the left, or less than 43% to the right lung (Kang et al., 2003, Bachler et al., 2013).

Overall, a correlation appears to exist between the WSS distribution, the pressure ratios and the flow splits in the bifurcating models analysed in this study. More specifically, in the presence of different flow splits between the daughter branches (Table 3.3), the peak WSS value (Fig. 3.9c, 3.10b) and the pressure (Table 3.2) decreased in the branch with the higher flow rate; for example, cases Fig. 3.9a (i) and 3.9a (ii). The only exception in this trend is for cases with a flow split greater than 12:88% (Q_{LPA}:Q_{RPA}) where the peak WSS value was slightly higher in the RPA (Fig. 19d and Fig 3.10a (i)).

3.5. Concluding remarks

Congenital heart defects represent a great challenge in the medical sector and patients with tetralogy of Fallot are commonly diagnosed with pulmonary valve regurgitation and pulmonary local stenosis, hypoplastic LPA, or with LPA kinking. These complications are associated with RV dysfunction, and pulmonary valve replacement is deemed necessary.

Despite some simplifications, overall, this study highlights some previously undocumented aspects of the flow in bifurcating geometries, such as the pulmonary bifurcation: The geometric location of the flow divider, which depends on the geometry and the branch origin, influences the WSS distribution along the inner wall of the bifurcation. A stagnation point that is shifted from the MPA centreline

encourages differential pressures (P_{LPA}:P_{RPA} ≠ 1) in geometries with the same downstream pressure conditions, and, vice versa, altered peripheral conditions affect the area of flow impingement. The results also clarify that increased recirculation is not only an effect of increased branching angle, as suggested in previous studies (Zhang et al., 2016), but also of the origin of the pulmonary branches. More importantly, this work explains that the pressure in the left pulmonary artery is generally more elevated compared to the pressure in the right and main pulmonary arteries, unless there is a local obstruction in the LPA branch and with the exception of the symmetric T- and Y- Junctions. In addition, it demonstrates that downstream pressure conditions and peripheral resistance alter the flow in the pulmonary arteries and explain the occurrence of different flow splits between the branches. This, in turn, appears to reduce the peak WSS and pressure in the high flow-rate branch, for flows up to 12:88%, which may help assess pulmonary branch regurgitations. Finally, this study clarified some aspects of clinical observations in TOF patients through measurements of the mean pressure ratios in the pulmonary bifurcation, a haemodynamic index which could potentially contribute to the assessment of LPA stenosis, RV dysfunction, and PVR.

Chapter 4

Investigation of modelling parameters in idealised models of the pulmonary bifurcation

In this chapter different inlet and outlet boundary conditions, and modelling assumptions, including blood rheology, peripheral resistance and wall motion are investigated in 2D and 3D models, with the use of two separate solvers, based on FVM and FEM. Section 4.1. provides a brief introduction, then in Section 4.2 the methodology for each parameter investigated is presented. Section 4.3 analyses the results, divided based on the solver utilised. Section 4.4 summarises the key findings and makes comparisons with previous studies, and a brief conclusion is provided in Section 4.5.

4.1. Introduction

Computational fluid dynamics modelling has become increasingly popular in the study of the cardiovascular system and associated cardiovascular diseases, in clinical decision-making and in surgical planning (Taylor and Figueroa, 2009, Capelli et al., 2018). It can be used to compute flow parameters that cannot be easily extracted from commonly used experimental techniques but are yet important in order to predict cardiovascular diseases. Wall shear stress, time-averaged wall shear stress and oscillatory shear index are flow features used to anticipate the behaviour of the

pulmonary arteries under normal, exercise and disease conditions (Tang et al., 2011, Tang et al., 2012, Zhang et al., 2016).

Boundary conditions are a key factor in CFD studies, with the outcome of the simulations potentially varying up to 30%, based on the methodology followed (Conijn and Krings, 2021). It is therefore important to understand the effect of various inlet and outlet BCs. When clinical data are available, patient-specific time-dependent flow waveforms, flow splits or pressure waveforms are necessary for patient-specific simulations. Nevertheless, it can be difficult to access such physiological measurements and alternative boundary conditions can be specified.

Regarding the inlet boundary conditions, a plug or a parabolic velocity profile can be assigned, and the flow can be assumed either steady or pulsatile. A fully developed velocity profile is considered to reduce the variability between computational and physiological flows (Kheyfets et al., 2013). For the main pulmonary artery, it is suggested that a plug profile is more appropriate (Morgan et al., 1998), but it has been also found that maximum flow exist at the centre of the vessel and flow is decreased near the walls (Miyasaka and Takata, 1993).

With respect to the outflow boundary conditions, there are many different options that could be utilised. Prescribing a constant value of pressure, leads to the computational domain governing the flow split and non-physiological results can be expected (Vignon-Clementel et al., 2006). However, a good agreement has been found between experimental velocity profiles and computational results with the zero traction BC assigned in idealised geometries (Botnar et al., 2000). Another simple outlet BC commonly used in the cardiovascular research is the flow split ratio, which can be

derived using Murray's Law (Janiga et al., 2015, McElroy and Keshmiri 2018), the modified "splitting method" (Chnafa et al., 2018), or Murray's Law in combination with *in vivo* data (Vincent et al., 2011, Peiffer et al., 2013, McElroy and Keshmiri 2018). Alternatively, a resistance boundary condition (Greinberg and Karniadakis, 2008), an impedance boundary condition (Vignon-Clementel et al., 2006, Spilker et al., 2007), or a more complex Windkessel model (Westerhof et al., 2009, Kung and Taylor, 2011) may be coupled in the branch outlets.

There is a great variability in the methodology followed in the computational studies of the pulmonary arteries in relation to congenital heart diseases. In the review paper of Conijn and Krings (2021), they identified 34 research papers that use either patient-specific or idealised geometries to investigate the blood flow environment, and report 10 different approaches to define the inlet BC and 17 for the outlet BCs. This diversity partly derives from the lack of clinical data associated with the pulmonary arteries, which also makes validating the computational results of such studies rather difficult.

In this study, various BCs are investigated in order to understand how they affect the blood flow development in the pulmonary bifurcation. In addition, the elasticity of the arterial wall is considered and the non-Newtonian nature of blood. The symmetric geometry (Fig. 3.1 (vi)), and a similar 3D idealised model, are utilised to facilitate the comparisons.

4.2. Methodology

Further to the flow simulations presented on Chapter 3, a sensitivity analysis was performed, first, in the symmetric Y-Junction model (Fig. 3.1 (vi)) to investigate the

effects of other boundary conditions and how they could affect the computational results. OpenFOAM®, a Finite Volume solver, and Alya-Red, a Finite Element solver, were used to explore different modelling parameters.

Unless otherwise stated, all the numerical simulation were performed assuming a laminar flow model with a parabolic velocity profile of a U_{mean} = 0.1 m/s at the inlet of the MPA, zero-pressure condition at the branch outlets and rigid walls. The numerical calculations were performed assuming a dynamic viscosity of $4x10^{-3-}$ Pa s and a fluid density of 1060 kg/m^3.

For the numerical calculations performed on the OpenFOAM® open-source library, the simpleFoam solver was utilised, for steady-state incompressible flow. The solver is appropriate also for turbulent flow models, employing the semi-implicit method for pressure linked equations (SIMPLE) algorithm. The Gauss linear gradient and the second order bounded Gauss linear upwind divergence numerical schemes were used. Residual control was set to 10^{-6} for pressure and velocity.

Second, a preliminary investigation was conducted at the Barcelona Supercomputing Center (BSC), during a three-months period of a research visit to explore the capabilities of the BSC in-house code Alya-Red (Vazquez et al., 2014, 2015). Time discretisation was based on the second-order backward differential scheme. The generalised minimal residual (GMRES) (Saad and Schultz, 1986) and the deflated conjugate gradient (Nicolaides, 1987) methods were employed to solve the momentum and continuity equations, respectively. For the solid mechanics, the implicit Newmark method (Newmark, 1959) was used for the time discretization.

4.2.1. Modelling parameters investigated

In the following sections, the investigation conducted in the software OpenFOAM® is first presented (Section 4.2.1.1.), followed by the parameters tested on the in-house code Alya-Red (Section 4.2.1.2.).

4.2.1.1. OpenFOAM®

Tapering in the bifurcation: Tapering is an unequivocal characteristic of arterial conduits, from the larger arteries to the smaller ones, based on multiple studies (Caro et al., 2011, Qureshi and Hill, 2015). To investigate this effect a geometry was created, with the distal main pulmonary artery, and the proximal left and right pulmonary arteries tapered. The diameters were modified to ~0.95*D* for the MPA and ~1.02*d* for both daughter branches (where *D* and *d* the diameters of the MPA and the daughter branches, respectively, as defined on Section 3.1.). These reductions in diameters correspond to a 4% and a 2% tapering, respectively, which are representative of the percentages found in a healthy young male (Qureshi and Hill, 2015). No difference was found on the flow rate between the non-tapered and tapered asymmetric models, as measured at the entrance of the bifurcation (at a distance 0.01 m from the origin O).

Velocity profile at the inlet and MPA length: The sensitivity of the steady velocity profile at the inlet of the MPA was investigated, first, through the use of a uniform inlet profile to represent blood flow emanating from the pulmonary valve, and, second, by reducing the length of the MPA to ~*2D* (equal to 5cm), in order to reflect a more physiological MPA dimension (Qureshi and Hill, 2015). The uniform velocity profile assumed the same *Re* as the parabolic profile.

Time-dependent flow: To account for the unsteady nature of blood flow, a sinusoidal variation of the velocity profile at the MPA inlet was assumed, according to Eq. (3.2). Time-averaged results over a single cycle were compared with the steady-state numerical results for the same mean velocity.

Three-dimensional geometry: An additional three-dimensional (3D) symmetric Y-Junction geometry was created assuming the same proximal and distal diameters as the two-dimensional tapered model, and with the length of the MPA and the daughter branches assumed approximately 3.8*D* and 11.5*D*, respectively (Fig. 4.1 shows only a section of the model). The computational mesh of the 3D geometry consisted primarily of prismatic elements, with tetrahedral elements near the walls. A boundary layer was added near the arterial wall boundaries to capture the viscous effects, which included 17 layers with the first layer being at a distance of ~0.002*D* away from the wall. The total number of elements was ~3 800 000. The three-dimensional symmetric Y-Junction was tested by assuming a parabolic velocity profile at the MPA inlet, for both steady and unsteady flow, with the same mean velocity *U*.

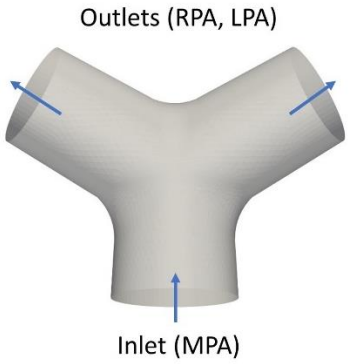

Figure 4.1: Schematic representation of 3D geometry.

Turbulent flow model: Simulations were performed assuming the k-ω shear stress transport (SST) turbulence flow model that utilizes two differential transport

equations, one for the turbulent kinetic energy *k*, and one for the dissipation rate, ω, as described in (Menter et al., 2003), and with model specifications (presented in Table 4.1) (Menter, 1994), calculated using the following formulas: turbulent intensity ($I = 0.16 \times Re_D^{-1/8}$), turbulent energy ($k = 3/2 \times (UI)^2$), turbulent length scale ($L = 0.07 \times D$), and specific dissipation rate ($\omega = \sqrt{k}/0.09L$). The Reynolds Averaged Navier-Stokes equations for turbulent flows were used (Liu at al., 2020):

$$\nabla \cdot \overline{u} = 0 \tag{4.1}$$

$$\rho \frac{\partial \overline{u}}{\partial t} + \rho \nabla \cdot (\overline{uu}) = -\nabla \overline{p} + \nabla \cdot \mu \left(\frac{\partial \overline{u}_i}{\partial x_j} + \frac{\partial \overline{u}_j}{\partial x_i} \right) \tag{4.2}$$

where $\overline{u}$ is the mean velocity field and p is the pressure.

Table 4.1: Parameters used for the k-ω SST turbulent model (U: mean velocity, Re: Reynolds number, I: turbulence intensity, k: turbulent energy, l: turbulent length scale, and ω: specific dissipation rate).

***U* (m/s)**	**Re**	**I**	**k (m^2/s^2)**	***L* (m)**	**Ω (1/s)**
0.1	650	0.071	7.6e-05	1.82e-03	5.32e01
0.3	1950	0.062	5.2e-04	1.82e-03	1.39e02
0.5	3250	0.058	1.2e-03	1.82e-04	2.11e02

Reynolds number with turbulent flow model: The effect of Reynolds number (calculated using Eq. (1.14)) was tested by increasing the Reynolds number from 650 to 1950 and 3250, which correspond to an increase of the mean velocity U from $0.1\,m/s$ to $0.3\,m/s$ and $0.5\,m/s$, respectively, for the specific MPA diameter, *D*. Such values of velocities can be observed in the pulmonary bifurcation during systole (Chern et al., 2012). The simulations were performed using the k-ω SST turbulent flow model previously described.

Non-Newtonian models: Additional simulations considered the non-Newtonian rheology of blood. For that, four different models were tested, namely the power law, the Cross power law, the Casson and Bird-Carreau models, with model specifications

presented in Table 4.2 (Karimi et al., 2014). The power law is the simplest non-Newtonian model to be considered. The Bird-Carreau and the Cross power law models have viscosities very close to the Newtonian one at high shear rates. In addition, the Cross power law model considers a short range of viscosities and therefore could be a good candidate for simulating blood flow in large arteries. Finally, the Casson model is expressed in terms of the hematocrit, which is assumed 40% for normal blood (Karimi et al., 2014). Fig. 4.2 presents the apparent viscosity of blood against the shear rate for the different rheological models assumed in this study. In lower shear rates there is a greater variability in the blood viscosity between the non-Newtonian and the Newtonian model, while the difference is reduced in higher shear rates. The high shear rate region in which the models of this study are operating was identified and is approximately within 100 to 220 s^{-1} (shown in Fig. 4.2).

Table 4.2: Non-Newtonian models of blood flow (ν: blood viscosity, ν_∞: infinite shear rate viscosity, ν_o: zero shear rate viscosity, k: relaxation time constant, $\dot{\gamma}$: shear rate, α: constant parameter, n: power law index, τ_0: yield stress). Wall shear stress values at the inlet MPA walls of the symmetric Y-Junction for the different models, are also presented.

Rheological Model	Viscosity	Specified Values	WSS at inlet MPA wall (dynes/cm^2)
Newtonian	ν	ν: 0.004 Pa s	0.922
Power Law	$\nu = (k\dot{\gamma})^{n-1}, \nu_{min} \leq \nu \leq \nu_{max}$	ν_{max}: 0.056 Pa s, ν_{min}: 0.0035 Pa s, k:0.017 s, n: 0.708	1.696
Cross power law	$\nu = \nu_\infty + \frac{\nu_0 - \nu_\infty}{1 + (m\dot{\gamma})^\alpha}$	ν_∞: 0.0035 Pa s, ν_o: 0.0364 Pa s, m: 0.38 s (consistency index), α:1.45	1.229
Casson	$\nu = (\sqrt{\tau_0/\dot{\gamma}} + \sqrt{m})^2$	m: 0.00414 Pa s (viscosity coefficient), τ_0: 0.0038 Pa	1.198
Bird-Carreau model	$\nu = \nu_\infty + (\nu_o - \nu_\infty)[1 + (k\dot{\gamma})^\alpha]^{(n-1)/\alpha}$	ν_∞: 0.0035 Pa s, ν_0: 0.056 Pa s, k: 3.313 s, n: 0.3568	1.696

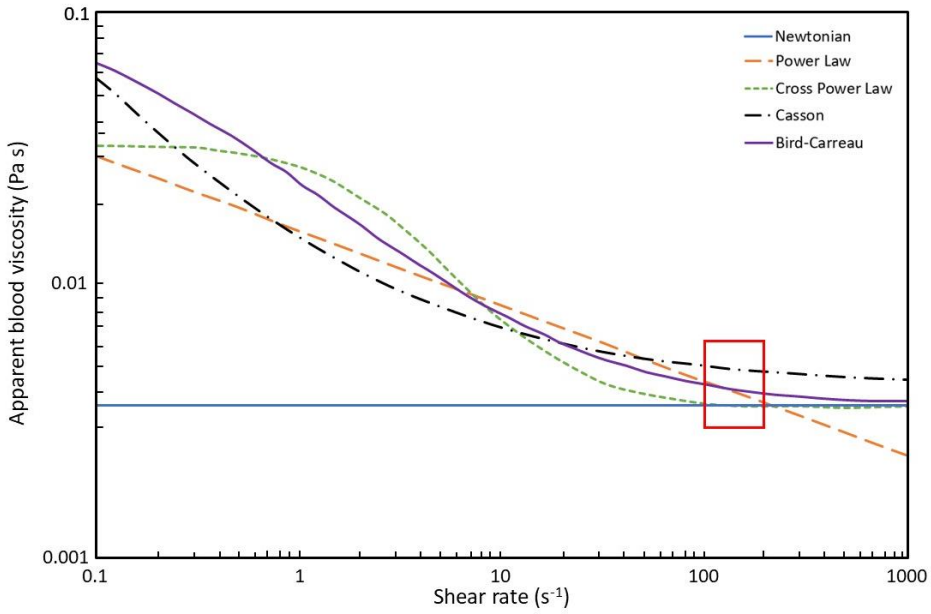

Figure 4.2: Apparent viscosity against shear rate for the different rheological models used. The high shear rate region in which the models of this study are operating was identified (red box) and is approximately within 100 to 220 s^{-1} (After Karimi et al., 2014).

4.2.1.2. Alya-Red

In this section the preliminary work conducted at BSC is described. The capabilities of the in-house code were explored and some functionalities still under-development were provisionally tested.

Pulmonary valve: The idealised 3D geometry of Fig. 4.1 was further modified to create two additional models that included the pulmonary valve in an open (Fig. 4.3a) and a closed configuration (Fig. 4.3b). The valve is an idealised aortic valve which can be found online at Grabcad, and was originally created using CAD by Dassault Systémes (https://grabcad.com/library/aorta-aortic-valve-1). The three leaflets were isolated and scaled in order to fit at the inlet of the 3D pulmonary arterial model. The valve was placed at a distance of 5 cm from the pulmonary bifurcation, to represent the normal MPA length. Alterations were also made in the thickness of the leaflets, to allow a higher number of elements with the scope to capture the valve movement using FSI

modelling, and the gaps between the edges of the leaflets were closed to ensure there will be no unwanted backflow. To create the different configurations of the valve, the morph function of ANSA v19.1 (BETA, CAE Systems) software was used. That allowed to implement shape changes in the leaflets of the valve by moving parts of the geometry to a new position (Fig. 4.3). The open (Fig. 4.3a) and closed (Fig. 4.3b) static configuration of the valve were tested assuming a steady flow, and a plug velocity profile of 0.5 m/s was assigned at the inlet of the model.

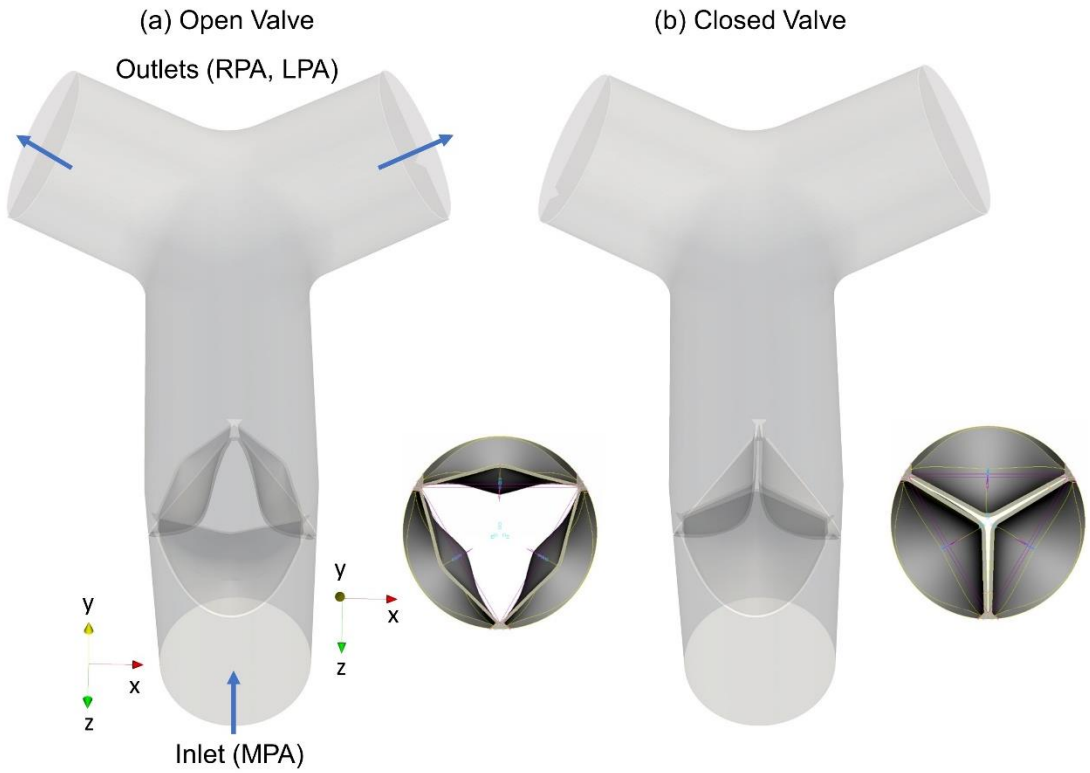

Figure 4.3: 3D idealised model of the pulmonary bifurcation with (a) the valve in open configuration and (b) the valve in closed configuration.

Peripheral resistance: Simulations were performed in the 3D geometry accounting the resistance of the downstream vasculature as described in Bazilevs et al. (Bazilevs et al., 2009), and by setting a physiological pressure of 20 mmHg, usually found in the

pulmonary arteries (Martini et al., 2014). The resistances for the RPA and LPA branches were assumed both equal to 300 dyn s cm^{-5} (Guibert et al., 2014).

Arterial wall: Fluid-Structure Interaction simulations were conducted in order to investigate the effect of the arterial wall in the flow development in the pulmonary arteries. To represent the arterial wall, a layer of approximately 640 000 elements was added on the pulmonary artery in the idealised 3D geometry, which was volumised in ANSA v19.1 (BETA CAE, software). The diameter of the arterial wall was assumed 10% of the diameter of the MPA at the inlet (Bazilevs et al., 2009) and was modelled using the hyper-elastic and isotropic Neo-Hookean solid material (Nolan et al., 2014). The material parameters assigned to the solid domain were a bulk (K) and shear (G) moduli of 1 MPa and 0.03 MPa, respectively, which are equivalent to a Poisson's ratio (v) of 0.485, and the density of the arterial wall was set to 1000 kg/m^3 (Nolan et al., 2014). Bulk modulus describes the resistance to compression, shear modulus the elastic shear stiffness and Poisson's ratio is a measure of the resistance perpendicular to the stress. These parameters are connected through the equation $2G(1+v) = E = 3K(1-2v)$, where E is the Young's modulus, describing the tensile stiffness of a material (Landau and Lifshitz, 1970). The nodes at the inlet and outlets of the model were fixed in space and no constrictions were applied at the wall boundary. The numerical scheme for the coupled problem was based on a staggered algorithm. For the numerical calculations, a Rayleigh damping* (Caughey, 1960) of 200 was applied, to enable convergence of the solution, with the same flow conditions as the simulation considering the pulmonary valve. The Arbitrary Lagrangian-Eulerian (ALE) method was used for the coupling of the blood flow and the arterial wall.

* Rayleigh damping, or proportional damping model has the form: $\mathbf{C} = \alpha\mathbf{K} + \beta\mathbf{M}$, where **C**, **K** and **M** the damping, stiffness, and mass matrices, respectively, and α and β the stiffness- and mass- proportional damping coefficients (Chowdhury and Dasgupta, 2003)

4.2.2. Post processing

Similar to Chapter 3.2.5, contours of velocity, velocity profiles and streamlines, as well as wall shear stress (WSS) distribution along the inner wall of the bifurcation (connecting the LPA and RPA) were analysed. Velocity values were non-dimensionalised by division with the U_{mean}. WSS was non-dimensionalised with the value corresponding to the inlet WSS magnitude of a long straight segment that has the same diameter of MPA inlet and same inflow conditions as the pulmonary bifurcation model. For a two-dimensional channel, this can be calculated for a Newtonian model with a fully developed axial velocity profile as $\tau_{w_{2D}} = 6\mu U/D$, and $\tau_{w_{3D}} = 8\mu U/D$, for a three-dimensional circular pipe (Katritsis et al., 2007). For each non-Newtonian model, WSS values were non-dimensionalised in a similar fashion, that is, with values calculated at the inlet of a straight geometry with the same MPA diameter and flow conditions, including a parabolic velocity profile (last column of Table 4.2). The time-averaged wall shear stress was further determined, according to Eq. (3.6).

4.2.3. OpenFOAM® vs Alya-Red comparison

As already discussed in Section 2.1.2, in the field of computational fluid dynamics, the finite element method (FEM) and the finite volume method (FVM), are two of the most widely used algorithms, implemented to obtain analytical solutions to the differential equations of fluid mechanics. Finite element method is considered more robust compared to the finite volume method at low *Re*. On the other hand, though, FVM is considered to be more accurate providing better results, in some cases (Rapp, 2017). In the FVM, the differential equations of interest, are integrated over the

volume, and by applying Gauss's theorem they are converted into surface integrals across the boundaries of the cells (Rapp. 2017). FEM divides the domain in small patches and solves the differential equations of interest in the boundary of the patch (Rapp, 2017).

As part of the transition from OpenFOAM® to Alya-Red solver, numerical results acquired from the different methods were compared and the difference between the two was quantified. A simulation was run in each solver using the idealised 3D geometry with the same mesh and initial boundary conditions. A difference of approximately 6% was quantified on the pressure values, which was reduced to 2.8% and 1.3% for the wall shear stress and the velocity, respectively. Higher values were obtained with the finite volume method for the wall shear stress and the pressure, while lower values for the velocity.

4.3. Results

In the following paragraphs the computational results are presented in a series of figures, that explore the effect of the different inlet and outlet boundary condition, blood rheology and the elasticity of the arterial wall. The investigation performed in OpenFOAM® is first presented in Section 4.3.1., followed by a brief analysis of preliminary results obtained in Alya-Red (Section 4.3.2.)

4.3.1. OpenFOAM®

Steady inlet velocity profile and MPA length

Fig. 4.4a presents velocity contours overlaid by streamlines of velocity, and the insets show the respective velocity profiles, non-dimensionalised by the mean MPA velocity. Due to symmetry of the branches, only a single branch is presented in Fig. 4.4a. The length of the MPA had no effect on the velocity distribution in the models with the same parabolic inlet profile, as expected (top row of Fig. 4.4a). However, there was an overall decrease in the maximum velocity values in the daughter branches, for the models with uniform inlet profiles, for both MPA lengths (bottom row of Fig. 4.4a), with the most significant differences observed for the model with the shorter MPA. The velocity streamlines depict recirculation zones for all four cases. Both models with parabolic inlet profiles and the model with the longer MPA and uniform profile exhibited similar recirculation zones, with a maximum difference of 2% for the longer MPAs. A smaller recirculation area was noticed for the shorter MPA model with uniform inlet profile, the length of which was about 10.5% smaller compared to that of the same-length MPA case with parabolic inlet profile (right column of Fig. 4.4a).

Fig. 4.4b displays non-dimensionalised WSS profiles. No apparent differences were found between the WSS distributions of the models with different MPA lengths but the same parabolic inlet profile. A considerable decrease in the WSS was, nevertheless, observed along the inner wall of the model with uniform inlet and long MPA, which was further reduced for the model with the shorter MPA. To quantify the decrease, the integral of the WSS distribution was calculated for each case and compared with the integral of the parabolic inlet and long MPA model. A small decrease of 2% is found in the integral of the WSS of the model with the parabolic inlet profile and shorter MPA; the difference is increased to ~27.7% and 53% for the models with the long and shorter MPA lengths with the uniform profile, respectively.

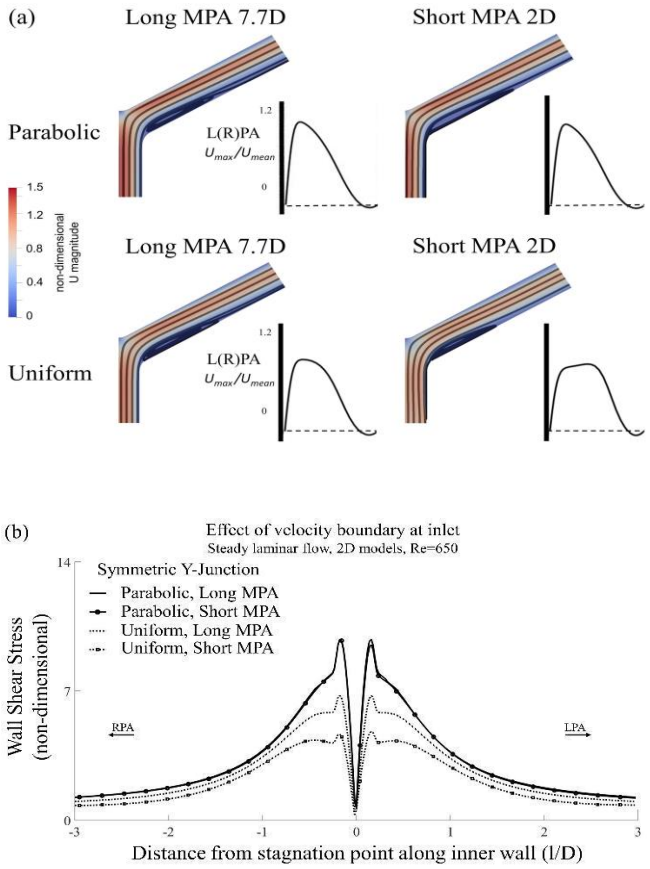

Figure 4.4: Effect of steady inlet velocity profile with varied MPA lengths for the symmetric Y-Junction (Fig. 3.1 (vi))). (a) Non-dimensionalised velocity contours, overlaid by velocity streamlines, for parabolic and uniform inlet profiles (only half of the geometry is shown due to axisymmetry). Insets at the bottom right display velocity profiles within the RPA or LPA taken at a distance of 3 cm (~1.15D) from the origin of the branches. (b) Non-dimensionalised WSS along the inner wall for parabolic and uniform inlet velocity profiles and different MPA lengths. Steady Newtonian flow, Re=650.

Unsteady inlet flow

For the time-dependent sinusoidal inlet profile of Eq. (3.2), a decrease of approximately 28% in the length of the recirculation zone was found based on the time-averaged velocity streamlines (Fig. 4.5a (ii)), as compared with those for steady-state inlet flow (Fig. 4.5a (i)). Time-averaged wall shear stress for the unsteady case, non-dimensionalised by the WSS value at the inlet wall, was further plotted along the inner wall of the arterial models (Fig. 4.5a). Although the WSS distribution was similar in shape for both steady and unsteady cases, the time-averaged WSS of the unsteady flow was slightly higher (1.66% difference in the integral of the WSS).

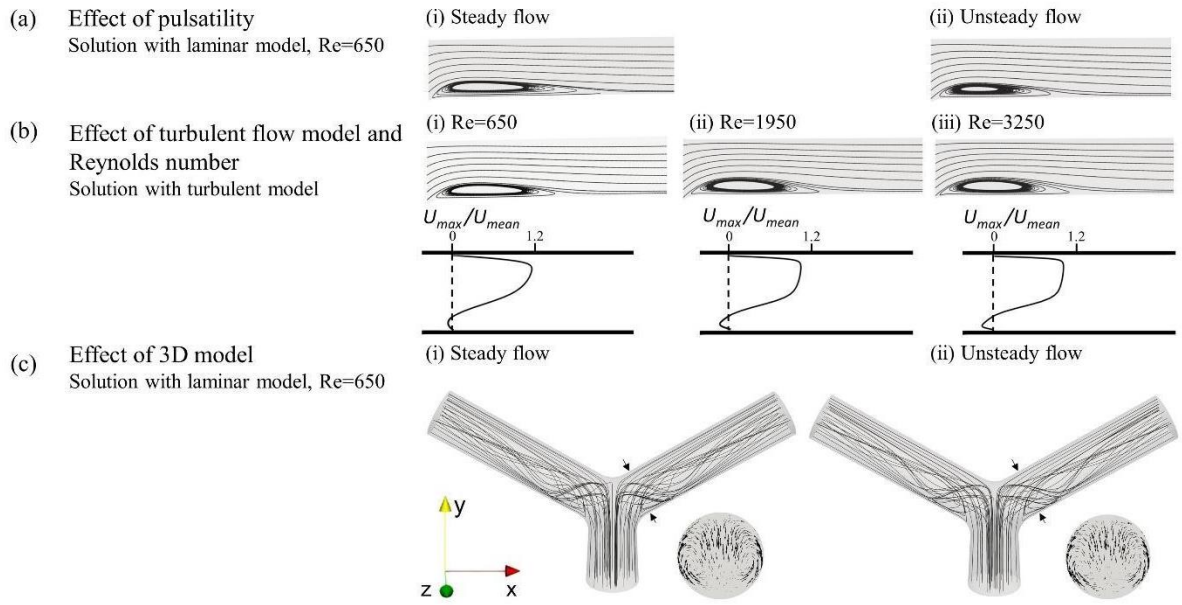

Figure 4.5: Streamlines of velocity for different boundary conditions tested in the symmetric Y-Junction (Fig. 3.1 (v)). Effects of: (a) pulsatile flow; (b) turbulent flow and Reynolds number (including velocity profiles, non-dimensionalised by division with the mean velocity at the inlet of MPA); and (c) three-dimensional flow.

Turbulent flow model

Streamlines of velocity for the laminar (Fig. 4.5a (i)) and the turbulent flow models (Fig. 4.5b (i)) were compared for a Reynolds number of 650 and parabolic inlet velocity profile. A decrease in the recirculation area was noticed for the turbulent flow model, with the length of the recirculation zone reduced by approximately 23.3%. The non-dimensionalised WSS profiles for the turbulent and laminar flow models, using parabolic inlet velocity profile, demonstrated a considerable decrease in the turbulent flow model (Fig. 4.6b). However, for a uniform inlet profile, the WSS profiles along the inner wall were almost identical for both the turbulent and laminar flow models (also in Fig. 4.6b) and very similar to the turbulent flow solution with parabolic velocity profile at the inlet. A possible explanation could be the dissipation in the velocity in the turbulent model, since the velocity is no longer parabolic and resembles

more of a uniform profile. Therefore, flow enters the pulmonary junction with a lower maximum velocity compared to the equivalent value for the laminar model.

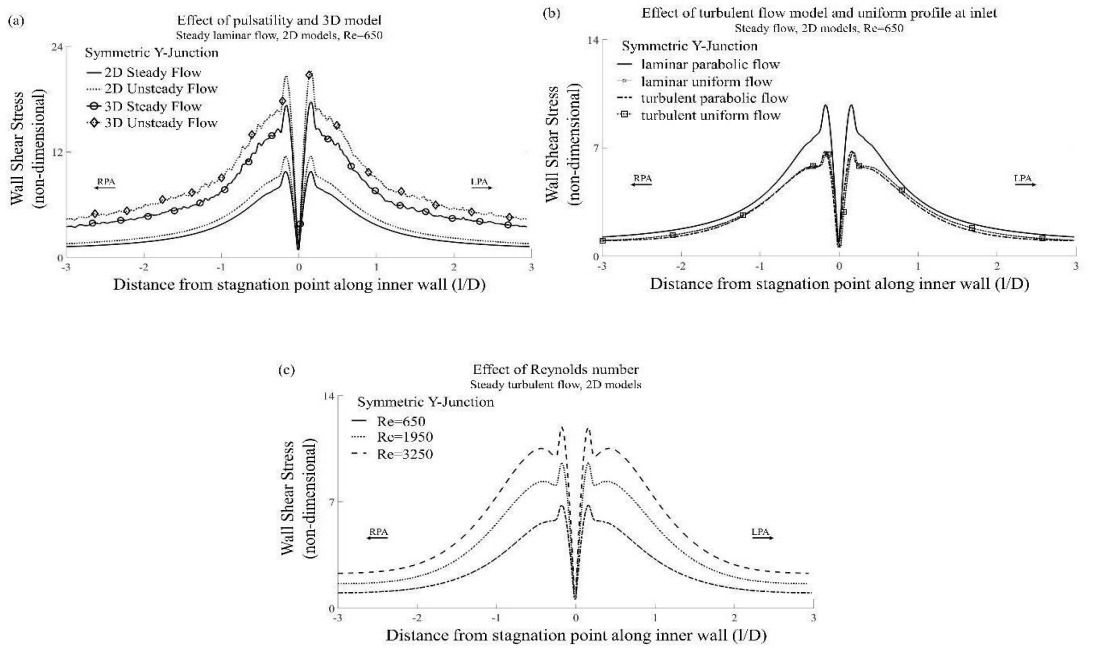

Figure 4.6: Non-dimensional wall shear stress distribution, plotted along the inner wall of the arterial models for (a) steady and unsteady flow, in the 2D and 3D models; (b) laminar and turbulent models with parabolic and uniform inlet velocity (Re=650); (c) different Reynolds numbers assuming turbulence flow.

Reynolds number with turbulent flow model

An investigation on the effect of different Reynolds numbers on the velocity streamlines and WSS are shown in Fig. 4.5b and Fig. 4.6c, respectively. The length of the recirculation zone was increased at higher Reynolds numbers, by 14.2% and 17%, for Re=1950 and Re=3250, respectively. Non-dimensionalised velocity profiles, based on division with the mean velocity at the entrance of the MPA for each Reynolds number respectively, were plotted at a distance of 3cm (1.15*D*) from the branch origin (Fig. 4.5b). The maximum forward velocities in the daughter branches slightly decreased in magnitude as the Reynolds number increased, with an equivalent increase in the retrograde flow, and the overall velocity profile was more uniform due to the

higher inertia of the fluid particles at the middle of the branch at higher Reynolds numbers. The non-dimensionalised WSS profiles along the inner wall of the arterial models (Fig. 4.6c) were increased in magnitude with increasing Reynolds number.

Unsteady flow in 3D model

The steady and time-averaged velocity streamlines, as presented in Fig. 4.5c, indicate extended recirculation zones in both cases, with no major differences between the two, indicating the quasi-steady nature of the flow. In-plane velocity streamlines are also presented, taken at distance of 1.7 cm (~0.65*D*) from the stagnation point (arrows on the 3D geometry indicate the point of slice section) (Fig. 4.5c). Two counter rotating vortices were visible which is the result of secondary flow motion. Higher velocities from near-wall locations rotated first towards the inner wall and then the centre of the branch (Pedley et al., 1971). Non-dimensionalised WSS profiles were further plotted (Fig. 4.6a) and were compared with WSS in the 2D models. WSS was significantly higher in the 3D models as compared to the 2D models, presenting up to 50% difference in the integrals of WSS for the steady flow and 52% difference in the unsteady cases. However, despite the quantitative difference, the WSS distribution was similar in shape for both 2D and 3D models, and steady or unsteady flow. The time-averaged WSS for the unsteady 3D flow was further elevated compared to the steady 3D flow, and a 2.84% difference in the integrals of the WSS was found between the two. The WSS distribution along the inner wall of the 3D models (Fig. 4.6a) is in close agreement with previous studies (Tang et al., 2012, Kanokjaruvijit et al., 2017), even though the WSS values are somewhat lower in the 2D models (Fig. 4.5a).

Non-Newtonian models

Four different non-Newtonian models were tested the power law, the Cross power law, the Casson, and the Bird-Carreau, and were compared with the Newtonian model. WSS was expressed in both a non-dimensionalised form (Fig. 4.7a), based on the WSS value at the inlet MPA wall of each respective model (see Table 4.2), and in dynes/cm^2 (Fig. 4.7b).

In Fig. 4.7a, the WSS values proximal to the stagnation point varied considerably depending on the non-Newtonian model. The highest non-dimensionalised WSS values were found for the Newtonian model, while the lowest values were exhibited with the power law and Bird-Carreau models, which were very similar. Due to the non-dimensionalisation, all the WSS values along the inner wall distal to the stagnation point tended to unity, therefore there was not much variation in the WSS distal to the junction.

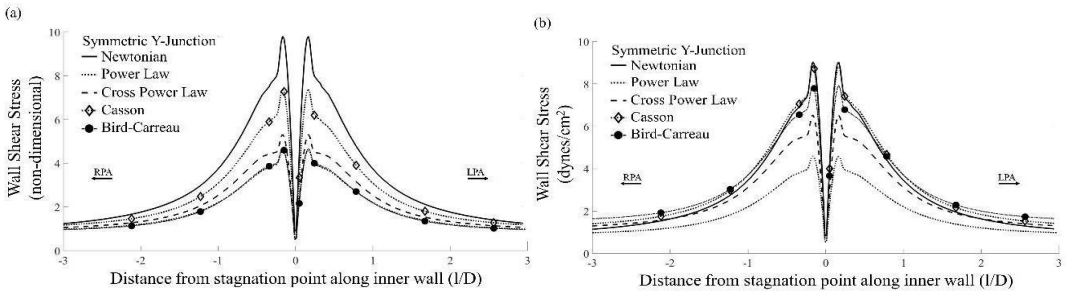

Figure 4.7: WSS plots along the inner wall of the symmetric 2D Y-Junction (Fig. 3.1(v)) for the Newtonian and non-Newtonian models (a) non-dimensionalised form; (b) expressed in dynes/cm^2. Steady flow, Re=650.

WSS values expressed in dynes/cm^2 (Fig. 4.7b) result in a slightly different distribution than in non-dimensionalised form (Fig. 4.7a). The largest deviations in the WSS values existed at locations at a short distance from the stagnation point. The Newtonian model resulted in the highest WSS values, while the power law in the lowest values. The

Casson model displayed the highest similarity with the Newtonian model, while the power law appeared the least appropriate, showing the highest deviation from the Newtonian and the rest of the non-Newtonian models, in both Figs. 4.7a, b, proximal to the bifurcation. The WSS developed at the inner wall distal to the stagnation point varies slightly among the different models, with the largest distal deviation from the Newtonian model by the Bird-Carreau model.

4.3.2. Alya-Red

Static valve

The effect of a static valve in the 3D model is visualised in Fig. 4.8. Streamlines of velocity coloured by non-dimensionalised velocity contours, are presented for the open and closed configurations. In the first case, where the valve is open, higher velocities are observed along the MPA, and the blood flow develops in a similar way as if the valve was not present, comparable with Figs 4.5c and 4.10a, 4.10b. Nevertheless, disturbed flow is visible at the entrance of the valve due to tapering (Fig. 4.8a). In the second case, where the valve is closed, the highest velocities develop at the tip of the valve due to the restriction of the flow and very complex flow patterns of low velocity appear within the pulmonary bifurcation (Fig. 4.8b).

Peripheral resistance

The effect of the pressure boundary condition was investigated by accounting the physiological pressure and the downstream resistance at the outlets of the models (Fig. 4.9), with the scope to validate that no other differences in the flow parameters would exist when the zero-pressure BC is used. The pressure distribution (Fig. 4.9a), velocity contours (Fig. 4.9b) and the wall shear stress distribution (Fig. 4.9c), were compared

with the zero-pressure condition. The results indicate that only the pressure values (quantitively differences) are affected when the more physiological pressure is considered, reflected by the different range of values in the colourbar in Fig. 4.9a. A 0% difference was found between the velocity contours and the wall shear stress distribution (Fig. 4.9b-c).

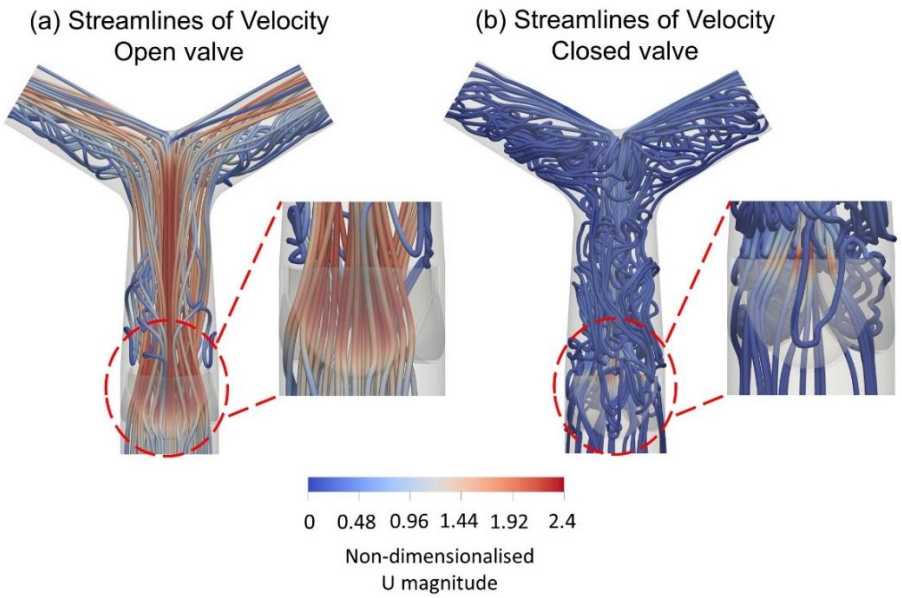

Figure 4.8: Streamlines of velocity coloured with non-dimensionalised velocity contours on a static model of the idealised valve in (a) the open and (b) the closed configuration.

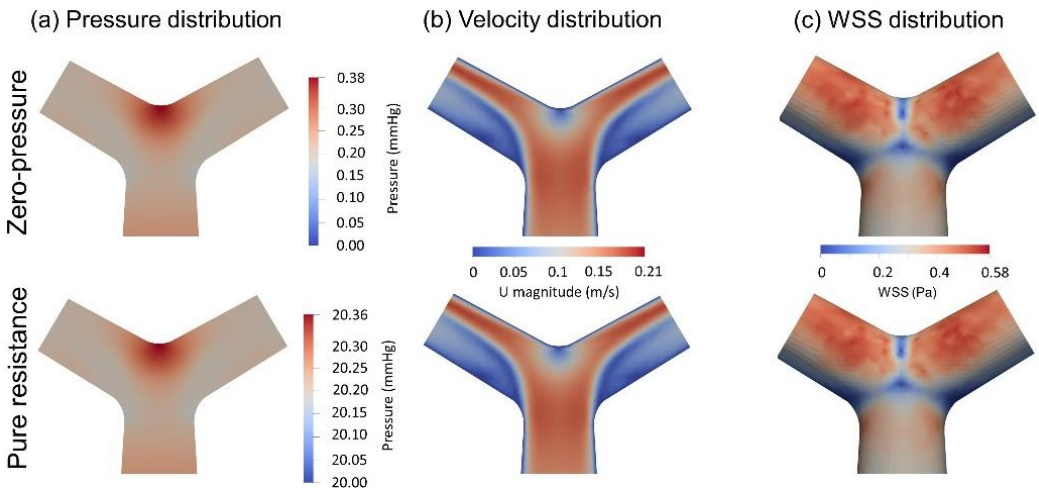

Figure 4.9: Effect of pressure outlet boundary condition. (a) Pressure distribution; (b) velocity contours; and (c) wall shear stress distribution. (a) and (b) are plots over a slice along the mid plane of the model.

Elasticity of arterial wall

An investigation of the effect of the arterial wall was conducted using FSI, and the results are presented in Fig. 4.10.

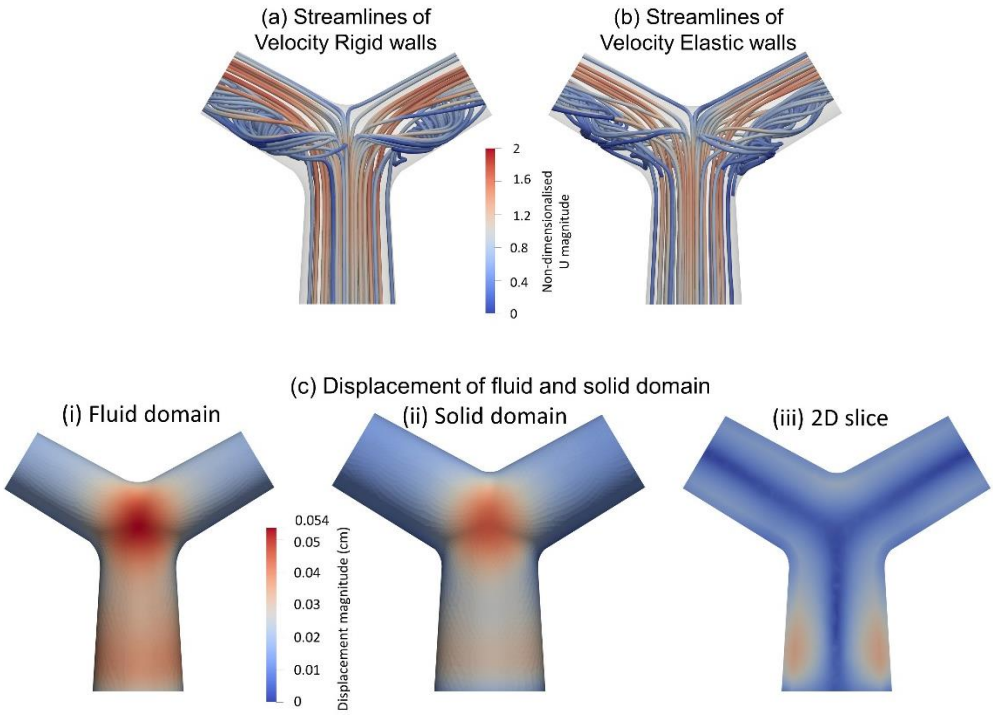

Figure 4.10: (a) and (b) Streamlines of velocity coloured with non-dimensionalised velocity contours in the models with (a) rigid walls, and (b) elastic walls (only fluid domain presented). (c) Displacement distribution when elasticity of the arterial walls is considered in (i) the fluid domain, (ii) the solid domain, and (iii) a 2D slice of both the solid and the fluid.

Streamlines of velocity coloured by non-dimensionalised velocity contours are plotted for the three-dimensional geometry with (a) rigid walls (Fig. 10a), and (b) the elasticity of the arterial wall taken into account (Fig. 4.10b). The elasticity of the arterial wall does not seem to greatly affect the velocity distribution in the arterial models. The integral of velocity was calculated on slices of the models (as shown on Fig. 4.10c (iii)) and a 5.8% difference was found based on FSI case. In Fig. 4.10c, the displacement distribution is presented separately for the fluid (Fig. 4.10c (i)) and the solid domain (Fig. 4.10c (ii)). Higher displacement is visible in the fluid domain and the maximum displacement is noticed at the centre of the bifurcation. An area of high

displacement is also found at the entrance of the MPA, where the solid and fluid domains interact and are constrained in space, not allowing the movement of the nodes in any direction. The 0.054 cm of maximum displacement in the fluid accounts for approximately 2.6% change in the diameter of the vessel at the specific location.

4.4. Discussion

This Chapter presents a sensitivity analysis of the effects of various boundary conditions on the blood flow in two- and three- dimensional models, representative of the pulmonary bifurcation. There is a lot of discussion in the literature about how much the different assumptions at the model's boundaries can alter the flow development (Vignon-Clementel et al., 2006, Kheyfets et al., 2013, Chnafa et al., 2018, McElroy and Keshmiri 2018, Conijn and Krings, 2021). Various commonly utilised BCs were, therefore, compared and variations in the flow development were identified.

The influence of pulsatility in the WSS distribution is discussed in previous studies and similarities are reported between the steady state and time-averaged results (Kazakidi et al., 2009, Jodko et al., 2016, Baidar and Cervantes, 2017). A difference of up to 7% between time-averaged and steady wall shear is reported by Baidar and Cervantes (2017) in simulations performed at a test case in a pipe and utilising different turbulent flow models, suggesting that steady simulations can capture time-averaged results. Jodko et al. (2016) came to a similar conclusion, with simulations performed in patient-specific models of the fistula when they compared pulsating and stationary flow, and the two reached comparable results with the stationary simulations greatly reducing computational time. Kazakidi et al. (2011), in an investigation performed in

models of aortic branches to examine the effect of pulsatility found that the time averaged WSS was similar to the WSS of the steady flow case. The results of this study for the 2D and 3D geometries are in agreement with those previously reported.

Laminar and turbulent flow models for a parabolic and a plug velocity profile, and the effect of Reynolds number, were also investigated in the 2D geometry. The results indicate that when a plug profile is assigned at the inlet of the models, the flow development is not impacted by the laminar or turbulent flow assumption for the specific Reynolds number. For the different Reynolds numbers tested, it is shown that higher *Re* affects the extent of recirculation zones and the WSS along the inner wall of the models, which are both increased. The effect of increasing the Reynolds number on WSS values around arterial junctions (Fig. 4.6c) is in agreement with previous studies of similar effects (Kazakidi et al., 2009). Kazakidi et al. (2009) investigated the effects of Reynolds number on patterns of WSS in idealised branching models of the intercoastal arteries and found that increasing the Re from 30 to 1500 led to enlarged regions of high WSS at the branch orifices.

The non-Newtonian nature of blood was tested through four commonly used non-Newtonian models, the power law, the Cross power law, the Casson and the Bird-Carreau. The WSS profiles calculated for the non-Newtonian models (Fig. 4.7) are, comparable with the results from the study of Karimi et al. (2014). In their work, they study the blood flow in models of the human aorta and compare wall shear stress distribution in different rheological models. They observe similar wall shear stress patterns for all models, but with variations in the magnitude of the wall shear stress. They conclude that the Cross model exhibited the highest discrepancies with the Newtonian and the other non-Newtonian models and recommend not to be used as an

alternative rheological approximation. Finally, they observed an underestimation of the low WSS values with the Newtonian model (Karimi et al., 2014). In this study, the Power law and the Cross power law showed the highest deviations from the rest of the models (Fig. 4.7b). The Power law model shows a linear decline in the apparent blood viscosity with increasing shear rate, deviating from the rest of the non-Newtonian models, while the apparent viscosity of the Cross Power law is almost steady in high shear rates and close to the Newtonian (Fig. 2). The Newtonian model had lower wall shear stress values in the regions of low WSS but not deviating much from the Casson and Bird-Carreau models, both of which follow a similar trend in the region of high shear rate that the simulations are operating (Fig. 2). The range of values chosen for each rheological model affects the computational results, and therefore, assuming a more physiological relevant range of values for each model may alter the above observations.

Simulating the pulmonary valve and wall compliance is remarkably challenging and require the assignment of vessel wall properties. Computational simulations were performed using a static valve within the 3D model in different configurations. Despite the significant simplification in the valve movement, these preliminary results indicate that blood flow is affected by the configuration of the valve, with complex flow patterns developing when the valve is closed. The above findings are expected, as in this case the closed valve can be considered as a stenosed region along the main pulmonary artery that restricts the flow. Further simulations are necessary to allow the movement of the valve, from a closed to an open state, to capture the changes in the flow during the cardiac cycle. Although an attempt was made to recreate the movement of the valve, starting from the semi-open configuration, it was not feasible using the

FSI models available in the Alya-Red solver. Considering the elasticity of the arterial wall, the numerical simulations demonstrated that it can quantitatively affect the flow in the pulmonary bifurcation, but the difference is small (5.8%). Bazilevs et al. (2009) analysed the haemodynamics and wall motion in a patient-specific Fontan configuration (procedure performed to treat single ventricle congenital heart defects) under rest and exercise conditions and reported a maximum wall displacement of 0.064 cm, close to the pulmonary bifurcation, similar to the results of this work. Jin et al. (2003) investigated the blood flow in the ascending aorta and compared rigid and compliant wall models and found that flow is minimally affected by the consideration of wall motion. The results presented in this study are in agreement with those previously reported. In distal vessels, the effect of wall compliance may be larger. In a previous study of a model of a carotid bifurcating artery, the authors concluded that wall compliance affects the results quantitatively and reported a maximum deformation of approximately 16% on the vessel radius (Perktold and Rappitsch, 1995).

Finally, a pure resistance boundary condition was also considered in the 3D geometry, and a physiological pressure was assigned in the model. The results indicate that the velocity and the wall shear stress distributions are not affected by the pressure outlet in the symmetric model, where a 50-50 flow split is obtained with both boundary conditions. Nevertheless, it is important to consider the downstream resistance and pressure in order to obtain more clinically-relevant pressures in the models. Arbia et al. (2014), suggested that the zero-pressure boundary does not affect the pressure gradient or the flow distribution when the walls are assumed rigid in computational modelling. The results of this study indicate that there is a difference in the pressure

when a zero-pressure or pure resistance boundary condition is used, but only quantitatively. It is important to mention that peripheral resistance is found to be a major factor in the flow development in bifurcating arterial models, and can highly impact the flow distribution in stenotic and asymmetric models (Vignon-Clementel et al., 2006, Boumpouli et al., 2020).

4.4.1. Limitations and Future Work

Several limitations exist in the results presented in this Chapter through the different assumptions made for the numerical simulations conducted. Idealised two- and three-dimensional geometries are used to facilitate this extensive analysis of the different modelling parameters, which would have been more difficult and computational expensive to perform in patient-specific models. In addition, a sinusoidal variation of flow is considered to represent the unsteady nature of blood flow, which may not capture correctly the effects of pulsatility of the blood flow. Nevertheless, as it is part of a parametric investigation performed in idealised and not in patient-specific models, it is expected to provide a good indication of the fundamental unsteady flow characteristics. Moreover, it is recognised that the results obtained with the static valve in the pulmonary arteries, are not representative of the physiological blood flow dynamics through a moving valve. Alya-Red, the in-house code used for these simulations was still under development, and there was no such functionality to allow the simulation of a moving valve; although FSI was tested, it did not prove capable of capturing the valve movement. Finally, to model the arterial wall, the isotropic Neo-Hookean solid material was assumed, which does not account for the anisotropic behaviour of the collagen fibers. An attempt was made to recreate the collagen fibers

in the idealised pulmonary arterial model and use the Holzapfel-Gasser-Ogden (HGO) anisotropic hyperelastic solid material for the arterial wall, but the coupling between the fluid and the solid domain was not successful and the solution did not converge.

Further studies are required in order to verify the results of this study in patient-specific models and with the specification of patient-specific boundary conditions. Including a moving pulmonary valve will also provide valuable information about the flow development in the pulmonary arterial models. The immersed boundary method could be utilised to allow such simulations. Finally, the HGO anisotropic hyperelastic model can better represent the physiological environment of the arterial wall, and therefore it should be considered in future work.

4.5. Concluding remarks

Modelling parameters have a key role in computational fluid dynamics, as they can alter the numerical results in a considerable extent. Many different methodologies are reported in the literature considering the computational investigation of the blood flow in pulmonary arterial models, which makes comparisons of the numerical results rather difficult, as there is no standard methodology in the numerical studies. This work is an extended analysis performed in order to investigate the effect of various commonly used inlet and outlet boundary conditions and quantify their differences. In addition, other modelling parameters such as the non-Newtonian nature of blood and the elasticity of the arterial wall were considered.

Overall, quantitative differences exist in the flow features of the pulmonary arteries when different boundary conditions are used. Steady flow underestimates the WSS

along the inner wall, while a laminar flow model with a parabolic velocity profile overestimates the WSS values. The length of the MPA inlet is found to affect the flow development and therefore is considered important when a uniform profile is assigned at the inlet boundary. Complex flow patterns are developed when the pulmonary valve is included in the pulmonary artery, while a resistance boundary in symmetric idealised models did not affect the WSS and velocity distribution. Finally, the results indicate that wall motion quantitatively changes only minimally the velocity distribution, while non-Newtonian blood rheology can alter the WSS, showing different developments depending on the rheological model assumed.

Chapter 5

Blood flow in patient-specific pulmonary arteries of repaired Tetralogy of Fallot patients

In this chapter, the morphological parameters and flow patterns are investigated in the pulmonary bifurcation of seven patient-specific models of rTOF patients, and of an anatomical average geometry, derived from the adult patient-specific models. An introduction is first given in Section 5.1. Then Section 5.2. describes the reconstruction of the models, the extraction of flow data, the steps followed to create the anatomical average geometry, the numerical parameters and boundary conditions used. Section 5.3. is divided in four subsections, the geometry (Section 5.3.1.) and flow characterisation (Section 5.3.2.), and the computational results of the averaged (Section 5.3.3.1.) and patient specific (Section 5.3.3.2.) boundary conditions. Section 5.4. gives a discussion of the findings, and finally Section 5.5. provides an overview of the key results.

5.1. Introduction

Transannular patch repair (TAP) is the predominant surgical approach that is used to repair pulmonary insufficiency in patients with tetralogy of Fallot (Al Habib et al., 2010). However, long term complications, including right ventricular dilatation and dysfunction, pulmonary regurgitation, residual right ventricular outflow tract (RVOT) obstruction, kinking of the left pulmonary artery and atrial tachyarrhythmia (Babu-

Narayan and Gatzoulis, 2018), are common in the repaired population. Pulmonary valve replacement is performed in the repaired tetralogy of Fallot population to prevent ongoing volume overloading and dilation of the right ventricle, and is recommended prior to the significant clinical symptoms to increase the likelihood of successfully RV remodeling; nevertheless, there is no common consensus on the reliability of current indices to determine the right timing for intervention (Geva 2011, Kordybach-Prokopiuk et al., 2015, Babu-Narayan and Gatzoulis, 2018). Understanding the haemodynamic environment in the pulmonary bifurcation of rTOF patients is therefore crucial to foresee long term outcomes of the interventions.

The advancement of medical imaging techniques over the past decades has allowed the application of computational fluid dynamics for the assessment of blood flow in arteries. Magnetic resonance (MR) and computed tomography (CT) has enabled the reconstruction of patient-specific models of detailed anatomic variations (Pennati et al., 2013, Schievano and Taylor, 2020), while 2D phase-contrast MRI is used to extract flow information from a vessel's cross-sectional lumen (Van Doormaal et al., 2012, Steinman and Taylor, 2005). Such techniques are now routinely performed and are used to assess the haemodynamic conditions in both healthy (Capuano et al., 2019) and diseased subjects (Schievano et al., 2011, Johnston et al., 2020, 2021), under normal or exercise conditions (Tang et al., 2011), in order to compare morphological and geometrical features (Ntinjana et al., 2014) to predict surgical outcomes (Schievano et al, 2007, Alharbi et al., 2020) and facilitate the treatment and device design (Randles et al., 2017).

Patients with tetralogy of Fallot have a significant variability in the anatomy of the pulmonary arteries and it is therefore crucial to characterise the effect of geometric

parameters in the haemodynamic environment in these patients. Although the pulmonary bifurcation in healthy subjects is found haemodynamically efficient (Capuano et al., 2019), studies in TOF models have indicated reversal of flow in the left pulmonary artery (LPA) and an influence of the branching angles in pulmonary regurgitation (Zhang et al., 2016, Chern et al., 2008, Chern et al., 2012). Recently, Louvelle et al. (Louvelle et al., 2019) tried to link geometric parameters such as diameter, length, tortuosity and the angle of the branches, in TOF patients repaired with preservative and non-preservative techniques with the haemodynamic characteristics that can influence reversal of flow.

In this computational study, the blood flow environment in patient-specific models of rTOF patients is described. This study is a continuation of the work performed in the idealised models of Chapter 3 in relation to TOF patients, where the impact of morphology and the role of the stagnation point in the wall shear stress distribution were discussed. A correlation was identified between the wall shear stress distribution, the pressure difference in the daughter branches and the flow splits. To further explore the above findings, the patient-specific models are analysed and parameters such as the angle of branches, curvature, tortuosity and planarity are reported. The haemodynamic environment of the geometries is also examined with the aim to better understand the flow development in the pulmonary junction of these patients and potentially correlate specific geometrical features with blood flow patterns. The layout of this Chapter is as follows: First the methodology is presented (Section 5.2.), followed by the results (Section 5.3.). In discussion the main findings of this work are summarised, and comparisons are made with previous studies (Section 5.4.). Finally, this Chapter ends with a brief conclusion (Section 5.5.).

5.2. Methodology

In this section the patients' cohort, the extraction of flow data and the segmentation of the models are introduced. Additionally, the computational model setup is presented, and the method used to compute the parameters for the geometry and flow characterisation is explained.

5.2.1. Patients Population

Retrospective clinical data from seven patients with rTOF were used to study the blood flow in models of the pulmonary bifurcation. Demographic information about each patient is reported in Table 5.1, with an average age of the population being 26.3±15.7, and their grade of regurgitation fraction varying from moderate to severe. Images of the pulmonary trunk of these patients, used for model reconstruction (Figs. 5.1a-b), were acquired between 2012 and 2017 with a Siemens Avanto 1.5-Tesla MRI scanner (Siemens Healthcare, Erlangen, Germany), using the protocol "3D and Phase contrast" (TE= 2.08 or 2.18 ms, TR= 8.01-32.04 ms, FOV= 240-450 x 250-450 mm, Pixel resolution 192-256 x 192-256, Pixel spacing [1.2500;1.2500] – [1.5625;1.5625]). The scans were acquired with both ECG and respiratory gating. The clinical data include part of the clinical assessment of patients in the Great Ormond Street Hospital for Children, London, UK, and the retrospective use of the image data for research was granted by the Institute of Child Health/Great Ormond Street Hospital Research Ethics Committee, and written consent was obtained from all subjects or parents/legal guardians (Ref: 06/Q0508/124).

*Table 5.1: Demographic and haemodynamic data of the rTOF cases. PA: pulmonary artery; RF: regurgitation fraction, Grade refers to the regurgitation fraction, *: the flow split of patient 7 was calculated as described in the methodology (Section 5.2.2).*

Patient	Sex	Age at scan	PA RF (%)	Grade	Flow Split (Q_{RPA}:Q_{LPA})
1	Male	5 years	45	Severe	55.3 : 44.7
2	Male	12 years	41	Severe	64.8 : 35.2
3	Male	19 years	30	Severe	55.5 : 44.4
4	Male	23 years	40	Moderate	63.9 : 36.1
5	Male	30 years	48	Severe	75.4 : 24.6
6	Female	41 years	50	Moderate	76.6 : 23.4
7	Female	54 years	50	Severe	45.7 : 54.3 *

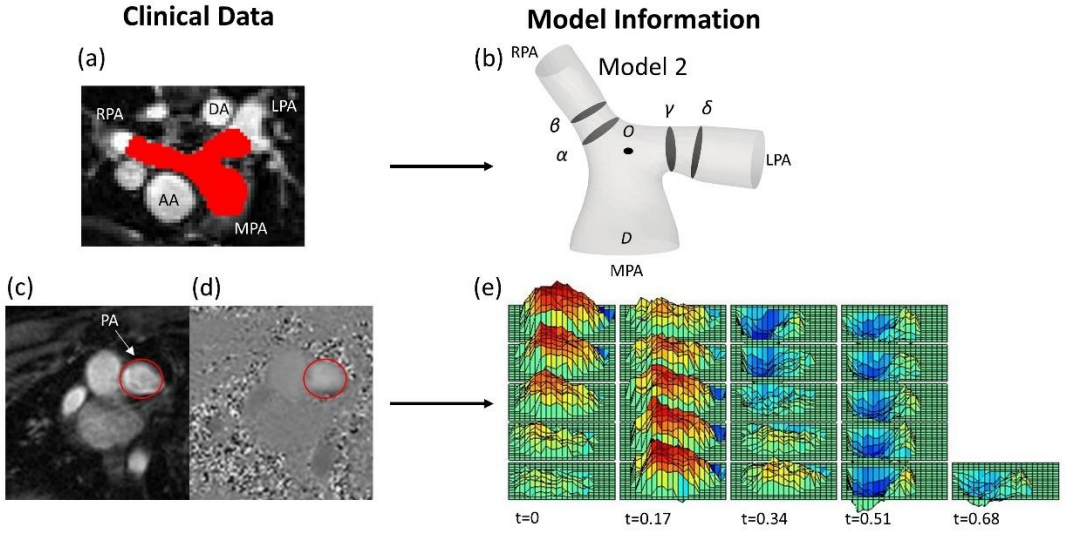

Figure 5.1: (a) MRI image with red colour depicting the pulmonary arteries (PAs), including the main (MPA), left (LPA) and right pulmonary artery (RPA), and showing the descending (DA) and ascending aorta (AA) relevant to the PAs, for reference. (b) One of the reconstructed patient-specific models (Model 2), with slices (α) and (β) over the RPA, and (γ) and (δ) over the LPA shown in the model. (c)-(d) PC-MRI data from the same patient used for the extraction of the velocity profile at the MPA root, with the MPA encircled in red; (c) magnitude and (d) phase contrast (PC-MRI) image. (e) 3D-velocity profile extracted from PC-MRI data displaying the variation of the velocity both in space and time over a cardiac cycle.

5.2.2. Extraction of flow data

To extract the 3D velocity profile at the MPA root from the phase-contrast MRI images (PC-MRI), the software Segment Research (Heiberg et al., 2010) for medical image

analysis was used. Phase contrast and magnitude image stacks, over a cardiac cycle, were loaded as inputs for all geometries (Fig. 5.1c-d). The lumen circumference of each branch (MPA) was marked on each frame of the cardiac cycle, and the diameter and flow rate profiles were exported for each stack of images for post processing. The flow rate extracted at each time point was then divided by the area of the vessel at the specific time in order to consider the diameter changes during the cardiac cycle (van Doormaal et al., 2012). The total inlet flow rate waveforms over the cardiac cycle are presented (Fig. 5.2a) for all seven patients. An average flow rate waveform, Qi, was calculated based on the seven flow waveforms after time was normalised with the period of the cardiac cycle of each patient (Fig. 5.2a). This average flow waveform is also presented in Fig. 5.2b normalised by the mean value of the average flow rate over each cardiac cycle Qm* (Fig. 5.2b). The average flow rates of each patient can be found in Table 5.2. In addition to the time-dependent flow rate waveforms, time and spatially resolved 3D inlet velocity profiles were extracted for every time step of the cycle (Fig. 5.1e).

PC-MRI data were also available from the right and left pulmonary branches, except for patient 7 which lacked this information, and were used to calculate the flow split in each model, based on the net volume (forward minus backward volume, in ml, over the cardiac cycle) retrieved from Segment Research (Table 5.1). For patient 7, we used the information available from the other six patients to calculate the flow split, based on the following formula:

$$\frac{Q_{RPA-7}}{Q_{LPA-7}} = \frac{Q_{RPA-av}}{Q_{LPA-av}} \cdot \left(\frac{R_{RPA-7}}{R_{LPA-7}} \cdot \frac{R_{LPA-av}}{R_{RPA-av}}\right)^2 \quad (5.1)$$

where $\frac{Q_{RPA-av}}{Q_{LPA-av}}$ is the ratio of the average flow rate for the RPA and LPA branches of the six patients, and $\left(\frac{R_{LPA-av}}{R_{RPA-av}}\right)^2$, the ratio of the average radii of the LPA and the RPA squared. The result indicates a flow split Q_{RPA} : Q_{LPA} of 45.7% : 54.3%, which is in accordance with the flow split reported in the clinical record for the specific patient. The average flow split based on the six patients with available patient specific data was found ~65.3% : 34.7% ($Q_{RPA\text{-}av}$: $Q_{LPA\text{-}av}$).

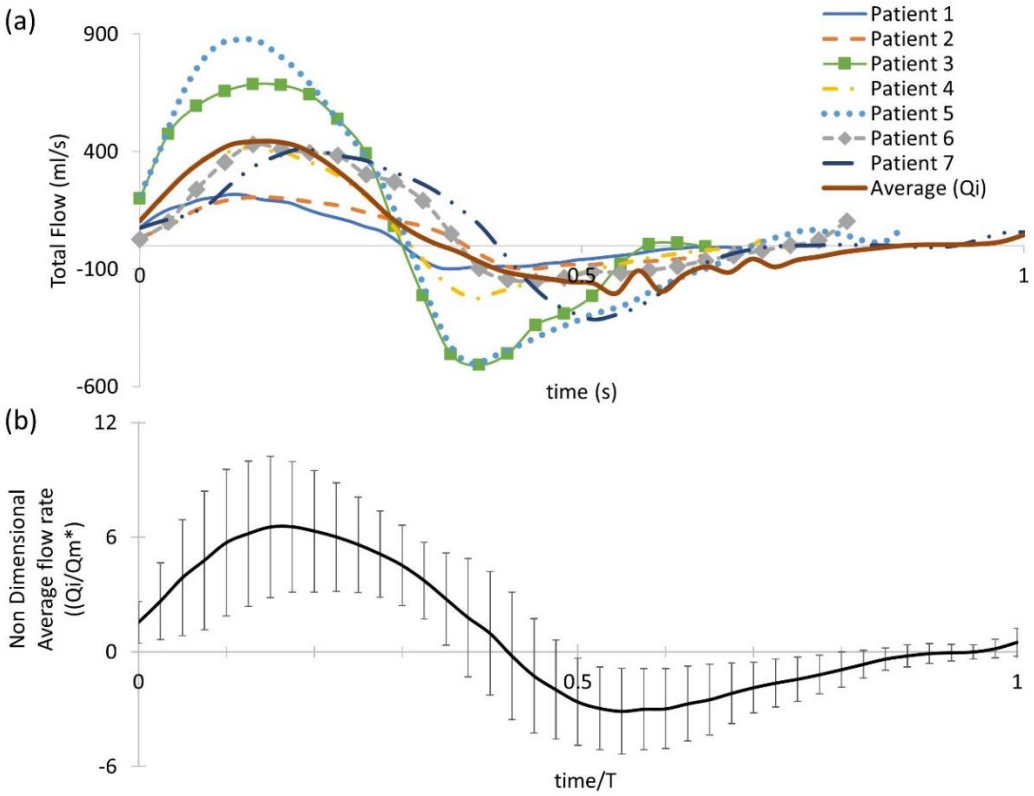

Figure 5.2: (a) Patient-specific pulsatile inlet flow rate waveform for all seven subjects and an averaged flow rate waveform (Qi) derived from the seven patient-specific waveforms. (b) The averaged flow rate waveform derived from the seven patient-specific waveforms and normalised with the mean value of the average flow rate over the cardiac cycle Qm. Time was normalised with the period of the cardiac cycle of each patient. Error bars represent the standard deviation of the patient-specific flow waveforms from the average flow waveform.*

Table 5.2: Diameters, mean flow rate, and mean and max velocities for the MPA, the RPA and the LPA branches of each model.

Model	D_{MPA} (m)	D_{RPA} (m)	D_{LPA} (m)	Q_{mean} (ml/s)	Umean $_{MPA}$(m/s)	Umean $_{RPA}$(m/s)	Umean $_{LPA}$(m/s)	Umax $_{MPA}$(m/s)	Umax $_{RPA}$(m/s)	Umax $_{LPA}$(m/s)
1	0.017	0.010	0.013	33.9	0.086	0.133	0.148	0.696	1.076	0.534
2	0.022	0.013	0.013	47.2	0.086	0.154	0.087	0.699	1.252	0.703
3	0.050	0.016	0.015	114.4	0.131	0.696	0.676	0.346	1.843	1.797
4	0.018	0.009	0.015	69.6	0.148	0.391	0.071	1.210	3.302	1.260
5	0.024	0.017	0.022	103.0	0.048	0.066	0.020	1.043	1.454	0.308
6	0.025	0.019	0.019	85.0	0.158	0.201	0.063	0.685	0.982	0.312
7	0.028	0.017	0.028	54.4	0.069	0.134	0.119	0.508	1.581	0.648
Average	0.025	0.014	0.017	49.0	0.150	0.260	0.092	0.974	1.691	0.599

5.2.3. Reconstruction of patient-specific models

Clinical whole heart MRI images were used to segment the patient-specific three-dimensional structures using the open-source software ITK-SNAP (www.itksnap.org) (Fig. 5.1a) (Yushkevich et al., 2006). Initially, a semi-automatic active contour segmentation tool was used, followed by manual segmentation of the pulmonary trunk in each slice of the datasets to refine the process. The segmentation was extended until the first daughter branch on the right and left pulmonary branches. The geometries were then exported as surface mesh, in the stereolithography (STL) format. Smoothing was necessary to remove artefacts due to the image resolution and segmentation processes, while extensions were added in the model branches to avoid any effects from the boundaries. An extension of 0.5*D* was also added at the MPA inlet, where *D* is the diameter of the MPA inlet for each model. Two cross-sections of the lumen were taken on each branch of the PAs (Fig. 5.1b). Cross sections (α) and (γ) were taken at 0.4*D* and sections (β) and (δ) at 0.6*D* from the bifurcation origin, denoted as O. Point

O is defined as the point where the branch splitting occurs, according to the branch splitting function of the open-source software VMTK (www.vmtk.org).

5.2.4. Geometry characterisation

A geometric analysis of the models was conducted in the open-source software VMTK to identify parameters, including: the curvature of the RPA and LPA branches, torsion, tortuosity, the minimum inscribed sphere radius along the daughter branches, and in-plane and out-of-plane angles.

First, the centrelines *c(s)* of the models were generated, where *(s)* is the curvilinear abscissa (Antiga et al., 2008). Curvature and torsion measure, respectively, the deviation of a curve from a straight line and its divergence from lying on the oscillating plane, computed as (Piccinelli et al., 1987):

$$\kappa(s) = \frac{\|c'(s) \times c''(s)\|}{\|c'(s)\|^3}, \tau(s) = \frac{[c'(s) \times c''(s)] \cdot c'''(s)}{\|c'(s) \times c(s)\|} \quad (5.2)$$

The curvature and torsion were measured in 1/mm and evaluated along the centreline on a curvilinear abscissa, normalised by the distance corresponding to the peak curvature value closer to the bifurcating branches. Therefore, the value of 1.0 in the normalised curvilinear abscissa represents the location of peak curvature for each branch. Error bars were used to signify the deviation of the patient-specific values from the calculated averages.

Tortuosity describes the relative increment in the length of the curve from a straight line and was calculated by $x = L/D - 1$, where L is the length of the centreline and D the Euclidean distance between its endpoints (Antiga et al., 2008). The maximal inscribed sphere radius measures the radius of the vessel locally and by identifying the

minimum radius along the centrelines, stenotic regions can be assessed (Doyle et al., 2018). The in-plane and out-of-plane angles were calculated based on the bifurcation plane, defined by points along the centreline of the model, providing information on the bifurcation angle and planarity, respectively (Fig. 5.3) (Thomas et al., 2005). The in-plane angle is presented with respect to the angle formed between the MPA and each daughter branch and, therefore, takes only positive values. A positive sign of the out-of-plane angle is related to the clockwise rotation of the branch.

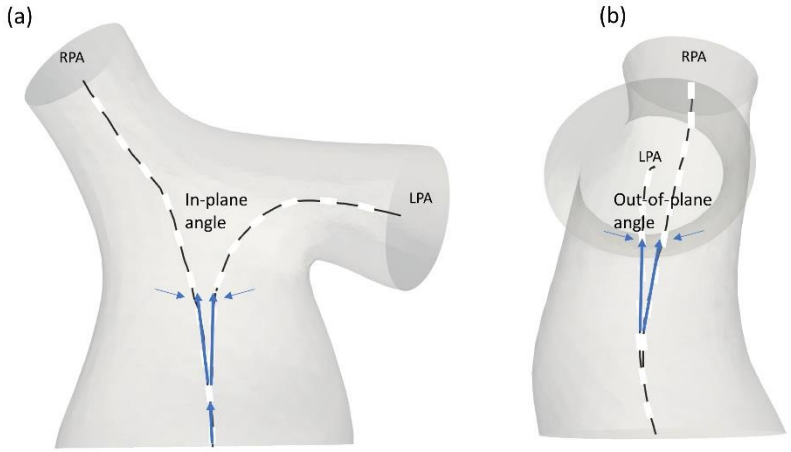

Figure 5.3: Schematic representation of the (a) in-plane and (b) out-of-plane angles.

5.2.5. Anatomical average geometry

An anatomical average geometry was created using the statistical shape analysis software Deformetrica (https://www.deformetrica.org/, Bone et al., 2018) based on a forward approach as described by Bruse et al. (Bruse et al., 2016). Only the adult patients of this study were considered to compute the anatomical average geometry; the models of patients 3 to 7 were registered with the model from the 6th patient, also assumed as the reference model, and using point O (Fig. 5.1b) as the common origin for the alignment. To account for the initial assumption of the reference geometry, the process was repeated six more times, utilising the computed template as the reference

geometry in every following iteration of the process. The anatomical average geometry used for the flow simulations was decided based on the distance between the surfaces of the reference and the calculated template on each repetition, and until the maximum surface distance reached 1 mm, which accounts for approximately 1% of difference (Fig. 5.4a).

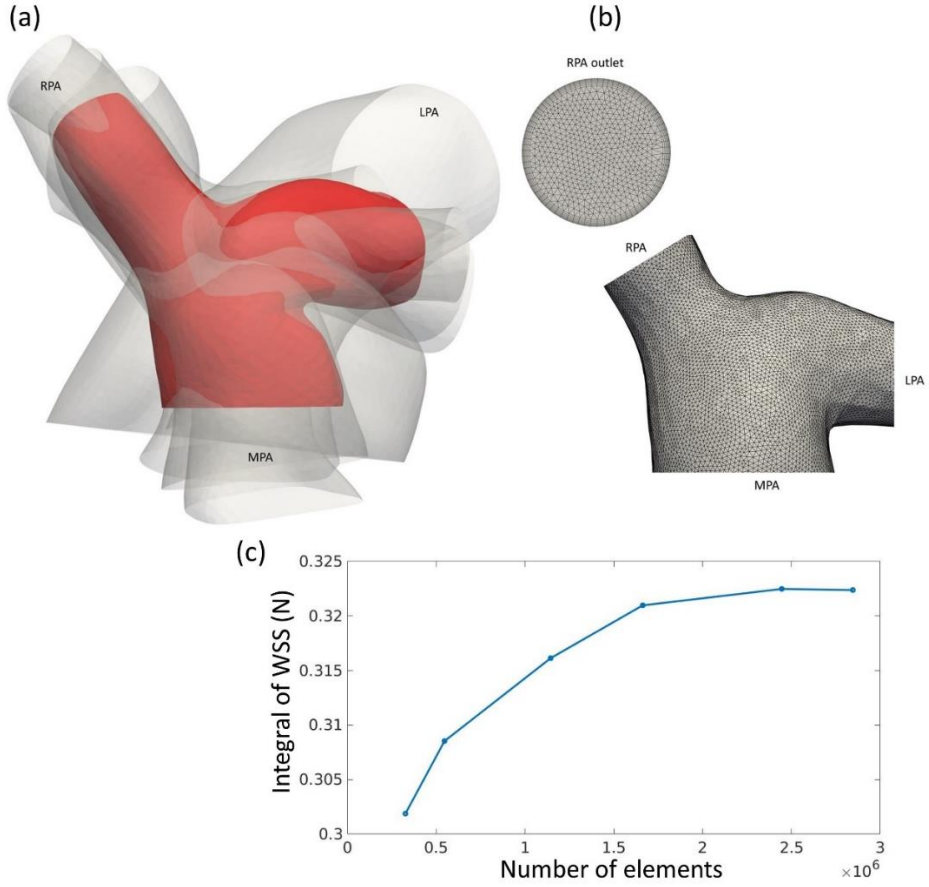

Figure 5.4: (a) Average geometry of the five adult TOF patients (red) with the seven patient-specific models shown transparent. Models are co-registered based on point O of Fig, 5.1b. (b) Computational mesh of the average geometry around the pulmonary junction. The boundary layer at the RPA outlet is also displayed. (c) Mesh independence test based on the integral of WSS.

In addition, in order to better understand how the initial assumption of the reference geometry affects the end result, the process was repeated by assuming the model of the 2nd patient as the reference geometry and the anatomical mean geometry had a maximum surface distance of 4.16 mm in the first iteration of the process (11.3% of

difference). A template kernel width of 15 and a deformation kernel width of 7 were used for the computations; the kernel width controls the length of the deformations allowed and the larger its value, the more global shape variations the atlas captures. Nevertheless, it is found that no fine parameter tuning is needed as the atlas is stable for a large range of values (Durrleman et al., 2014).

5.2.6. Numerical simulations

The methodology followed to set the numerical simulations is described in the next sections, including mesh generation, boundary conditions setup, and computational approximation.

5.2.6.1. Computational mesh

The computational mesh was generated using the commercial software ANSA v20.0 (BETA CAE Systems). The volume mesh consisted primarily of tetrahedra elements and a boundary layer mesh composed of 7 layers of prismatic cells was added, with the first layer at a distance of 0.005 cm away from the wall (Fig. 5.4b). The y+ value was calculated based on the maximum WSS and using Eq. (2.1), (2.2), and its value over a cardiac cycle was smaller than 1. The same computational mesh strategy was adopted for all models. According to a grid independence analysis, where the integral of the wall shear stress on a cross-section of the pulmonary bifurcation was measured, the total number of elements was set around 2.5 million for each geometry (Fig. 5.4c).

5.2.6.2. Mapping of 3D velocity profile

An in-house python code (https://github.com/emisau/3DFlowProfile_MRI2CFD) was used for mapping the spatially-varying velocity profiles of the patients, extracted from

the PC-MRI data, to the inlet of each patient-specific mesh. The code takes two inputs. The first is a comma-separated value (CSV) file exported from the Segment Research software package. It stores spatial coordinates, time in the cardiac cycle and velocity magnitude information for each voxel of a PC-MRI image. The second input file is a triangulation of the inlet surface of the fluid domain holding coordinates and connectivity information for each element of that mesh. The latter file is stored in ascii format (*.msh) exported from the open-source mesh generator Gmsh (Geuzaine and Remacle, 2009). The main idea of the code is to transfer the flow profile information from the voxel grid to the inlet surface triangulation by overlaying them in a common coordinate system. A polar coordinate transformation is applied to both grids. Subsequently, a closest node search algorithm is used to obtain spatial correspondence between the grids. Finally, flow information from the voxel grid is mapped onto the mesh grid, by applying to each node of the mesh grid the mean flow, calculated based on the six nodes from the voxel grid, closest to the correspondent node of the mesh grid. The orientation of the 3D velocity profile was assumed aligned with the inlet of each model and was provisionally checked using anatomical landmarks in the MRI and PC-MRI images. A small addition to the code allowed to output a series of text files containing velocity and coordinates information, one for each time step, that could be directly read by the numerical solver to set the inlet flow condition of the fluid domain.

5.2.6.3. Computational model

Flow simulations, assuming a uniform velocity profile at the inlet of the models and zero-pressure at the outlets, were carried out in the open-source CFD software

OpenFOAM® v.1812 (https://www.openfoam.com/) and the Reynolds Averaged Navier-Stokes equations for turbulent flows were used (Eqs. (4.1), (4.2)). To capture any turbulence effects, the k-ω shear stress transport (SST) turbulence model was assumed, with the model specifications as described in Chapter 4.

Two sets of simulations were performed. In the first set, the uniform pulsatile (time- but not space dependent) average flow waveform (Fig. 5.2a) was specified at the inlet of all seven models, including the anatomical average geometry, and the average flow split of ~65.3% : 34.7% (Q_{RPA}:Q_{LPA}) was applied at the branch outlets. The assumption of the same BCs on all geometries allows the identification of differences in the flow patterns due to geometrical variations. In the second set of simulations, the patient-specific boundary conditions were used with the corresponding patient model. 3D velocity profiles (time- and space- dependent, Fig. 5.1e) were assigned at all geometry inlets. At the outlets of the models, the flow splits presented in Table 5.1 were specified. In the LPA and RPA outlets, the flow splits in both sets of simulations were imposed by specifying the transient flow rate in each branch, and velocity was uniform and only time varying. The walls of all geometries were assumed rigid, and the no-slip boundary condition was assigned. All numerical simulations were performed with the pisoFoam solver, of the OpenFOAM® open-source library, for transient incompressible, turbulent flow, using the pressure-implicit with splitting operators (PISO) algorithm and the second order bounded Gauss linear upwind divergence scheme, the backward differential scheme for the time discretization and the Gauss linear gradient numerical scheme were utilised. PISO was chosen over PIMPLE to reduce computational cost as the time step was small and met the Courant-Friedrichs-Lewy (CFL) condition. The results are obtained between the 4th and 7th cycle, based

on a time-averaged wall shear stress (TAWSS) test performed. More specifically, the integral of the TAWSS at the pulmonary junction was calculated at each cycle, for each model separately, and when a plateau was reached in the TAWSS plots the solution was considered converged. Eq. (3.6) was used to calculate the TAWSS. The TAWSS distribution is normalised by the value at the inlet of each model (denoted as $TAWSS_n$), and the values used for the non-dimensionalisation are reported on Table 5.3.

Table 5.3: TAWSS value at the inlet of the models when average and patient-specific boundary conditions (BCs) are assigned.

Model	TAWSS (dynes/cm^2)	
	Average BCs	Patient-specific BCs
1	42	20
2	20	16
3	10	6
4	14	13
5	12	10
6	2	7
7	16	2
Average geometry	9	-

In all computational simulations, blood was considered as a Newtonian, incompressible fluid. The decision was based on the results of Chapter 4.3.1. where the WSS, when plotted in dynes/cm^2 along the inner wall of the pulmonary bifurcation, did not show significant variations between the Newtonian and three of the non-Newtonian models tested. Blood density and viscosity were set to 1060 kg/m^3 and 4 $\times 10^{-3}$ Pa s, respectively. The mean Reynolds (*Re*), Womersley (*Wo*) and Dean (*De*) numbers for all geometries were calculated based on Eq. (1.14), (1.22) and (1.23), respectively. Re_{max} was calculated using the local velocity of each branch, while to calculate the Dean number in the RPA and LPA branches, Re_{max}, as calculated for the MPA branch, was multiplied by the percentage of flow split in Eq. (5.5), as suggested

by another study in the literature (Capuano et al., 2019). To calculate the *Re* at the inlet and the outlets of the models, the diameter at each boundary was considered. A table with the diameters, the mean flow rate, the mean and the max velocity of all three branches for each model is provided (Table 5.2).

The oscillatory shear index (OSI) was also calculated, using the following formula:

$$OSI = \frac{1}{2}\left(1 - \frac{\left|\frac{1}{T}\int_0^T t_S dt\right|}{\frac{1}{T}\int_0^T |t_S| dt}\right) \tag{5.6}$$

where t_s the tangential component of the traction vector. The OSI represents the level of disturbed flow and takes values from 0 (indicating unidirectional shear stress through the cardiac cycle) to 0.5 (corresponds to an average shear stress value of zero during the cardiac cycle) (Tang et al., 2010).

5.2.7. Study sensitivity

In an attempt to confirm the methodology followed in this study, the effect of various parameters was investigated. Firstly, different smoothing factors were considered in model 1 at the reconstruction stage of the process (Section 5.2.3), and the wall shear stress distribution in the models were compared. The comparison indicated that doubling the smoothing factor in the model, did not alter the development of flow and therefore, the higher smoothing factor was adapted in this study for all models. In addition, the point from which the left and the right pulmonary arterial branches were extended was altered in model 4 and a difference of 5.4% was found on the integral of the wall shear stress values developed around the pulmonary junction. Moreover, a comparison between the 3D velocity profile and a pulsatile waveform with a plug profile, was conducted in model 1, and higher shear stress areas were apparent when

the 3D velocity profile was assigned at the inlet of the models. The difference was evaluated for slices (α) and (γ) of Fig. 5.1b, and was about 10% for the RPA, and approximately 19% for the LPA branch. Finally, the flow obtained from the outlets of the models, when the flow split was specified, was compared with the respective clinical flow waveforms. A simulation was performed where the numerical solution was saved at each time step during the cardiac cycle. The total flow, as exported from the RPA and LPA branches of the model is sub-plotted with the clinical total flow waveforms and is presented in Fig. 5.5. The computational results match the clinical data considering that 1) the clinical data for each of the MPA, RPA and LPA branches are acquired during different cardiac cycles, and therefore a difference is expected, and 2) the flow splits are calculated based on the net volume and not the total flow.

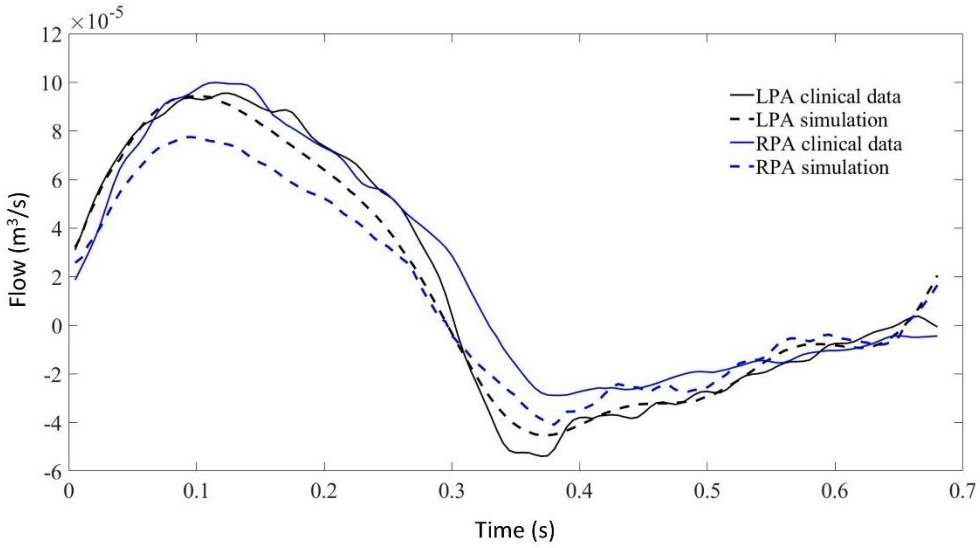

Figure 5.5: Comparison of clinical flow waveforms of the right and left pulmonary branches with those calculated at the outlets of the model when the flow split was specified.

5.3. Results

In the following paragraphs the effect of the morphology and flow characteristics are presented in a series of figures and tables. The three main sections in which the results

are separated are the geometry characterisation (Table 5.4, 5.5 and Fig. 5.6), the flow characterisation (Table 5.6) and the computational analysis, which is further divided on the averaged boundary conditions (Figs. 5.7, 5.8) and patient-specific boundary conditions (Figs. 5.9-5.15).

5.3.1. Geometry characterisation

The morphological features described on Section 5.2.3 of the methodology are listed in Tables 5.3, 5.4. In the majority of the models, the curvature of the LPA branch was higher compared to the RPA (Table 5.4, Fig. 5.6a, 5.6b), with the highest mean curvature of 0.044 mm^{-1} in the LPA of the average model. The results indicate higher torsion in the RPA branch of the models, with the maximum mean value of 0.183 mm^{-1} observed in the LPA of the average model. The mean torsion was found very close to zero for both daughter branches (Table 5.4). Tortuosity was higher in the LPA branch of all models, and the largest value of 0.258 was observed in the LPA of patient 5 (Table 5.5). The minimum sphere radius was smaller on average in the RPA branch (Table 5.5). Curvature in the LPA branch increased on average along the centrelines of all patients (Fig. 5.6b) until it reached a peak approximately at the entrance of the daughter branches, before decreasing. Two peaks were observed in the average torsion plots (Fig. 5.6c) for both the RPA and the LPA further downstream along the daughter branches. For the RPA, the peaks were positive, indicating a counter-clockwise rotation of the branch, whilst they were negative for the LPA, signifying the clockwise shift of the branch. Nevertheless, a mean torsion close to zero is observed along the centrelines of both branches, also indicated on Table 5.4.

Table 5.4: Geometric analysis of the patient-specific models: curvature and torsion.

Model	Curvature RPA (mm^{-1}) (mean / max)	Curvature LPA (mm^{-1}) (mean / max)	Torsion RPA (mm^{-1}) (min / mean / max)	Torsion LPA (mm^{-1}) (min / mean / max)
1	0.021 / 0.066	0.036 / 0.103	-0.430 / 0.135 / 1.798	-0.074/ 0.024 / 0.182
2	0.015 / 0.036	0.029 / 0.110	-0.500 / -0.055 / 0.183	-0.864 / -0.138 / 0.005
3	0.014 / 0.087	0.012 / 0.068	-0.400 / -0.004 / 0.841	-0.971 / 0.026 / 0.742
4	0.018 / 0.035	0.036 / 0.105	-1.017 / -0.030 / 0.367	-0.046 / 0.059 / 0.837
5	0.014 / 0.053	0.032 / 0.131	-1.338 / -0.032 / 0.709	-2.083 / -0.061 / 0.606
6	0.016 / 0.034	0.042 / 0.094	-0.008 / 0.128 / 0.495	-0.888 / -0.004 / 0.294
7	0.019 / 0.046	0.015 / 0.058	-0.329 / 0.004 / 0.709	-0.343 / 0.009 / 0.930
Average	0.022 / 0.040	0.044 / 0.189	-0.220 / 0.162 / 0.825	-0.144 / 0.183 / 0.990
Mean value	0.017 / 0.050	0.031 / 0.107	-0.530 / 0.039 / 0.741	-0.677 / 0.013 / 0.573

Table 5.5: Geometric analysis of the patient-specific models: tortuosity, minimum inscribed sphere radius along the daughter branches, and in-plane and out-of-plane angles.

Model	Tortuosity (RPA/LPA)	Min Sphere Radius (mm) (RPA/LPA)	In-Plane angles (RPA/LPA)	Out-of-Plane Angles (RPA/LPA)
1	0.017 / 0.115	4.8 / 5.8	132.1° / 118.7°	1.3° / 27°
2	0.017 / 0.132	4.5 / 4.8	142.6° / 119.9°	9.4° / -21.4°
3	0.044 / 0.091	5.7 / 4.8	163.8° / 168.2°	7.1° / -3.8°
4	0.013 / 0.121	3.5 / 4.1	142.2° / 110.1°	-15.4° / 11.2°
5	0.011 / 0.258	7.0 / 6.5	135.9° / 118.6°	-35.1° / 58.9°
6	0.003 / 0.182	6.3 / 5.3	160.3° / 126.7°	-26.1° / 31.5°
7	0.103 / 0.111	6.7 / 10.8	124.4° / 160.1°	-12.5° / 16.9°
Average	0.011 / 0.176	7.1 / 7.0	147.2° / 117.0°	-32° / 11.4°
Mean value	0.027 / 0.148	5.7 / 6.1	143.6° / 129.9°	-12.9° / 16.5°

The in-plane bifurcating angle of the RPA (Table 5.5) was in most cases bigger compared to the LPA, indicating a more acute angle between the MPA and the LPA. Exception to this were patients 3 and 7, where in 3 the two branches had very similar bifurcating angles. The average in-plane angles for the RPA and LPA branches were,

respectively, 143.6° and 129.9°. The out-of-plane angles suggest that the LPA deviated more from the bifurcation plane. In the majority of models, the rotation of the LPA was clockwise, while in four out of seven patients and in the average model, the rotation was anti-clockwise for the RPA branch. The mean value of the out-of-plane angles as calculated for the RPA and LPA branches were -12.9° and 16.5°, respectively (Table 5.5).

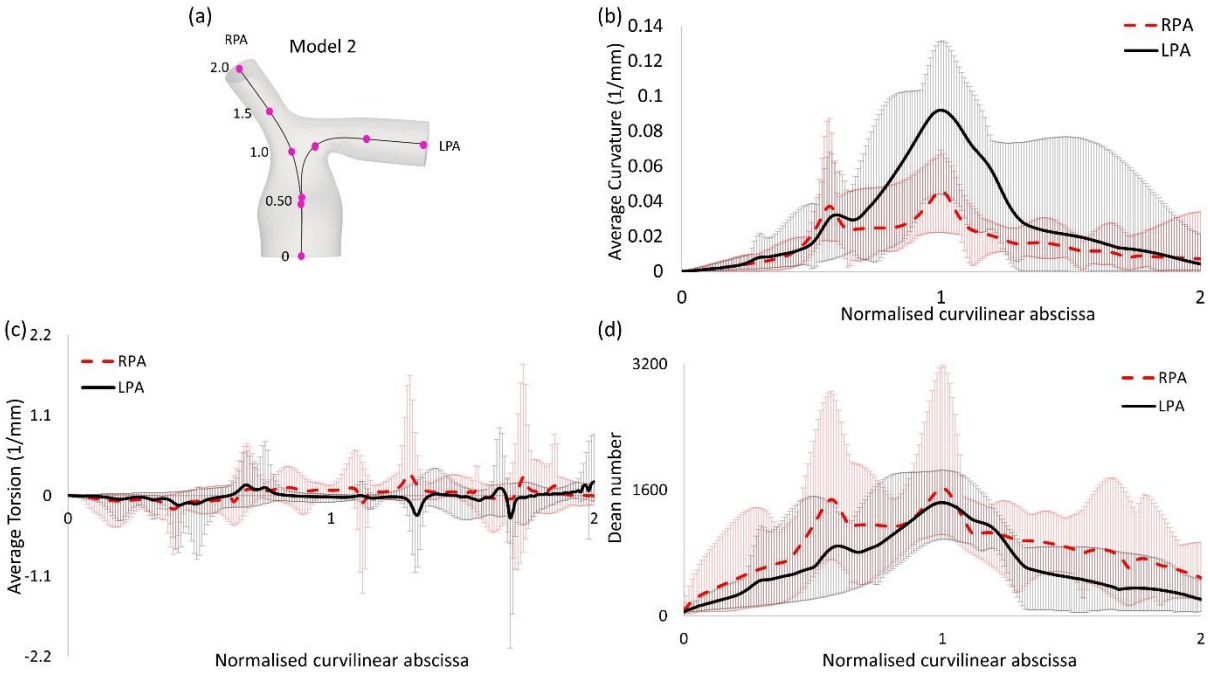

Figure 5.6: (a) Centerlines along the LPA and RPA of model 2, with points indicating the curvilinear abscissa, normalised by the distance corresponding to the peak curvature value closer to the bifurcating branches. Therefore, the value of 1.0 represents the location of peak curvature for each branch. (b) Average curvature plot. (c) Average torsion plot, and (d) Average Dean number plot, with x-axis indicating distance from point O. Shaded areas represent the standard deviation of the patient-specific values from the average calculated.

5.3.2. Flow characteristics

Following Eqs. (1.14), (1.22) and (1.23), the Reynolds (mean and maximum), Womersley and Dean numbers were calculated for all models and are reported in Table 5.6. The mean *Re* varied during the cardiac cycle of the seven cases and the average model between 297 to 1722 and, therefore, different flow patterns were expected

during the cardiac cycle. The average calculated Re_{mean} values were 768 for the MPA, 983 for the RPA and 687 for the LPA, therefore, the highest *Re* was observed in the RPA branch. *Wo* was in the range of 13.6 – 40.3, as calculated at the inlet of the models for the seven cases examined, indicating a large frequency of pulsations (Nichols and O'Rourke, 2005), and with the highest value found in model 3. Finally, the average Dean number calculated for the RPA (De_{max_RPA} = 1779) was higher compared to the LPA (De_{max_LPA} = 1643). The Dean plots for the two branches (Fig. 5.6d), indicate a similar increase as with the curvature plots, with the maximum Dean number located approximately at the entrance of the daughter branches.

Table 5.6: Mean and maximum Reynolds (Re), Womersley (Wo) and Dean number (De).

Model	Re_{mean_MPA} (Re_{max_MPA})	Re_{mean_RPA} (Re_{max_RPA})	Re_{mean_LPA} (Re_{max_LPA})	Wo	De_{max_RPA}	De_{max_LPA}
1	397 (3199)	367 (2958)	520 (1873)	13.6	1034	1178
2	504 (4093)	542 (4408)	300 (2434)	17.3	1302	1215
3	1722 (4561)	2962 (7846)	2615 (6925)	40.3	2115	1450
4	696 (5694)	905 (7638)	290 (5127)	13.6	1412	1844
5	297 (6529)	305 (6695)	116 (1760)	16.3	3180	1851
6	1023 (4450)	1011 (4936)	315 (1537)	17.7	1934	972
7	521 (3823)	718 (6918)	886 (4807)	18.3	1085	1854
Average	985 (6414)	1052 (6832)	454 (2950)	18.4	2172	2778
Mean value	768 (4845)	983 (6029)	687 (3427)	19.4	1779	1643

5.3.3. Computational analysis

In the following paragraphs, a top-down analysis is followed by examining first the use of averaged boundary conditions on the anatomically average and personalised geometries (effect of geometry, section 5.3.3.1) and then, the application of patient-

specific boundary conditions on individualised geometries (patient-specific effects, section 5.3.3.2.).

5.3.3.1. Averaged boundary conditions

Initially, the average flow waveform of Fig. 5.2a and the average flow split (Section 5.2.2) were used as the boundary conditions in the patient-specific models and the anatomical average geometry in order to better understand the effect of geometry in the flow development in the pulmonary arteries (Figs. 5.7, 5.8). Although the anatomical average geometry was derived from a small number of TOF patients and cannot be considered representative of the population, its purpose is to help clarify the importance of patient-specificity in the models.

Fig. 5.7 displays the secondary flow in cross sections (α) and (γ) along the RPA and LPA, as defined in Fig. 5.1b, in models 2, 3 and the average geometry, using averaged BCs, at three different time points: (i) peak systole, (ii) mid deceleration at systole and (iii) mid diastole. Models 2 and 3 were chosen because the patients are of similar age and with a severe grade of regurgitation fraction, but have different flow characteristics (Table 5.6), which could facilitate the comparison between observed differences. The description of the flow patterns is based on Perry and Steiner's (Perry and Steiner, 2006). Looking at the orientation of the streamlines, the terms stable and unstable refer to the vectors of flow pointing towards the inner and outer of a node, focus or line, respectively, while a saddle point is a location where four streamlines form a rhombus of a stationary region.

During peak flow, a stable node was noticed in the RPA of all models (Fig. 5.7a.i (α), 5.7b.i (α), 5.7c.i (α)). In addition, two pairs of counter rotating vortices were observed

in the LPA of model 2 (Fig. 5.7a.i (γ)). The pair positioned cranial and posteriorly, consisted of a stable and an unstable focus, while the other pair was positioned caudally in the LPA slice, and consisted of two unstable foci. In model 3, an unstable bifurcation line was visible in the LPA (Fig. 5.7b.i (γ)), while for the average model a a stable bifurcation line positioned cranially, and an unstable focus positioned caudally were developed (Fig. 5.7c.i (γ)).

During mid deceleration at systole, the stable bifurcation line in the RPA of model 2 developed in a stable focus (Fig. 5.7a.ii (α)), while in the average model two counter rotation vortices were additionally developed posteriorly (Fig. 5.7c.ii (α)). In the LPA of model 2, only three vortices remained; a stable focus positioned cranially, and two unstable foci positioned caudal anteriorly and posteriorly, respectively (Fig. 5.7a.ii (γ)). A saddle was visible cranially and anteriorly in the LPA of model 3, with an unstable focus further caudally and posteriorly and a stable focus caudally (Fig. 5.7b.ii (γ)). For the average model, 2 vortices, positioned cranially and caudally were developed, while a saddle was also visible cranially during mid diastole (Fig. 5.7c.ii (γ)).

At mid diastole, two unstable foci appeared cranially in the RPA of model 2, and one located more centrally (Fig. 5.7a.iii (α)). For the LPA, an unstable bifurcating line, and an unstable focus were visible cranially and caudally, respectively (Fig. 5.7a.iii (γ)). In model 3, an unstable bifurcating line was visible in the RPA cross-section (Fig. 5.7b.iii (α)), while a pair of counter-rotating vortices, consisting of two stable foci, positioned caudally in the LPA cross-section (Fig. 5.7b.iii (γ)). For the average model, an unstable bifurcating line appeared posteriorly in the RPA (Fig. 5.7c.iii (α)), while

in the LPA a stable bifurcating line and an unstable focus were formed caudally and cranially, respectively (Fig. 5.7c.iii (γ)).

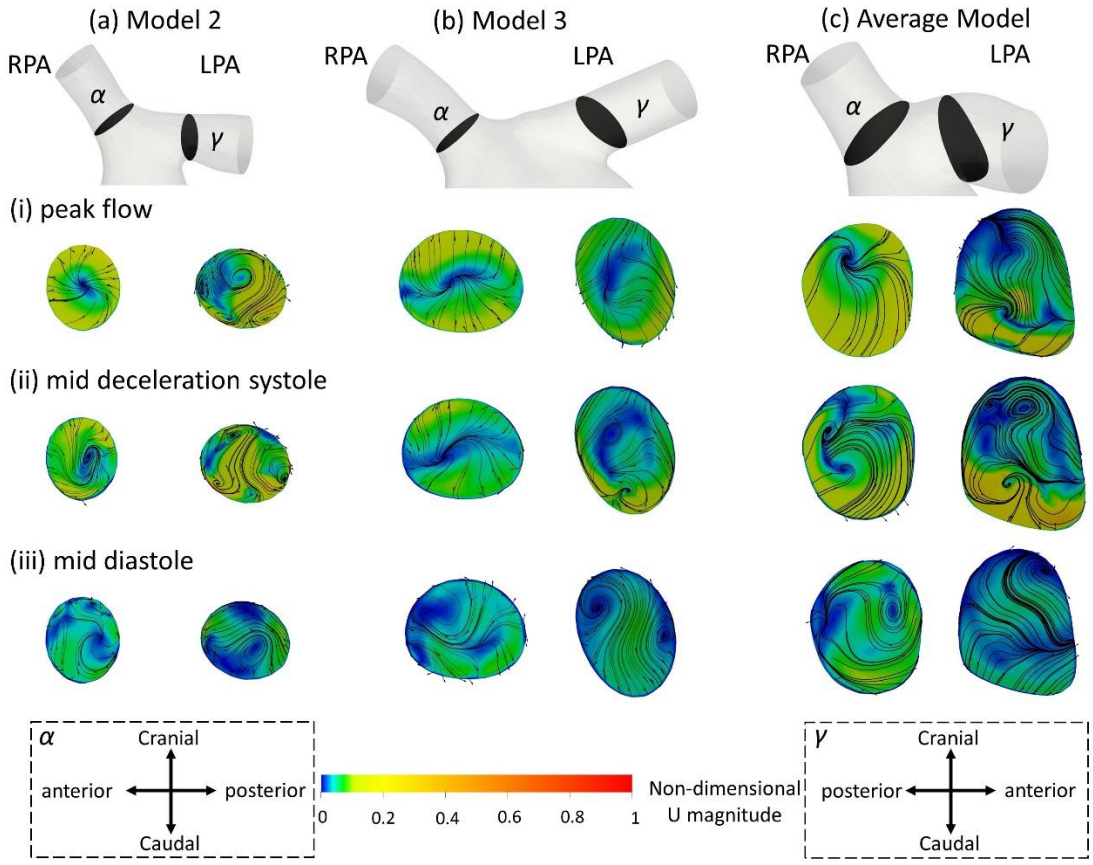

Figure 5.7: Secondary flow visualised by in plane velocity vectors and contours of normalised velocity normal to the slice during (i) peak flow; (ii) mid deceleration at systole; and (iii) mid diastole, for (a) model 2; (b) model 3; and (c) the average model. Non-dimensionalisation was performed by division with the maximum velocity of each patient during the cardiac cycle. Points where slices α and γ are taken are visible in Fig. 5.1b. Cross-sections are oriented with the top and the bottom edges corresponding to the cranial and caudal positions, respectively and left and right to the anterior and posterior of the pulmonary artery, for the RPA, and to the posterior and anterior of the pulmonary artery, for the LPA, respectively. Cross-sections are in scale.

TAWSS distribution, normalised by the value at the inlet of each model (denoted as TAWSSn), is presented in Fig. 5.8, for all models. In general, higher wall shear stresses were observed at the entrance of the LPA and the RPA branches, while lower TAWSSn values were visible further downstream at the LPA branch. In model 4 (Fig. 5.8d), high TAWSSn was also developed along the MPA branch. A small region of low TAWSSn was found at the bifurcating wall in all models, indicating the stagnation point, where flow impinged before splitting and entering the daughter branches. Model

3 (Fig. 5.8c) had an extensive area of low shear stress values in the enlarged MPA, while the lowest non-dimensionalised TAWSS values were found in model 7 (Fig. 5.8g). The average model (Fig. 5.8h) captured some main characteristics of the TAWSS patterns of models 1, 2, 3 and 6 (Figs. 5.8a-c, 5.8f), particularly the localisation of high TAWSSn regions at the entrance of the branches and lower values near the flow divider.

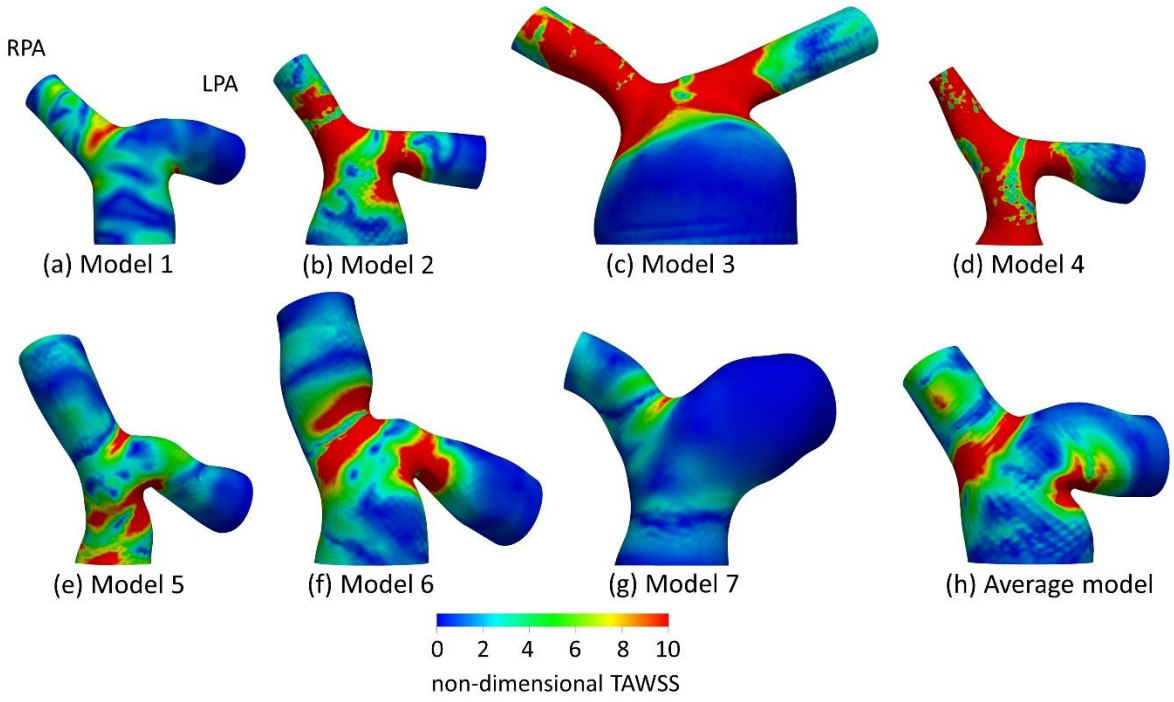

Figure 5.8: Non-dimensionalised time-averaged wall shear stress (TAWSSn) distribution, normalised with the corresponding value at the inlet of each model for (a) model 1; (b) model 2; (c) model 3; (d) model 4; (e) model 5; (f) model 6; (g) model 7; (h) the average model. Averaged boundary conditions are used at the inlet and the outlets of all models.

5.3.3.2. Patient-specific boundary conditions

In the following subsections, computational results from matching patient-specific boundary conditions with their respective geometry are presented, analysing velocity streamlines, secondary flow and the time-averaged wall shear stress distribution.

5.3.3.2.1. Contours of velocity and velocity streamlines

Velocity streamlines coloured by non-dimensionalised velocity at three time points, peak flow (Fig. 5.9.i), mid deceleration during systole (Fig. 5.9.ii), and mid diastole (Fig. 5.9.iii), are examined. The patient-specific waveforms are also provided to indicate these time points. At peak systole, high velocities were developed at the entrance of the RPA and in the LPA opening, close to the MPA wall, in all models (Figs. 5.9a.i – 5.9g.i). In models 5 and 7 (Figs. 5.9e.i, 5.9g.i), and to a smaller extend in model 4 (Fig. 5.9d.i), high velocities were also visible along the MPA. A small recirculation zone was developed at the entrance of the LPA branches proximal to the MPA wall (Figs. 5.9b.i – 5.9f.i), except in models 1 and 7 (Figs. 5.9a.i, 5.9g.i).

During deceleration (Fig. 5.9.ii), the recirculation zone at the entrance of the LPA of all models was enlarged and flow recirculation was also visible in the LPA of geometries 1 and 7 (Figs. 5.9a.ii, 5.9g.ii). In models 3, 5 and 6 (Figs. 5.9c.ii, 5.9e.ii, 5.9f.ii), flow separation occurred additionally within the MPA, while in the MPA of model 1 (Fig 5.9a.ii), a small area of reversed flow was observed. Along the RPA, complex flow was mostly observed for models 6 and 7 (Fig. 5.9f.ii, 5.9g.ii).

Finally, during mid diastole (Fig. 5.9.iii), complex flow patterns appeared in the pulmonary junction of the models. Highly disturbed flow was visible in models 2, 5, 6 and 7 (Figs. 5.9b.iii, 5.9e.iii – 5.9g.iii). In model 3 (Fig. 5.9c.iii), reverse flow was observed in the MPA and flow recirculation zones appeared in both the RPA and LPA. Only model 1 (Fig. 5.9a.iii) did not exhibit recirculation along the RPA and LPA branches.

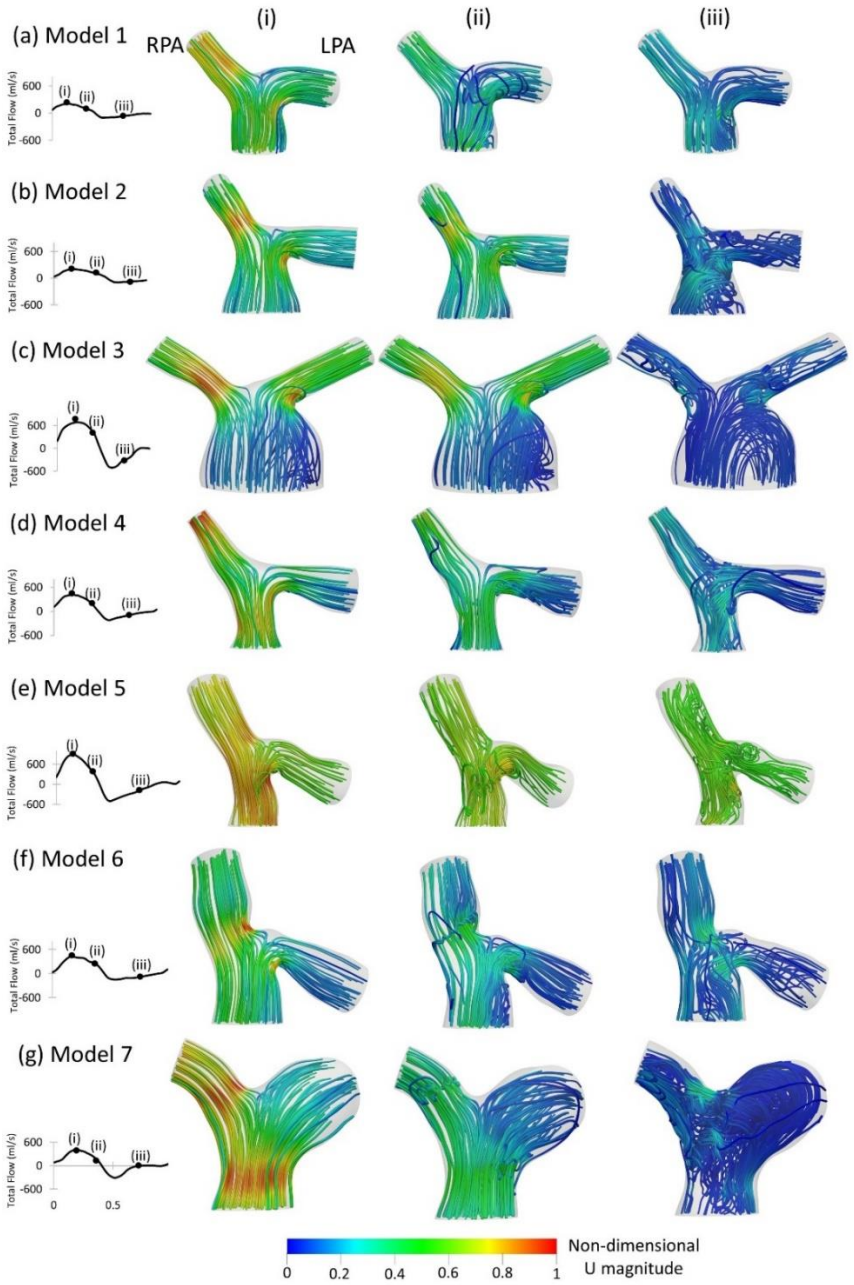

Figure 5.9: Left to Right: Patient-specific flow waveforms and velocity streamlines at (i) peak flow; (ii) mid deceleration at systole; and (iii) mid diastole for (a) model 1; (b) model 2; (c) model 3; (d) model 4; (e) model 5; (f) model 6; (g) model 7. Streamlines are coloured by non-dimensionalised velocity magnitude based on the maximum velocity during the cardiac cycle of each patient. The RPA and the LPA branches are indicated in model 1.

5.3.3.2.2. Secondary flow

To investigate the secondary flow developed during the cardiac cycle, contours of velocity normal to the cross sections of the models are presented in Fig. 5.10-5.12,

overlaid by the in-plane velocity vectors at (i) peak systole (Fig. 5.10), (ii) mid deceleration of systole (Fig. 5.11) and (iii) mid diastole (Fig. 5.12). Velocity values are presented non-dimensionalised with the corresponding maximum velocity developed in each model during the cycle.

During peak flow, no vortices were present in the RPA branch of any of the models (Fig. 5.10). A stable bifurcation line was formed, which developed into a saddle point on model 7 (Fig. 5.10g (β)), and into an unstable focus (Fig. 5.10b (β)) with reversed flow (Fig. 5.10b (β), 5.10c (β)) in models 2 and 3. In addition, two counter rotating vortices, were visible in the LPA of model 2 (Fig. 5.10b (γ)), which then disappeared further downstream, and an unstable bifurcation line was instead visible (Fig. 5.10b (δ)). In model 3, a stable focus was formed posteriorly (Fig. 5.10c (γ)), which remained further downstream (Fig. 5.10c (δ)), while a saddle point was also developed cranially (Fig. 5.10c (δ)). In models 4 and 6, a pair of counter-rotating vortices was visible, located posteriorly and caudally, respectively. Both pairs consisted of a stable and an unstable focus (Figs. 5.10d (γ), 5.10f (γ)). The vortices in model 4, moved anteriorly further downstream (Fig. 5.10d (δ)). A small vortex was visible cranially in model 1 (Fig. 5.10a (γ)), and two vortices, cranially and anteriorly, and a bifurcation line were noticed in model 5 (Fig. 5.10e (γ)). The vortices developed on the models were not symmetric; the asymmetry of the vortices is expected due to the higher curvature and the velocity profile of the flow entering the bifurcation. For the remaining of the models, stable bifurcation lines were observed (Figs. 5.10 (γ)-(δ)).

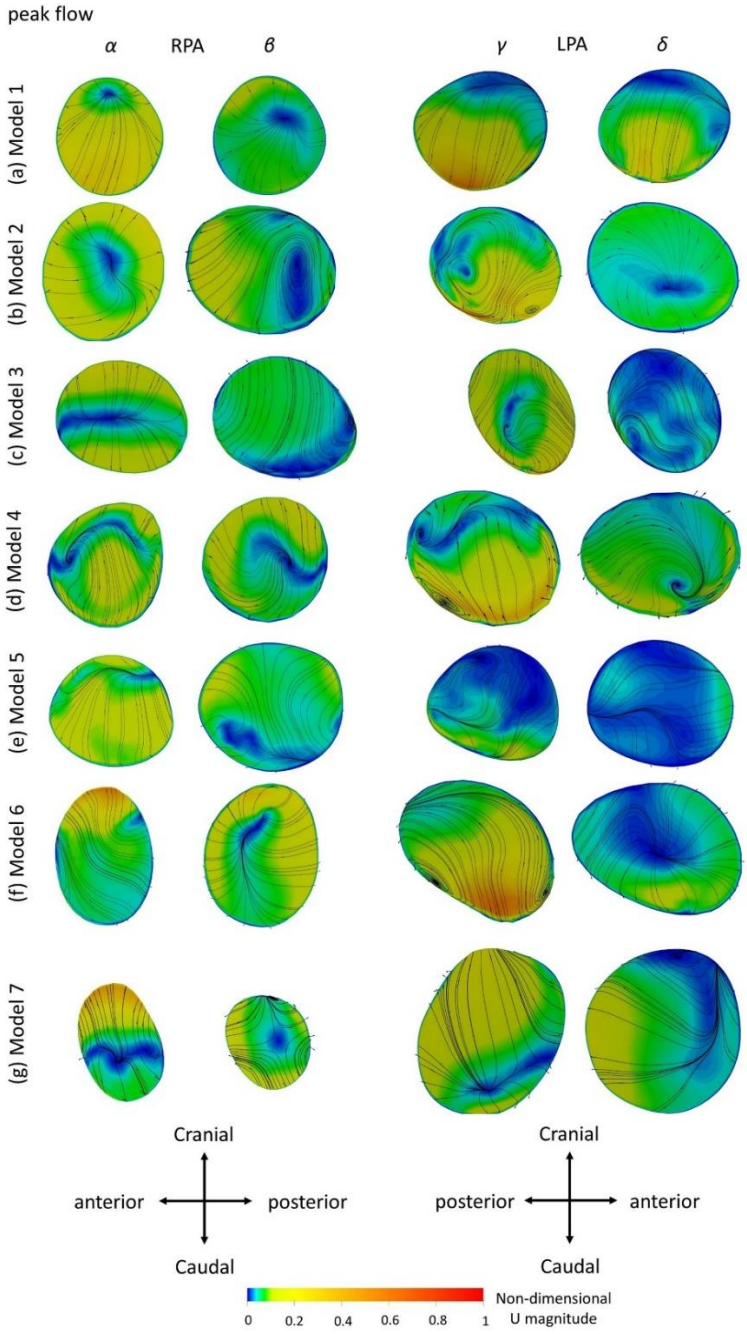

Figure 5.10: Secondary flow visualised by in plane velocity vectors and contours of normalised velocity normal to the slice during peak flow for (a) model 1; (b) model 2; (c) model 3; (d) model 4; (e) model 5; (f) model 6; (g) model 7. Non-dimensionalization was performed by division with the maximum velocity of each patient during the cardiac cycle. Points where slices α to δ are taken are visible in Fig. 5.1b. Cross-sections are oriented with the top and the bottom edges corresponding to the cranial and caudal positions, respectively and left and right to the anterior and posterior of the pulmonary artery, for the RPA, and to the posterior and anterior of the pulmonary artery, for the LPA, respectively. Cross-sections are in scale.

During mid deceleration at systole, vortices were apparent in the majority of the models, in both the RPA and LPA branches. A stable bifurcation line in model 1 (Fig. 5.11a (α)), developed into a stable focus (Fig. 5.11a (β)), while in model 4 the stable

focus was formed in (α) and moved posteriorly in (β) (Fig. 5.11d), as is in model 5 (Fig. 5.11e). In both models 2 and 3 a stable focus was visible, located centrally in model 2 (Fig. 5.10b (α)), which then moved posteriorly (Fig. 5.11b (β)), and posteriorly in model 3 (Fig. 5.11c (α)), moving cranially (Fig. 5.11c (β)). A stable bifurcation line also existed cranially in the RPA of model 3 (Fig. 5.11c (α)). In model 7 a saddle point and a stable focus were observed (Fig. 5.11g). Models 6 was the only model with two counter rotating vortices formed on the RPA branch (Fig. 5.11f (β)). More complex flow patterns were visible in the LPA branches of the models. An unstable focus positioned caudally and anteriorly in model 1 (Fig. 5.11a (γ)) developed in two counter rotating vortices (Fig. 5.11a (δ)). In model 2, two unstable foci located posteriorly, a stable focus and a saddle point located anteriorly, were formed (Fig. 5.11b (γ)), which further downstream fused into one stable focus moving cranially (Fig. 5.11b (δ)). In the LPA of model 3, two relatively symmetric vortices were visible (Fig. 5.11c (γ)), which moved cranially downstream (Fig. 5.11c (δ)), with an additional vortex formed in the caudal position. Model 4 had two unstable foci caudally, and another vortex consisting of a stable focus cranially (Fig. 5.11d (γ)), which they remained in (δ). Model 5 had a single vortex and a stable bifurcation line (Fig. 5.11e (γ)), while model 6 had two counter-rotating vortices caudally (Fig. 5.11f (γ)) that were fused into one further downstream; a stable bifurcating line also was visible (Fig. 5.11f (δ)). Model 7 had two relatively small counter-rotating vortices cranially and a stable bifurcation line caudally (Fig. 5.11g (γ)).

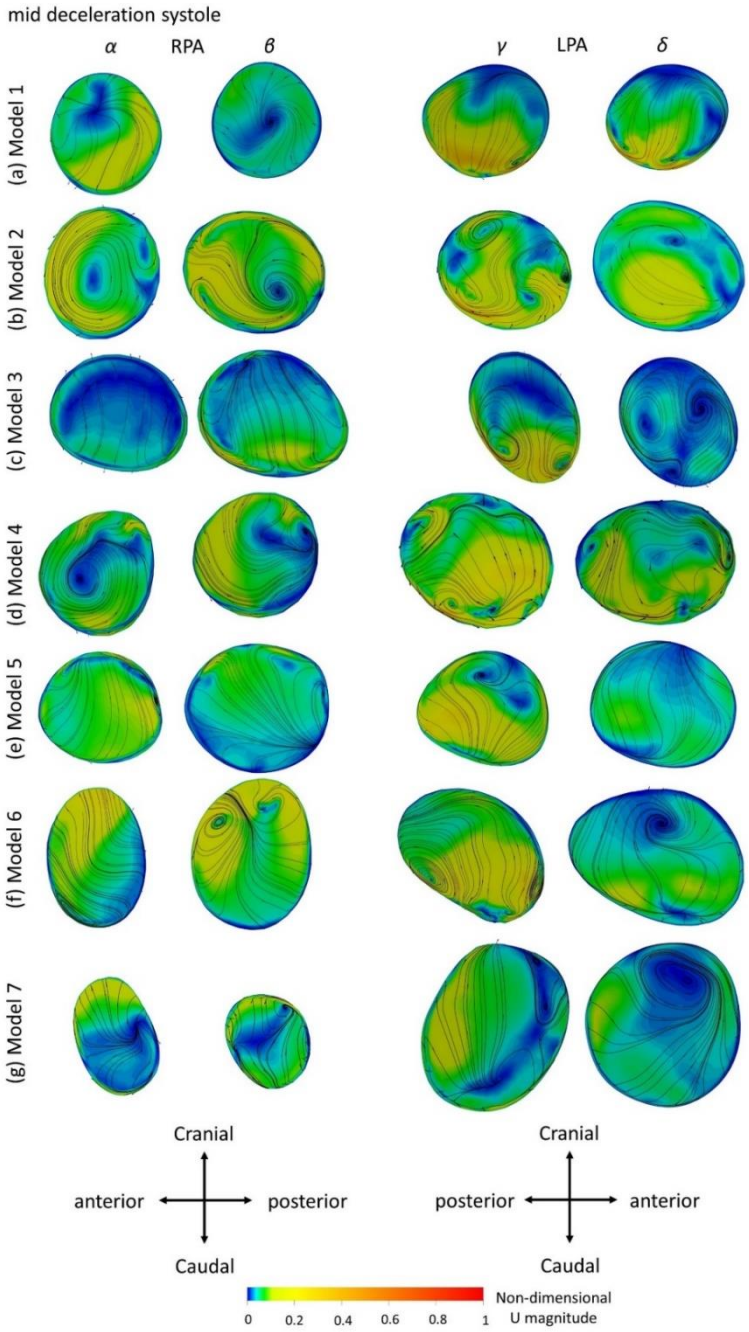

Figure 5.11: Secondary flow visualised by in plane velocity vectors and contours of normalised velocity normal to the slice during mid deceleration at systole for (a) model 1; (b) model 2; (c) model 3; (d) model 4; (e) model 5; (f) model 6; (g) model 7.. Non-dimensionalisation was performed by division with the maximum velocity of each patient during the cardiac cycle. Points where slices α to δ are taken are visible in Fig. 5.1b. Cross-sections are oriented with the top and the bottom edges corresponding to the cranial and caudal positions, respectively and left and right to the anterior and posterior of the pulmonary artery, for the RPA, and to the posterior and anterior of the pulmonary artery, for the LPA, respectively. Cross-sections are in scale

In mid diastole, unstable bifurcating lines were observed in the RPA branch in the majority of models. A pair of counter-rotating vortices appeared during mid diastole in the RPA of model 3, positioned caudally in the upstream cross-section (Fig. 5.12c

(α)), but then moving posteriorly further downstream (Fig. 5.12c (β)). Vortices consisting of stable foci were visible in models 2 (Fig. 5.12b (α, β)), 5 (Fig. 5.12e (β)), 6 (Fid. 5.12f (β)) and 7 (Fig. 5.12g (β)). In model 6 three vortices and a saddle point were initially formed (Fig. 5.12f (α)), while in model 7 five vortices were seen (Fig. 5.12g (α)). For the LPA branch of the models, vortices were visible in most of the models (Figs. 5.12a (γ)-(δ), 5.12d (γ), 5.12e (γ), 5.12g); unstable bifurcating lines could also be distinguished (Figs. 5.12a (γ), 5.12d (γ), 5.12e (γ)). A stable and an unstable focus were visible in the cross-section of model 2 (Fig. 5.12b (γ)), which fused into a stable focus downstream (Fig. 5.12b (δ)). The opposite was observed for model 3, where a stable focus (Fig. 5.12c (γ)), transitioned to two counter-rotating vortices in the downstream cross-section (Fig. 5.12c (δ)).

The geometrical and flow parameters of the models (Tables 5.4, 5.5 and 5.6) indicate higher *Re* and *De* numbers in the RPA branch of the models, while the LPA branches demonstrate elevated curvature and tortuosity. In general, more complex secondary flow patterns appeared in the LPA branches of the models, indicating that curvature and tortuosity have a greater impact in vortex formation. Nevertheless, a number of vortices have formed in the RPA branch during mid diastole, especially in models 6 and 7 (Figs. 5.12f, 5.12g), which are also the models with the highest RPA flow split (above 75% in both cases), indicating the effect of the BCs in the observed flow field. Finally, an increased number of vortices exists in the LPA of model 2 when the averaged BCs are used, however this difference could be explained by the considerable difference in the peak inlet flow between patient-specific and averaged velocity waveforms. For model 3, although an increase in the inlet peak flow is also observed, it is relatively small (6.6%).

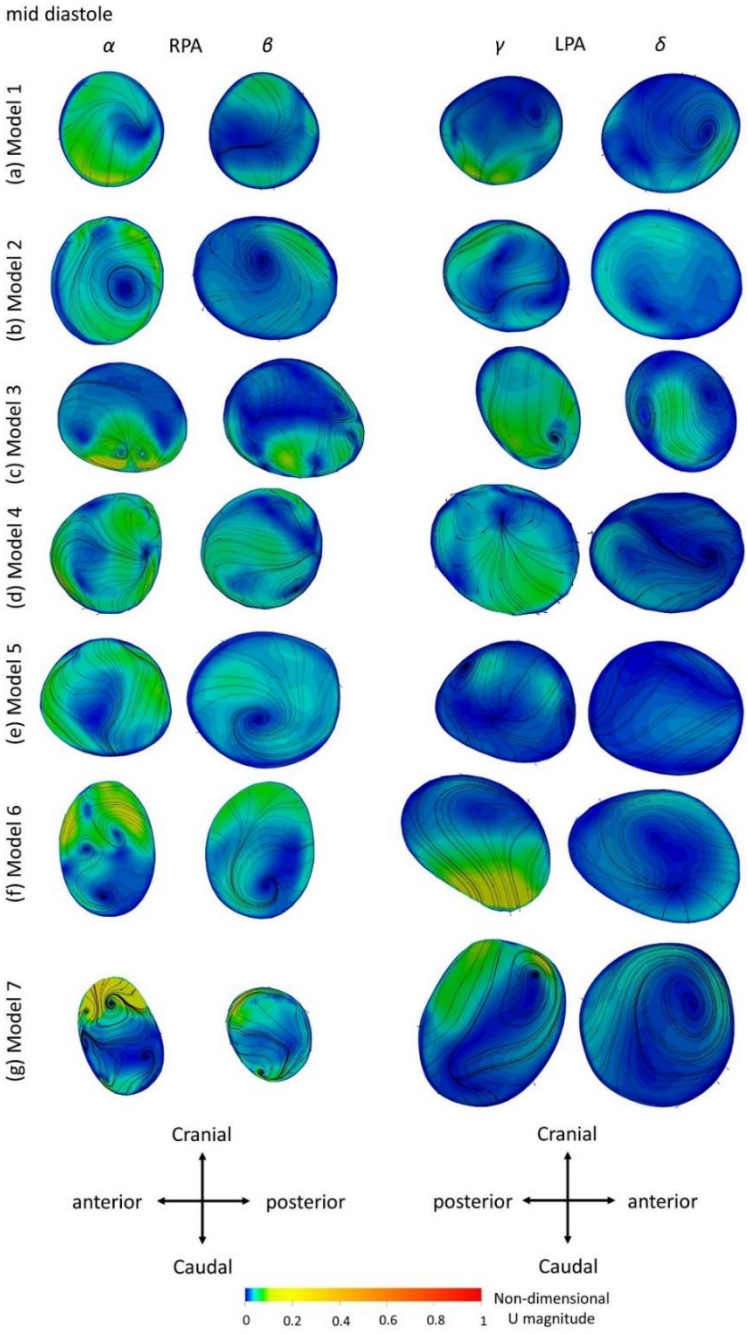

Figure 5.12: Secondary flow visualised by in plane velocity vectors and contours of normalised velocity normal to the slice during mid diastole for (a) model 1; (b) model 2; (c) model 3; (d) model 4; (e) model 5; (f) model 6; (g) model 7. Non-dimensionalisation was performed by division with the maximum velocity of each patient during the cardiac cycle. Points where slices α to δ are taken are visible in Fig. 5.1b. Cross-sections are oriented with the top and the bottom edges corresponding to the cranial and caudal positions, respectively and left and right to the anterior and posterior of the pulmonary artery, for the RPA, and to the posterior and anterior of the pulmonary artery, for the LPA, respectively. Cross-sections are in scale

5.3.3.2.3. Time-averaged wall shear stress

Normalised TAWSS distributions using the patient-specific BCs are presented in Fig. 5.13. Areas of high TAWSSn were found at the entrance of the daughter branches. More extended high TAWSSn areas were observed on the LPA and RPA branches of model 3 (Fig. 5.13c), and the RPA and MPA branches of models 4 (Fig. 5.13d) and 7 (Fig. 5.13g). The lowest TAWSSn was noticed in patient 1 (Fig. 5.13a), while the MPA of model 3 had also lower TAWSSn values compared to the rest of the models (Fig. 5.13c). A small area of high TAWSSn was also seen in the MPA of model 5 (Fig. 5.13e).

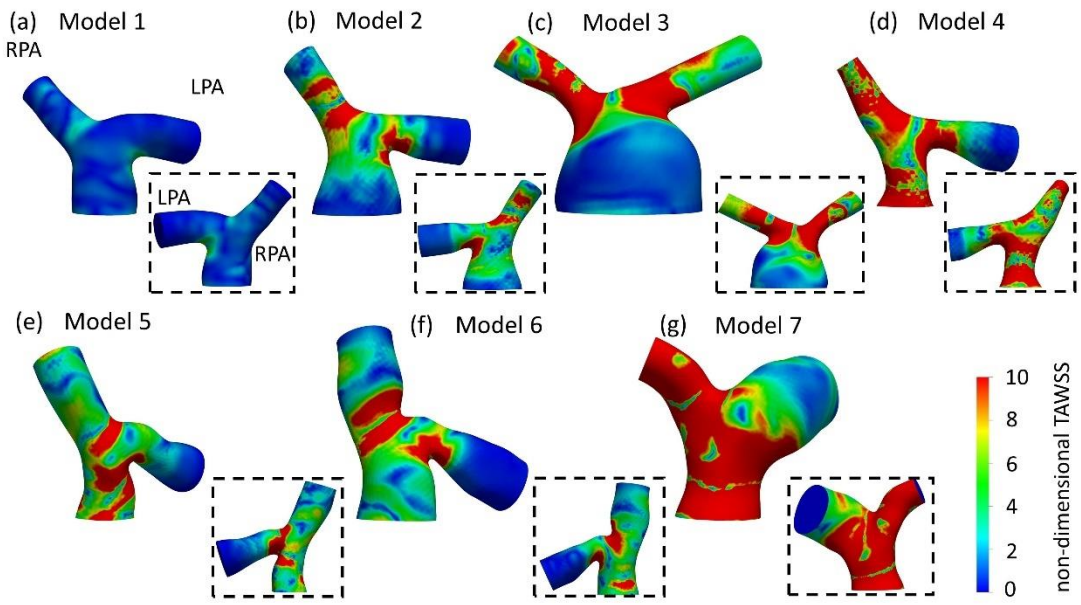

Figure 5.13: Non-dimensionalised time-averaged wall shear stress (TAWSSn) distribution, normalised by the wall shear stress value at the inlet of each model, respectively, for (a) model 1; (b) model 2; (c) model 3; (d) model 4; (e) model 5; (f) model 6; (g) model 7. Insets show the back view of the models. The LPA and RPA branches are indicated in Model 1.

Overall, the TAWSS patterns observed in figures 5.13 and 5.8 are similar in character, in particular with regard to the high wall shear stresses developed at the entrance of the daughter branches. Table 5.7 provides the percentage difference between the

average and patient-specific flow splits. Smaller areas of high TAWSS were noticed in models 1-4 (Figs. 5.13a-d), which coincide with increased flow split in the RPA and with an increase in the peak inlet flow when the averaged BCs are specified in the models (Table 5.7). On the contrary, higher wall shear stress values were developed in the pulmonary bifurcation of models 5-7 (Figs. 5.13e-g) for patient-specific BCs. For models 5 and 6 (Figs. 5.13e and 5.13f), there was an increase in the LPA flow split and a decrease in the RPA flow split and peak inlet flow, compared to the average values (Table 5.7). Model 7 had the largest difference in the TAWSSn pattern. A possible explanation could be that although the patient-specific flow split was 45.7% : 54.3% (Q_{RPA}:Q_{LPA}), the average flow split had most of the flow diverted to the RPA branch (65.3% : 34.7%, $Q_{RPA\text{-}av}$:$Q_{LPA\text{-}av}$), highlighting the importance of the BCs in the flow development. Furthermore, model 7 was the exception in the general trend observed for the rest of the models, where an increase in the RPA flow split and the peak inlet flow resulted in increased TAWSSn values in the pulmonary junction.

Table 5.7: Percentage difference between the average and patient-specific values for flow splits and inlet flow waveform ($((Q_{average}\text{-}Q_{patient\_specific})/Q_{average})*100$).

Patient	Flow Split % difference (RPA)	Flow Split % difference (LPA)	Inlet flow Waveform % difference	Peak Inlet flow % difference
1	+15.3%	-28.8%	+55.5%	+51.6%
2	+0.8%	-1.4%	-3.2%	+54.5%
3	+15.0%	-28.0%	+57.7%	+6.6%
4	+2.1%	-4.0%	-10.8%	+6.5%
5	-15.5%	+29.1%	-166.3%	-94.8%
6	-17.3%	+32.6%	+68.4%	-52.6%
7	+30.0%	-56.5%	-1.2%	+9.0%

To quantify the differences between the patient-specific models with patient-specific or averaged boundary conditions, and the average geometry, the time averaged wall shear stress from the cross-sections (α) and (γ) (Fig. 5.1), was compared. Eight points located along the wall of the cross-sections and equally distanced, were taken for each geometry, and the average TAWSS from the eight individual values was calculated. The measured TAWSS was then averaged for Models 1-7, with patient-specific boundary conditions, and for the same models with averaged boundary conditions. The results are presented in Table 5.8, both in dynes/cm^2 and non-dimensionalised (TAWSSn). The TAWSS values of the averaged geometry is reported separately to allow comparisons. The TAWSS values of the average geometry is lower compared to the average values calculated for Models 1-7 when both averaged and patient-specific BCs are used. In addition, the range of the TAWSS values are comparable when average (~47-450 dynes/cm^2) and patient-specific BCs (~33-237 dynes/cm^2) are assigned. Table 5.8 also indicates that there is a large variability in the TAWSS values between the different models. To further compare the TAWSS values of the different models, the average TAWSS value calculated for the RPA and LPA cross-sections of each patient were plotted and are presented in Fig. 5.14, for both patient-specific and average BCs. When the adult patients were compared (Figs. 5.14a.3-5.14a.7) the TAWSS value was found to be decreasing with age, while the lowest TAWSS value of 27 dynes/cm^2 was noticed in model 1 (Fig. 5.14a.1). In Fig. 5.14b, much higher TAWSS values were calculated for model 2 (~450 dynes/cm^2, Fig. 5.14b.2), while models 5 to 7 have very similar TAWSS values (Figs. 5.14b.5 – 5.14b.7). The TAWSS value of the average model was at the lower levels (~65 dynes/cm^2, Fig. 5.14b.8), but

comparable to the values calculated in the adult population with averaged boundary conditions (47-290 dynes/cm^2, Figs. 5.14b.3 – 5.14b.7).

Table 1.8: Averaged TAWSS, derived from the TAWSS values of eight points located along the perimeter of cross-sections (α) and (γ), are presented both in dynes/cm^2 and non-dimensionalised (TAWSSn).

		TAWSS (dynes/cm^2)	TAWSS$_n$
Cross-section (α)	Average geometry	87	95
	Models 1-7 average BCs	182 ± 135	173 ± 173
	Models 1-7 patient specific BCs	129 ± 67	187 ± 155
Cross-section (γ)	Average geometry	42	45
	Models 1-7 average BCs	179 ± 148	150 ± 110
	Models 1-7 patient specific BCs	109 ± 70	146 ± 113

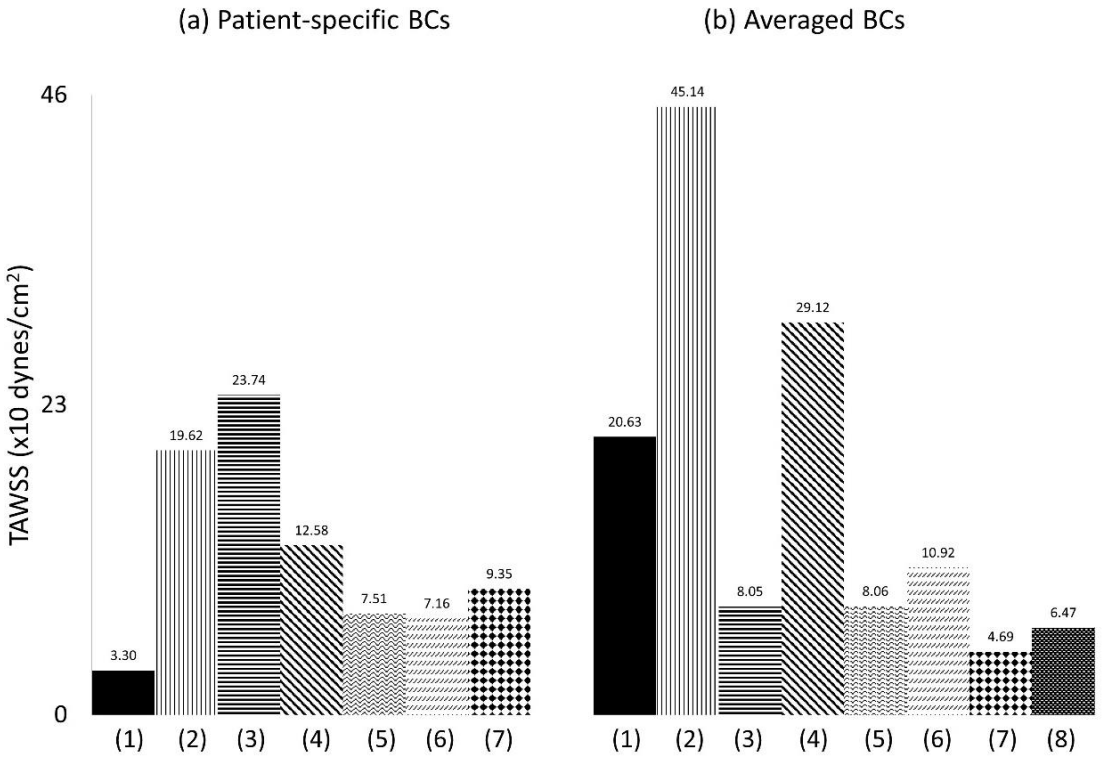

Figure 5.14: Time-averaged wall shear stress (TAWSS) plot, derived from the TAWSS values of eight points located along the perimeter of cross-sections (α) and (γ), and presented in dynes/cm^2, when (A) patient-specific, and (B) averaged boundary conditions are specified, and for (1) model 1; (2) model 2; (3) model 3; (4) model 4; (5) model 5; (6) model 6; (7) model 7; (8) the average model.

5.3.3.2.4. Oscillatory Shear Index

Relatively high OSI was observed in the pulmonary junction of the models, indicating a fluctuation in the wall shear stress during the cardiac cycle. Higher OSI was noticed in model 1 (Fig. 5.15a) and in the LPA of model 7 (Fig. 5.15g). Lower OSI was seen at the entrance of the daughter branches, around the stagnation point in the bifurcation of the branches (Fig. 5.15), and a more extended low region was found in model 3 (Fig. 5.15c). In general, the high and low OSI regions corresponded to the low and high TAWSSn areas, respectively (Fig. 5.13).

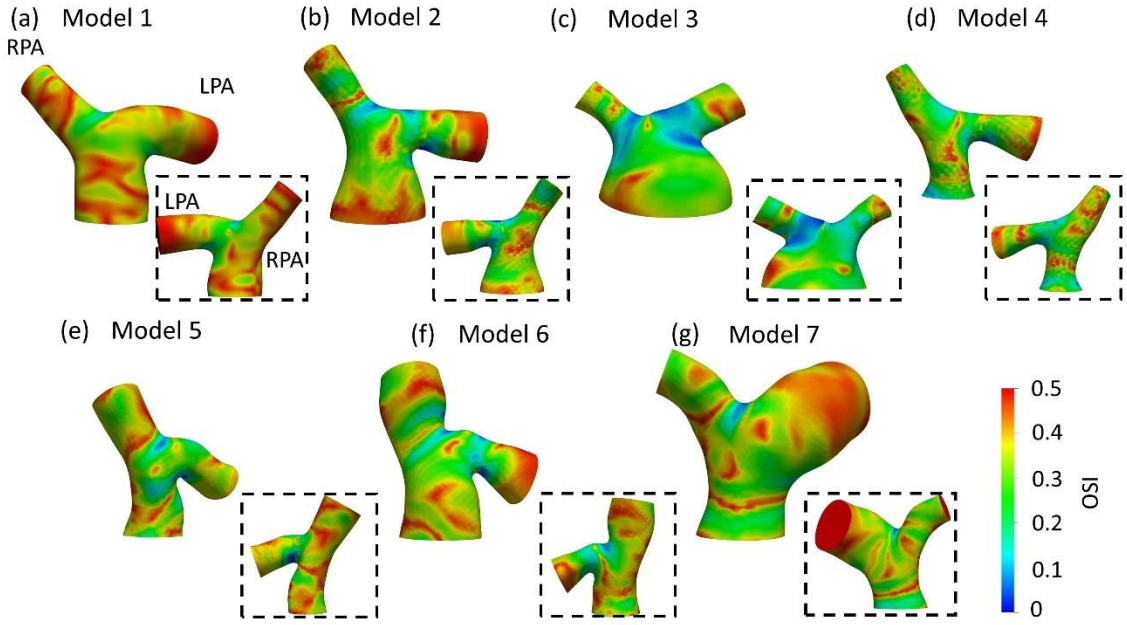

Figure 5.15: Oscillatory Shear Index distribution for (a) model 1; (b) model 2; (c) model 3; (d) model 4; (e) model 5; (f) model 6; (g) model 7. The RPA and LPA branches are indicated in model 1.

5.4. Discussion

This study demonstrates that the anatomy of the pulmonary arteries of repaired tetralogy of Fallot patients varies greatly within the population. A characteristic

difference from healthy subjects is that the left pulmonary artery is highly curved (Capuano et al., 2019). The scope of this study was to evaluate the effect of morphological characteristics on the flow development in models of rTOF patients. Seven patient cases were initially analysed geometrically and information including the curvature, tortuosity, the radius and the angles of the daughter branches were reported. The flow development was investigated through numerical simulations that were performed using patient-specific and averaged boundary conditions. The novelty of this work lies in the analysis of both the morphological and the hemodynamic characteristics of rTOF models, and in the assignment of the patient-specific 3D velocity profile of the pulmonary arteries, which is usually neglected in computational studies. The main findings of this work concern the correlation of tortuosity with the secondary flow patterns (Section 5.3.3.2.2), and the association of the flow splits and the peak inlet flow with the time averaged wall shear stress distribution (Section 5.3.3.2.3).

The morphological analysis of the TOF models in this study suggests that: 1) the LPA has a higher curvature compared to the RPA; 2) the LPA branch has a higher tortuosity; 3) the average radius of the LPA is higher compared to the RPA radius (Table 5.5); 4) the in-plane-angles suggest a more acute angle of the LPA branch; and 5) the out-of-plane angles indicate a counter-clockwise and clockwise shift of the RPA and LPA branches, respectively, while also suggesting a small bend of the RPA on the 3D-space.

Comparison with previous studies

Capuano and his co-workers (Capuano et al., 2019) studied the blood flow in a healthy pulmonary artery and reported a steeper but planar curvature in the right pulmonary

branch compared to the left, while Louvelle et al. (Louvelle et al., 2019) who assessed the geometric complexity of TOF patients, reported higher tortuosity in the LPA, in agreement with the results of this work. Regarding the cross-sectional area between the RPA and the LPA branches, this was previously found slightly lower in the RPA for healthy subjects (Capuano et al., 2019), while the opposite was observed in TOF patients, where the difference between the diameters of the two branches was noticeable (Louvelle et al., 2019). In the present study, a small difference was seen between the minimum sphere radius of the RPA and LPA branches. Comparing the branching angles in the right and left branches, the LPA was found to bifurcate almost as a continuation of the MPA in healthy subjects (Capuano et al., 2019), while its course was much different, with smaller branching angles, in TOF patients (Louvelle et al., 2019), which is in agreement with what was observed in this work.

To characterise the flow, the Reynolds, Womersley and Dean numbers were reported in this study, which are associated with alterations in secondary flow structure (Sudo et al., 1992, Evergen et al., 2010) and wall shear stress patterns (Kazakidi et al., 2009, Kazakidi et al., 2011). The RPA was found to have the highest mean Reynolds number, compared to the MPA and LPA branches, which could be explained by the smaller average branch radius. Finally, the average Dean number was found to be more elevated in the RPA branch, than the LPA branch. The Womersley number reported in the pulmonary arteries of healthy volunteers is in the range of approximately 14-21 (Sloth et al., 1994), which is in agreement with the range reported for the TOF population in this study. Recently, Loke et al. (Loke et al., 2019) studied the pulmonary artery bending in healthy subjects and patients that have undergone arterial switch operation (ASO) and reported a Dean number in the range of 803 ± 280 in the RPA

and 566 ± 140 in the LPA in the control group, and 1902 ± 1125 in the RPA and 1067 ± 584 in the LPA of the ASO patients (Loke et al., 2019). These patients are often diagnosed with post-operative complications including right ventricular afterload and right ventricular hypertrophy, most commonly from left pulmonary arterial stenosis (Morhan et al., 2017), similar to TOF patients. In this study, the average Dean numbers were within the range of the ASO patients. Plotting the average Dean number along the centrelines of the models showed that it reached its peak value approximately at the entrance of the daughter branches (Fig. 5.6d), following the same trend as the curvature plot (Fig. 5.6b). In general, high Dean numbers are associated with complex vortical flows (Hidesato, 1987), and a Dean number above 36 was found to be the critical value above which secondary motions are formed in a curved pipe (Lyne, 1971).

The flow patterns developed in the arteries of the models are comparable with those reported in previous studies for tetralogy of Fallot patients. Flow recirculation was observed first in the LPA of the models early in the cardiac cycle (Fig. 5.9.i), while recirculation zones developed in the MPA and/or RPA branches later during the cardiac cycle in agreement with the study of Chern at al. (Chern et al., 2012). Various different types of secondary flow patterns have been discussed in the literature (Sudo et al., 1992, Boiron et al., 2007, Evergen et al., 2010, Chern et al., 2012, Capuano et al., 2019), for different numerical and geometrical parameters, which makes the comparison with the secondary flow patterns reported in this study rather difficult. Nevertheless, in general, more complicated flow patterns were found in the LPA branch (Figs. 5.10-5.12) of the models, which is in agreement with other studies (Chern et al., 2012). The TAWSSn distribution was, overall, elevated at the openings

of the daughter branches (Figs. 5.8, 5.13), which is comparable with the results reported by Zhang et al. (Zhang et al., 2016). Very low TAWSSn values were found at the stagnation point, while a high TAWSSn gradient was developed adjacent to that area, as reported on Chapter 3. The range of TAWSS values reported in this study for the rTOF models (in the range of 0-440 dynes/cm^2, Fig. 5.14) was found much higher compared to those of healthy control volunteers presented in previous studies (up to 20.5 dynes/cm^2), and of patients with pulmonary arterial hypertension (up to 10.1 dynes/cm^2) (Tang et al., 2011, Tang et al., 2012). Nevertheless, the range of the TAWSS values in Zhang et al. (2016), a work also focused in rTOF, was also elevated, at 0-1000 dynes/cm^2 and it is anticipated that the pulmonary arteries of the specific population of patients is characterised by a high TAWSS environment. In general, higher wall shear stress values were observed in the RPA branch, which was also characterised with a smaller branch radius and higher *Re* and *De* numbers. Finally, the OSI was found relatively high in the models, with relatively low OSI observed in the openings of the daughter branches (Fig. 5.15). Previous work conducted in healthy subjects, reported low oscillatory shear index in the pulmonary arterial models (Tang et al., 2010), while in another study where they compared the OSI in a healthy population with a group of patients suspected of secondary pulmonary arterial hypertension (PAH), higher OSI values were reported for the PAH group (Terada et al., 2016). The latter is in agreement with the results of this study.

Importance of patient-specificity

Anatomically mean geometries have been used in several cardiovascular studies to reduce complexity in patient-specific simulations (Guibert et al., 2014), investigate morphological characteristics and extract 3D shape biomarkers (Bruse et al., 2016),

and, lately, study the blood flow in a healthy average geometry of the pulmonary bifurcation derived from 5 young patients (Capuano et al., 2019). To this end, the patient-specific results were compared with those of an averaged geometry derived from the 5 adult rTOF patients of this study. The regions of high TAWSSn (Fig. 5.8h) were in agreement with those predicted with the patient-specific models (Figs. 5.13a-g), more closely resembling models 1, 2 and 6 (Figs. 5.13a-b, f). Nevertheless, the extent of the high shear regions differed considerably with morphology and an anatomically mean geometry cannot capture this variability. This study also demonstrates a similarity in character between results obtained with patient specific boundary conditions and those utilising averaged conditions. This indicates that morphology is a crucial parameter in the flow development. However, the TAWSSn distribution varied in cases with the highest percentage difference in flow split and peak inlet flow between patient-specific and averaged values (Table 5.7), particularly for model 7 (Fig. 5.8g) where this was more visible, indicating that the flow field observed is due to the inflow and outflow BCs. In models 5 and 6, where the flow split in the RPA branch and peak inlet flow increased with the patient-specific boundary conditions, higher values of TAWSSn were observed (Figs. 5.13e-f). A correlation therefore exists between the TAWSSn distribution and flow splits which has been previously reported in the idealised models, representative of the pulmonary bifurcation of Chapter 3. Finally, the results of Fig. 5.14 indicate a decrease in the TAWSS in the cross-sections of the RPA and LPA branches with age in the adult population, with the exception of patient 7, when the patient-specific BCs are considered (Fig. 5.14a).

Patient-specificity is therefore deemed necessary for a better characterisation of the flow development in the pulmonary bifurcation of rTOF patients. Geometric analysis of the patient-specific models provides information about curvature and tortuosity, parameters that affect the flow in the daughter branches, and more specifically recirculation (Fig. 5.9) and secondary flows (Fig. 5.10). Curvature and torsion that exist in arterial geometries are found to create a favourable environment through generation of mixing, which has been linked with thrombosis prevention (Cookson et al., 2019). On the other hand, Dean flow patterns are referred to as no mixing, as the two vortices formed are symmetric (Cookson et al., 2019). In addition, assuming patient-specific boundary conditions is also important, as the flow split and peak inlet flow have an impact on the TAWSSn distribution (Figs. 5.8, 5.13), and on the secondary flow vortices developed on localised cross-sections (Figs. 5.7, 5.10). Significant changes on the wall shear stress of the pulmonary vasculature could affect pulmonary remodelling and endothelial health (Tang et al., 2012). Although similarities existed between the TAWSSn of the patient-specific and averaged boundary conditions, and one would argue that it could suffice to predict the wall shear stress patterns, model 7, in particular, highlights the value of patient-specificity.

Clinical relevance

The reversal of blood flow into the right ventricle, known as pulmonary regurgitation, and branch pulmonary artery stenosis, in the form of LPA kinking, are two of the most common complications in the rTOF population. PR is the result of pressure difference between the right ventricle and the pulmonary artery during diastole, and is associated with the geometry of the branch pulmonary arteries, and with the pulmonary vascular resistance and pressure (Kilner et al., 1997, Harris et al., 2011). Chronic PR typically

results in right ventricular dilatation and dysfunction, and in combination with the dilation of the pulmonary trunk, the RVOT is restricted and turns cranially and left-laterally resulting in an acute angle between the MPA and the LPA (Kilner et al., 1997, MacElhinney et al., 1998). Branch stenosis is associated with increased PR, increased pressure drop, restricted flow to the corresponding lung and with increased retrograde flow in the larger artery leading to increased pulmonary vascular resistance in the non-stenotic branch (Harris et al., 2011, Chen and Kilner 2013, Schiavazzi et al., 2015, D'Souza et al., 2018).

Endothelial cells (ECs) and elastic fibres are organised in a layer of connective tissue that surrounds the endothelial lining of the tunica intimate (inner layer) of the blood vessels (Martini et al., 2014, Rubenstein et al., 2016). ECs play a crucial role in regulating vascular homeostasis (Gimbrone 1995, Sabri et al., 2012) and remodel in response to the wall shear stress applied to the vessel's wall. Increased levels of WSS increase the production of the potent vasodilator nitric oxide (NO), while decreased WSS increase the production of the potent vasoconstrictor endothelin-1 (ET-1) (Taylor and Figueroa 2009). In addition, TAWSS values <4 dynes/cm^2 are linked to atherosclerosis, while higher TAWSS (150-450 dynes/cm^2) with thrombosis (Ling et al., 2021). Pulmonary arteries have high shear stress compared to other arteries, but changes observed in the pulmonary vasculature could still affect endothelial function and remodeling (Tang et al., 2012). The results of this study indicate that the TAWSS in the pulmonary arteries of the rTOF patients is highly increased, with values up to 240 dynes/cm^2 (when the patient-specific boundary conditions are considered) at the entrance of the daughter branches and with slightly higher TAWSS values noticed at the RPA branch. These regions of sudden change in the TAWSS at the bifurcation of

the pulmonary artery may be potential areas of local stenosis and neointimal growth (Zhang et al., 2016). The haemodynamic environment of these patients could be potentially correlated with the two-way link between pulmonary regurgitation and LPA kinking, were when present, may lead to RV dilation and dysfunction.

Limitations

Several limitations exist in the specific study, including the assumption of rigid walls. Nevertheless, previous studies have indicated that the flow patterns observed with the rigid walls would not differ significantly from those predicted when dynamic arterial compliance is taken into account (Capuano et al., 2019, Jin et al., 2003), also shown on Chapter 4 of this work. In addition, the peripheral resistance of the vessels was neglected, although patient-specific flow splits were assigned at the outlets of the models. Also, the pulmonary valve was not included in the simulations, which would affect the inlet flow, however patient-specific 3D velocity profiles were assigned at the inlet of the models which are more representative compared to a pulsatile waveform. Furthermore, it is recognised that the anatomical mean geometry cannot be considered representative of the rTOF patients, due to the small number of models used in the study. Finally, specific disease indications of the rTOF patients are not available, which consist another limitation of this study. Future work will include a larger cohort of patients to verify the findings presented and to address some of the limitations. Finally, it is acknowledged that the examined cohort of patients varied greatly in terms of age and gender, which may influence particularly the averaged BCs and geometry used.

5.5. Conclusion

This study investigated the impact of morphological characteristics in the blood flow development in the pulmonary arteries of rTOF patients, assuming patient-specific and averaged boundary conditions. Higher curvature and tortuosity were found on the LPA branch, which also formed a more acute angle with the MPA and had a more pronounced rotation in the 3D space. Zones of recirculation and more complex flow patterns also developed in the specific daughter branch as indicated by the computational results. The LPA was characterised by lower Reynolds and Dean numbers, and the results correlated with higher curvature and tortuosity of the branch. Nevertheless, the higher Re and De numbers, which imply more distributed flow in the domain, can correlate with increased regions of TAWSSn in the RPA branch. The averaged boundary conditions and the average geometry can capture some general characteristics of the flow, supporting the importance of morphology in flow development, but the differences observed in the flow development also indicate the effect of the BCs. The present work highlights the importance of patient-specificity and especially of the spatial varying flow, which is usually neglected in computational studies. Further investigation is required in larger cohorts of TOF patients to validate the findings of this study and to allow the analysis based on the age and gender of the population.

Chapter 6

Haemodynamic analysis in personalised arterial models of healthy volunteers

In this chapter, morphological and flow pattern are investigated in five subject-specific models of healthy volunteers and an anatomical average model of the five, similar to Chapter 5 for the rTOF patients. An introduction is given on Section 6.1., while Section 6.2. described briefly the reconstruction of the models and the boundary conditions used. Section 6.3. presents the calculated morphological and flow characteristics, and the computational results. A summary of the key findings is given in Section 6.4., where comparisons with Chapter 5 and previous studies are also made, and this Chapter ends with a conclusion in Section 6.5.

6.1. Introduction

Pulmonary arteries are a distinct system of complex anatomy and unique biomechanical characteristics. Under normal conditions the pulmonary bifurcation is characterised as a low pressure, low resistance, and high flow environment. Several pathological conditions can disturb the flow environment, or lead to remodelling of the pulmonary arteries (Hanna, 2005, Caro et al., 2012), such as those described in Chapter 1. In Chapters 3 and 5 the investigation is focused in idealised and patient-specific models of rTOF patients. Describing the haemodynamic conditions in normal

states can be also important in disease diagnosis and mechanisms of progression, and treatment.

Further to Tetralogy of Fallot presented in the previous Chapters, there are further pathophysiologies related to the pulmonary arteries, and many studies exist that investigate the blood flow in arterial models of patients of various conditions. Transposition of the great arteries (TAG) is a cyanotic congenital heart disease where new-borns are diagnosed with an aorta connected to the right ventricle, and a pulmonary artery to the left ventricle. The arterial switch operation (ASO) is the currently-used surgical option to treat TAG (Shaher, 1964, Villafañe et al., 2014), and many studies have utilised CFD techniques to investigate the post-operative environment of these patients (Ntsinjana et al., 2014, Loke et al., 2019, Capuano et al., 2019). Several computational studies have also focused on understanding the blood flow in cases of total cavopulmonary connection (Dubini et al., 1996, Migliavacca et al., 1999a,b, Migliavacca et al., 2000, Ensley et al., 2000, Marsden et al., 2007), which is the outcome of two consecutive surgical treatments for single ventricle congenital heart defects, such as tricuspid atresia and hypoplastic left heart syndrome. Patients are diagnosed with one functional ventricle and following completion of the surgical procedures, pulmonary arteries have a modified T-shaped junction, where the inferior vena cave is connected to the pulmonary arteries, so that blood flow bypasses the venous circulation (de Leval et al., 1988). Finally, pulmonary arterial hypertension (PAH) is a chronic disease which has drawn the attention of many researchers (Tang et al., 2012, Bordones et al., 2018, Spazzapan et al., 2018). Elevated pulmonary blood pressure decreases wall compliance and increases wall thickness, leading to

remodelling of the proximal and distal pulmonary vasculature (Galié et al., 2004, Humphrey et al., 2008).

Although knowledge of the physiological haemodynamic environment is a key factor in understanding pathological conditions, few studies exist that are trying to assess the haemodynamic environment in the pulmonary arteries of healthy subjects. Tang et al. (2011) investigated the blood flow in healthy subjects under rest and exercise conditions, focusing mainly of the WSS, and showed an increase in the WSS values with exercise. Bächler et al. (2013) utilised 4D flow and found that helical structures develop in the RPA and LPA branches in healthy volunteers. Recently, Capuano et al. (2019) analysed the blood flow in an anatomical average model, derived from five young subject-specific models, and concluded that the pulmonary bifurcation is haemodynamically efficient in healthy volunteers. In addition, they explain the mechanism of the helical structure formation in RPA, which was linked to the MPA curvature leading to WSS detachment.

In this computational study, the blood flow environment is investigated in five subject-specific models and in an anatomical average geometry, derived from this cohort of volunteers. This work is closely related with that of Chapters 5, where the impact of morphology and the flow conditions is explored in personalised models of TOF patients. To this end, the morphological and flow features in healthy volunteers were investigated. In the following sections, the methodology is first presented (Section 6.2.), followed by the results (Section 6.3.). Section 6.4. provides a summary of the findings and makes comparison with previous studies and with Chapter 5, and finally, Section 6.5 gives a brief conclusion.

6.2. Methodology

In this section information about the healthy subjects, the extraction of flow data and the setup of the computational models are provided. Many parts of the methodologies followed are similar to those described in Section 5.2, and therefore, to avoid repetition, the relevant Sections are suggested for a more detailed analysis.

6.2.1. Healthy Population

Retrospective data from five healthy subjects were used to study the blood flow in the pulmonary bifurcation of healthy volunteers (range of age 27 to 59 years). The images used for the reconstruction of the models were acquired on 2019 with a Siemens Prisma 4D flow 3-Tesla MRI scanner, Siemens Healthcare, Erlangen, Germany (TR=5.3 ms, TE=3.1 ms, FOV in the range of 68.75 to 78.13, and pixel spacing [1.4844;1.4844] to [2.375;2.375]). The clinical data include part of research data from the Queen Elizabeth Hospital, Glasgow, UK (approved by the local ethics committee, Glasgow CRIF approval group, and written informed consent was obtained from all participants. Research Ethics Committee West of Scotland REC3, reference 16/WS/0220). Demographic data of the subjects are presented on Table 6.1.

Table 6.1: Demographic and haemodynamic data of the heathy subjects.

Subject	Sex	Age at scan	Flow Split (Q_{RPA}:Q_{LPA})
1	Female	47 years	56.2 : 43.8
2	Male	59 years	53.2 : 46.8
3	Male	33 years	52.2 : 47.8
4	Male	57 years	54.1 : 45.9
5	Male	27 years	44.0 : 56.0

To extract the flow information from the 4D flow MRI, the data were imported on the software Circle Cardiovascular Imaging, cvi42 (https://www.circlecvi.com/). In order to isolate the pulmonary trunk, the 'track vessel' feature available within the software was used, and centerlines along the MPA and the main daughter branches were created. The threshold for each tracked branch had to be adapted to ensure the best fit. Once the result was satisfactory, the flow information could easily be extracted by taking slices perpendicular to each branch.

The total inlet flow rate waveforms over the cardiac cycle are presented (Fig. 6.1). An average flow rate waveform was calculated based on the five flow waveforms, after time was normalised with the period of the cardiac cycle of each patient. The mean values of the flow rates are also calculated (Table 6.2). Flow waveforms from the RPA and the LPA were also acquired. The net volumes from the inlet flow rates were used to calculate the flow splits in the daughter branches, as previously described in Chapter 5.2.2., and are presented on Table 6.1 for all subjects. The average flow split was calculated and was found approximately 52% : 48% ($Q_{RPA\text{-}av}$: $Q_{LPA\text{-}av}$).

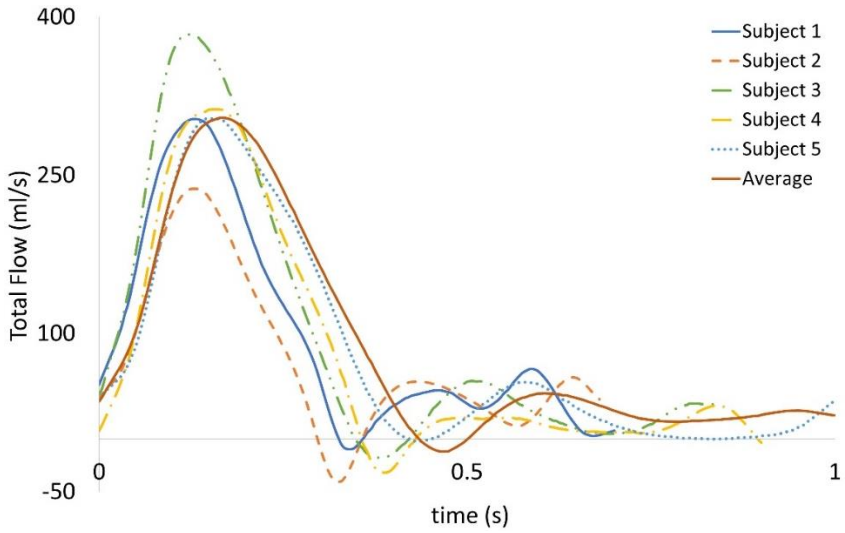

Figure 6.1: Subject-specific pulsatile inlet flow rate waveform for all five subjects and an averaged flow rate waveform derived from the five subject-specific waveforms.

Table 6.2: Diameters, mean flow rate, and mean and max velocities for the MPA, the RPA and the LPA branches of each model.

Subject	D_{MPA} (m)	D_{RPA} (m)	D_{LPA} (m)	Q_{mean} (ml/s)	Umean $_{MPA}$(m/s)	Umean $_{RPA}$(m/s)	Umean $_{LPA}$(m/s)	Umax $_{MPA}$(m/s)	Umax $_{RPA}$(m/s)	Umax $_{LPA}$(m/s)
1	0.028	0.018	0.019	98.7	0.161	0.213	0.160	0.495	0.652	0.490
2	0.027	0.020	0.019	75.7	0.133	0.129	0.130	0.417	0.404	0.407
3	0.030	0.022	0.021	100.2	0.145	0.138	0.146	0.553	0.526	0.557
4	0.029	0.024	0.021	78.3	0.117	0.094	0.109	0.466	0.371	0.432
5	0.032	0.020	0.021	78.6	0.098	0.106	0.127	0.382	0.411	0.493
Average	0.028	0.017	0.017	86.3	0.161	0.196	0.179	0.493	0.689	0.632

6.2.2. Reconstruction of subject-specific models

To segment the subject-specific structures, the same methodology as reported in Chapter 5.2.3. was followed. In sort, a combination of semi-automatic and manual segmentation was used in the open-source software ITK-SNAP (www.itksnap.org) (Yushkevich et al., 2006). The segmentation was extended until the first daughter branch on the right and left pulmonary branches and the geometries were exported as surface mesh using the stereolithography (STL) format. Different smoothing scaling was necessary in each of the geometries to adequately remove artifacts due to the image resolution and segmentation process. An anatomical average geometry was created following the same methodology described in Chapter 5.2.5, and using the model of the 1st subject as the initial template model (Fig. 6.2).

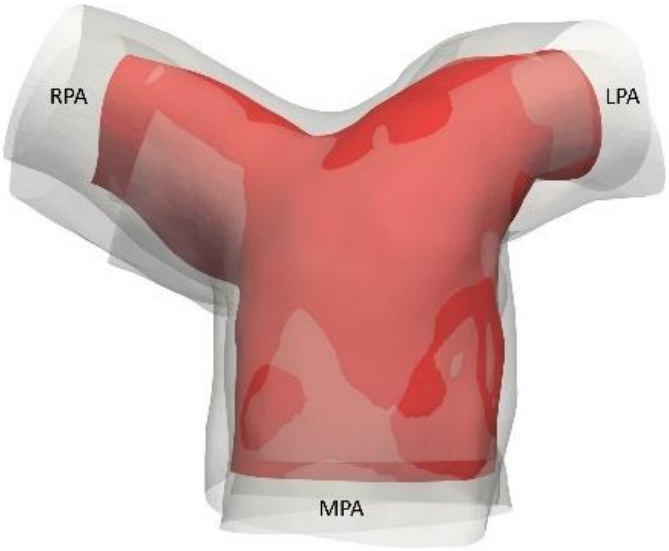

Figure 6.2: Anatomical average geometry of all healthy subjects (red) with the five subject-specific models shown transparent.

6.2.3. Geometry characterisation

A geometric analysis, similar to Chapter 5.2.5. reported for the rTOF models, was conducted, to quantify the curvature of the RPA and LPA branches, the torsion, tortuosity, the minimum inscribed sphere radius along the daughter branches, and in-plane and out-of-plane angles. The differences in the anatomical characteristics between healthy and patient populations are important to be identified, especially in cases of clinical intervention, or evaluation of disease progression.

6.2.5. Numerical simulations

The methodology followed to set the numerical simulations, including the generation of the computational mesh, boundary conditions and computational approximation are similar to those described in Chapter 5.2.6.

The computational mesh was generated using the commercial software ANSA v20.0 (BETA CAE Systems), and the volume mesh consisted primarily of tetrahedra

elements. A boundary layer mesh composed of 7 layers of prismatic cells was added, with the first layer at a distance of 0.005 cm away from the wall, while the total number of elements was around 2.5 million, similar to the rTOF models (Chapter 5.2.6.1.). The y+ value was calculated based on the maximum WSS values, and was found smaller than 1.

For the flow simulations, the k-ω shear stress transport (SST) turbulence model was assumed (Chapter 4.2.1.1.). The patient-specific pulsatile inlet waveforms were specified at the inlet of the models and the flow rates at the outlets. In the average model, the average pulsatile inlet waveform and average flow splits, were considered in the model's inlet and outlets, respectively. The walls were assumed rigid, and the no-slip boundary condition was assigned.

All the numerical simulations were performed with blood considered as a Newtonian, incompressible fluid, governed by the Reynolds-Averaged Navier-Stokes equations (Eqs. (4.1), (4.2)). Blood density and viscosity were set to 1060 kg/m^3 and 4×10^{-3} Pa s, respectively. The pisoFoam solver for transient incompressible, turbulent flow was utilised, using the pressure-implicit with splitting operators (PISO) algorithm of the OpenFOAM® library. The second-order bounded Gauss linear upwind divergence scheme, the backward differential scheme for the time discretization and the Gauss linear gradient numerical scheme were specified.

The time-averaged wall shear stress and the oscillatory shear index were calculated according to Eqs. (3.6) and (5.6), respectively. The TAWSS distribution is normalised by the value at the inlet of each model (denoted as $TAWSS_n$), and the values used for the non-dimensionalisation are reported on Table 6.3. In addition, the Reynolds, Womersley and Deans numbers were calculated for all models following Eqs. (1.14),

(1.22) and (1.23). A table with the diameters, the mean flow rate, the mean and the max velocity of all three branches for each model is provided (Table 6.2).

Table 6.3: TAWSS value at the inlet of the models.

Subject	1	2	3	4	5	Average geometry
TAWSS (dynes/cm^2)	11	7	8	6	5	10

6.3. Results

In the following paragraphs the results from the geometry characterisation of the models (Tables 6.4, 6.5 and Fig. 6.3), the flow characterisation (Table 6.6) and the computational analysis (Fig. 6.4-6.6) are presented.

6.3.1. Geometry characterisation

The morphological features of the five models are listed on Tables 6.4, 6.5. Average curvature and torsion plots are also presented on Fig. 6.3, with curvilinear abscissa normalised based on the curvilinear abscissas of the point with the highest curvature closest to the bifurcation.

Similar values of minimum and maximum curvature (Table 6.4), mean torsion (Table 6.4) and mean in-plane angle (Table 6.5) were noticed between the right and left pulmonary branches. Slightly higher values of curvature and maximum torsion are noticed in the RPA branch, while the minimum values of torsion in the LPA branch (Table 6.4, Fig. 6.3). The curvature of the RPA, based on the mean curvature plot, appears to decrease more rapidly further downstream, compared to the LPA curvature (Fig. 6.3). Both the RPA and LPA branches are characterised by relatively small

torsion, with their mean plots varying close to zero. Tortuosity is found higher in the LPA, with a mean value of 0.110, compared to the 0.085 calculated for the RPA branch. Finally, the out-of plane angles, indicate a clockwise shift of the RPA and an anti-clockwise shift of the LPA branch, with the LPA displaying higher planarity (Table 6.5).

Table 6.4: Geometric analysis of the subject-specific models: curvature and torsion.

Healthy Subject	Curvature RPA (mm^{-1}) (mean / max)	Curvature LPA (mm^{-1}) (mean / max)	Torsion RPA (mm^{-1}) (min / mean / max)	Torsion LPA (mm^{-1}) (min / mean / max)
1	0.018 / 0.063	0.014 / 0.046	-1.59 / 0.00 / 0.57	-1.63 / 0.00 / 0.45
2	0.017 / 0.063	0.015 / 0.062	-1.08 / 0.00 / 1.63	-2.02 / 0.04 / 0.59
3	0.018 / 0.057	0.015 / 0.053	-0.98 / 0.00 / 0.54	-0.49 / -0.03 / 0.51
4	0.019 / 0.093	0.020 / 0.093	-1.08 / -0.03 / 0.37	-1.13 / 0.22 / 0.65
5	0.016 / 0.062	0.017 / 0.068	-0.29 / 0.00 / 0.15	-4.33 / -0.7 / 0.10
Average	0.024 / 0.077	0.020 / 0.048	-1.40 / 0.01 / 0.88	-0.20 / 0.04 / 0.67
Mean value	0.019 / 0.069	0.017 / 0.062	-1.07 / -0.003 / 0.69	-1.63 / -0.072 / 0.56

Table 6.5: Geometric analysis of the subject-specific models: tortuosity, minimum inscribed sphere radius along the daughter branches, and in-plane and out-of-plane angles.

Healthy Subject	Tortuosity (RPA/LPA)	Min Sphere Radius (mm) (RPA/LPA)	In-Plane angles (RPA/LPA)	Out-of-Plane Angles (RPA/LPA)
1	0.073 / 0.080	8.36 / 7.90	142.9° / 152.2°	-0.6° / 17°
2	0.114 / 0.100	8.39 / 5.79	136.6° / 131.8°	3.0° / -1.9°
3	0.092 / 0.154	9.20 / 8.62	137.2° / 149.1°	-7.1° / -10.5°
4	0.066 / 0.126	10.27 / 8.82	134.3° / 115.6°	8.8° / -24.9°
5	0.069 /0.113	9.09 / 8.79	141.0° / 144.6°	6.0° / -17.7°
Average	0.095 / 0.089	7.3 / 7.5	139.8° / 132.5°	-6.3° / 18.4°
Mean value	0.085 / 0.110	8.77 / 7.90	138.6° / 142.6°	0.63° / -3.3°

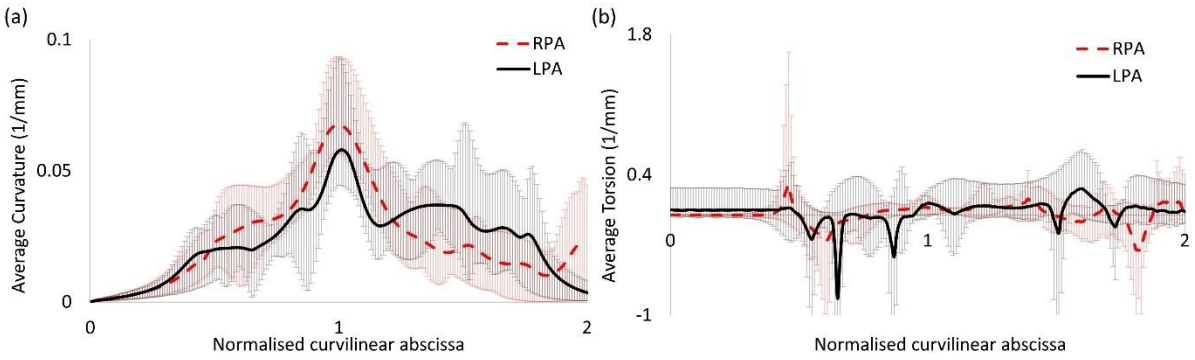

Figure 6.3: (a) Average curvature plot, and (b) average torsion plot, for the healthy subjects. X-axis is normalised by the distance corresponding to the peak curvature value closer to the bifurcating branches. Shaded areas represent the standard deviation of the patient-specific values from the average calculated.

6.3.2. Flow characterisation

The mean and maximum Reynolds number for the MPA, RPA and LPA, and the Womersley and Dean numbers were calculated according to Eqs. (1.14), (1.22) and (1.23), and are reported on Table 6.6. A mean Re_{mean} of 1038 was calculated for the MPA, which dropped to 763 and 725 for the RPA and LPA, respectively. A similar decrease was also noticed for Re_{max}. Wo was in the range of 19.8-21.6, with a mean value of 20.9. Finally, the average Dean number, as calculated for the RPA, was slightly higher but very close to the LPA (De_{max_RPA} = 1283, compared to De_{max_LPA} =1221). In general, *Re*, *Wo* and *De* did not vary greatly within the models and similar values of Reynolds and Dean numbers were noticed for the right and left pulmonary artery.

6.3.3. Computational analysis

In the following paragraphs the computational results are presented in a number of figures, including contours of velocity and velocity streamlines (Fig. 6.4), time-averaged wall shear stress distribution (Fig. 6.5), and the oscillatory shear index distribution (Fig. 6.6).

Table 6.6: Mean and maximum Reynolds (Re), Womersley (Wo) and Dean numbers (De).

Model	Re_{mean_MPA} (Re_{max_MPA})	Re_{mean_RPA} (Re_{max_RPA})	Re_{mean_LPA} (Re_{max_LPA})	*Wo*	De_{max_RPA}	De_{max_LPA}
1	1199(3678)	1032(3165)	790(2423)	21.6	1179	885
2	952(2977)	684(2138)	644(2012)	21.0	1027	882
3	1141(4365)	804(3076)	792(3029)	21.0	1673	1468
4	907(3598)	595(2362)	591(2347)	19.8	1241	1391
5	831(3237)	572(2228)	707(2752)	20.6	1033	1573
Average	1199 (3666)	888 (3121)	815 (2871)	21.6	1547	1129
Mean value	1038(3587)	763(2682)	723(2572)	20.9	1283	1221

6.3.3.1. Contours of velocity and velocity streamlines

Velocity streamlines coloured by non-dimensionalised velocity at three time points, peak flow (Fig. 6.4.i), mid-deceleration during systole (Fig. 6.4.ii), and mid-diastole (Fig. 6.4.iii), are examined. The subject-specific and the average waveforms are also provided to indicate these time points. At peak systole, slightly higher velocities were developed at the entrance of the RPA and in the LPA opening in all models (Figs. 6.4a.i-f.i). Increased velocity was noticed at the RPA for models 1, 4 and the average geometry (Figs. 6.4a.i, 6.4d.i, 6.4f.i), and at the LPA of models 2 and 5 (Figs. 6.4b.i, 6.4e.i). During deceleration (Fig. 6.4.ii), the largest recirculation zones appeared in the RPA of models 2 and 4 (Figs. 6.4b.ii, 6.4d.ii), while smaller areas of recirculation of flow were visible at the entrance of LPA, in all models (Figs. 6.4a.ii-f.ii). Finally, during mid diastole (Fig. 6.4.iii) more complex flow patterns appeared in the pulmonary junction of the models, and especially in models 1, 2, 4 and the average geometry (Figs. 6.4a.iii, 6.4b.iii, 6.4d.iii, 6.4f.iii). The average geometry in general captured well the main characteristics of the flow development.

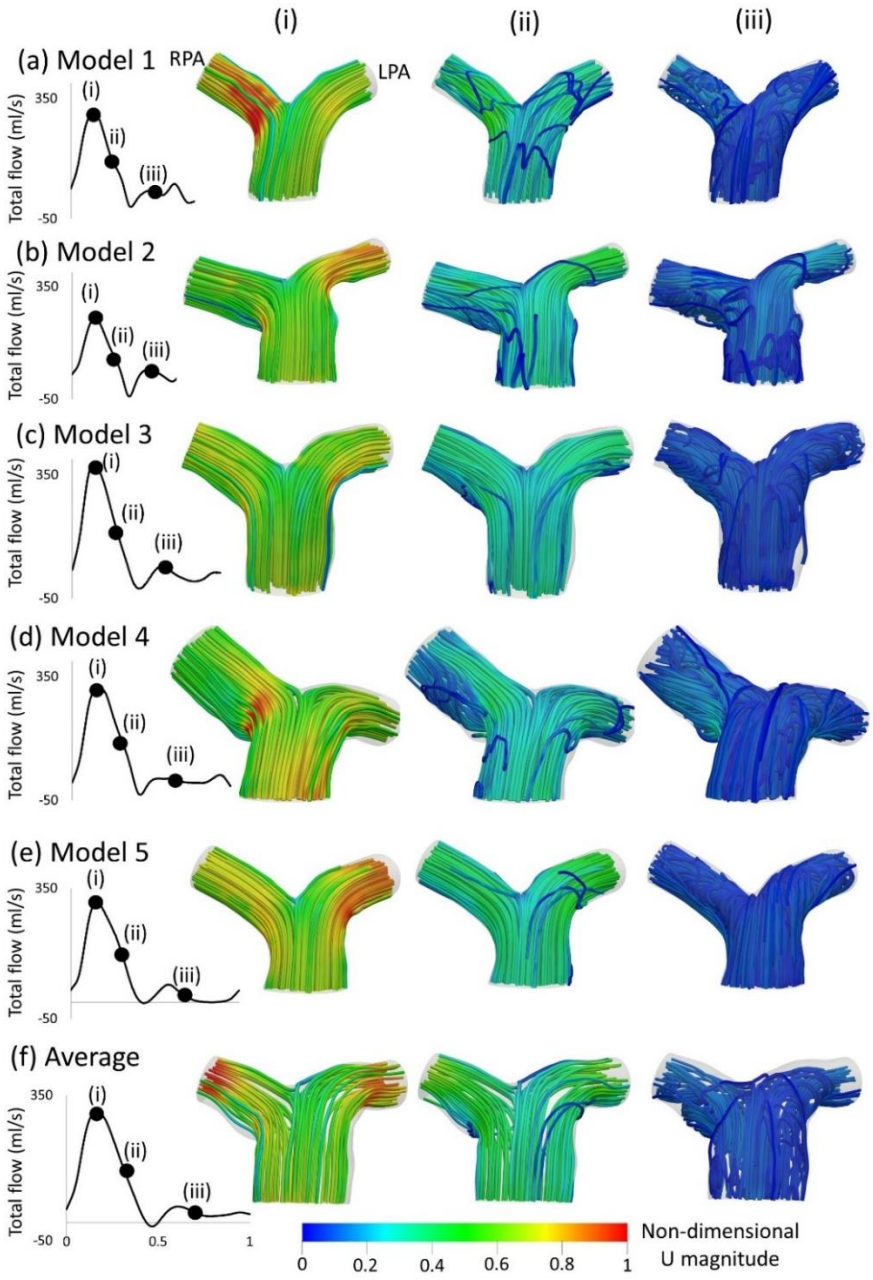

Figure 6.4: Left to Right: Subject-specific flow waveforms with (i) peak flow; (ii) mid-deceleration at systole; and (iii) mid-diastole, for (a) model 1; (b) model 2; (c) model 3; (d) model 4; (e) model 5; (f) the average model. Velocity streamlines coloured by non-dimensionalised velocity based on the maximum velocity during the cardiac cycle of each healthy subject at the three time points (a), (b), and (c). The RPA and the LPA are indicated in model 1.

6.3.3.2. Time-averaged wall shear stress

TAWSS distribution, normalised by the TAWSS value at the inlet of each model, is presented in Fig. 6.5. Higher wall shear stresses were observed at the entrance of the LPA and the RPA branches, while the wall shear stress distribution on the pulmonary

junction of the healthy subjects appeared relatively uniform. The highest $TAWSS_n$ was noticed at the RPA of models 1 and 4 (Figs. 6.5a, d), and the LPA of model 2 (Fig. 6.5b). The lowest $TAWSS_n$ was noticed at the MPA of the average geometry (Fig. 6.5f).

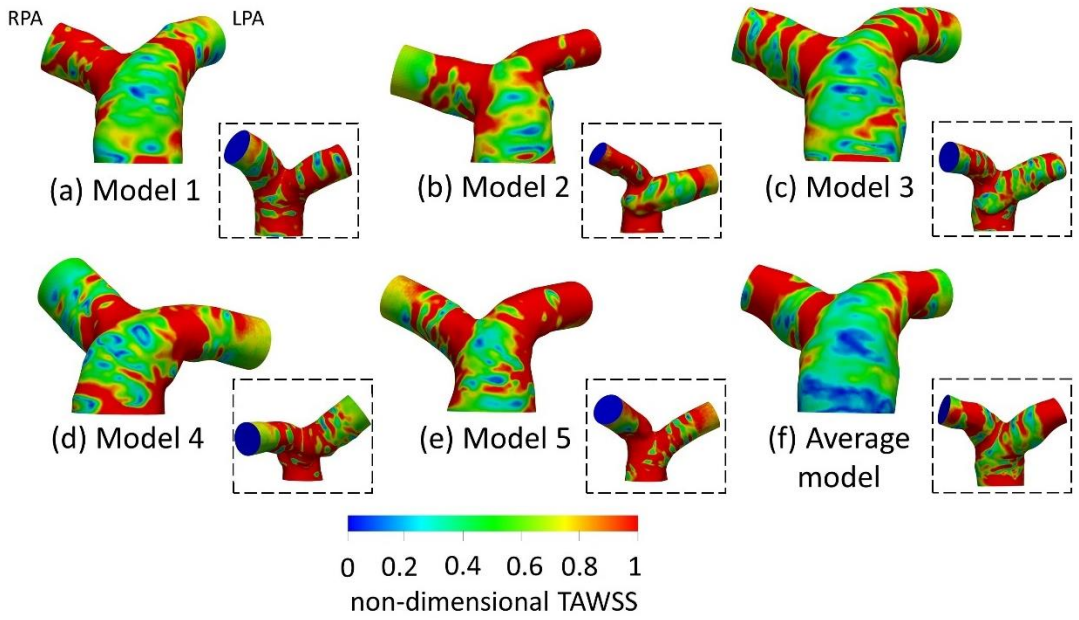

Figure 6.5: Non-dimensionalised time-averaged wall shear stress distribution normalised with the wall shear stress developed at the inlet of each model, respectively, for (a) model 1; (b) model 2; (c) model 3; (d) model 4; (e) model 5; (f) the average model. Insets show the back view of the models. The LPA and the RPA and indicated in model 1.

To quantify the differences in the time averaged wall shear stress in the cross-sections (α) and (γ) (Fig. 5.1), located at a distance of 0.4*D* from the point where the branch splitting occurs, eight points located along the wall of the cross-sections and equally distanced, were taken for each geometry, and the average TAWSS from the eight individual values was calculated. The measured TAWSS was then averaged for Models 1-5 and the results are presented in Table 6.7 in dynes/cm^2. The TAWSS value of the averaged geometry is reported separately to allow comparisons. The TAWSS values of the average geometry is slightly lower compared to the average values calculated for Models 1-5 (7.43 dynes/cm^2 vs 8.22 dynes/cm^2 for cross-section (α), and

7.48 dynes/cm^2 vs 13.5 dynes/cm^2 for cross-section (γ)), while there is no great variability in the TAWSS values between the different models. The mean TAWSS value as calculated in cross-sections (α) is higher compared to the mean TAWSS calculated in cross-sections (γ) of the models (Table 6.7). In addition, the average TAWSS value calculated for the RPA and LPA cross-sections of each subject were plotted and are presented in Fig. 6.6. The range of the TAWSS values is between 7.1 to 13.6 dynes/cm^2, with the lowest value calculated for model 5 (Fig. 6.6e) and the highest value for model 1 (Fig. 6.6a). The TAWSS value of the average model was at the lower levels (~7.5 dynes/cm^2, Fig. 6.6f), but within the range calculated for the subject-specific models.

Table 6.7: Averaged TAWSS, derived from the TAWSS values of eight points located along the perimeter of cross-sections (α) and (γ), are presented in dynes/cm^2.

		TAWSS (dynes/cm^2)
Cross-section (α)	Average geometry	7.43
	Models 1-5	8.22 ± 2.63
Cross-section (γ)	Average geometry	7.48
	Models 1-5	13.5 ± 3.33

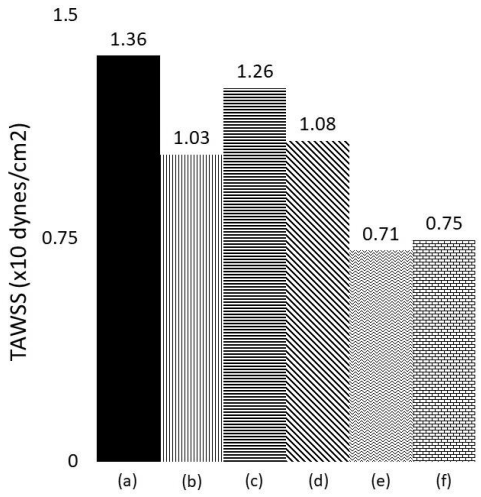

Figure 6.6: Time-averaged wall shear stress (TAWSS) plot, derived from the TAWSS values of eight points located along the perimeter of cross-sections (α) and (γ), and presented in dynes/cm^2, for (a) model 1; (b) model 2; (c) model 3; (d) model 4; (e) model 5; (f) the average model.

6.3.3.3. Oscillatory Shear Index

The OSI distribution is presented for all models on Fig. 6.7. High OSI was generally observed in the pulmonary bifurcation of the healthy volunteers. The MPA of the models is found with the highest OSI values, while at the entrance of the daughter branches lower OSI values were noticed. The high and low OSI regions corresponded to the low and high $TAWSS_n$ areas, respectively (Fig. 6.5). Lower OSI values were found posteriorly in all models (insets of Fig. 6.7).

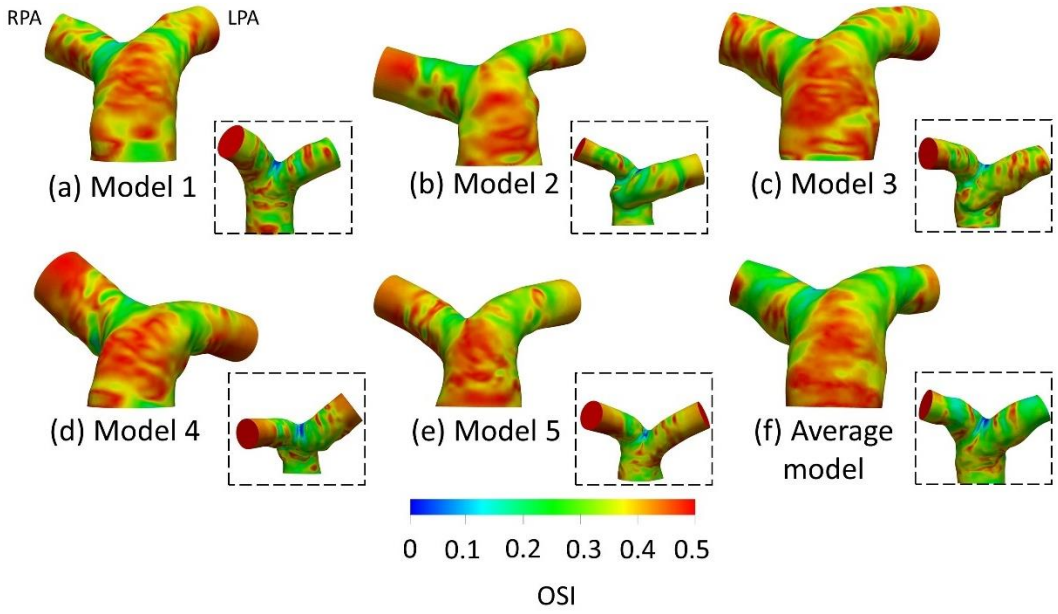

Figure 6.7: Oscillatory Shear Index distribution, for (a) model 1; (b) model 2; (c) model 3; (d) model 4; (e) model 5; (f) the average model. The RPA and LPA branches are indicated in model 1.

6.4. Discussion

There is a growing number of studies that investigate the blood flow in the pulmonary arteries of healthy and patient populations (Bordones et al., 2018, Robinson et al., 2019, Capuano et al., 2019, Boumpouli et al., 2020), in an attempt to better understand

the haemodynamic environment of the arteries, and explain alterations induced by diseases and clinical interventions. The objective of this study was to evaluate morphological and haemodynamic parameters in individualised healthy models of the pulmonary bifurcation. Image data of five healthy volunteers were post-processed to reconstruct subject-specific models of the pulmonary junction. The findings of this work were further compared with those reported for the rTOF patients in Chapter 5. The main outcome of this study is related to the similarity in the morphological and flow characteristics between the RPA and LPA branches in normal pulmonary arteries, in contrast to the morphological differences observed in Chapter 5 for the rTOF models.

Comparison with previous work

The morphological analysis of this study suggests that the curvature and the in-plane angles are very similar for the RPA and the LPA branches. Average torsion is close to zero for both branches, while lower torsion is observed in the LPA branch of the models, also characterised with a higher average tortuosity. The minimum sphere radius is smaller for the LPA, indicating a smaller diameter of the LPA branch. Finally, a clockwise rotation is observed for the RPA branch by the average of the out-of-plane angles, and an anti-clockwise rotation for the LPA branch. These results are different from those reported on Section 5.3.1. for the TOF population, where curvature is found to be higher in the LPA branch of the models, the radius of the RPA is smaller compared to the LPA, the in-plane angle of the LPA branch is more acute, and there is a change and higher rotation in the out-of-plane angles of both the RPA and LPA branches. A steeper curvature and a smaller section area in the RPA branch, are also

reported in the study of Capuano and his co-workers (Capuano et al., 2019) in healthy pulmonary arteries.

The Reynolds, Womersley and Dean numbers were also calculated, and a smaller range of values was observed in healthy people, for all three parameters, as compared to the TOF population. The highest mean *Re* was found in the MPA, while RPA and LPA displayed similar *Re* values. On the contrary, RPA had the highest mean *Re* in the TOF models. *Wo* was approximately 20, which is very close to that reported in Section 5.3.2. for the rTOF patients. Finally, *De* was similar between the RPA and LPA and approximately 1250 in the healthy population, which is smaller than the *De* number reported for TOF, and especially that of the RPA branch (~1779 in the TOF study). The flow parameters, as calculated in this study, are in line with those presented in previous studies for the pulmonary arteries of healthy subjects (Sloth et al., 1994, Capuano et al., 2019, Loke et al., 2019).

The flow patterns developed in the pulmonary arterial models of the healthy population indicate there is not much disturbance of flow during the cardiac cycle. No recirculation of flow is visible on the LPA branch of the healthy models during peak flow (Fig. 6.4.i), and small recirculation areas were visible during deceleration at systole (Fig. 6.4.ii). The results are quite different compared to the flow patterns developed in the TOF population (Section 5.3.3.2.1.), as are the inlet flow waveforms, with higher and lower flow values noticed in the TOF patients. Recirculation of flow is visible in the LPA branch of the TOF models from peak flow (Fig. 5.9.i), and more complex flow patterns also develop during mid diastole (Fig. 5.9.iii). Similar results are reported in previous studies for both healthy and TOF models (Chern et al., 2012, Zhang et al., 2016, Capuano et al., 2019).

High $TAWSS_n$ was observed at the entrance of the RPA and LPA branches (Fig. 6.5), similar to TOF models (Fig. 5.13); nevertheless, much higher $TAWSS_n$ are reported in the latter (Fig. 5.13). More specifically, the TAWSS values (calculated from the cross-sections (α) and (γ)) reported in this study for the healthy models are up to 13.6 dynes/cm^2 (Fig. 6.6) which is comparable to those of healthy control volunteers presented in previous studies (up to 20.5 dynes/cm^2), and of patients with pulmonary arterial hypertension (up to 10.1 dynes/cm^2) (Tang et al., 2011, Tang et al., 2012). Elevated $TAWSS_n$ are noticed in the RPA branch of model 1 and the LPA branch of model 5 of the healthy cases, and are both found with elevated *Re* and *De*. This is in agreement with the trend noticed in the TOF models (Section 5.4). The importance of initial BCs is further highlighted when the TAWSS value in cross-sections (α) and (γ) is compared. Both in the rTOF (Table 5.8) and in the healthy subjects (Table 6.7) a higher mean TAWSS value is found in the RPA which is in the majority of cases the branch with the higher flow rate, and higher mean *Re* and mean *De* numbers. Finally, high OSI values were found in the pulmonary arteries of the healthy subjects (Fig. 6.6), similar to what is observed in the pulmonary junction of the rTOF patients (Fig. 5.14).

An anatomical average geometry was created based on the five subject-specific models, and averaged boundary conditions, derived from the patient-specific BCs, were assigned at the model. The streamlines of velocity, $TAWSS_n$ and OSI distribution of the average geometry are comparable with the results derived from the subject-specific simulations. Although only five models were used to compute the average geometry, it appears able to capture, and possible predict, the flow characteristics of the subject-specific models. That is in contrast with the average geometry derived from the TOF population, which cannot capture the variability of the $TAWSS_n$ observed in

that cohort of patients. The results, therefore, indicate that the anatomy of the pulmonary bifurcation does not vary greatly within healthy volunteers; the same is also true for the flow splits and flow waveforms (Table 6.1. and Fig. 6.1, respectively).

Clinical relevance

Understanding the haemodynamic environment of the normal pulmonary arteries is a key factor when assessing the diseased state of the branches, and parameters that could indicate when further surgical interventions are required, could be useful to clinicians. The morphology of the pulmonary arteries is considered one crucial factor in the flow development, mostly correlated with reversal of flow (Zhang et al., 2016, Chern et al., 2008, Chern et al., 2012), while the flow conditions affect the wall shear stress, a biomechanical factor related with the endothelial cell function and disease progression (Gimbrone 1995, Sabri et al., 2012, Tang et al., 2012). To that end, in this study a comparison between the healthy and diseased pulmonary arteries attempts to identify key characteristics that could be related to disease diagnosis and progression.

Starting with the demographic and haemodynamic data of all the patients, an increase in the RPA flow split is observed in the rTOF population (Tables 5.1, 6.1), with over 60% of the flow diverted to the branch in 4 out of 7 cases. The mean initial flow rates, as presented on Tables 5.2, 6.2, do not vary significantly between healthy and diseased individuals, but reversal of flow is higher in the rTOF patients (Figs. 5.2, 6.1). An increase is also visible in the maximum velocities developed in the daughter branches of the rTOF population, which are also smaller compared to the healthy pulmonary arteries. In addition, the calculated maximum *Re* and *De* numbers are found elevated in the rTOF patients (Tables 5.6, 6.6). Except from the curvature of the LPA, which is

increased in the rTOF population, higher absolute out-of-plane angles are noticed in both the RPA and LPA branches, related to the planarity of the branches. Finally, although the TAWSS at the inlet of the models (Tables 5.3, 6.3) is comparable between the healthy and rTOF patients, much higher TAWSS values are calculated in cross-sections (α) and (γ) of the rTOF models (Tables 5.8, 6.7, and Figs. 5.14, 6.6). The results of this study, therefore, suggest that some of the key parameters that affect the pulmonary environment are: 1) the flow splits and flow reversal from the initial flow conditions, and 2) the curvature of the LPA, the diameter and the planarity of both daughter branches from the morphological characteristics.

Limitations and Future Work

This study is limited to a small number of volunteers, nevertheless, all of them are healthy adults and 4 out of 5 males. Pulmonary vascular resistance and compliance are also neglected, but are compensated with the assignment of subject-specific flow splits at the models' outlets. Another limitation of this work is the inlet velocity, which is only varying in time, while the spatial variability of the flow, induced by the movement of the valve, is not captured. Future work will include a larger sample of healthy volunteers to validate the findings of this study, and will consider the pulmonary vascular resistance and compliance of both healthy and diseased population. The latter could potentially help clarify the remodelling mechanism in the pulmonary arteries due to diseased downstream conditions.

6.5. Concluding remarks

Geometrical and haemodynamic characterisation of the pulmonary arteries of healthy volunteers is considered important in order to gain knowledge of the normal flow patterns, and better understand pathological alterations. The morphological and flow features of the five healthy models of the pulmonary junction appeared rather similar, which is in contrast with what is observed in the repaired tetralogy of Fallot patients. In addition, the average geometry, although derived from a small cohort of healthy volunteers, appeared to capture well the flow characteristics of the subject-specific models. The differences in the morphological and flow characteristics of healthy and diseased pulmonary arteries, as identified in this study, could be potentially useful to clinicians and help with clinical decisions for further surgical interventions on haemodynamic indices.

Chapter 7

Conclusion and Future Work

7.1. Conclusions

The aim of this research was to investigate morphological and flow features in the pulmonary bifurcation of patients with tetralogy of Fallot, using computational fluid dynamic methods. The novelty of this work lies in the comprehensive investigation of various parameters, their correlation with the flow development and the comparison between healthy and diseased models. Three new studies relevant to the blood flow in the pulmonary arteries were published in the course of this PhD (Capuano et al., 2019, Conijn and Krings, 2021, Ling et al., 2021), which cited this research work, further highlighting how this is a timely study. The objectives were, first, to understand how the wall shear stress, flow splits and pressure, are affected by geometrical changes commonly found in the rTOF patients; second, to evaluate the effect of modelling parameters in the blood flow development; third, to correlate morphological patterns of curvature and tortuosity and flow characteristics of Reynolds and Dean number, with wall shear stresses and secondary flow patterns; and finally, using healthy subject-specific models, to better understand the alterations induced in the blood flow in diseased pulmonary arteries. The objectives were met but further studies are still required in larger cohorts of patients. Limitations of the work are also acknowledged throughout.

This thesis contributes towards a better understanding of the haemodynamics in the pulmonary bifurcation as follows:

(i) It demonstrates how the geometric location of the flow divider, which depends on the geometry and the branch origin, influences the WSS distribution along the inner wall of the bifurcation. A shifted stagnation point encourages differential pressures, while also, altered peripheral conditions affect the area of flow impingement.

(ii) It shows how downstream pressure conditions and peripheral resistance alter the flow in the pulmonary arteries and dictate the occurrence of different flow splits between the branches. WSS and pressure are found to decrease in the high flow-rate branch, and until a flow split of 12%:88%.

(iii) It quantifies the differences in the WSS when flow is assumed steady and a parabolic or a plug profile is assigned at the inlet. The effect of pulsatility is small, in agreement with previous studies, while a parabolic profile overestimates the WSS along the inner wall of the pulmonary bifurcation.

(iv) It demonstrates that the elasticity of the arterial wall has a small effect on the flow development in the pulmonary arterial models, while complex patterns are developed when the pulmonary valve is included.

(v) It shows variations in the WSS along the inner wall of the pulmonary bifurcation when different rheological models are assumed. The Newtonian model calculated the highest wall shear stresses.

(vi) It correlates higher curvature and tortuosity with more complex secondary flow patterns, and higher Reynolds and Dean numbers with increased regions of TAWSS.

(vii) It highlights the importance of patient-specificity and of spatial-varying flow in the models. Repaired TOF patients have unique morphologies and

therefore an anatomical mean geometry, or averaged boundary conditions cannot adequately characterise the flow development in this population of patients, but can nevertheless be useful for a model analysis.

(viii) It clearly shows the differences in the morphological and flow features between healthy volunteers and TOF patients. The RPA and LPA branches of the healthy population appear with similar curvature, branch angles, Reynolds and Dean numbers, and also flow splits. Under such conditions, the use of an anatomical average geometry was found to capture well the flow characteristics in the normal pulmonary arteries.

(ix) It highlights some key parameters of the pulmonary arteries which could be related to disease diagnosis and progression. These are the flow splits and flow reversal from the initial flow conditions and the curvature of the LPA, the diameter and the planarity of both daughter branches from the morphological characteristics.

7.2. Future Work

Several proposals can be made for future work that would increase the complexity of the simulations and could add to the flow characterisation of the pulmonary arteries. The focus of this study was only on the pulmonary bifurcation omitting the right ventricle, the pulmonary valve and multiple branches of the pulmonary tree. It would be of great value to investigate the blood flow in patient-specific models where all these features of the heart are included. Right ventricle hypertrophy and obstruction of the right outflow tract are two of the four TOF defects and, pulmonary regurgitation is a common complication in these patients. As already shown in the preliminary

investigation with the static valve, different flow patterns develop along the MPA with its presence, and the effect could be greater with a moving valve. In addition, including the wall motion could produce different flow patterns in the patient-specific simulations; however, the displacement of the fluid domain was relatively small when the pulmonary arterial wall was coupled in the idealised model. Further studies could validate, and further extend, the findings presented in this thesis.

Similarly, pulmonary vascular resistance, compliance and inductance could be used in the outlets of the models to better represent the downstream conditions. That also requires optimisation of these values for every patient-specific model, so that flow diverted to each branch matches the clinically observed flow splits. Clinical data are therefore essential both for the reconstruction of the models, but also for the extraction of flow information. Computational results can greatly vary based on the boundary conditions, and therefore, it is important to have appropriate BCs to characterise the flow environment.

In addition, clinical data are required to validate the computational outcomes. Part of this work investigated blood rheology and found that the WSS along the inner wall of the models varies with different rheological approximations. Further studies could compare clinical data with computational results, and identify the model which better captures the flow development in the pulmonary arteries.

Finally, this study is limited to a small number of subjects, and it could be extended to a larger cohort, and perhaps of different gender and age groups, to identify intraspecies variability. Longitudinal data are also missing and could be included in future studies.

Idealised geometries helped clarify some fundamental characteristics of the underlying flow in the pulmonary arteries, such as the elevated pressure in the LPA and the interplay between flow splits and differential pressures. On the other hand, subject-specific models demonstrated the significance of patient-specificity and the effect of curvature and tortuosity in the flow development. The findings of this thesis may help clinicians understand the haemodynamic environment of each patient's particular anatomy, and potentially disease progression, and facilitate their decision about the optimal timing for the pulmonary valve replacement. Furthermore, this work is hoped to benefit future research studies in the field.

Appendix A

Appendix

A.1 MATLAB® code for the three-element Windkessel model

The Windkessel equation implemented is given in Eq. (3.5). The constant β (Beta) is incorporated within the Windkessel equation when solved for pressure:

$$\beta = (RC) / dt$$

To calculate the percentages of difference (*PD*) the following formula is used:

$$PD = [(x_2 - x_1) / x_1] * 100$$

where x_2 the final value and x_1 the initial value.

```
%% Beginning of code
close all;clear all;clc;

        f_h=xlsread('40004_flowdata.xlsx', '1');          %Flow data from a healthy subject,
                                                          flow in ml/sec
Q_mpa=f_h(1:701, 1) )*1e-6;    % MPA flow from ml/sec to m^3/sec
Q_lpa=f_h(1:701, 4)*1e-6;              % LPA flow from ml/sec to m^3/sec
Q_rpa=f_h(1:701, 7)*1e-6;              % RPA flow from ml/sec to m^3/sec
T=f_h(1:701,1) /1000;          % time in sec
dt=0.001;                              %time step
T_Cardiac=T(end);                      % period of cardiac cycle
nt=T_Cardiac/dt;                       % number of time steps

%Pulmonary arteries: 20 mmHg is the normal pressure, and 1mmHg=133.33 Pa
Po_lpa=20*133.33;                      % pressure at outlet of LPA in Pa
Po_rpa=20*133.33;                      % pressure at outlet of RPA in Pa

Rp_lpa=4e7;            %proximal resistance assumed for LPA in Pa*s m^3
Rd_lpa=3e8;            %distal resistance assumed for LPA in Pa*s m^3
Clpa=1e-10;            % capacitance in m^3/Pa

Rp_rpa=4e7;    %proximal resistance assumed for RPA in Pa*s m^3
Rd_rpa=3e8;    %distal resistance assumed for RPA in Pa*s m^3
Crpa=1e-10;            % capacitance in m^3/Pa
```

```
Beta_lpa=(Rd_lpa*Clpa)/dt;
Beta_rpa=(Rd_rpa*Crpa)/dt;

% Windkessel Equation (Continuous)% Steps followed:
% 1. assume that Q_mpa=Q_lpa+Q_rpa and therefore Q_lpa=Q_mpa/2, and
Q_rpa=Q_mpa/2
% and we calculate pressure based on this assumption
% 2. use directly Q_lpa and Q_rpa to calculate pressure
% 3. compare the calculated pressures (also presented in the end of Appendix A.1)
% Step 1
%pressure calculation
%Backwards Euler for LPA
P_lpa_in(1)=Po_lpa;
P_lpa_in(2)=Po_lpa;

for n=2:nt-1

        P_lpa_in(n+1)=((P_lpa_in(n)*Beta_lpa)+((Q_mpa(n+1)/2)*(Rd_lpa+Rp_lpa*(1+Beta
        _lpa)))-((Q_mpa(n)/2)*(Rp_lpa*Beta_lpa)))/(1+Beta_lpa);

end

P_lpa_1=P_lpa_in.';                     %returns the transpose
T_1=T(1:699, 1);

%Backwards Euler for RPA
P_rpa_in(1)=Po_rpa;
P_rpa_in(2)=Po_rpa;

for n=2:nt-1

        P_rpa_in(n+1)=((P_rpa_in(n)*Beta_rpa)+((Q_mpa(n+1)/2)*(Rd_rpa+Rp_rpa*(1+Bet
        a_rpa)))-((Q_mpa(n)/2)*(Rp_rpa*Beta_rpa)))/(1+Beta_rpa);

end

P_rpa_1=P_rpa_in.';             %returns the transpose

% Step 2
%Backwards Euler for LPA
P_lpa_in2(1)=Po_lpa;
P_lpa_in2(2)=Po_lpa;

for n=2:nt-1

        P_lpa_in2(n+1)=((P_lpa_in2(n)*Beta_lpa)+((Q_lpa(n+1))*(Rd_lpa+Rp_lpa*(1+Beta_l
        pa)))-((Q_lpa(n))*(Rp_lpa*Beta_lpa)))/(1+Beta_lpa);

end
```

```
P_lpa_2=P_lpa_in2.';                %returns the transpose

% %Backwards Euler for RPA
P_rpa_in2(1)=Po_rpa;
P_rpa_in2(2)=Po_rpa;

for n=2:nt-1

        P_rpa_in2(n+1)=((P_rpa_in2(n)*Beta_rpa)+((Q_rpa(n+1))*(Rd_rpa+Rp_rpa*(1+Beta
        _rpa)))-((Q_rpa(n))*(Rp_rpa*Beta_rpa)))/(1+Beta_rpa);

 end

 P_rpa_2=P_rpa_in2.';               %returns the transpose

% Calculate the integrals of pressures using trapezoidal numerical integration
Pint_lpa_1=trapz(P_lpa_1);
Pint_lpa_2=trapz(P_lpa_2);
Pint_rpa_1=trapz(P_rpa_1);
Pint_rpa_2=trapz(P_rpa_2);
Q_int_rpa=trapz(Q_rpa);
Q_int_lpa=trapz(Q_lpa);

% Step 3 comparison of pressures
% Calculate percentage differences
Pl_1_Pl_2=(Pint_lpa_1- Pint_lpa_2)/ Pint_lpa _2*100     %Percentage difference of the LPA
                                                        pressures

Pr_1_Pr_2=(Pint_rpa_1- Pint_rpa _2)/ Pint_rpa _2*100  %Percentage difference of the RPA
                                                        pressures

Pl_2_Pr_2=(Pint_rpa_2- Pint_lpa_2)/ Pint_lpa_2*100     %Percentage difference between
                                                        the LPA and RPA pressures from Step 2

Qr_Ql=(Q_int_rpa-Q_int_lpa)/Q_int_lpa*100 %Percentage difference between the LPA and
                                                        RPA flow waveforms

% Plot pressures waveforms
figure
plot (T_1, P_lpa_1, 'Color',[0 0 0], 'LineWidth',1)
hold on
plot (T_1, P_lpa_2, '-.', 'Color',[0 0 0], 'LineWidth',3)
plot (T_1, P_rpa_1, '--' ,'Color',[0 0 0], 'LineWidth',3)
plot (T_1, P_rpa_2, ':' ,'Color',[0 0 0], 'LineWidth',3)
xlim([0 0.6]);
ylim([-0.3E04 5.5E04]);

% Plot flow waveforms
figure
plot (T_mpa, Q_mpa, 'Color',[0 0 0], 'LineWidth',3)
```

```
hold on
plot (T_mpa, Q_lpa, '-.', 'Color',[0 0 0], 'LineWidth',3)
plot (T_mpa, Q_rpa, '--' ,'Color',[0 0 0], 'LineWidth',3)
xlim([0 0.6]);
ylim([-0.3E-04 3.5E-04]);

%% End of code
```

Running the code

The pressure as calculated at Step 1 for the LPA and RPA branches, where it is assumed that $Q_{LPA}=Q_{RPA}=(Q_{MPA}/2)$, was identical. This is reasonable as it is also assumes the same RCR values, for both daughter branches. When the flow data from the LPA and RPA branches was used to calculate the pressure (Step 2), higher pressures are noticed at the RPA, which is also the branch with higher flow splits (56.2%). A percentage difference of approximately 45.6% and 6.1% was found when the pressure as calculated at Step 1 was compared with the pressure as calculated at Step 2, for the LPA and RPA branches, respectively. The difference between the LPA and RPA pressure, as computed at Step 2, was found approximately 37.2%, which is similar to the 38% difference calculated based on the integrals of the flow waveforms.

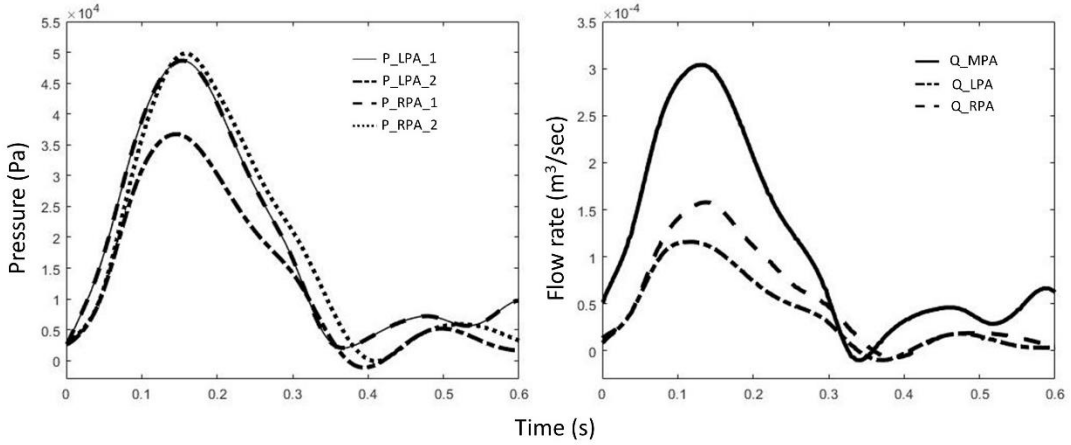

A.2 codedFixedValue boundary conditions in OpenFOAM®

A2.1. Parabolic and sinusoidal velocity profile:

First, the coordinates of the patch (inlet) need to be identified. The formula to implement the parabolic profile is:

$$U_{max}(1 - \frac{(y - p\_ctr)^2}{p\_r^2})$$

where, p_ctr patch midpoint (centre) and p_r patch semi-height or radius. Surface normal for the idealised model was along the y-axis and patch midpoint was at (0,0,0).

The formula for the unsteady flow is given by:

$$U_{max}(1 - \frac{(y - p\_ctr)^2}{p\_r^2})[1 - Asin(wt)]$$

The body of the boundary condition is:

```
type     codedFixedValue;
                value uniform (0 0 0);
                redirectType parabolicInlet;      //unique name of the boundary condition

                codeOptions                       //compilation options
                    #{
                        -I$(LIB_SRC)/finiteVolume/lnInclude \
                        -I$(LIB_SRC)/meshTools/lnInclude
                    #};

                codeInclude                       //files needed for compilation
                    #{
                        #include "fvCFD.H"
                        #include <cmath>
                        #include <iostream>
                    #};

                Code                              //actual implementation of BC
```

```
#{
        const fvPatch& boundaryPatch = patch();          //give
access to mesh and field information in the patch
        const vectorField& Cf= boundaryPatch.Cf();
        vectorField& field = *this;          //initialise vector field

        scalar U_0 = 0.15, p_ctr = 0, p_r = 0.013; //constants

        scalar t = this->db().time().value(); // this should be added
to access time in unsteady cases
        forAll(Cf, faceI) // for steady flow
        {
                field[faceI]=vector(0,       U_0*(1-(pow(Cf[faceI].x()-
p_ctr,2))/(p_r*p_r)), 0);
        }
        //Alternatively, for the sinusoidal variation of flow
        forAll(Cf, faceI)
        {
                field[faceI]=vector(0,U_0*(1-(pow(Cf[faceI].x()-
p_ctr,2))/(p_r*p_r))*(1+sin(t)), 0);
        }
#};
```

A.2.2 Flow splits:

```
type codedFixedValue;
                value uniform (0 0 0);
                redirectType     flowSplit;


                code
                #{
                        scalar flowRatio=0.56;                  //flow rate
                        const word refPatchName="inflow";       //name of reference patch
                // ------------------------------------------------//
                        const scalar& pi = constant::mathematical::pi;


                        const fvPatchVectorField& thisBF = *this; //access boundary mesh information and initialise vector field
                        scalar thisPatchArea = gSum(thisBF.patch().magSf()); //global sum of this patch's face area magnitudes
                        vector nf = gSum(thisBF.patch().magSf()*thisBF.patch().nf())/thisPatchArea;    //normal face vector


                        const volVectorField& U = thisBF.db().lookupObject<volVectorField>("U");              //lookup and return velocity from objectRegistry for this patch
                        const surfaceScalarField& phi = thisBF.db().lookupObject<surfaceScalarField>("phi");      //lookup and return phi from objectRegistry for this patch
                        const label refPatchLabel = U.mesh().boundaryMesh().findPatchID(refPatchName); //return boundary mesh of the reference patch
                        const fvPatchVectorField& refBF = U.boundaryField()[refPatchLabel];                   //initialise velocity field of reference patch
                        const fvsPatchScalarField& refBflux = phi.boundaryField()[refPatchLabel];       //initialise phi field of reference patch
```

scalar refFlowRate = gSum(refBflux); //global sum of the flow rate of the reference patach

//Info << nl << "Flow rate at" << refPatchName

// << ":" << refFlowRate << endl;

operator==(-nf*flowRatio*refFlowRate/thisPatchArea); //returns velocity based on the flow ratio specified and the flow rate retrieved from the reference patch

#};

Bibliography

Alegre-Martínez C., Choi K.-S., Tammisola O., McNally D., 2019. On the axial distribution of plaque stress: Influence of stenosis severity, lipid core stiffness, lipid core length and fibrous cap stiffness. Medical Engineering and Physics. 68, 76-84.

Al Habib H.F., Jacobs J.P., Mavroudis C., Tchervenkov C.I., O'Brien S.M., Mohammadi S., Jacobs M.L., 2010. Contemporary Patterns of Management of Tetralogy of Fallot: Data from the Society of Thoracic Surgeons Database. Ann Thorac Surg, 90, 813-820.

Alharbi Y., Otton J., Muller D.W.M., Geelan-Small P., Lovell N.H., Abed A.A., Dokos S., 2020. Predicting the outcome of transcatheter mitral valve implantation using image-based computational models. Journal of Cardiovascular Computed Tomography, 14, 335-342.

Ammash N.M., Dearani J.A., Burkhart H.M., Connolly H.M., 2007. Pulmonary Regurgitation after Tetralogy of Fallot Repair: Clinical Features, Sequalae, and Timing of Pulmonary Valve Replacement. Congenit Hear Dis. 2, 386-403.

Antiga L., Piccinelli M., Botti L., Ene-Iordache B., Remuzzi A., Steinman D.A., 2008. An image-based modeling framework for patient-specific computational hemodynamics. Medical and Biological Engineering and Computing, 46, 1097-1112.

Apitz C., Webb G.D., Redington A.N., 2009. Tetralogy of Fallot. Lancet. 374, 1462-1471.

Arbia G., Corsini C., Moghadam M.E., Marsden A.L., Migliavacca F., Pennati G., Hsia T.Y., Vignon-Clementel I.E., 2014. Numerical blood flow simulation in surgical corrections: what do we need for an accurate analysis?. Journal of Surgical Research. 186, 44-55.

Arimon J.A., 2006. Numerical modelling of pulse wave propagation in the cardiovascular system: development, validation and clinical applications. PhD Thesis. Imperial College London, London.

Babu-Narayan S., Gatzoulis M.A., 2018. Tetralogy of Fallot. In: Diagnosis and Management of Adult Congenital Heart Disease, Elsevier. 474-488.

Bächler P., Pinochet N., Sotelo J., Crelier G., Irarrazaval P., Tejos C., Uribe S., 2013. Assessment of normal flow patterns in the pulmonary circulation by using 4D magnetic resonance mapping. Magnetic Resonance Imaging. 31, 178-188.

Bailliard F., Anderson R.H., 2009. Tetralogy of Fallot. Orphanet Journal of Rare Diseases, 4, 1-10.

Ballyk, P. D., Steinman, D. A., & Ethier, C. R., 1994. Simulation of non-Newtonian blood flow in an end-to-side anastomosis. Biorheology. 31 (5), 565–586.

Baretta A., Corsini C., Yang W., Vignon-Clementel I.E., Marsden A.L., Feinstein J.A., Hsia T.-Y., Dubini G., Migliavacca F., Pennati G., 2011. Virtual surgeries in patients with congenital heart disease: a multi-scale modelling test case. Phil. Trans. R. Soc. 369, 4316-4330.

Bazilevs Y., Gohean J.R., Hughes T.J.R., Moser R.D., Zhang Y., 2009. Patient-specific isogeometric fluid-structure interaction analysis of thoracic aortic blood flow due to implantation of the Jarvik 2000 left. Comput. Methods Appl. Engrg. 198, 3534-3550.

Bazilevs Y., Hsu M.C., Benson D.J., Sankaran S., Marsden A.L., 2009 Computational fluid-structure interaction: methods and application to a total cavopulmonary connection. Comput. Mech. 45, 77-89.

Benson D.W., Silberbach G.M., Kavanaugh-McHugh A., Cottrill C., Zhang Y., Riggs S., Smalls O., Johnson M.C., Watson M.S., Seidman J.G., Seidman C.E., Plowden J., Kugler J.D., 1999. Mutations in the cardiac transcription factor NKX2.5 affect diverse cardiac developmental pathways. J Clin Invest. 104 (11), 1567-73.

Bhakade S., Kumbhar S., Mohite Y., Prasad K., 2016. A Review on Fluid Structure Interaction Analysis Methodology. International Journal of Trend in Research and Development. 3, 2394-9333.

Bhansali S., Phoon C., 2021. Truncus Arteriosus. In: StatPearls [Internet]. Treasure Island (FL). StatPearls Publishing.

Black S., Ritos K., Maclean C., Kazakidi A., 2020. P14 Blood flow analysis of the aortic arch using computational fluid dynamics in a coupled 3D-0D framework. Heart. 106:A10-A11.

Blazek J., 2015. Chapter 11 - Principles of Grid Generation. In: Computational Fluid Dynamics: Principles and Applications. Butterworth-Heinemann. Third Edition. 357-393.

Botnar R., Rappitsch G., Scheidegger MB., Liepsch D., Perktold K., Boesiger P., 2000. Hemodynamics in the Carotid Artery Bifurcation: A Comparison Between Numerical Simulations and *In Vitro* MRI Measurements. J Biomech. 33 (2), 137-144.

Boumpouli M., Danton M., Gourlay T., Kazakidi A., 2018. Hemodynamics in the Pulmonary Bifurcation in Relation to Adults with Congenital Heart Disease: Effect of Branching Angle and Origin. 6th European Conference on Computational Mechanics-7th European Conference on Computational Fluid Dynamics. 1-12.

Boumpouli M, Danton M, Gourlay T, Kazakidi A., 2020. Understanding the blood flow in realistic and idealised models of the pulmonary bifurcation. Heart Journal. 106, A3–4.

Boumpouli M, Danton MHD, Gourlay T, Kazakidi A., 2020. Blood flow simulations in the pulmonary bifurcation in relation to adult patients with repaired tetralogy of Fallot. Med Eng Phys. 85, 123-138.

Bove E.L., Migliavacca F., de Level M.R., Balossino R., Pennati G., Lloyd T.R., Khambadkone S., Hsia T.-Y., Dubini G., 2008. Use of mathematic modeling to compare and predict hemodynamic effects of the modified Blalock–Taussig and right ventricle–pulmonary artery shunts for hypoplastic left heart syndrome. J Thorac Cardiovasc Surg. 136, 12-20.

Breitenbach J.E., 2007. Putting an end to perfusion confusion. Nursing Made Incredible Easy. 5, 50-60.

Brickner M.E., Hillis L.D., Lange R.A., 2000. Congenital Heart Disease in Adults: First of Two Parts. The New England Journal of Medicine. 342, 256-263.

Brickner M.E., Hillis L.D., Lange R.A., 2000. Congenital Heart Disease in Adults: Second of Two Parts. The New England Journal of Medicine. 342, 334-342.

Bronzino J., 2000. In: The Biomedical Engineering Handbook, Second Edition. CRC Press LLC. 30-33.

Bruse J.L., McLeod K., Biglino G., Ntsinjana H.N., Capelli C., Hsia T.-Y., Sermesant M., Pennec X., Taylor A.M., Schievano S., 2016. A statistical shape modelling framework to extract 3D shape biomarkers from medical imaging data: assessing arch morphology of repaired coarctation of the aorta. BMC Medical Imaging, 16, 1-19.

Boiron O., Deplano V., Pelissier R., 2007. Experimental and numerical studies on the starting effect on the secondary flow in a bend. Journal of Fluid Mechanics, 574, 109-129.

Bone A., Colliot O., Durrleman S., 2018. Learning Distributions of Shape Trajectories from Longitudinal Datasets: A Hierachical model on a manifold of diffeomorphisms. IEEE/CVF Conference on Computer Vision and Pattern Recognition, pp9271-9280.

Bordones A.D., Leroux M., Kheyfets V.O., Wu Y.-A., Chen C.-Y., Final E.A., 2018. Computational Fluid Dynamics Modeling of the Human Pulmonary Arteries with Experimental Validation. Annals of Biomedical Engineering. 46 (9), 1309-1324.

Botney M.D., 1999. Role of hemodynamics in pulmonary vascular remodeling: implications for primary pulmonary hypertension. Am. J. Respir. Crit. Care Med. 159, 361–364.

Buechel ER, Dave HH, Kellenberger CJ, Dodge-Khatami A, Pretre R, Berger F, Bauersfeld U., 2005. Remodelling of the right ventricle after early pulmonary valve replacement in children with repaired tetralogy of Fallot: assessment by cardiovascular magnetic resonance. Eur Heart J. 26, 2721-2727.

Burattini R, Natalucci S., 1998. Complex and frequency-dependent compliance of viscoelastic windkessel resolves contradictions in elastic windkessels. Med Eng Phys. 20, 502-514.

Capelli C., Sauvage E., Giusti G., Bosi GM., Ntsinjana H., Carminati M., Derrick G., Marek J., Khambadkone S., Taylor AM., Schievano S., 2018. Patient-specific simulations for planning treatment in congenital heart disease. Interface Focus. 8 (1), 20170021.

Capuano F., Loke Y.H., Cronin I., Olivieri L.J., Balaras E., 2019. Computational Study of Pulmonary Flow Patterns after Repair of Transposition of Great Arteries. J. Biomech. Eng. 141, 051008.

Capuano F., Loke Y.-H., Balaras E., 2019. Blood Flow Dynamics at the Pulmonary Bifurcation. Fluids. 4, 1-20.

Caretto L.S., Gosman A.D., Patankar S.V., Spalding D.B., 1973. Two calculation procedures for steady, three-dimensional flows with recirculation. In: Cabannes H., Temam R. (eds) Proceedings of the Third International Conference on Numerical Methods in Fluid Mechanics. Lecture Notes in Physics, vol 19. Springer, Berlin, Heidelberg.

Caro C.G., Pedley T.J., Schroter R.C., Seed W.A., 1978. The Mechanics of the Circulation. Oxford University Press.

Caselles, V., Catte, F., Coll, T., Dibos, F., 1993. A geometric model for active contours. Numer. Math. 66, 1 –31.

Caselles, V., Kimmel, R., Sapiro, G., 1997. Geodesic active contours. Int. J. Comput. Vis. 22, 61– 79.

Caughey T.K., 1960. Classical Normal Modes in Damped Linear Dynamic Systems. J Appl Mech. 27 (2), 269-271.

Cengel Y.A., Cimbala J.M., 2014. Fluid mechanics: fundamentals and applications. New York McGraw-Hill.

Cetta F., Lichtenberg R.C., Clark S.E., 1992. Adults with Congenital Heart Disease. Comprehensive Therapy. 18, 33-37.

Chaturvedi R.R., Kilner P.J., White P.A., Bishop A., Szwarc R., Redington A.N., 1997. Increased Airway Pressure and Simulated Branch Pulmonary Artery Stenosis Increase Pulmonary Regurgitation After Repair of Tetralogy of Fallot. Circulation. 95, 643-649.

Chaturvedi R.R., Redington A.N., 2007. Pulmonary Regurgitation in Congenital Heart Disease. Heart. 93, 880-889.

Chen S.S.M., Kilner P.J., 2013. Unilateral pulmonary artery branch stenosis: Diastolic prolongation of forward flow appears to maintain flow to the affected lung if the pulmonary valve is competent. International Journal of Cardiology. 168, 3698-3703.

Chen G., Xiong Q., Morris P.J., Paterson E.G., Sergeev A., Wang Y.-C., 2014. OpenFOAM for Computational Fluid Dynamics. Notices of the AMS. 61, 354-363.

Cheng C.P, Herfkens R.J., Taylor C.A., Feinstein J.A., 2005. Proximal pulmonary artery blood flow characteristics in healthy subjects measured in an upright posture using MRI: The Effects of Exercise and Age. Journal of Magnetic Resonance Imaging. 21, 752-758.

Chern M.J., Wu M.T., Wang H.L., 2008. Numerical investigation of regurgitation phenomena in pulmonary arteries of Tetralogy of Fallot patients after repair. Journal of Biomechanics. 41, 3002-3009.

Chern M.J., Wu M.T., Wei-Her S., 2012. Numerical Study for Blood Flow in Pulmonary Arteries after Repair of Tetralogy of Fallot. Computational and Mathematical Methods in Medicine. 2012, 1-18.

Chnafa C., Brina O., Pereira V.M., Steinman D.A., 2018. Better Than Nothing: A Rational Approach for Minimizing the Impact of Outflow Strategy on Cerebrovascular Simulations. American Journal of Neuroradiology. 39, 337-343.

Cho, Y. I., & Kensey, K. R., 1991. Effects of the non-Newtonian viscosity of blood on flows in a diseased arterial vessel. Part 1: Steady flows. Biorheology. 28 (3-4), 241–262.

Chowdhury I., Dashgupta S., 2003. Computation of Rayleigh Damping Coefficients for Large Systems. Int. J. Space Struct. 43, 6855-6868.

Churchill SW., 1977. Friction Factor Equation Spans All Fluid Flow Regimes. Chem Eng J. 84, 91–92.

Colin S., 2014. Chapter 2- Single-Phase Gas Flow in Microchannels. In: Heat Trasfer and Fluid Flow in Minichannels and Microchannels. Butterworth-Heinemann. Second Edition. 11-102.

Conijn M., Krings GJ., 2021. Computational Analysis of the Pulmonary Arteries in Congenital Heart Disease: A Review of the Methods and Results. Computational and Mathematical Methods in Medicine. 2021, Article ID 2618625, 10 pages.

Cookson A.N, Doorly D.J., Sherwin S.J., 2019. Efficiently Generation Mixing by Combining Differing Small Amplitude Helical Geometries. Fluids, 4, 1-26.

Davlouros P.A., Kilner P.J., Hornung T.S., Li W., Francis J.M., Moon J.C.C., Smith G.C., Tat T., Pennell D.J., Gatzoulis M.A., 2002. Right Ventricular Function in Adults With Repaired Tetralogy of Fallot Assessed With Cardiovascular Magnetic Resonance Imaging: Detrimental Role of Right Ventricular Outflow Aneurysms or Akinesia and Adverse Right-to-Left Ventricular Interaction. Journal of the American College of Cardiology. 40, 2044-2052.

Dean W.R., 1928. Fluid Motion in a Curved Channel. Proceeding of the Royal Society of London. Series A, 121, 402-420.

Defraeye T., Blocken B., Carmeliet J., 2010. CFD analysis of convective heat transfer at the surfaces of a cube immersed in a turbulent boundary layer. International Journal of Heat and Mass Transfer. 53, 297-308.

de Leval M.R., Kilner P., Gewillig M., Bull C., McGoon D.C., 1988. Total cavopulmonary connection: A logical alternative to atriopulmonary connection for complex Fontan operations: Experimental studies and early clinical experience. J Thorac Cardiovasc Surg. 96 (5), 682-695.

Digilio M.C., Marino B., Giannotti A., Toscano A., Dallapiccola B., 1997. Recurrence risk figures for isolated tetralogy of Fallot after screening for 22q11 microdeletion. J Med Genet. 34 (3), 188-190.

Donea J., Huerta A., Ponthot J.-P., Rodríguez-Ferran A., 2004. Arbitrary Lagrangian-Eulerian Methods. In: The Encyclopedia of Computational Mechanics. Wiley, 1, 413-437.

Doyle M.G., Crawford S.A., Osman E., Eisenberg N., Tse L., Amon C.H., Forbes T.L., 2018. Analysis of Iliac Artery Geometric Properties in Fenestrated Aortic Stent Graft Rotation, 52, 188-194.

Drikakis D., Frank M., Tabor G., 2019. Multiscale Computational Fluid Dynamics. Energies. 12 (17), 3272.

D'Souza G.A., Banerjee R.K., Taylor M.D., 2018. Evaluation of pulmonary stenosis in congenital heart disease patients using functional diagnostic parameters: An *in vitro* study. Journal of Biomechanics. 81, 58-67.

Dubini G., de Leval M.R., Pietrabissa R., Montevecchi F.M., Fumero R., 1996. A numerical fluid mechanical study of repaired congenital heart defects. Application to the total cavopulmonary connection. J. Biomech. 29 (1), 111–121.

Durrleman S., Prastawa M., Charon N., Korenberg J.R., Joshi S., Gerig G., Trouvé A., 2014. Morphometry of anatomical shape complexes with dense deformations and sparse parameters. Neuroimage, 101, 35-49.

Ensley A.E., Ramuzat A., Healy T.M., Chatzimavroudis G.P., Lucas C., Sharma S., Pettigrew R., Yoganathan A.P., 2000. Fluid mechanic assessment of the total cavopulmonary connection using magnetic resonance phase velocity mapping and digital particle image velocimetry. Ann. Biomed. Eng. 28, 1172–1183.

Evergen P., Fuchs L., Revstedt J., 2010. On the secondary flow through bifurcating pipes. Physics of Fluids, 22, 1-15.

Ferziger J.H., Perić M., 2002. Computational Methods for Fluid Dynamics. 3rd Edition. Springer-Verlag.

Formaggia L., Quarteroni A., Veneziani A., 2009. Physiology and pathology of the cardiovascular system: a physical perspective. In: Cardiovascular Mathematics. Modeling and

simulation of the circulatory system. Springer. Volume 1. 1-45.

Frigiola A, Tsang V, Bull C, Coats L, Khambadkone S, Derrick G, Mist B, Walker F, van Doorn C, Bonhoeffer P, Taylor AM., 2008. Biventricular response after pulmonary valve replacement for right ventricular outflow tract dysfunction: is age a predictor of outcome? Circulation. 118, S182-90.

Gabe I.T., Gault J.H., Ross J., Mason D.T., Mills C.J., Schillingford J.P., Braunwald E., 1969. Measurements of instantaneous blood flow velocity and pressure in conscious man with a catheter-tip velocity probe. Circulation. 40, 603-614.

Galié N., Torbicki A., Barst R., Dartevelle P., Haworth S., Higenbottan T., Dartevelle P., Haworth S., Higenbottam T., Olschewski H., Peacock A., Pietra G., Rubin L.J., Simonneau G., Priori S.G., Garcia M.A., Blanc J.J., Budaj A., Cowie M., Dean V., Deckers J., Burgos E.F., Lekakis J., Lindahl B., Mazzotta G., McGregor K., Morais J., Oto A., Smiseth O.A., Barbera J.A., Gibbs S., Hoeper M., Humbert M., Naeije R., Pepke-Zaba J.; Task Force., 2004. Guidelines on diagnosis and treatment of pulmonary arterial hypertension: the task force on diagnosis and treatment of pulmonary arterial hypertension of the European Society of Cardiology. Eur. Heart J. 25, 2243–2278.

Geva T., 2011. Repaired tetralogy of Fallot: the roles of cardiovascular magnetic resonance in evaluating pathophysiology and for pulmonary valve replacement decision support. Journal of Cardiovascular Magnetic Resonance. 13, 1-24.

Geva T., 2013. Indications for Pulmonary Valve Replacement in Repaired Tetralogy of Fallot: The Quest Continues. Circulation. 128, 1855-1857.

George H.F., Quresh F., 2013. Newton’s Law of Viscosity, Newtonian and Non-Newtonian Fluids. In: Wang Q.J., Chung YW. (eds) Encyclopedia of Tribology. Springer, Boston, MA.

Geuzaine C., Remacle J.-F., 2009. Gmsh: a three-dimensional finite element mesh generator with built-in pre- and post-processing facilities. International Journal for numerical methods in engineering, 0, 1-24.

Ghio S., Schirinzi S., Pica S., 2015. Pulmonary arterial compliance: How and why should we measure it?. Global Cardiology Science and Practise. 58.

Gilmanov A., Sotiropoulos F., 2005. A hybrid cartesian/immersed boundary method for simulating flows with 3d, geometrically complex, moving bodies. J Comput Phys. 207, 457-492.

Gimbrone M.A., 1995. Vascular Endothelium: An Integrator of Pathophysiologic Stimuli in Atherosclerosis. Am J Cardiol. 75, 67B-70B.

Goldberger A.L., Goldberger Z.D., Shvilkin A., 2018. Chapter 7 - Atrial and Ventricular Enlargement. In: Goldberger's Clinical Electrocardiography (Ninth Edition), Elsevier. 50-60.

Griffin H.R., Töpf A., Glen E., Zweier C., Stuart A.G., Parsons J., Peart I., Deanfield J., O'Sullivan J., Rauch A., Scambler P., Burn J., Cordell H.J., Keavney B., Goodship J.A., 2010. Systematic survey of variants in TBX1 in non-syndromic tetralogy of Fallot identifies a novel 57 base pair deletion that reduces transcriptional activity but finds no evidence for association with common variants. Heart. 96 (20), 1651-5.

Grinberg L., Karniadakis G.E., 2008. Outflow Boundary Conditions for Arterial Networks with Multiple Outlets. Annals of Biomedical Engineering. 36, 1496-1514.

Grochowski C.M., Loomes K.M., Spinner N.B., 2016. Jagged1 (JAG1): Structure, expression,

and disease associations. Gene. 576(1 Pt 3), 381-4.

Gu H., Alghamdi A.A., van Arsdell G.S., 2018. Double-Outlet Right Ventricle. In: Diagnosis and Management of Adult Congenital Heart Disease, Elsevier. 553-561.

Guibert R., McLeod K., Caiazzo A., Mansi T., Fernandez M.A., Sermesant M., Pennec X., Vignon-Clementel I., Boudjemline Y., Gerbeau J.F., 2014. Group-wise construction of reduced models for understanding and characterization of pulmonary blood flows from medical images. Medical Image Analysis. 18, 63-82.

Gurtin E.M., 1982. An introduction to continuum mechanics. Academic press. 158.

Hanna B.D., 2005. Blood flow in normal and diseased pulmonary arteries. In Ventricular Function and Blood Flow in Congenital Heart Disease;Wiley-Blackwell: Hoboken, NJ, USA, 275–285.

Harris M.A., Whitehead K.K., Gillespie M.J., Liu T.Y., Cosulich M.T., Shin D.C., Goldmuntz E., Weinberg P.M., Fogel M.A., 2011. Differential Branch Pulmonary Artery Regurgitant Fraction is a Function of Differential Pulmonary Arterial Anatomy and Pulmonary Vascular Resistance. Cardiovascular Imaging. 4, 506-513.

Hashemi Z., 2018. The Lattice Boltzmann Modeling: Solving Complex Flows Including Biological Cells, In: Numerical Methods and Advanced Simulation in Biomechanics and Biological Processes. Academic Press.

Heiberg E., Sjögren J., Ugander M., Carlsson M., Engblom H., Arheden H., 2010. Design and validation of Segment – freely available software for cardiovascular image analysis. BMC Medical Imaging, 10, 1-13.

Hidesato I.T.O., 1987. Flow in Curved Pipes. JSME International Journal, 30, 543-552.

Holmes D.G., Snyder D.D., 1988. The generation of unstructured triangular meshes using Delaunay triangulation. In: Numerical Grid Generation in Computational Fluid Dynamics. Swansea: Pineridge. 643–652.

Holzmann T., 2016. Mathematics, Numerics, Derivations and OpenFOAM®, URL www.holzmann-cfd.de.

Houzeaux G., Principe J., 2008. A variational subgrid scale model for transient incompressible flows. International Journal of Computational Fluid Dynamics. 22 (3), 135-152.

Houzeaux G., Vázquez M., Aubry R., Cela J., 2009. A massively parallel fractional step solver for incompressible flows. J Comput Phys. 228 (17), 6316–6332.

Houzeaux G., Aubry R., Vázquez M., 2011. Extension of fractional step techniques for incompressible flows: the preconditioned orthomin(1) for the pressure schur complement. Comput Fluids. 44, 297–313.

Hu H.H., 1996. Direct Simulation of Flows of Solid-Liquid Mixtures. Int. J. Multiphase Flow. 22 (2), 335-352.

Hughes T.J.R., Liu W.K., Zimmermann T.K., 1981. Lagrangian-Eulerian finite element formulation for incompressible viscous flows. Computer Methods in Applied Mechanics and Engineering. 29 (3), 329-349.

Humphrey J., 2008. Mechanisms of arterial remodeling in hypertension: coupled roles of wall shear and intramural stress. Hypertension. 52 (2), 195–200.

Hunter W., 1784. Medical observations and inquiries. London: Private publication. 417-419.

Hunter K.S., Feinstein J.A., Ivy D.D., Shandas R., 2010. Computational Simulation of the Pulmonary Arteries and Its Role in the Study of Pediatric Pulmonary Hypertension. Prog. Pediatr. Cardiol. 30 (1-2), 63-69. Ilbawi M.N., Idriss F.S., DeLeon S.Y., Muster A.J., Gidding S.S, Berry T.E., Paul M.H., 1987. Factors that exaggerate the deleterious effects of pulmonary insufficiency on the right ventricle after tetralogy repair. The Journal of Thoracic and Cardiovascular Surgery. 93, 36-44.

Hyde-Linaker G., Black R., Kazakidi A., 2020. P2 Fluid-Structure Interaction simulation of multiple bifurcations in arm under transient boundary conditions due to Flow mediated dilation. Heart. 106:A6.

Iaizzo P.A., 2015. General Features of Cardiovascular System. In: Handbook of Cardiac Anatomy, Physiology, and Devices. Springer, Third Edition, 3-12.

Ishigaki M., Abe S., Sibamoto Y., Yonomoto T., 2017. Influence of mesh non-orthogonality on numerical simulation of buoyant jet flows. Nuclear Engineering and Design. 314, 236-337.

Issa R.I., 1986. Solution of the implicitly discretised fluid flow equations by operator-splitting. Journal of Computational Physics. 62, 40-65.

Jager GN, Westerhof N, Noordergraaf A., 1956. Oscillatory Flow Impedance in Electrical Analog of Arterial System: Representation of Sleeve Effect and Non-Newtonian Properties of Blood. Circ Res. 16, 121-133.

Jang W.S, Kim W.-H., Cho S., 2017. Effects of Angle Correction Angioplasty for Pulmonary Artery Stenosis With Tetralogy of Fallot. Ann Thorac Surg. 103, 862-868.

Janiga G., Berg P., Sugiyama S., Kono K., Steinman DA., 2015. The computational fluid dynamics rupture challenge 2013 - Phase I: Prediction of rupture status in intracranial aneurysms. AJNR Am J Neuroradiol. 36 (3), 530-536.

Jasak H., Jemcov A., Tuković Ž., 2007. OpenFOAM: A C++ Library for Complex Physics Simulations. International Workshop on Coupled Methods in Numerical Dynamics.

Jasak H., 2009. OpenFOAM: Open source CFD in research and industry. Inter J Nav Archit Oc Engng. 1, 89-94.

Jin S., Oshinski J., Giddens D.P., 2003. Effects of Wall Motion and Compliance on Flow Patterns in the Ascending Aorta. Journal of Biomechanical Engineering. 125, 347-354.

Johnson L.R., Rush J.W., Turk J.R., Price E.M., Laughlin M.H., 2001. Short-term exercise training increases ACh-induced relaxation and eNOS protein in porcine pulmonary arteries. J. Appl. Physiol. 90, 1102–1110.

Johnston L., Allen R., Hall-Barrientos P., Mason A., Kazakidi A., 2020. P13 Computational haemodynamics in turner syndrome patient-specific aortae with PC-MRI obtained boundary conditions. Heart. 106:A10.

Johnston L., Allen R., Hall-Barrientos P., Mason A., Kazakidi A., 2021. Hemodynamic Abnormalities in the Aorta of Turner Syndrome Girls. Front Cardiovasc Med. doi: 10.3389/fcvm.2021.670841.

Kang I.-S., Redingtin A.N., Benson L.N., Macgowan C., Valsangiacomo E.R., Roman K., Kellenberger C.J., Yoo S.-J., 2003. Differential Regurgitation in Branch Pulmonary Arteries After Repair of Tetralogy of Fallot. A Phase-Contrast Cine Magnetic Resonance Study. Circulation. 107, 2938-2943.

Kanokjaruvijit K., Donprai-on T., Phanthura N., Noidet P., Siripokharattana J., 2017. Wall shear stress and velocity distributions in different types of stenotic bifurcations. Journal of Mechanical Science and Technology. 31, 2339-2349.

Karimi S., Dabagh M., Vasava P., Dadvar M., Dabir B., Jalali P., 2014. Effect of rheological models on the hemodynamics within human aorta: CFD study on CT image-based geometry. Journal of Non-Newtonian Fluid Mechanics. 207, 45-52.

Katritsis D., Kaiktsis L., Chaniotis A., Pantos J., Efstathopoulos E.P., Marmarelis V., 2007. Wall shear stress: Theoretical considerations and methods of measurement. Progress in Cardiovascular Disease. 49, 307-329

Katritsis D.G., Theodorakakos A., Pantos I., Andriotis A., Efstathopoulos E.P., G. Siontis, Karcanias N., Redwood S., Gavaises M., 2010. Vortex formation and recirculation zones in left anterior descending artery stenoses: computational fluid dynamics analysis. Physics in Medicine and Biology. 55, 1395-1411.

Kazakidi A., 2008. Computational studies of blood flow at arterial branches in relation to the localisation of atherosclerosis. Thesis. Imperial College London.

Kazakidi A., Sherwin S.J., Weinberg P.D., 2009. Effect of Reynolds number and flow division on patterns of haemodynamic wall shear stress near branch points in the descending thoracic aorta. Journal of the Royal Society Interface. 6, 539-548.

Kazakidi A., Plata A.M., Sherwin S.J., Weinberg P.D., 2011. Effect of reverse flow on the pattern of wall shear stress near arterial branches. Journal of the Royal Society Interface. 8, 1594-1603.

Kazakidi A., Tsakiris D.P., Angelidis D., Sotiropoulos F., Ekaterinaris J.A., 2015. CFD study of aquatic thrust generation by an octopus-like arm under intense prescribed deformations. Computers & Fluids. 115, 54-65.

Kheyfets VO., O'Dell W., Smith T., Reilly JJ., Finol EA., 2013. Considerations for Numerical Modeling of the Pulmonary Circulation – A review with a focus on Pulmonary Hypertension. Journal of Biomechanical Engineering. 135 (6), 61011-15

Kheyfets V.O., Rios L., Smith T., Schroeder T., Mueller J., Murali S., Lasorda D., Zikos A., Spotti J., Reilly Jr J.J., Finol E.A., 2015. Patient-specific computational modeling of blood flow in the pulmonary arterial circulation. Computer Methods and Programs in Biomedicine. 120, 88-101.

Kilner P.J., White P.A., Bishop A., Szwarc R., Redington A.N., 1997. Increased Airway Pressure and Simulated Branch Pulmonary Artery Stenosis Increase Pulmonary Regurgitation After Repair of Tetralogy of Fallot. Circulation. 95, 643-649.

Kiran U., Aggarwal S., Choudhary A., Uma B., Kapoor P.M., 2017. The Blalock and Taussig Shunt Revisited. Annals of cardiac anaesthesia. 20 (3), 323-330.

Kloesel B., DiNardo J.A., Body S.C., 2016. Cardiac Embryology and Molecular Mechanisms of Congenital Heart Disease: A Primer for Anesthesiologists. Anesthesia and analgesia, 123(3), 551–569.

Kordybach-Prokopiuk M., Kowalski M., Spiewak M., Piotrowicz E., Hoffman P., 2015. What can pulmonary regurgitation indices reflect in patients after tetralogy of Fallot repair?. Kardiologia Polska. 1, 31-39.

Kung E., Taylor C., 2011. Development of a Physical Windkessel Module to re-Create In Vivo Vascular Flow Impedance for In Vitro Experiments. Cardiovasc Eng Tech. 2 (1), 2-14.

Landau L.D., Lifshitz E.M., 1970. Theory of Elasticity, vol. 7. Course of Theoretical Physics. Pergamon:Oxford (2nd Edition).

Landes G., 1943. Einige untersuchungen an elektrischen analogieschaltungen zum kreitslaufsystem. Z Biol. 101, 418-429.

Laganà K., Balossino R., Migliavacca F., Pennati G., Bove E.L., de Level M.R., Dubini G., 2005. Multiscale modeling of the cardiovascular system: application to the study of pulmonary and coronary perfusions in the univentricular circulation. J Biomech. 38 (5), 1129-1141.

Le Cras T.D., Tyler R.C., Horan M.P., Morris K.G., Tuder R.M., McMurtry I.F., Johns R.A., Abman S.H., 1998. Effects of chronic hypoxia and altered hemodynamics on endothelial nitric oxide synthase expression in the adult rat lung. J. Clin. Invest. 101, 795–801.

LeVeque R.J., Li Z., 1997. Immersed interface method for stokes flow with elastic boundaries or surface tension. SIAM J Sci Comput. 18, 709-735.

Lewandowska N., Mosiężny J., 2019. Meshing strategy for bifurcation arteries in the context of blood flow simulation accuracy. in E3S Web of Conferences

Li JK-J., 2000. The arterial circulation: Physical principles and clinical applications Humana Press Inc.

Liepsch D., Moravec S., 1982. Measurement and calculations of laminar flow in a ninety degree bifurcation. Journal of Biomechanics. 15, 473-485.

Ling Y., Tang J., Liu H., 2021. Numerical investigation of two-phase non-Newtonian blood flow in bifurcate pulmonary arteries with a flow resistant using Eulerian multiphase model. Chemical Engineering Science. 223, 116424.

Lintermann A., 2021. Computational Meshing for CFD Simulations. In: Clinical and Biomedical Engineering in the Human Nose. Biological and Medical Physics, Biomedical Engineering. Springer, Singapore.

Liu M., Martino S., Salerno M., Quadrio M., 2020. On the Turbulence Modeling of the Blood Flow in a Stenotic Vessel. Journal of Biomedical Engineering. 142, 011009.

Löhner R., 1996. Progress in Grid Generation via the Advancing Front Technique. Engineering with Computers. 12, 186-210.

Löhner R, Mut F., Cebral J., Aubry R., Houzeaux G., 2011. Deflated preconditioned conjugate gradient solvers for the pressure-poisson equation: extensions and improvements. Int J Numer Methods Eng. 87, 2–14.

Loke Y.-H., Capuano F., Mandell J., Cross R.R., Cronin I., Mass P., Balaras E., Olivieri L.J., 2019. Abnormal Pulmonary Artery Bending Correlates With Increased Right Ventricular Afterload Following the Arterial Switch Operation. World Journal for Pediatric and Congenital Heart Surgery,10, 572-581.

Lorensen, W.E., Cline, H.E., 1987. Marching cubes: a high resolution 3D surface construction algorithm. Comput. Graph. 21 (4), 163–169.

Loudon C., Tordesillas A., 1998. The Use of the Dimensionless Womersley Number to Characterize the Unsteady Nature of Internal Flow. J. theor. Biol. 191, 63-78.

Louvelle L.M., Doyle M.G., Van Arsdell G.S., Amon C.H., 2019. A Methodology to Assess Subregional Geometric Complexity for Tetralogy of Fallot Patients. Journal of Engineering and Science in Medical Diagnostics and Therapy, 2, 1-11.

Lyne W.H., 1971. Unsteady viscous flow in a curved pipe. J. Fluid Mech, 45, 13-32.

Lyons I., Parsons L.M., Hartley L., Li R., Andrews J.E., Robb L., Harvey R.P., 1995. Myogenic and morphogenetic defects in the heart tubes of murine embryos lacking the homeo box gene Nkx2-5. Genes and Dev. 9, 1654-1666.

MacElhinney D.B., Parry A.J., Reddy V.M., Hanley F.L., Stanger P., 1998. Left Pulmonary Artery Kinking Caused by Outflow Tract Dilatation After Transannular Patch Repair of Tetralogy of Fallot. Ann Thorac Surg. 65, 1120-1126.

MacKenzie Ross R.V., Toshner M.R., Soon E., Naeije R., Pepke-Zaba J., 2013. Decreased time constant of the pulmonary circulation in chronic thromboembolic pulmonary hypertension. Am J Physiol Heart Circ Physiol. 305 (2), H259-64.

MacMahon B., McKeown T., Record R.G., 1953. The incidence and life expectation of children with Congenital Heart Disease. British Heart Journal. 15, 121-129.

Malatos S., Raptis A., Xenos M., 2016. Advances in Low-Dimensional Mathematical Modeling of the Human Cardiovascular System. J Hypertens Manag. 2:017.

Marelli A., Gatzoulis M.A., Webb G.D., 2018. Adults With Congenital Heart Disease: A Growing Population. In: In: Diagnosis and Management of Adult Congenital Heart Disease, Elsevier. 2-9.

Marino B., Digilio M.C., Grazioli S., Formigari R., Mingarelli R., Giannotti A., Dallapiccola B., 1996. Associated Cardiac Anomalies in Isolated and Syndromic Patients With Tetralogy of Fallot. Am J Cardiol. 77, 505-508.

Marsden A.L., Vignon-Clementel I.E., Chan F.P., Feinstein J.A., Taylor C.A., 2007. Effects of Exercise and Respiration on Hemodynamic Efficiency in CFD Simulations of the Total Cavopulmonary Connection. Annals of Biomedical Engineering. 35 (2), 250-263.

Martini F.H., Nath J.L., Bartholomew E.F., 2014. Fundamentals of Anatomy and Physiology. Pearson, Tenth Edition. 724-775.

Martinsen B.J., Lohr J.L., 2015. Cardiac Development. In: Handbook of Cardiac Anatomy, Physiology, and Devices. Springer, Third Edition, 23-33.

McElhinney D.B., Parry A.J., Reddy M., Hanley F.L., Stanger P., 1998. Left pulmonary artery kinking caused by outflow tract dilation after transannular patch repair of tetralogy of Fallot. Ann Thorac Surg. 65, 1120–6.

McElroy M., Keshmiri A., 2018. Impact of Using Conventional Inlet/Outlet Boundary Conditions on Haemodynamic Metrics in a Subject-Specific Rabbit Aorta. Journal of Engineering in Medicine. 232, 103-113.

Menter F.R., Kuntz M., Langtry R., 2003. Ten Years of Industrial Experience with the SST Turbulence Model. Turbulence, Heat and Mass Transfer 4. In Proceedings of the fourth international symposium on turbulence, heat and mass transfer. Antalya, Turkey. Begell House. 625–632.

Menting M.E., van den Bosch A.E., McGhie J.S., Eindhoven J.A., Cuypers J.A.A.E., Witsenburg M., Geleijnse M.L., Helbing W.A., Roos-Hesselink J.W., 2015. Assessment of ventricular function in adults with repaired Tatralogy of Fallot using myocardial deformation imaging. European Heart Journal-Cardiovascular Imaging. 16, 1347-1357.

Michielon G., Marino B., Formigari R., Gargiulo G., Picchio F., Digilio M.C., Anaclerio S., Oricchio G., Sanders S.P., Di Donato R.M., 2006. Genetic syndromes and outcome after surgical correction of tetralogy of Fallot. Ann Thorac Surg. 81 (3), 968-975.

Migliavacca F., de Level M.R., Dubini G., Pietrabissa R., Fumero R., 1999. Computational fluid dynamic simulations of cavopulmonary connections with an extracardiac lateral conduit. Medical Engineering and Physics. 21 (3), 187-193.

Migliavacca, F., Kilner P. J., Pennati G., Dubini G., Pietrabissa R., Fumero R., de Leval M.R., 1999. Computational fluid dynamics and magnetic resonance analyses of flow distribution between the lungs after total cavopulmonary connection. IEEE Trans. Biomed. Eng. 46 (4), 393–399.

Migliavacca, F., Dubini G., Bove E.L., de Leval M.R., 2003. Computational fluid dynamics simulations in realistic 3-D geometries of the total cavopulmonary anastomosis: The influence of the inferior caval anastomosis. J. Biomech. Eng. 125, 805–813.

Migliavacca F., Balossino R., Pennati G., Dubini G., Hsia T.-Y., de Level M.R., Bove E.L., 2006. Multiscale modelling in biofluidynamics: application to reconstructive paediatric cardiac surgery. J Biomech. 39 (6), 1010-1020.

Mitchell S.C., Korones S.B., Berendes H.W., 1971. Congenital Heart Disease in 56,109 Births. Circulation. 43, 323-332.

Miyasaka K., Takata M., 1993. Flow Velocity Profile of the Pulmonary Artery Measured by the Continuous Cardiac Output Monitoring Catheter. Can J Anaesth. 40 (2), 183-187.

Morgan V.L., Roselli R.J., Lorenz C.H., 1998. Normal Three-Dimensional Pulmonary Artery Flow Determined by Phase Contrast Magnetic Resonance Imaging. Ann Biomed Eng. 26 (4), 557-566.

Morgan C.T., Mertens L., Grotenhuis H., Yoo S.J., Seed M., Grosse-Wortmann L., 2017. Understanding the mechanism for branch pulmonary artery stenosis after the arterial switch operation for transposition of the great arteries. Eur Heart J Cardiovasc Imaging, 18(2), 180-185.

Morgenthau A., Frishman W.H., 2018. Genetic Origins of Tetralogy of Fallot. Cardiol Rev. 26 (2), 86-92.

Moukalled F., Mangani L., Darwish M., 2016. The Finite Volume Method in Computational Fluid Dynamics. An Advanced Introduction with OpenFOAM® and Matlab®. Springer. 113, 3-5.

Murray C.D., 1926. The physiological principle of minimum work applied to the angle of branching of arteries. The Journal of General Physiology. 9, 835-841.

Muster A.J., Van Grondelle A., Paul M.H., 1982. Unequal Pressures in the central pulmonary arterial branches in patients with pulmonary stenosis. Pediatric Cardiology. 2, 7-14.

Neofytou P., Housiadas C., Tsangaris S.G., Stubos A.K., Fotiadis D.I., 2014. Newtonian and Power-Law fluid flow in a T-Junction of rectangular ducts. Theoretical and Computational Fluid Dynamics,.28, 233-256.

Newmark N.M., 1959. A method of computation for structural dynamics Journal of Engineering Mechanics, ASCE. 85 (EM3), 67-94.

Nichols W.W., O'Rourke M.F., 2005. McDonald's Blood Flow in Arteries (5th ed.), London (England): Hodder-Arnold.

Nicolaides R.A., 1987. Deflation of conjugate gradients with applications to boundary value problems. SIAM J. Numer. Anal. 24, 355-365.

Nicolarsen J., Kay J., 2019, Overview of the Intensive Care of the Adult with Congenital Heart Disease. In: Intensive Care of the Adult with Congenital Heart Disease. Springer. 15-24.

Nina V.J.S., 2014. Surgical Repair of Stenotic Pulmonary Arteries in Tetralogy of Fallot. In: Cardiac Surgery-A Commitment to Science, Technology and Creativity (Maluf M.A, Evora R.B, ed). 125-147. IntechOpen.

Nolan D.R., Gower A.L., Destrade M., Ogden R.W., McGarry J.P., 2014. A robust anisotropic hyperelastic formulation for the modelling of soft tissue. J Mech Behav Biomed Mater, 39, 48-60.

Ntsinjana H.N., Capelli C., Biglino G., Cook A.C., Tann O., Derrick G., Taylor A.M., Schievano S., 2014. 3D Morphometric Analysis of the Arterial Switch Operation Using In Vivo MRI Data. Clinical Anatomy, 27, 1212-1222.

Olufsen M.S., Hill N.A., Vaughan G.D.A., Sainsbury C., Johnson M., 2012. Rarefaction and blood pressure in systemic and pulmonary arteries. Journal of Fluid Mechanics. 705, 280-305.

Oosterhof T, van Straten A, Vliegen HW, Meijboom FJ, van Dijk AP, Spijkerboer AM, Bouma BJ, Zwinderman AH, Hazekamp MG, de Roos A, Mulder BJ., 2007. Preoperative thresholds for pulmonary valve replacement in patients with corrected tetralogy of Fallot using cardiovascular magnetic resonance. Circulation. 116, 545-51.

Osher, S., Sethian, J., 1988. Fronts propagating with curvature speed: algorithms based on Hamilton-Jacobi formulations. J. Comput. Phys. 79, 12–49.

Pederson E.M., Stenbog E.V, Frund T., 2002. Flow during exercise in the total cavopulmonary connection measured by magnetic resonance velocity mapping. Heart. 87, 554-558.

Pedley T.J., Schroter R.C., Sudlow M.F., 1971. Flow and pressure drop in systems of repeatedly branching tubes. Journal of Fluid Mechanics 46, 365-383.

Peiffer V., Sherwin SJ., Weinberg PD., 2013. Computation in the rabbit aorta of a new metric – the transverse wall shear stress – to quantify the multidirectional character of disturbed blood flow. J Biomech. 46 (15), 2651-2658.

Peiró J., Sherwin S., 2005. Finite Difference, Finite Element and Finite Volume Methods for Partial Differential Equations. In: Handbook of Materials Modeling. Springer, Dordrecht.

Pekkan K., Kitajima H. D., de Zelicourt D., Forbess J.M., Parks W.J., Fogel M.A., Sharma S., Kanter K.R., Frakes D., Yoganathan A.P., 2005. Total cavopulmonary connection flow with

functional left pulmonary artery stenosis: angioplasty and fenestration in vitro. Journal of the Americal Heart Association. 112, 3264-3271.

Pennati G., Migliavacca F., Duhini G., Pietrabisse R., de Leval M.R., 1997. A mathematical model of circulation in the presence of the bidirectional cavopulmonary anastomosis in children with a univentricular heart. Medical Engineering and Physics. 19 (3), 223-234.

Pennati G., Corsini C., Cosentino D., Hsia T-Y., Luisi S., Dubini G., Migliavacca F., 2011. Boundary conditions of patient specific fluid dynamics modelling of cavopulmonary connections: possible adaptation of pulmonary resistances results in a critical issue for a virtual surgical planning. Interface Focus. 1, 297-307.

Pennati G., Corsini C., Hsia T.-Y., Magliavacca F., 2013. Computational fluid dynamics models and congenital heart diseases. Frontiers in Pediatrics, 1, 1-7.

Peraire J., Peiro J., Formaggia L., Morgan K., Zienkiewicz O.C., 1988. Finite element Euler computations in three dimensions. Int. J. Numer. Meth. Engng. 26, 2135-2159.

Peraire J., Morgan K., 1997. Unstructured mesh generation including directional refinement for aerodynamic flow simulation. In: Finite Elements in Analysis and Design. 25 (3-4), 343-356.

Perktold K., Rappitsch G., 1995. Computer Simulation of local Blood Flow and Vessel Mechanics in a Compliant Carotid Artery Bifurcating Model. J. Biomechanics. 28 (7), 845-856.

Perloff J.K., 1991. Congenital Heart Disease in adults: A new cardiovascular subspecialty. Circulation. 84, 1881-1890.

Perry AE, Steiner TR., 2006. Large-scale vortex structures in turbulent wakes behind bluff bodies. Part 1. Vortex formation processes. Journal of Fluid Mechanics, 174, 233-270.

Peskin C.S., 1972. Flow Patterns Around Heart Valves: A Numerical Method. Journal of Computational Physics. 10, 252-271.

Piccinelli M., Veneziani A., Steinman D.A., Remuzzi A., Antiga L., 1987. A framework for geometric analysis of vascular structures: Application to cerebral aneurysms. IEEE Transactions on medical imaging, 28, 1141-1155.

Pijls N.H.J., van Son J.A.M., Kirkeeide R.L., De Bruyne B., Gould K.L., 1993. Experimental basis of determining maximum coronary, myocardial, and collateral blood flow by pressure measurements for assessing functional stenosis severity before and after percutaneous transluminal coronary angioplasty. Circulation. 86, 1354-1367.

Pirzadeh S. Unstructured viscous grid generation by the advancing-layers method. AIAA J. 32, 1735-1737.

Pirzadeh S., 1996. Three-dimensional unstructured viscous grids by the advancing-layers method. AIAA J. 34, 43-49.

Puga F.J., McGoon D.C., Julsrud P.R., Danielson G.K., Mair D.D., 1982. Complete Repair of Pulmonary Atresia with Nonconfluent Pulmonary Arteries. The Society of Thoracic Surgeons. 35, 36-44.

Qureshi M.U., Hill N.A., 2015. A computational study of pressure wave reflections in the pulmonary arteries. Journal of Mathematical Biology. 71, 1525-1549.

Randles A., Frakes D.H., Leopold J.A., 2017. Computational Fluid Dynamics and Additive Manufacturing to Diagnose and Treat Cardiovascular Disease. Trends in Biotechnology, 35, 1049-1061.

Rao B.N.S., Anderson R.C., Edwards J.E., 1971. Anatomic variations in the tetralogy of Fallot. American Heart Journal. 81, 361-371.

Rapp B.E., 2017. Microfluidics: Modeling, Mechanics, and Mathematics. Elsevier. 609-678.

Rauch R., Hofbeck M., Zweier C., Koch A., Zink S., Trautmann U., Hoyer J., Kaulitz H., Singer H., Rauch A., 2010. Comprehensive genotype-phenotype analysis in 230 patients with tetralogy of Fallot. J Med Genet. 47 (5), 321-31.

Rizvi M.A.D., Katwa L., Spadone D.P., Myers P.R., 1996. The effects of endothelin-1 on collagen type I and type III synthesis in cultured porcine coronary artery vascular smooth muscle cells. Journal Of Molecular And Cellular Cardiology. 28, 243–52.

Rizvi M.A.D., Myers P.R., 1997. Nitric oxide modulates basal and endothelin-induced coronary artery vascular smooth muscle cell proliferation and collagen levels. Journal Of Molecular And Cellular Cardiology. 29, 1779–89.

Rubenstein D.A., Yin W., Frame M.D., 2016. Biofluid Mechanics. (Second Edition) Academic Press. 63-223.

Saad Y., Schultz M.H., 1986. GMRES: a generalized minimal residual algorithm for solving nonsymmetric linear systems. SIAM J. Sci. Statist. Comput., 7, 856-869.

Sabri M.R., Daryoushi H., Gharipour M., 2015. Endothelial function state following repair of cyanotic congenital heart disease. Cardiology in the Young. 25, 222-227.

Samyn M.M., LaDisa J.F., 2016. Novel Applications of Cardiovascular Magnetic Resonance Imaging-Based Computational Fluid Dynamics Modeling in Pediatric Cardiovascular and Congenital Heart Disease. In: Assessment of Cellular and Organ Function and Dysfunction using Direct and Derived MRI Methodologies. 27-56, InTech.

Schiavazzi D.E., Kung E.O., Marsden A.L., Baker C., Pennati G., Hsia T.Y., Hlavacek A., Dorfman A.L., 2015. Hemodynamic effects of left pulmonary artery stenosis after superior cavopulmonary connection: A patient-specific multiscale modeling study. The Journal of Thoracic and Cardiovascular Surgery. 149, 689-696.

Schievano S., Migliavacca F., Normal W., Frigiola A., Deanfield J., Bonhoeffer P., Taylor A.M., 2007. Variations in Right Ventricular Outflow Tract Morphology Following Repair of Congenital Heart Disease: Implications for Percutaneous Pulmonary Valve Implantation. Journal of Cardiovascular Magnetic Resonance, 9, 687-695.

Schievano S., Capelli C., Young C., Lurz P., Nordmeyer J., Owens C., Bonhoeffer P., Taylor A.M., 2011. Four-dimensional computed tomography: a method of assessing right ventricular outflow tract and pulmonary artery deformations throughout the cardiac cycle. Eur Radiol, 21, 36-45.

Schievano S., Taylor A.M., 2020. The Evolution of 3D Modeling in Cardiac Disease, In: 3-Dimensional Modeling in Cardiovascular Disease. Elsevier, 1-15.

Sethian, J.A., 1999. Level Set Methods and Fast Marching Methods. Cambridge Univ. Press.

Shaher R.M., 1964. Complete and inverted transposition of the great vessels. British Heart Journal. 26 (1), 51-66.

Sherstyuk A., 1999. Kernel functions in convolution surfaces: a comparative analysis. The Visual Computer 15, 15– 4. 3.

Shi Y., Lawford P., Hose R., 2011. Review of Zero-D and 1-D Models of Blood Flow in the Cardiovascular System. BioMedical Engineering OnLine, 10:33.

Skaperdas V., Ashton N., 2018. Development of high-quality hybrid unstructured meshes for the GMGW-1 workshop using ANSA. 2018 AIAA Aerospace Sciences Meeting. 1-22.

Skorton D.J., Garson A., 1993. Training in the care of adult patients with Congenital Heart Disease. Cardiology Clinics. 11, 717-720.

Sloth E., Houlind K.C., Oyre S., Kim W.Y., Pedersen E.M., Jørgensen H.S., Hasenkam J.M., 1994. Three-dimensional visualization of velocity profiles in the human main pulmonary artery with magnetic resonance phase-velocity mapping. American Heart Journal, 128, 1130-1138.

Sochi T., 2015. Fluid Flow at Branching Junctions. International Journal of Fluid Mechanics Research. 42, 59-81.

Spazzapan M., Sastry P., Dunning J., Nordsletten D., de Vecchi A., 2018. The use of Biophysical Flow Models in the Surgical Management of Patients Affected by Chronic Thromboembolic Pulmonary Hypertension. Frontiers in Physiology. 9, 1-13.

Spiegel M.R., Lipschutz S., Spellman D., 2009. Vector Analysis. Schaum's Outlines (2nd ed.). USA: McGraw Hill.

Spilker R.L., Feinstein J.A., Parker D.W., Reddy V.M., Taylor C.A., 2007. Morphometry-based impedance boundary conditions for patient-specific modeling of blood flow in pulmonary arteries. Annals of Biomedical Engineering. 35, 546-559.

Steimle J.D., Moskowitz I.P., 2017. TBX5: A Key Regulator of Heart Development. Curr Top Dev Biol. 122, 195-221.

Steinman D.A., Taylor C.A., 2005. Flow Imaging and Computing: Large Artery Hemodynamics. Annals of Biomedical Engineering, 33, 1704-1709.

Stensen N., 1691. Embrio monstro affinis parisiis dissectum. Acta Med Philos Hafniensa. 1, 202-203.

Stergiopulos N, Westerhof BE, Westerhof N., 1999. Total arterial inertance as the fourth element of the windkessel model. Am J Physiol. 276, H81-88.

Struble, L. J., Ji, X., 2001. Rheology. Handbook of Analytical Techniques in Concrete Science and Technology. 333–367.

Sudo K., Sumida M., Yamane R., 1992. Secondary motion of fully developed oscillatory flow in a curved pipe. Journal of Fluid Mechanics, 237, 189-208.

Szymanski M.P., Metaxa E., Meng H., Kolega J., 2008. Endothelial Cell Layer Subjected to Impinging Flow Mimicking the Apex of an Arterial Bifurcation. Annals of Biomedical Engineering. 36, 1681-1689.

Tang B.T., Fonte T.A., Chan F.R., Tsao P.S., Feinstein J.A., Taylor C.A., 2011. Three-

dimensional hemodynamics in the human pulmonary arteries under resting and exercise conditions. Annals of Biomedical Engineering. 39, 347-358.

Tang B.T., Pickard S.S., Chan F.P., Tsao P.S., Taylor C.A., Feinstein J.A., 2012. Wall shear stress is decreased in the pulmonary arteries of patients with pulmonary arterial hypertension: An image-based, computational fluid dynamics study. Pulmonary Circulation, 2, 470-476.

Tao C., Kutchko B.G., Rosenbaum E., Massoudi M., 2020. A Review of Rheological Modeling of Cement Slurry in Oil Well Applications. Energies. 13, 570.

Taylor C.A., Figueroa C.A., Patient-specific Modeling of Cardiovascular Mechanics., 2009. Annu Rev Biomed Eng. 11, 109-134.

Terada M., Takehara Y., Isoda H., Uto T., Matsunaga M., Alley M., 2016. Low WSS and High OSI Measured by 3D Cine PC MRI Reflect High Pulmonary Artery Pressures in Suspected Secondary Pulmonary Arterial Hypertension. Magn Reson Med Sc, 15, 193-202.

Thenappan T., Prins K.W., Pritzker M.R., Scandurra J., Volmers K., Weir E.K., 2016. The critical role of pulmonary arterial compliance in pulmonary hypertension. Annals of the American Thoracic Society. 13, 276-284.

Therrien J, Provost Y, Merchant N, Williams W, Colman J, Webb G., 2005. Optimal timing for pulmonary valve replacement in adults after tetralogy of Fallot repair. Am J Cardiol. 95, 779-782.

Thomas J.B., Antiga L., Che S.L., Milner J.S., Steinman D.A.H., Spence J.D., Rutt B.K., Steinman D.A., 2005. Variation in the carotid bifurcation geometry of young versus older adults. Implications for geometric risk of atherosclerosis. Stroke, 36, 2450-2456.

Van Doormaal M.A., Kazakidi A., Wylezinska M., Hunt A., Tremoleda J.L., Prottis A., Bohraus Y., Gsell W., Weinberg P.D., Ethier C.R., 2012. Haemodynamics in the mouse aortic arch computed from MRI-derived velocities at the aortic root. Journal of the Royal Society Interface, 9, 2834-2844.

Van der Linde D., Konings E.E.M., Slager M.A., Witsenburg M., Helbing W.A., Takkenberg J.M., Roos-Hesselink J.W., 2011. Birth Prevalence of Congenital Heart Disease Worldwide. A Systematic Review and Meta-Analysis, 58, 2241-2247.

Van de Vosse F.N., 2003. Mathematical modelling of the cardiovascular system. Journal of Engineering Mathematics. 47, 175-183.

Vázquez M., Houzeaux G., Koric S., Artigues A., Aguado-Sierra J., Arís R., Mira D., Calmet H., Cucchietti F., Owen H., Taha A., Cela J.M., 2014. Alya: Towards Exascale for Engineering Simulation Codes. arxiv:1404.4881.

Vázquez M., Arís R., Aguado-Sierra J., Houzeaux G., Santiago A., López M., Córdoba P., Rivero M., Cajas J.C., 2015. Alya Red CCM: HPC-Based Cardiac Computational Modelling. In: Klapp J., Ruíz Chavarría G., Medina Ovando A., López Villa A., Sigalotti L. (eds) Selected Topics of Computational and Experimental Fluid Mechanics. Environmental Science and Engineering. Springer, Cham.

Vázquez M., Houzeaux G., Koric S., Artigues A., Aguado-Sierra J., Arís R., Mira D., Calmet H., Cucchietti F., Owen H., Taha A., Burness E.D., Cela J.M., Valero M., 2016. Alya: Multiphysics engineering simulation toward exascale. Journal of Computational Science. 14, 15-27.

Vignon-Clementel I.E., Figueroa C.A., Jansen K.E., Taylor C.A., 2006. Outflow boundary conditions for three-dimensional finite element modeling of blood flow and pressure in

arteries. Comput. Methods Appl. Mech. Engrg. 195, 3776-3796.

Vijayaratnam, P. R. S., O'Brien, C. C., Reizes, J. A., Barber, T. J., & Edelman, E. R., 2015. The Impact of Blood Rheology on Drug Transport in Stented Arteries: Steady Simulations. PLOS ONE. 10(6), e0128178.

Villafañe J., Lantin-Hermoso M.R., Bhatt A.B., Tweddell J.S., Geva T., Nathan M., Elliott M.J., Vetter V.L., Paridon S.M., Kochilas L., Jenkins K.J., Beekman R.H. 3rd, Wernovsky G., Towbin JA., 2014. D-transposition of the great arteries: the current era of the arterial switch operation. J Am Coll Cardiol. 64 (5), 498-511.

Vincent PE., Plata AM., Hunt AAE., Weinberg PD., Sherwin SJ., 2011. Blood flow in the rabbit aortic arch and descending thoracic aorta. J R Soc Interface. 8 (65), 1708-1719.

Walburn, F. J., & Schneck, D. J., 1976. A constitutive equation for whole human blood. Biorheology. 13 (3), 201–210.

Warming R.F., Beam R.M. Upwind Second-Order Difference Schemes and Applications in Aerodynamic Flows. AIAA Journal. 14 (9), 1241-1249.

Westerhof N., Lankhaar J-W., Westerhof B., 2009. The Arterial Windkessel. Med Bio Eng Comput. 47 (2), 131-141.

Yang Y.-Q., Gharibeh L., Li R.-G., Xin Y.-F., Wang J., Liu Z.-M., Qiu X.-B., Xu Y.-J., Xu L., Qu X.-K., Liu X., Fang W.-Y., Huang R.-T., Xue S., Nemer G., 2013. GATA4 loss-of-function mutations underlie familial tetralogy of fallot. Hum Mutat. 34(12), 1662-1671.

Young A., 2014. Patient-Specific Mathematical Modelling of the Hybrid Procedure in the Treatment of Hypoplastic Left Heart Syndrome. PhD Thesis. University of Strathclyde, Glasgow.

Young A., Gourlay T., McKee S., Danton M. H.D., 2014. Computational modelling of the hybrid procedure in hypoplastic left heart syndrome: A comparison of zero-dimensional and three-dimensional approach. Medical Engineering and Physics. 36, 1549-1553.

Yushkevich P.A., Piven J., Cody H., Ho S., Gee J.C., Gerig G., 2015. User-Guided Level Set Segmentation of Anatomical Structures with ITK-SNAP. IJ – 2005 MICCAI Open-Source Workshop.

Yushkevich P.A., Piven J., Hazlett H.C., Smith R.G., Ho S., Gee J.C., Gerig G., 2006. User-guided 3D active contour segmentation of anatomical structures: Significantly improved efficiency and reliability. NeuroImage. 31, 1116-1128.

White F.M., 2011. Chapter 4 – Differential Relations for Fluid Flow. In: Fluid Mechanics. Mcgraw Hill. Seventh Edition. 229-290.

Zhang W., Liu J., Yan Q., Liu J., Hong H., Mao L., 2016. Computational haemodynamic analysis of left pulmonary artery angulation effects on pulmonary blood flow. Interactive CardioVascular and Thoracic Surgery. 23, 519-525.

Zhang Y., 2017. Critical transition Reynolds number for plane channel flow*. Appl. Math. Mech. -Engl. Ed. 38 (10), 1415-1424.

Zhu, S.C., Yuille, A., 1996. Region competition: unifying snakes, region growing, and Bayes/mdl for multiband image segmentation. IEEE Trans. Pattern Anal. Mach. Intell. 18 (9), 884–900 (ISSN 0162-8828).